Changing patterns in Aerosols Optical, Physical, and Chemical properties across the globe

A thesis submitted to

Indian Institute of Space Science and Technology

in partial fulfilment for the award of the Degree of

Doctor of Philosophy

in

Physics

by

Gopika Gupta

National Atmospheric Research Laboratory
Department of Space, Govt. of India
Gadanki-517112, INDIA

June 2022

DECLARATION

I hereby declare that this Ph.D. thesis titled, ***"Changing patterns in Aerosols Optical, Physical, and Chemical properties across the globe"*** submitted in partial fulfilment for the award of the degree of **Doctor of Philosophy** in **Physics,** is based on the original work carried out by me and has not formed the basis for the award of any degree, diploma, associateship, fellowship, or other titles in this or any other Institution or University of higher learning. In keeping with the ethical practice in reporting the scientific information, due acknowledgements have been made wherever the findings of others have been cited.

Place: Thiruvananthapuram
Date: June, 2022

Gopika Gupta
SC18D017

CERTIFICATE

This is to certify that the Ph.D. thesis titled, ***"Changing patterns in Aerosols Optical, Physical, and Chemical properties across the globe"*** submitted by Gopika Gupta to the **Indian Institute of Space Science and Technology, Thiruvananthanpuram,** in partial fulfilment for the award of the degree of **Doctor of Philosophy** in **Physics,** is a bonafide record of original work carried out by her under our supervision. The contents of this thesis, in full or in parts, have not been submitted to any other Institute or University for the award of any degree or diploma.

Dr. M. Venkat Ratnam
Sci./Eng. SG & Head
NARL
Department of Space, Govt. of India
Gadanki-517112

Prof. C.S. Narayanamurthy
Department of Physics
IIST
Thiruvananthapuram-695547

All have their worth and each contributes to the worth of the others.

-J.R.R. Tolkien

Acknowledgements

Despite just the one name on the front page, completing this Ph.D. journey is something I could not have done alone. Firstly, I would like to thank all my teachers because of whom I could reach this point in my life. However, these past four and a half years were full of excitement but at the same time had their challenges too, which has led to a lot of improvement in my work. At every point, I have enjoyed this journey even more due to the great people I have been surrounded with and their constant support.

Words are not enough to express my gratitude towards my research supervisor ***Dr. M. Venkat Ratnam****, Scientist, SG, at National Atmospheric Research Laboratory (****NARL****). Not only a research supervisor but you are also an affectionate guardian as well who has provided me with a continuous motivation which has led to further refinement in my work. Your great vision and belief has nurtured an independent researcher in me. The best thing about working with you Sir is that you give all the freedom to a student to carry out their research activities. It indeed was a privilege for me to have worked under your enriching guidance. A special note of gratitude to my joint-supervisor* ***Prof. C.S. Narayanmurthy****, department of Physics****, IIST****, for his consistent guidance and for helping me in various ways to have smoothly carry out my Ph.D. in IIST.*

My heartfelt thanks to ***Dr. B. L. Madhavan****, Scientist, SD, NARL for his meticulous guidance and suggestions given to me, right from the start of my work. You have imparted the flavour of aerosol science in me and I am very much thankful to you for spending your valuable time during the discussions.*

I also owe gratitude to ***NARL****, Department of Space, for providing the fellowship and the best facilities to carry out my research. I would like to thank* ***Dr. Amit Kumar Patra****, Director, NARL, Gadanki, for providing necessary support and resources to accomplish my work. NARL has also provided me with great opportunities to participate in national and international conferences/ workshops as well.*

I would like to thank ***Dr. D Sam Dayala Dev****, Director, IIST,* ***Dr. YVN Krishnamurthy,*** *Registrar, IIST,* ***Prof. A. Chandrasekar,*** *Dean Academics, IIST,* ***Prof. Raju K George****, Dean R&D, IIST,* ***Prof. Kuruvilla Joseph,*** *Dean SA, IIST and all the other dignitaries at IIST, for their consistent support. My sincere thanks to* ***Prof Sudheesh Chethil****, HOD, Department of Physics, IIST. I would also like to mark my special gratitude to all the*

members of the Academic and Doctoral Committee at NARL for their insightful and critical comments during different phases of the thesis. My deepest gratitude to the Doctoral Committee external members, ***Dr. Tarun Kumar Pant****,* ***Space Physics Laboratory,*** *and* ***Dr. M. Govindhan Kutty****, at IIST,.*

At this point, I fondly thank my NARL family, ***Dr. V. Ravi Kiran****,* ***Smt. A. Sai. Krishnaveni****,* ***Dr. Shaik Ghouse Basha****,* ***Mr. V. N. Santhosh, Ms. Jayasri, and Ms. S. Sindhu*** *for their loving support. A special thanks to* ***Dr. D. Chaitanya Jain*** *for providing encouragement and kind-hearted affection during my research work. I am very thankful to my dear friends at NARL,* ***Ms. Renju****,* ***Dr. A. Hemanth Kumar, Dr. S.T. Akhil Raj, and Dr. P. Prasad*** *for their moral support and for lighting up my time at NARL. I would also like to thank* ***Dr. Sanjeev Dwivedi*** *for his fruitful discussions during my initial Ph.D. period. I wish to acknowledge my friend,* ***Mr. Sajith****, at IIST, for their help in university matters.*

It is my pleasure to thank all those working in various departments of NARL such as ***Accounts****,* ***Administration****,* ***CMD****,* ***CDMG****, and* ***Canteen*** *for their kind cooperation. I would also like to thank the* ***Aerosol Radiation and Trace Gases Group****, NARL technical and scientific staff for their help during various stages of my work.*

Lastly, words are not enough to thank my grandfather ***Mr. B.D. Gupta****, who has waited a long for this achievement. It is all because of your blessings and wishes that today I am able to accomplish this stage in my life and could make you proud. Also, I would be remiss in not mentioning my parents (****Mr. Rajesh*** *and* ***Mrs. Sudha Gupta****), brother (****Mr. Karan****), and sister-in-law (****Mrs. Pooja****) for always giving me moral support throughout my work. A special mention to my niece, baby* ***Raadhya****, for always giving me much needed happiness. Last but not the least, a very special thanks to my best friend* ***Ms. Bindu,*** *who has always stood firm with me through my thick and thin, since years. Without you, I may not have been able to end this journey. Finally, I would like to thank all my aunts, uncles, cousins, and well-wishers for their constant encouragement in completion of this work successfully.*

I am obligated to you all.

Gopika Gupta

Contents

Preface

Aerosols are considered to be the most concerned human induced pollutants in the atmosphere, having a net negative radiative forcing, which can offset nearly one-third of the global warming induced by the greenhouse gases. However, the evaluation of the direct effects of the aerosols (known as aerosol-radiation interaction (ARI)) involves an uncertainty with a factor of three, due to their highly variable nature with short residence time, and the uneven vertical distribution. Most of the uncertainties in evaluation of ARI emerges from its inadequate observational pieces of evidences, which further leads to the inaccurate representation of aerosols in the state-of-the-art global climate models.

*In this regard, the best parameter to quantify the long-term changes in ARI is the Aerosol Optical Depth (AOD). The evaluation of the AOD measurements are strongly influenced by the vertical distribution of aerosols, which was conventionally assumed to be decreasing exponentially with the altitude variations. Nevertheless, the recent understanding has depicted that the aerosols can be transported to the altitudes above ABL and the formation of these kinds of layers is popularly known as 'Elevated Aerosols Layers' or EALs. However, the presence of different types of aerosols in the EAL altitudes can alter the thermodynamic stability of the atmosphere and hence modifies the cloud properties as well. Therefore, the characterization of the aerosols at these altitudes becomes very crucial. Thus, the aim of the thesis entitled '***Changing patterns in Aerosols Optical, Physical, and Chemical properties across the globe****' is to find the long-term changing patterns in the 3-dimensional (3D) distribution of the various columnar and vertical properties of the aerosols, across the globe. This objective is achieved by using the multi-source ground-based and space-borne/ reanalysis datasets. Although aerosols peak near their source regions but the background meteorology also plays a crucial role in the evaluation of the 3D distribution of the aerosols. Therefore, to evaluate the long-term changing patterns in various aerosol properties, a multivariate linear regression trend model has been implemented in this study, in which the highly variable background dynamical aspects are isolated from the dataset. In this regard, the present thesis consists of 7 Chapters, out of which **Chapter 1** introduces the topic and details the complex problems to be addressed in the study. **Chapter 2** elaborates the instruments, datasets, and techniques used to carry out the objectives marked in the first chapter.*

The uncertainty in the evaluation of vertical distribution of aerosols arises due to the transport of aerosols to the altitudes above the atmospheric boundary layer via long-range

transport processes or being directly injected at these altitudes or via the convective activities taking place. Therefore, a comprehensive understanding explaining the complete vertical distribution and the dominant aerosols types, using LIght Detection And Ranging (LIDAR), has been evaluated in ***Chapter 3.*** *The presence of two EALs over the Gadanki region during monsoon season i.e., one in free troposphere (FT) and the other in Upper Troposphere and Lower Stratosphere (UTLS) altitudes, is found in this study. It is further supported with the background meteorology playing a crucial role in the formation of EALs.*

However, the AOD parameter is a composition of the highly substantial variations in the complex refractive index, size distribution, and optical properties of the aerosols. To fulfil this objective across the globe, a fusion of numerous aerosol products such as ground-based, space-borne, and reanalysis, at regular grids is the need of hour. In this regard, in ***Chapter 4****, the long-term variations in the total AOD has been evaluated using multivariate linear regression trend analysis approach. Here, a high (above 0.7) to medium (from 0.3 to 0.7) spatial correlation is observed among all the satellite/reanalysis datasets with respect to ground-based measurements. From this study, 8 regions of interests (RoI) are selected where huge changes due to aerosols over nearly two decades i.e., between 2001 and 2020, are spotted. Over these 8 selected RoI, the characterization of the aerosols optical, physical, and morphological properties and their long-term variations are finally comprehended in* ***Chapter 5****. Region-wise analysis has shown that the decrease (increase) in the total AOD trends observed over North-Eastern America, South America, Europe, North-Western Africa, and Eastern and Central China (Indian) regions are mainly in connection with the decrease (increase) in the fine-mode and scattering aerosols. This study also details the region-wise response accompanying the implementation of stringent mitigation strategies to ensure accurate quantification of the changing aerosol patterns in the atmosphere.*

The spatial and temporal variations in the columnar and vertical distribution of aerosols different chemical composition and their long-term variations are presented in ***Chapter 6****. The columnar distributions due to different components of aerosols such as dust, sea salt, black carbon, organic carbon, and sulfate are apprehended using the reanalysis datasets. However, the vertical long-term variations due to the mixture of the different components of aerosols such as polluted dust, dust, and elevated smoke are examined using the satellite dataset, over all the selected 8 RoI. Along with this, the study is further sub-divided based on its measurement timings such as during the day-time and night-time and the altitude-wise i.e., FT and ABL, distribution of aerosols is also discussed.*

Finally, the summary and the future scope of the thesis is presented in ***Chapter 7****.*

Abbreviations

A	**A**qua
A-Train	**A**fternoon-**Train**
aAOD	**A**bsorbing **A**erosol **O**ptical **D**epth
ABL	**A**tmospheric **B**oundary **L**ayer
AE	**A**ngstrom **E**xponent
AERONET	**AE**rosol **RO**botic **NET**work
AO	**A**nnual **O**scillations
AOD	**A**erosol **O**ptical **D**epth
ARI	**A**erosol-**R**adiation **I**nteraction
AS	**A**rabian **S**ea
ASM	**A**sian **S**ummer **M**onsoon
ATAL	**A**sian **T**ropopause **A**erosol **L**ayer
AVHRR	**A**dvanced **V**ery **H**igh **R**esolution **R**adiometer
BATAL	**B**alloon measurements of **A**sian **T**ropopause **A**erosol **L**ayer
BB	**B**iomass **B**urning
BC	**B**lack **C**arbon
BoB	**B**ay **o**f **B**engal
BrC	**B**rown **C**arbon
CAA	**C**lean **A**ir **A**ct
CAD	**C**loud **A**erosol **D**iscrimination
CALIOP	**C**loud **A**erosol **Li**dar with **O**rthogonal **P**olarization
CALIPSO	**C**loud-**A**erosol **L**idar and **I**nfrared **P**athfinder **S**atellite **O**bservation
cAOD	**C**oarse-mode **A**erosol **O**ptical **D**epth
CCN	**C**loud **C**ondensation **N**uclei
CI	**C**entral **I**ndia
CM	**C**lean **M**arine
COH	**C**onvective **O**utflow **H**eight
CPT	**C**old **P**oint **T**ropopause
D	**D**imensional
Db	**D**eep **b**lue
DMS	**D**i**m**ethyl **S**ulfide
DPSS	Pulsed **D**iode **P**umped **S**olid **S**tate Laser

Dt	**D**ark **t**arget
DT	**D**ay **t**ime
DU	**Du**st
EAL	**E**levated **A**erosol **L**ayer
ECC	**E**astern and **C**entral **C**hina
EE	**E**xpected **E**rror
EHP	**E**levated **H**eat **P**ump
EMR	**E**lectro-**M**agnetic **R**adiations
ENSO	**E**l-**N**iño **S**outhern **O**scillations
EOF	**E**mpirical **O**rthogonal **F**unctions
EOS	**E**arth **O**bserving **S**ystems
ERA	**E**uropean Centre for Medium-Range Weather Forecasts **R**e-**a**nalysis
ES	**E**levated **S**moke
EU	**Eu**rope
fAOD	**F**ine-mode **A**erosol **O**ptical **D**epth
FMF	**F**ine **M**ode **F**raction
FOV	**F**ield **o**f **V**iew
FRSM	**F**ull **R**esolution **S**earch **M**ode
FT	**F**ree **T**roposphere
GEOS-5	**G**oddard **E**arth **O**bserving **S**ystem-V**5**
GHG	**G**reen **H**ouse **G**ases
GOCART	**Go**ddard **C**hemistry, **A**erosol, **R**adiation, and **T**ransport
HERA	**H**ybrid **E**xtinction **R**etrieval **A**lgorithm
HYSPLIT	**Hy**brid **S**ingle-**P**article **L**agrangian **I**ntegrated **T**rajectory
ICARB	**I**ntegrated **C**ampaign for **A**erosols, gases, and **R**adiation **B**udget
IGP	**I**ndo-**G**angetic **P**lain
INDOEX	**Ind**ian **O**cean **Ex**periment
IR	**I**nfra**R**ed
IST	**I**ndian **S**tandard **T**ime
LIDAR	**LI**ght **D**etection **A**nd **R**anging
LLJ	**L**ow **L**evel **J**et
LR	**L**inear **R**egression
LST	**L**ocal **S**tandard **T**ime

LUT	**L**ook-**U**p **T**able
MAE	**M**ean **A**bsolute **E**rror
ME	**M**iddle-**E**ast
MERRA-2	**M**odern-**E**ra **R**etrospective analysis for **R**esearch and **A**pplication-V**2**
MISR	**M**ultiangle **I**maging **S**pectro-**R**adiometer
MLR	**M**ultivariate **L**inear **R**egression
MODIS	**MOD**erate Resolution **I**maging **S**pectroradiometer
MPL	**M**icro-**P**ulse **L**idar
MPLNET	**M**icro-**P**ulse **L**idar **Net**work
N	**N**umber of samples quantified
nAOD	**N**on-spherical **A**erosol **O**ptical **D**epth
NARL	**N**ational **A**tmospheric **R**esearch **L**aboratory
Nd: YAG	**N**eo**d**ymium-doped **Y**ttrium **A**luminium **G**arnet
NE	**N**orth-**E**ast
NEA	**N**orth **E**astern **A**merica
NH	**N**orthern **H**emisphere
NR	**N**it**r**ates
NRCS	**N**ormalised **R**ange **C**orrected **S**ignal
NT	**N**ight **t**ime
NWA	**N**orth **W**estern **A**frica
OA	**O**rganic **A**erosols
OC	**O**rganic **C**arbon
PD	**P**olluted **D**ust
POM	**P**articulate **O**rganic **M**atter
PV	**P**redicted **V**alue
QBO	**Q**uasi-**B**iennial **O**scillations
RCS	**R**ange **C**orrected **S**ignal
RF	**R**adiative **F**orcing
RH	**R**elative **H**umidity
RMB	**R**elative **M**ean **B**ias
RMSE	**R**oot **M**ean **S**quare **E**rror
RoI	**R**egion **o**f **I**nterest
SAA	**S**outh **A**tlantic **A**nomaly

SAF	**S**outh **A**frica
SAGE	**S**tratosphere **A**erosol and **G**as **E**xperiment
SAM	**S**outh **Am**erica
SAO	**S**emi-**A**nnual **O**scillations
sAOD	**S**cattering **A**erosol **O**ptical **D**epth
SC	**S**olar **C**ycle
SCA	**S**cene **C**lassification **A**lgorithm
SD	**S**tandard **D**eviation
SE	**S**tandard **E**rror
SEA	**S**outh and **E**ast **A**sia
SF	**S**ul**f**ate
SH	**S**outhern **H**emisphere
SI	**S**outh **I**ndia
SIBYL	**S**elective **I**terated **B**oundar**y** **L**ocator
SM	**Sm**oke
SNR	**S**ignal to **N**oise **R**atio
SS	**S**ea **S**alt
SSA	**S**ingle **S**cattering **A**lbedo
SVU	**S**ri **V**enkateswara **U**niversity
SW	**S**outh-**W**est
SWJ	**S**ubtropical **W**esterly **J**et
T	**T**erra
TEJ	**T**ropical **E**asterly **J**et
TOA	**T**op **o**f the **A**tmosphere
TOMS	**T**otal **O**zone **M**apping **S**pectrometer
TP	**T**ibetan **P**lateau
TTL	**T**ropical **T**ropopause **L**ayer
TV	**T**rue **V**alue
UTLS	**U**pper **T**roposphere **L**ower **S**tratosphere
UV	**U**ltra-**V**iolet
V	**V**ersion
VA	**V**olcanic **A**sh
WCT	**W**avelet **C**ovariance **T**ransform

Nomenclature

$\boldsymbol{\alpha_{aer}}$	Aerosol volume extinction coefficient
$\boldsymbol{Q_{ext}}$	Extinction efficiency of the particles
α(t)	Seasonal coefficient
β(t)	Seasonal trend coefficient
γ (t)	Seasonal QBO coefficient
δ (t)	Seasonal Solar coefficient
ε (t)	Seasonal ENSO coefficient
λ	Wavelength
$\boldsymbol{\sigma_{ext}}$	Extinction cross-section
r	Range distance
R	Correlation coefficient
P(r)	Backscattered raw signal
P_0	Laser pulse power
$\boldsymbol{S_a}$	Lidar Ratio
$\boldsymbol{\beta}$	Mean attenuated backscatter coefficient
$\boldsymbol{\chi}$	Integrated total color ratio
$\boldsymbol{\chi_{aer}}$	Particulate color ratio
$\boldsymbol{\beta_{aer}}$	Particulate depolarization ratio
$\boldsymbol{\eta(r)}$	Multiple scattering by particles
$\boldsymbol{T^2(r)}$	Probability of two-way transmission of light
$\boldsymbol{T_y}$	Transmission of absorbing gases
T (t)	Total AOD time series
V	Digital voltage
$\boldsymbol{V_0}$	Extra-terrestrial voltage

Chapter 1

Introduction to Atmospheric Aerosols

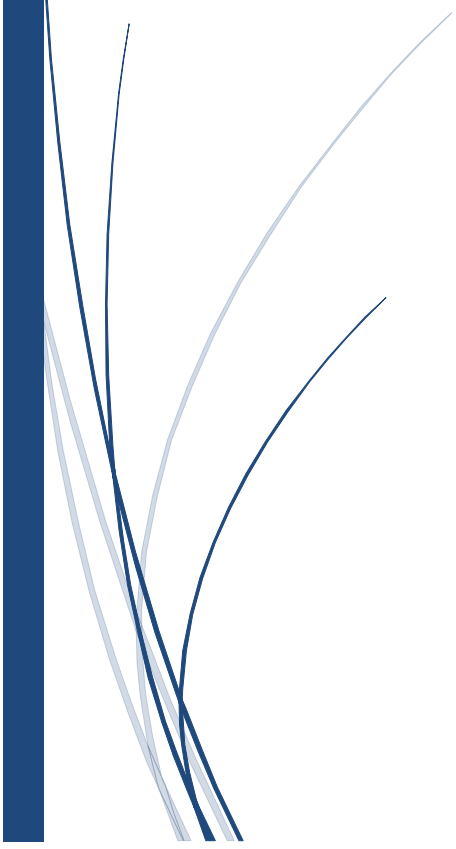

1.1 Background

The rapid increase in industrialization or economic developments has led to an increase in the burden on the atmosphere due to the atmospheric pollutants. Today, the current topic worldwide concerns global warming (IPCC, 2021; Ramanathan and Carmichael, 2008) and its associated climatic impacts, which are due to the major climate forcing agents, such as the anthropogenically induced infrared (IR)-active Greenhouse Gases (GHG). Specifically, the globally averaged temperatures have been rising at the rate of 0.17°C per decade since the 1970s (NOAA et al., 2016), ultimately influencing the global retreat of the glaciers. Human (or anthropogenic) interferences are considered to be the main drivers for this increase (**Figure 1.1**), which consequently leads to the increase in the sea levels, ocean melting, and ocean acidification events (IPCC, 2021). Apparently, the aerosols (considered as the short-lived climate forcers) are considered to partially mitigate the one-third of the warming effects induced by the GHG by exhibiting the cooling effects at the Top of the Atmosphere (TOA) and the surface of Earth (known as solar dimming).

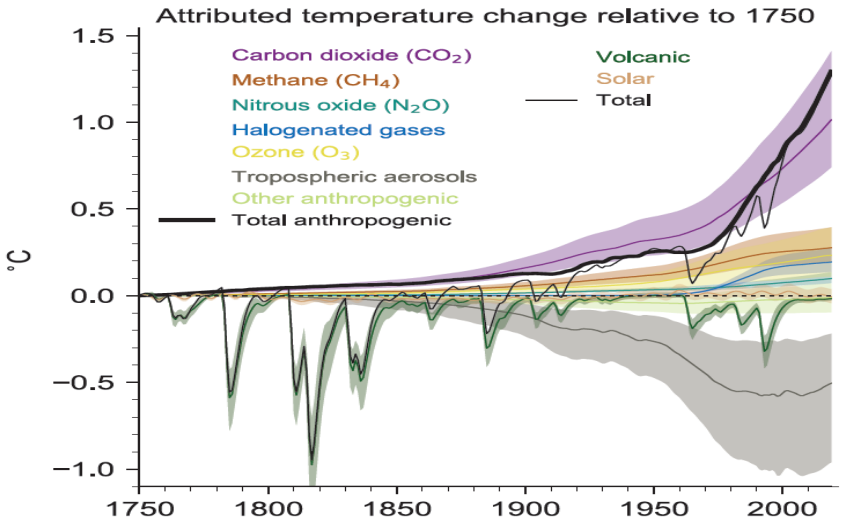

Figure 1.1 *The variations in the global surface temperature (between 1750 and 2019) for the key climate factors (based on IPCC, 2021).*

However, the radiative influences exerted by the highly variable anthropogenic aerosols are even more adverse than that of well-mixed GHG present in the atmosphere (Charlson et al., 1992). One of the major impacts due to aerosols concerns the Lethal smog (smoke (SM)+fog) event emerged in London for nearly five consecutive days in

December 1952, the cause of which was associated with the combination of pollution caused by the industries and the high-pressure weather conditions (Wilkins, 1953), thereby killing nearly 4000 people. This marked the importance of understanding aerosols and their effect on climate in the scientific community. The El Chichón volcanic eruption in 1982 produced the high sulfur explosions, which devastated nearly nine villages at that time (Varekamp, 1984), and subsequently, the eruption of Mount Pinatubo in the Philippines in the year 1991 was considered to be one of the most significant eruptions of the 20th century (Hansen et al., 1992). These major events have caused many perturbations in the stratospheric sulfate (SF) layer or '*Junge layer*', the effect of which was seen up to years later. Further, the increase of the SF aerosols in the stratosphere led to the decrease in the stratospheric ozone in the Antarctic region due to the emissions of anthropogenic chemicals and hence was reported in Farman et al. (1985).

In this scenario of heating of Earth, there was a coincident decrease in the precipitation and globally averaged surface temperatures (known as 'hiatus') during the 1950s and 1960s, attributed to the influence of anthropogenic aerosols (Wilcox et al., 2013). Also, the very recent global warming hiatus from 1998 to 2012 was linked to the factors such as the cooling up of the tropical eastern pacific ocean due to inter-decadal natural variability (Kosaka and Xie, 2013). One of the plausible reasons for this includes the reduction in the heat content at the surface (due to the increase in aerosols in the atmosphere) or dimming effects due to the aerosols. However, till date, only a partial understanding has been made on this topic due to its highly variable nature (or short residence time), which depends mainly on their regional sources and therefore, only a limited number of observations are available for the same. Unlike aerosols, the GHG are thoroughly mixed in the atmosphere and hence their behaviour is widely understood till now. But, since 1990s, many advancements have been made in understanding the role of aerosols on climate using different measurement techniques, (Charlson et al., 1992; Jacobson, 2016; Myhre et al., 2013; Ramanathan and Carmichael, 2008), after the outbreak of the major events mentioned above. These available long-term datasets can be further explored to understand the in-depth behaviour of the aerosols, but before that, a detailed understanding of aerosols characteristics is required and hence is discussed in the subsequent section.

1.2 Aerosols in the Earth's Atmosphere

Aerosols can be classified based on their sources, size distribution, shape distributions, composition, and optical properties. Indeed, the sources of the atmospheric aerosols have been further divided as either primary or secondary, based on their chemical reactions, defined as follows:

(**a**) **Primary aerosols** are directly emitted into the atmosphere in the solid phase through bulk-to-particle conversion, including lifting of dust (DU) aerosols (from the desert regions, agriculture, deforestation, or roads), wind erosions of tilled land surfaces, sea salt (SS) or marine aerosols, volcanic ash (VA), SM from the forest fires, and biogenic aerosols (which includes fragments of plants and animals, pollen, bacteria, algae, fungi, viruses, spores).

(**b**) **Secondary aerosols** involve the chemical conversion of the gas particles to less volatile species, followed by the nucleation and condensation processes. These particles are generally hygroscopic in nature and can act as cloud condensation nuclei (CCN) for the cloud formations. Here, the main precursors include SF, nitrates (NR), organic, carbonaceous materials, etc (Bauer et al., 2007a, 2007b). The SF aerosols are mainly produced from H_2S, CS_2, COS, and dimethyl sulfide (DMS), whereas the NR aerosols can be produced from N_2O_5, organics (released from biospheres), volatile organic compounds, and the carbonaceous aerosols (emitted from biomass burning activities) (Wallace, John M, 2006).

The details of the sources due to each aerosol type are given in **Figure 1.2**. Another important parameter to characterize aerosols includes their size distribution, which has been classified based on their radius, into three following categories:

(**a**) **Nucleation-mode** (1-10 nm) aerosols are formed by the gas-to-particle conversion mechanism. These aerosols are numerous in concentration but are least stable in the atmosphere. These aerosols can grow (in a couple of hours) to **Aitkin-mode** (10-100 nm) aerosols via coagulation or condensation processes.

(**b**) **Accumulation-mode** (100-1000 nm) aerosols are formed either from the Aitkin aerosol (through coagulation) or via direct emissions (can include natural/ anthropogenic). These aerosols are considered to be the most stable, having high residence times and high scattering efficiencies in the visible region.

(**c**) **Coarse-mode** (> 1000 nm) aerosols are formed by bulk-to-particle conversion, which includes natural aerosols such as DU, VA, and SS, but with low number concentrations in the atmosphere.

Hence, the nucleation-mode and coarse-mode aerosols have a lesser residence time in the atmosphere when compared with the accumulation-mode aerosols (Seinfeld and Pandis, 2006). Also, the accumulation-mode aerosols have severe impacts on human health as well. Further detailed information on the size distribution due to various aerosol types has been provided in **Figure 1.2**.

Along with this, the shape of the aerosols is considered to be arbitrarily 3-dimensional (3D), which are further classified as (**a**) spheres, which are the isometric particles having equal contributions among all dimensions, or (**b**) the fiber-like structure, having a comparatively large length in one direction, like mineral fibers, and (**c**) platelets, having two large dimensions, like leaf fragments (Steven N. Rogak, 1993). Generally, the aerosols made via gas-to-particle conversions are spherical in shape, but those formed by mechanical disintegration are irregular in shape. Therefore, for simplicity, the aerosols are defined based on size using the concept of the diameter of equivalent spheres, including **aerodynamic diameter** (Mark et al., 1998) or **stokes diameter**.

Thus, all the above characteristics have shown that the aerosols exhibit polydisperse nature. However, the micro-physical processes (such as internal or external mixing) involved in the compositions of aerosols (which are closely related to the regional emission sources) lead to further complexity in studying the aerosol properties. For instance, among the various aerosol species, SF (SO_4^{2-}), NR (NO_3^-), and ammonium (NH_4^+) are one of the prime contributors directly scattering the incoming radiations and thus exhibiting cooling effects on the atmosphere. These aerosols can further act as CCN as they are hygroscopic in nature, as shown in Mitchell and Johns, 1997 and **Figure 1.2**. Ammonium is considered as the primary cation associated with the SF aerosols in the continental regions (Wallace, John M, 2006). The aerosols optical properties exhibited by these aerosols can be altered when they are coated with the other particles, including black carbon (BC) and DU aerosols (Bauer et al., 2007a; Kahnert, 2017; Lim et al., 2018; Ma et al., 2020). However, the urban (remote) regions have high contributions from the SF as well as carbonaceous (SF) aerosols (Seinfeld

and Pandis, 2006). On the other hand, the aerosols such as BC are among the absorbing aerosols having strong absorption of radiations ranging from the ultra-violet (UV) to near IR wavelengths and hence are hydrophobic in nature (**Figure 1.3**).

Aerosol Species	Size Distribution	Main Sources	Main Sinks	Tropospheric Lifetime	Key Climate Relevant Properties
Sulphate	Primary: Aitken, accumulation and coarse modes Secondary: Nucleation, Aitken, and accumulation modes	Primary: marine and volcanic emissions. Secondary: oxidation of SO_2 and other S gases from natural and anthropogenic sources	Wet deposition Dry deposition	~ 1 week	Light scattering. Very hygroscopic. Enhances absorption when deposited as a coating on black carbon. Cloud condensation nuclei (CCN) active.
Nitrate	Accumulation and coarse modes	Oxidation of NO_x	Wet deposition Dry deposition	~ 1 week	Light scattering. Hygroscopic. CCN active.
Black carbon	Freshly emitted: <100 nm Aged: accumulation mode	Combustion of fossil fuels, biofuels and biomass	Wet deposition Dry deposition	1 week to 10 days	Large mass absorption efficiency in the shortwave. CCN active when coated. May be ice nuclei (IN) active.
Organic aerosol	POA: Aitken and accumulation modes. SOA: nucleation, Aitken and mostly accumulation modes. Aged OA: accumulation mode	Combustion of fossil fuel, biofuel and biomass. Continental and marine ecosystems. Some anthropogenic and biogenic non-combustion sources	Wet deposition Dry deposition	~ 1 week	Light scattering. Enhances absorption when deposited as a coating on black carbon. CCN active (depending on aging time and size).
... of which brown carbon	Freshly emitted: 100–400 nm Aged: accumulation mode	Combustion of biofuels and biomass. Natural humic-like substances from the biosphere	Wet deposition Dry deposition	~ 1 week	Medium mass absorption efficiency in the UV and visible. Light scattering.
... of which terrestrial PBAP	Mostly coarse mode	Terrestrial ecosystems	Sedimentation Wet deposition Dry deposition	1 day to 1 week depending on size	May be IN active. May form giant CCN
Mineral dust	Coarse and super-coarse modes, with a small accumulation mode	Wind erosion, soil resuspension. Some agricultural practices and industrial activities (cement)	Sedimentation Dry deposition Wet deposition	1 day to 1 week depending on size	IN active. Light scattering and absorption. Greenhouse effect.
Sea spray	Coarse and accumulation modes	Breaking of air bubbles induced e.g., by wave breaking. Wind erosion.	Sedimentation Wet deposition Dry deposition	1 day to 1 week depending on size	Light scattering. Very hygroscopic. CCN active. Can include primary organic compounds in smaller size range
... of which marine POA	Preferentially Aitken and accumulation modes	Emitted with sea spray in biologically active oceanic regions	Sedimentation Wet deposition Dry deposition	~ 1 week	CCN active.

Figure 1.2 *The various properties of the atmospheric aerosol species (based on IPCC, 2013).*

BC aerosols are perceived as the second most responsible factor for global warming after the carbon dioxide emissions in the atmosphere (Ramanathan and Carmichael, 2008). The BC aerosols are mainly emitted with the condensable gases therefore, these aerosols age quickly due to coagulation, or coating processes (Riemer et al., 2009) and hence becomes internally mixed with the other species (Kompalli et al., 2021; Ma et al., 2020; Wu et al., 1992). The mass absorption coefficients due to these aerosols are amplified when internally mixed (Khalizov et al., 2009; Peng et al., 2016; Scarnato et al., 2013; Xu et al., 2018). Furthermore, recently, it is realised that the organic carbon (OC) aerosols can absorb light in the UV wavelength region, known as Brown Carbon (BrC) (Kirchstetter et al., 2004; Shamjad et al., 2015). However, the mass concentration of the OC aerosols can be converted to the Organic Aerosols (OA), which depends on the source and age of the particle (Russell et al., 1999; Xing et al., 2013). Lastly, the DU aerosols are one of the most significant contributors to the total aerosols concentration over the Earth as they cover nearly one-third of the land region.

The absorption of these aerosols also decreases with the increasing wavelength in the visible wavelength range. This property of the DU aerosols is similar to the BrC aerosols, but since the DU aerosols have a larger size, higher density, and are non-spherical in shape characteristics (Li et al., 2013), thereby distinguishes both the species. Also, there is a compelling evidence that the DU aerosols significantly impact large-scale dynamical systems such as tropical cyclones (Rosenfeld et al., 2012). In addition to this, the DU aerosols also have a considerable impact on the air quality (Prospero, 1999), radiation budget (Li et al., 1996), and suppress the clouds and precipitation properties (Rosenfeld et al., 2001). However, it has also been stated in the previous studies that the overall natural aerosols contributes up to 81% to the total aerosol mass and nearly 52% to the column optical depth (Satheesh and Krishna Moorthy, 2005). Nevertheless, after their short residence time (i.e., days to weeks, see **Figure 1.2**), aerosols suspended in the atmosphere are finally removed from the atmosphere by:

(**a**) **Dry deposition:** This mechanism takes place in a simple three steps, as mentioned in Wu et al. (1992). The first step includes carrying particles from the lowest levels of the atmosphere to the viscous sub-layer surrounding the particle. Then, the second step involves the transport of particles via the Brownian diffusion or the inertial forces such as impaction and sedimentation. Lastly, the particles interact with the surface. Also, according to the Einstein's theory of Brownian motion, the particles suspended in the atmosphere are under the influence of the gravitational force, against the viscous force exerted by the surrounding medium, based on which the residence time (=**M/F**, where **M** is the amount of constituents (kg), and **F** is the rate of removal (kg/sec)) of the particles are decided.

This is the most efficient removal mechanism for the aerosols, which depends on the size, meteorology, and the underlying surfaces. For instance, the coarse-mode aerosols are removed under the influence of gravitational or turbulent settling. The Brownian motion has a lesser effect on the coarse-mode aerosols than the gravitational settling, and hence they are scavenged by gravity via deposition on the surface. Impaction or diffusional transfer and sedimentation to the surface are essential dry deposition removal mechanisms. Also, the coagulation of the ultrafine particles can grow to form bigger particles, hence reducing the number of ultrafine particles in the atmosphere.

(**b**) **Wet removal:** In this mechanism, aerosols are removed by either in-cloud or below-cloud scavenging. In the former case, the aerosols acts as CCN and are usually scavenged out or rain-out, known as 'nucleation scavenging'. While in the latter case, aerosols are removed by the falling hydrometeors from the clouds or wash-out by raindrops (Seinfeld and Pandis, 2006).

The inhalation of the aerosols can also be considered a further sinking mechanism. However, during this short lifespan or residence time of the aerosols (see **Figure 1.2**) in the atmosphere, they interact with the incoming radiations and ultimately impacting the climate, thereby influencing the Earth's energy budget, and hence this topic will be elaborated in the following section.

1.3 Aerosol-Radiation interaction (ARI)

The solar radiations reaching the Earth (maximum in the visible region of the spectrum) gets attenuated by the atmosphere's aerosols. This effect which alters the climate system through the direct interaction of radiations with aerosols via scattering (leading to an increase in albedo and thus cooling at the surface) or absorption (leading to diabetic heating) processes, is termed the aerosols *Direct effect* (Charlson et al., 1992). However, apart from this, the aerosols can also interact indirectly with the atmosphere by acting as a CCN and thereby altering the cloud micro-physical properties such as cloud albedo (*first indirect effect*, (Twomey, 1977)) and cloud effective radius (*second indirect effect*, (Albrecht, 1989)) as well.

In **Figure 1.3**, a comparison has been made between the Radiative Forcing (RF) induced by all the GHGs, carbon dioxide, absorbing aerosols, and non-absorbing aerosols in the atmosphere. We can see that the total dimming effects exhibited by the aerosols are -4.4 W/m^2 (due to combined direct and indirect effects), where -3.4 W/m^2 is from the direct effects whereas -1 W/m^2 is from the indirect effects (Ramanathan and Carmichael, 2008). However, massive heating in the atmosphere has been observed due to the direct effects of the aerosols alone (~ +2.6 W/m^2), which is much higher than the RF induced by GHGs (~ +1.4 W/m^2) and carbon dioxide (~ +1 W/m^2), as seen from **Figure 1.3**, and hence it becomes essential to evaluate the aerosols direct effects.

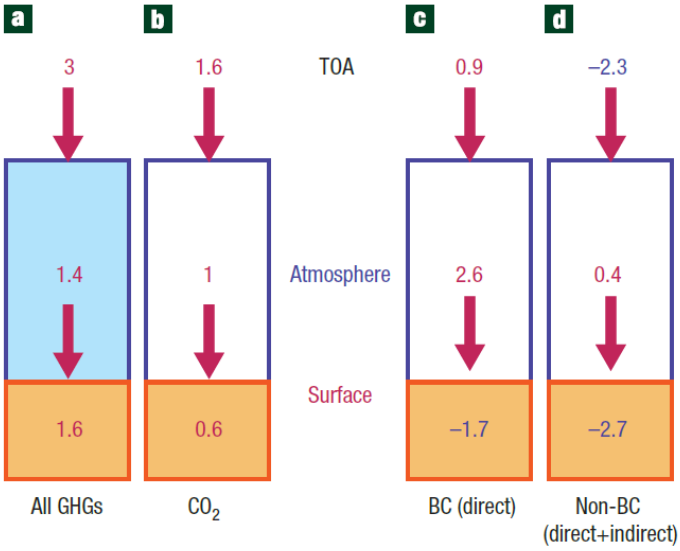

Figure 1.3 *The diagram illustrating the comparison between RF from (a) all GHGs (3, 1.4, 1.6), (b) carbon dioxide (1.6, 1, 0.6), (c) BC aerosols (0.9, 2.6, -1.7), and (d) non BC aerosols (-2.3, 0.4, -2.7), at TOA, Atmosphere, and Surface (based on Ramanathan and Carmichael, 2008).*

In this regard, the fundamental law to estimate this direct interaction of radiation with matter is famously known as the '*Beer-Bouguer-Lambert law*', which states that the change in the intensity of the incoming solar radiations is directly proportional to the amount of matter in the path:

$$dI_\lambda = -\boldsymbol{\alpha}\,(\boldsymbol{\lambda})\, I_\lambda dz \qquad (\mathbf{1.1})$$

where $\boldsymbol{\alpha}\,(\boldsymbol{\lambda})$ is the volume extinction (i.e., scattering + absorption) coefficient,

dz is the changes along the path (i.e., altitude-wise),

I_λ is the intensity of the incoming solar radiation at wavelength λ.

This law follows the linear behaviour provided the temperature, pressure, and composition components remains constant. In a column of the atmosphere (i.e., from surface to TOA), the prime parameter to understand this complex interaction of aerosols with radiation includes the spectral Aerosol Optical Depth (AOD), which is defined as:

$$\boldsymbol{AOD} = \int_{surface}^{TOA} \boldsymbol{\alpha}\,(\boldsymbol{\lambda})\; dz \qquad (\mathbf{1.2})$$

In **Equation 1.2**, the spectral extinction coefficient (α (λ)) is the combined number concentration (n_c) and the extinction cross-section (σ) of the particle, defined as follows:

$$\boldsymbol{\alpha}\,(\boldsymbol{\lambda}) = n_c\,\boldsymbol{\sigma_{ext}}\,,[\tfrac{1}{length}] \qquad (\mathbf{1.3})$$

Further, the extinction cross-section of the particles is defined as

$$\boldsymbol{\sigma_{ext}} = A\,\boldsymbol{Q_{ext}} \qquad (\mathbf{1.4})$$

where A is the geometric cross-section, and Q_{ext} is extinction efficiency of the particles, defined as the summation of the scattering efficiency and absorption efficiency:

$$\boldsymbol{Q_{ext}} = Q_{scat} + Q_{abs} \qquad (\mathbf{1.5})$$

The extinction efficiency (**Equation 1.5**) is generally calculated using the Mie theory, which is based upon the Maxwell equation calculations (Mie, 1908), where the main parameters required to estimate these values include the diameter (i.e., $\mathbf{x}=2\pi\mathbf{r}/\boldsymbol{\lambda}$, where **r** is the radius of the particle) and the complex refractive index (i.e., **m=n+ik**, where **n** is scattering and **k** is absorbing) of the particles. Here, the Mie theory is only applied to particles with a size comparable to or larger than the wavelength (i.e., **x~1**), for example, the aerosols. Generally, the Mie theory works on the assumption of a homogeneous (or isotropic) spherical shape (Bullrich, 1964) and does not include the non-spherical particles that exist in the atmosphere.

From the above discussions, it is clear that the direct effects of the aerosols depends on whether the aerosols are scattering (e.g., SS, SF, NR) or absorbing (e.g., BC) in nature. In addition to this, the ARI also depends on the underlying surfaces as well. For example, the absorbing aerosols over the dark surfaces (having low albedo) such as vegetation land or oceans will have a negligible effect, whereas the scattering aerosols in such scenarios can amplify the albedo. On the other hand, the scattering aerosols will have minor effects on the bright surfaces (such as urban or desert regions), whereas the absorbing aerosols will have a considerable effect and will warm the atmosphere in return (Myhre et al., 2013). Hence, these impacts will get even more complex when the aerosols are present at the altitudes aloft, and this crucial point will be pointed out in the next section.

1.4 Formation, Dynamics, and Impacts of EALs on the Atmosphere

For the accurate evaluation of the AOD parameter (defined as integral of total aerosols present in a column of air), there is a need to understand the complete vertical distribution of the aerosols. Conventionally, the altitude-wise variation of the aerosols is assumed to be decreasing exponentially with height (Charlson et al., 1992; Reus et al., 2001), where the particles are mostly confined within the atmospheric boundary layer (ABL). However, due to the activities such as volcanic eruptions or the transfer of pollutants from the Earth's surface to the atmosphere by atmospheric turbulences or winds (i.e., convection) or the long-range transport activities, the aerosols can be lifted above the ABL altitudes. The formation of these kinds of layers of aerosols above the well-mixed ABL altitudes is referred to as *'Elevated Aerosols Layers*' or EALs. Once these aerosols enter the free troposphere (FT) or Upper Troposphere and Lower Stratosphere (UTLS) regions (or do not return to the Earth's surface), they will stay there for longer periods due to their higher residence times in the FT and UTLS regions and hence impacting the climate systems.

1.4.1 EALs in the lower troposphere region

The presence of the absorbing aerosols such as BC in the FT altitudes can, in return, modify the cloud micro-physical properties (Li et al., 2013). The modification in the water cycles due to the presence of light-absorbing aerosols in the EALs can alter the Earth's energy budget (Lau and Kim, 2006; Ramanathan et al., 2005) as well. However, radiative impacts due to the absorbing aerosols result in warming of the atmosphere (see **section 1.3**), which leads to the increased temperatures above ABL, and the hence unstable free atmosphere is generated. This hypothesis was proposed by Wang et al. (2013), in which they have discussed that the aerosol induced warming can alter the ABL (**Figure 1.4**) in numerous ways, as discussed below:

(**a**). Aerosols present in the EALs can reduce the radiative energy reaching the surface and thus hinders the sensible heat fluxes that lead to the formation of ABL.

(**b**). However, when aerosols are confined below the ABL, trapping of a large amount of solar radiation takes place with the maximum heating near the top of ABL, known as temperature inversion. However, with the presence of absorbing aerosols at this altitude, the convective available potential energy (positive (negative) above (inside) ABL) gets strengthened (see **Figure 1.4**), leading to a more stable ABL and

more unstable FT region. Thus, the absorbing aerosols present in the EALs will heat up the elevated layer in the ABL, thus altering the thermodynamic structure of the atmosphere, and

(**c**). Aerosols and the ABL interact and, in return, induce positive feedback processes such as changes in relative humidity (RH) at the surface (Yu et al., 2002).

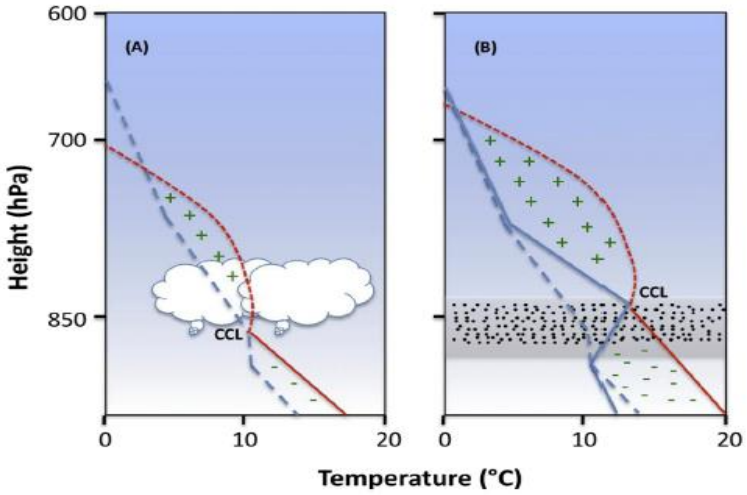

Figure 1.4 *The effects due to the presence of (A) without and (B) with, absorbing aerosols on the ABL. The dashed (solid) blue lines represent the vertical temperature profiles in the absence (presence) of absorbing aerosol layers, whereas the solid (dashed) red lines denote the dry (moist) adiabatic conditions. Cloud Condensation Level location is also superimposed in the figure (based on Wang et al. (2013)).*

At the same time, the Tibetan Plateau (TP) is considered the source of the elevated thermals and the mechanical forcing as well. In this regard, Lau and Kim, 2006 has proposed the '*Elevated Heat Pump'* or EHP hypothesis, which showed that the atmospheric heating induced by the aerosols such as DU and BC over the Himalayan foothills and the Indo-Gangetic Plains (IGP) regions could lead to atmospheric moisture convergence feedback mechanism prevailing during the monsoon season. According to this hypothesis, the incoming solar radiations are absorbed by the absorbing aerosols over the northern and southern slopes of the Himalayas, thus heating the lower and mid-troposphere altitudes around the TP region (**Figure 1.5**). This heated air rises via convection activities, inducing the formation of more warm and moist anti-cyclonic circulations and thereby leading to the onset of the Asian summer monsoon (ASM). This leads to an increase in the rainfall over the Himalayan foothill but a reduction in rainfall over the central India (CI) region (Lau and Kim., 2011). Also, there

has been an evidence that this strengthening of rainfall during early monsoon season (May-June) can lead to subsequent weakening in the monsoon during the July-August months (Lau and Kim., 2007). On the other hand, the increase in the scattering aerosols leads to the weakening of the monsoon circulation and thereby inhibits the precipitation over the region.

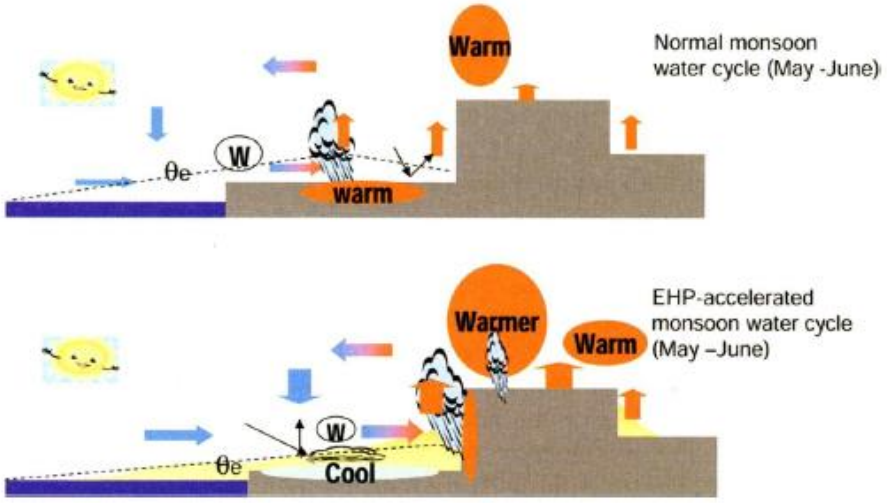

Figure 1.5 *Mechanism explaining the 'Elevated Heat Pump' hypothesis (based on Lau and Kim, 2006).*

In addition to this, another hypothesis was also proposed by (Bollasina et al., 2008; Hansen et al., 1992), which explains that the increase in the absorbing aerosol loading in elevated altitudes can further suppress the precipitation, leading to the events such as cloud 'burn off', known as the *Semi-direct effect.* Also, the presence of the absorbing aerosols in the elevated layers has led to the enhancement in the melting of snow during the spring season over the Himalayan regions as well (Nair et al., 2013). At the same time, the scientific community has also investigated the impact of different aerosols on the ASM (Nandini et al., 2022; Solmon et al., 2015; Vinoj et al., 2014). The modelling studies, such as Bollasina et al. (2008), have shown that the decrease in the precipitation was attributed to the increase in the anthropogenic aerosols. Also, Hazra et al. (2013) have stated the importance of aerosols through the complex interactions between the dynamics, clouds microphysics, and the direct radiation impacts. Despite the existence of modelling evidence on the role of aerosols and dynamics, the contributions of the local or the non-local aerosols through the large-scale atmospheric

circulation via observational evidence have not been appropriately understood and are still a topic of debate.

1.4.2 EALs in the UTLS region

It is well known that one of the main characteristics of the ASM also involves the anti-cyclonic (cyclonic) flow leading to divergence (convergence) in the upper (lower) troposphere region, coupled with the persistent deep convection activities (Randel and Park, 2006). The geographical center of this anticyclone formed in the UT region prevails over the TP region, and the air masses are well confined within this anticyclone by the tropical easterly jet (TEJ) and subtropical westerly jet (SWJ) from the south (10-15°N) and north (40-45°N) directions respectively, as mentioned in Dunkerton, 1995. These UT anti-cyclonic circulations extend into the LS region, surpassing the Tropical Tropopause Layer (TTL), which is considered as the transitional layer between the pollutants, thus entering the stratosphere region (Gettelman et al., 2004). This air transport from the troposphere into the stratosphere is mainly a tropical phenomenon and occurs due to the prevalent Brewer-Dobson circulations (Randel et al., 2010). Also, according to Garny and Randel, 2016, about 31% (via vertical velocities) or 48% (via slow adiabatic heating) of the trajectories are transported to the stratosphere within 60 days interval, or sometimes the overshooting convection can also be responsible for this transport (Fu et al., 2006).

Recent advancements in the satellite observations (in the last decade) could confirm the presence of trace gases such as carbon monoxide, hydrogen cyanide, methane, and water vapor in the UTLS region (Randel et al., 2010; Randel and Park, 2006; Xiong et al., 2009). However, satellites have also shown the simultaneous presence of the aerosols in the anticyclone region, confined within a layer famously known as the Asian Tropopause Aerosol Layer (or ATAL), shown in **Figure 1.6**. The formation of ATAL is attributed to the atmospheric circulation activities, such as deep convection occurring during the monsoon season, which serves as means for the transport of the ABL pollutants into the UTLS region (Lawrence and Lelieveld, 2010). This layer extends vertically in the UTLS region during the monsoon season from 13 to 18 km in altitude and geographically over the South Asia starting from the Eastern Mediterranean (till North Africa) up to Western China (till Thailand) region (0-100°E, 20-45°N), as mentioned in Vernier et al. (2011).

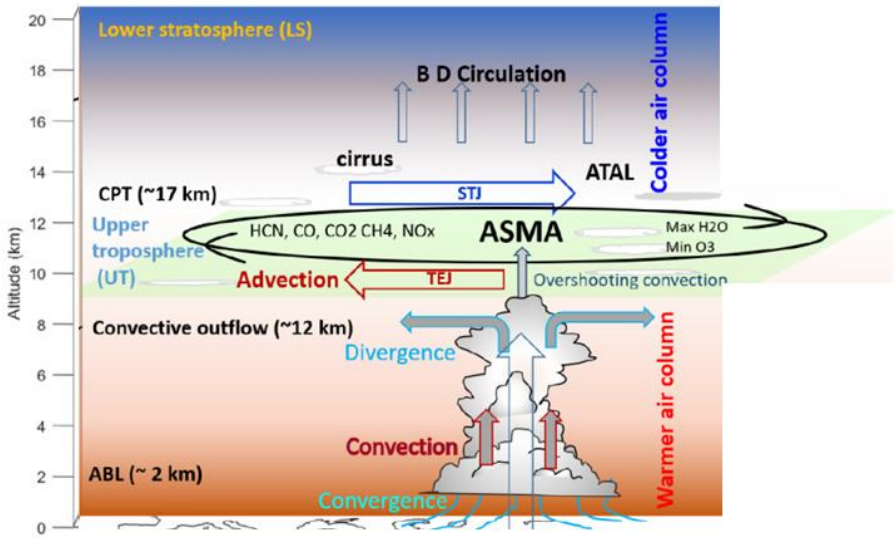

Figure 1.6 *Diagram showing the vertical transport of pollutants from the upper troposphere into lower stratosphere region (based on Mehta et al. (2020)).*

Apart from the transport of pollutants from ABL, the contributions from the activities such as volcanic eruptions (Pitari et al., 2016), lightning (Gu et al., 2016), and aviation (Righi et al., 2016) can directly inject the aerosols in the UTLS region. The cirrus clouds, which are well known to be present in these altitudes and are highly dependent upon the availability of hygroscopic CCN such as SF or NR, contributes to the atmospheric greenhouse warming (Haladay and Stephens, 2009; McFarquhar et al., 2000). Along with this, these thin subvisible clouds can also lead to the dehydration of the LS region as well (Jensen et al., 2013). The increase in the concentration of aerosols at these altitudes can affect the radiative properties of cirrus clouds as well. For instance, Pandit et al. (2015) have shown an increase in the cirrus clouds (approximately 9%) from the year 1998 to 2013 using the ground-based measurements. Due to the volcanic eruptions, the presence of the SF aerosols at these altitudes has a high chance of accelerating the heterogeneous chemistry. For example, an increase in the SF aerosols (near the tropopause) during the different major volcanic eruptions events has ultimately led to a decrease in the stratospheric ozone concentrations (Hofmann and Solomon, 1989; Angell and Korshover, 1985; Deshler et al., 1996; Grant et al., 1994). This has resulted in a decrease in the amount of NOx (Coffey and Mankin, 1993; Johnston et al., 1992; Koike et al., 1993) present in these altitudes as well. This stratospheric aerosol modification in the LS region is the potential source of global warming (as these aerosols absorb the outgoing long-wave radiations and incoming IR

radiations), thus enhancing the '*Junge layer*'. Recently, Fadnavis et al. (2019) has mentioned that the El-Niño events could amplify the draughts by 17% due to the presence of ATAL over the South Asia region. Apart from this, the presence of ATAL is suspected to have impact in controlling the amount of monsoon precipitation as well but since this layer has been found recently so a lot still remains to be investigated on this aspect.

1.5 Characteristics of EALs: An Indian perspective

The world's major monsoon systems, ASM, affects the Indian continent in a major way, mainly due to its geography, where the maximum population (two-third) depends on the monsoon for the hydroelectric generation and agriculture activities (Turner and Annamalai, 2012). Several theories have been proposed to understand its origin and variability, but the prediction for this monsoon system is still evolving till date. One of the main aspects of comprehending this variability still remains due to the partial knowledge of the impacts of aerosols vertical distribution on the monsoon systems. In this regard, the vertical profiling of the aerosols is been carried out using the LIght Detection And Ranging (LIDAR) instruments (which can include probing via ground-based or space-borne) or the in-situ measurements.

Over the Indian region, the first vertical profiling of the aerosols in this aspect using the LIDAR instrument was conducted in Thumba in 1981 (Parameswaran et al., 1984). It was then followed by many researchers such as Jayaraman et al. (1995) in Ahmadabad, Devara, 1998 in Pune, and Hegde, 2009 in the central Himalayan region. However, the LIDAR observations during the Indian Ocean Experiment (INDOEX) campaign became the first observations that depicted the presence of the EALs over the Indian Ocean (Ansmann et al., 2000), as shown in **Figure 1.7**. This experiment was carried out using six different wavelengths, which showed the existence of the aerosol plumes at 3 km altitude (i.e., above ABL), advected from the Indian subcontinent. After that, the aircraft experiments conducted during Integrated Campaign for Aerosols, gases, and Radiation Budget (ICARB) campaign in the pre-monsoon season also revealed the presence of EALs in the troposphere over the Bhubaneswar and Chennai regions (Satheesh et al., 2009). Here, a three-fold increase in the aerosol extinction coefficient (α_{aer}) was observed at the altitude above 2 km as compared to the α_{aer} near the surface.

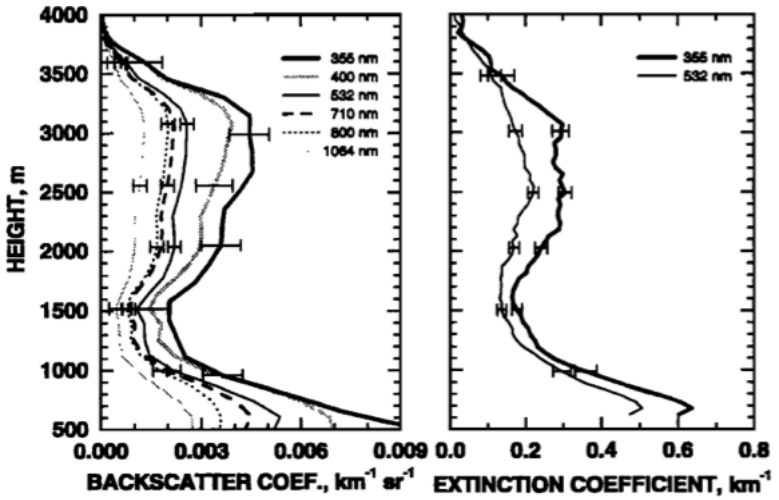

Figure 1.7 *Average profiles of the particles (a) backscatter coefficient and (b) extinction coefficient, at six different wavelengths on March 29, 1999 (based on Ansmann et al. (2000)).*

Further, the project named Aerosols Radiative Forcing NETwork or ARFINET was also carried out across the Indian region, to understand the complete characterization of the aerosols radiative impacts due to the formation of EALs. Later, Babu et al. (2011), found that these EALs were significantly contributed by the BC aerosols, when the research was carried out under the Regional Aerosols Warming EXperiment or RAWEX conducted in the urban Hyderabad region using an aethalometer instrument, which seemed to be majorly dominating during the pre-monsoon season compared to those in the winter season (Suresh Babu et al., 2016). The effects due to the presence of brown haze have been studied by Ramanathan et al. (2005), where they found that the presence of absorbing aerosols in the EALs can further weaken the sea surface temperature leading to a slow down of local meridional circulations over the north Indian Ocean. These slower circulations in the meridional winds reduce the evaporation processes and lead to positive feedback mechanisms, resulting in the weakening of monsoon patterns. Also, Devi et al. (2011), studied the complete vertical and spatial distribution of aerosol radiative properties over the Indian Continental Tropical Convergence Zone, which revealed the increase in the absorption coefficient near the Himalayan foothills in the lower troposphere during the monsoon season.

Over the east coast region of India, Niranjan et al. (2007) reported the presence of EALs between 2 to 3 km altitudes, cause of which has been attributed to the long-

term transport of DU aerosols from the desert regions. Later, during the aircraft observations conducted under Cloud-Aerosol Interaction and Precipitation Enhancement EXperiment or CAIPEEX (Padmakumari et al., 2013), found that these EALs extended up to 4 km altitude near the foothills of the Himalayas. Sarangi et al. (2016) have analysed the radiative impacts due to the formation of EALs between 1.5 to 5.5 km altitude over the Kanpur region in IGP using the Micro-Pulse Lidar NETwork (MPLNET) datasets. However, a recent study by Ratnam et al. (2018), also found the presence of EALs in the rural location in South India (SI) in the troposphere region during the monsoon season using the Micro-Pulse LIDAR (MPL). This study has associated the formation of these EALs with the long-range transport mechanisms such as Low-Level Jet (LLJ), prevailing during the monsoon season.

Apart from the tropospheric studies, Junge, 1960 reported the presence of the stratospheric aerosols up to 30 km altitude, famously known as the '*Junge layer*' using the Aitken nuclei counter (measuring radius between 0.01 to 0.1 microns) and the impactor (measuring radius between 0.1 to 1 microns) instruments. They concluded that the particles found with a radius less than 0.1 microns are of tropospheric origin, whereas the particles between 0.1 to 1 microns are of stratospheric origins. Later, the aerosols impacts due to the famous Mount Pinatubo eruption event were also studied extensively by Jayaraman et al. (1995) in the UTLS region using the elastic backscatter Mie LIDAR. The increase in the aerosol loading over the UT and LS regions was reported from 2001 to 2005 over the Gadanki region in SI by Kulkarni et al. (2008). In addition to this, few years later, what caught the scientists attention was the presence of ATAL (using the satellite measurements) and its climatic impacts, as discussed regressively in **section 1.4.2**. However, the enhancement in the scattering ratio profiles from the ground-based LIDARs over the TP region was reported between 10 to 20 km altitude (Kim et al., 2003). Nevertheless, the presence of ATAL (extending from 13 to 18 km altitude) was confirmed by Vernier et al. (2011), using the four years (2006-2009) of satellite datasets over the South Asian region, as shown in **Figure 1.8**. Also, Vernier et al. (2015) observed that the AOD has increased by about three times since the late 1990s in the 13 to 18 km altitude region.

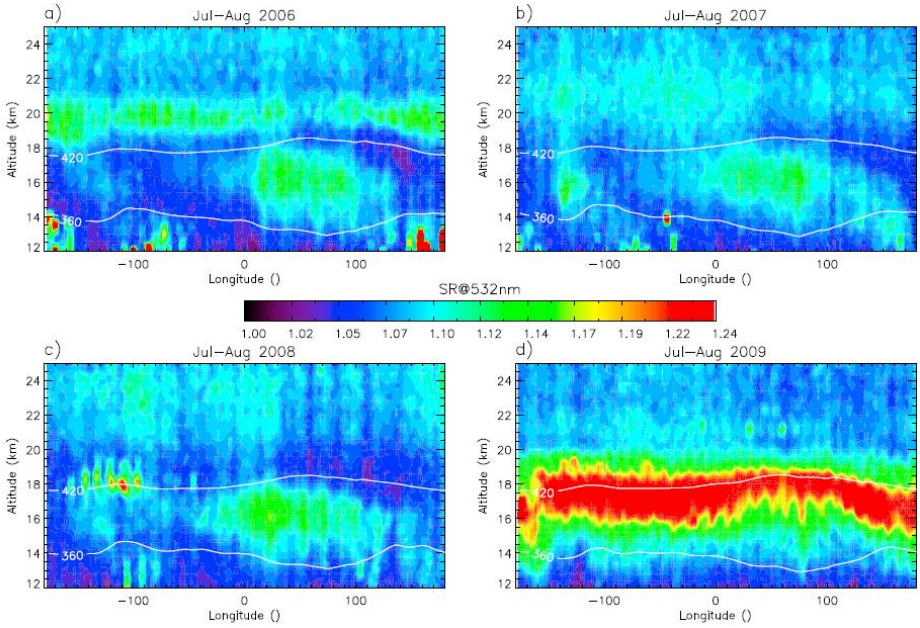

Figure 1.8 *The mean scattering ratio cross-section longitude profiles for (a) 2006, (b) 2007, (c) 2008, and (d) 2009, during July-August months (based on Vernier et al. (2011)).*

Later on, campaign studies such as Balloon measurements of Asian Tropopause Aerosol Layer (BATAL) were conducted under NASA and ISRO collaboration from 2014 over the Indian and Saudi Arabian countries to study the UTLS aerosols along with trace gases measurements (Vernier et al., 2018). Here, nearly 68 balloon flights were launched during the night time (NT) and found that particles in the UTLS region are mostly liquid aerosols (~ 80-95%, with a radius less than 0.25 µm). However, the chemical analysis of particles revealed the dominance of NR aerosols (100 ng/m^3) which is supported by activities such as lightning or transport by convection. Further, the StratoClim measurements during 2016 and 2017 also confirmed the enhanced aerosol backscatter above the 1.5 to 2 km altitudes to the Cold Point Tropopause (CPT) altitude (Brunamonti et al., 2018). However, an another study by Yu et al. (2015b) found the presence of SF, SF emitted organics, and secondary organics in the ATAL under Civil Aircraft for Regular Investigation of the atmosphere Based on Instrument Container (CARIBIC).

However, most of the scientific studies mentioned above are confined to independent researches taking place, either in the lower troposphere or in the UTLS region, but a complete picture of the vertical distribution of aerosols (and the contributing chemical compositions) over the Indian region is still missing. Apart from

this, there is a need to accurately measure the aerosol loading in both the columnar and vertical distribution across the globe for which the prior knowledge of the aerosols compositions, shape, and size is essential (see **section 1.2**), as the different aerosol properties aids in determining the complex refractive index of the aerosols. The current understanding prevails that there exist considerable uncertainties in the estimation of these properties due to different aerosol types (Myhre et al., 2013), which can be either due to the short lifespan or the internal/ external mixing (or coating) of the components taking place in the atmosphere (as discussed in **section 1.2**).

1.6 Long-term characterization of Aerosols: Global Perspective

The RF induced due to the aerosols direct effects are nearly -0.35 W/m^2, whereas it extends up to approximately +2.84 W/m^2 due to the well-mixed GHGs, out of which the carbon dioxide emissions alone have contributed +1.82 W/m^2 (IPCC, 2013) to the atmosphere. However, the uncertainties associated in the estimation of RF due to the total aerosols ranges from -0.85 to +0.15 W/m^2 whereas the same due to the carbon dioxide ranges from +1.63 to +2.01 W/m^2. From this, one can note that the uncertainties are nearly three times more (for aerosols) than that due to the GHGs. These significant uncertainties lies due to the inadequate quantification of ARI prevailing due to the different aerosol types, as each aerosol type varies hugely on a day-to-day basis, as discussed briefly in **section 1.2**. The different aerosols exhibit different RF, with the uncertainties in its estimation varying from -0.6 to -0.2, +0.05 to +0.8, -0.4 to +0.1, -0.3 to -0.03, and -0.3 to +0.1 for the SF, BC, organic, NR, and DU aerosols, respectively. These large variabilities estimated in the dominant aerosol compositions are well reported in IPCC, 2013, and are in consistence with the recent IPCC, 2021 report as well.

Realizing this issue, tremendous advancements have been made in the current understanding of the different aerosol types since then, in terms of in-situ, ground-based networks, aircraft, satellite, and the reanalysis measurements. For instance, the long-term measurements of aerosols from the ground-based networks such as AErosol RObotic NETwork (AERONET) under NASA have been installed all across the globe to study the columnar properties of the aerosols using the sun-radiometer instruments (Holben et al., 1998). Whereas the vertical distribution of the aerosols was estimated using the MPLNET elastic-scattering LIDARs distributed across the globe (Berkoff et

al., 2003). The observations for Asian Dust and air-pollution aerosols using the network of ground-based LIDARs (ADNET) have been carried out at 20 locations over Japan, aiming to assimilate the chemical transport models using the Mie LIDAR datasets (Sugimoto and Uno, 2009). Also, European Aerosol Research Lidar Network (EARLINET) was founded in the year 2000, which works in close cooperation with Aerosols, Clouds, Trace gases Research Infrastructure NETwork or ACTRIS (Pappalardo et al., 2014). In addition to this, several campaigns were also conducted from time-to-time to have real-time observations of the aerosols. One of such campaigns includes the Smoke, Clouds, and Radiation-Brazil (SCAR-B) project to study aerosols variations over the Amazon regions in 1995 (Kaufman et al., 1998). The Tropospheric Aerosol Radiative Forcing Observational Experiment (TARFOX) was conducted over the eastern United States seaboard region to estimate the uncertainty in the measurements associated with the aerosol effects (Russell et al., 1999). The aerosol number concentration and size distribution measurements were carried out over the north Indian Ocean during the INDOEX campaign (De Reus et al., 2001). The instruments were carried on the cruise named Aerosols99 to analyse the chemical, physical, and optical properties of the ABL from the Atlantic Ocean to Norfolk to Virginia to Cape town to South Africa (Bates et al., 2001). Later, the Southern African Regional Science Initiative (SAFARI) project was carried out in the southern Africa region to understand the earth-atmosphere-human systems (Swap et al., 2002). Note that the details of the ICARB campaign (Satheesh et al., 2009) conducted over the Indian region have already been discussed in **section 1.5**. The Puerto Rico Dust Experiment (PRIDE) project was conducted where the Light Aircraft Aerosol Package (LAAP) was developed to measure the aerosols microphysical and chemical properties (Maring et al., 2003). The measurements under the Saharan Dust Experiment (SHADE) were made to understand the optical and radiative properties of the DU aerosols (Tanré et al., 2003). A series of Aerosol Characterization Experiments (ACE) was conducted in the Southern Ocean, Northeast Atlantic Ocean, and Asia, utilizing in-situ, satellite, and modelling techniques to lower the uncertainty associated with the aerosol measurements (Huebert, 2003). The single wavelength LIDAR measurements were carried out under the European union's Mineral dust and Tropospheric Chemistry (MINATROC) campaign to measure the tropospheric profiles of α_{aer} (Gobbi et al., 2003). The flight experiment was conducted over United Arab Emirates to study the atmospheric thermodynamics and aerosols (Reid et al., 2008). The series of

experiments conducted specifically over the Indian region has already been detailed in **section 1.5**.

At the same time, the vast developments in the satellites and the reanalysis measurements during the last two decades have led to a significant enhancement in our current understanding of aerosols. For instance, the Total Ozone Mapping Spectrometer (TOMS) onboard Nimbus-7 measures the columnar backscattered radiances from the Earth's surface at 340-380 nm for the absorbing aerosol index and has been operational for the longest year, i.e., 1978, till date (Herman and Celarier, 1997). After discovering the well-known Antarctic Ozone hole and measuring the volcanic eruptions, the extinction values of the stratospheric aerosols were measured by the Stratosphere Aerosol and Gas Experiment I (SAGE I) instrument. It was launched in 1979 (till 1981) and worked on the solar occultation technique in the wavelength range from 0.3-1.02 μm and measured α_{aer} at 2 different wavelengths (Kent et al., 1988). Then the AOD measurements for the global oceans were started being measured using the Advanced Very High-Resolution Radiometer (AVHRR) at 0.63 μm (Husar et al., 1997). The revolution in aerosols understanding came with the introduction of MODerate Resolution Imaging Spectrometer (MODIS) onboard Aqua (2001) and Terra (2000) satellites covering multi-wavelength measurement ranges and having huge swath widths (Levy et al., 2007). This spectroradiometer could measure AOD over lands (through the 'Deep blue or Db' algorithm) and ocean (through 'Dark target or Dt' algorithm) regions. The study of the size and shape of the aerosol was made possible with the advent of the Multi-Angle Imaging Spectrometer (MISR) in 2001 (Martonchik et al., 1998). The successor of the SAGE I instrument was named SAGE II, which was launched in 1984 (till 2005), and it started measuring the aerosol at four different wavelengths (McCormick, 1987), SAGE III (launched in 2017) could measure the atmospheric components including aerosols (at multi-wavelength), and trace gases at the wavelength from 0.29-1.5 μm (Hernandez et al., 2014). Then came the successor of the TOMS instrument, known as the Ozone Monitoring Instrument (OMI) onboard Aura, which works on the same principle as TOMS, but it measures radiances in UV as well as visible (270-550 nm) wavelength regions (Torres et al., 2007). The vertical profiling of the aerosols optical and chemical properties has been made possible since 2006 with the advent of the Cloud Aerosol Lidar with Orthogonal Polarization (CALIOP) onboard Cloud Aerosol Lidar Infrared Pathfinder Satellite Observations or

CALIPSO (Omar et al., 2009). At the same time, reanalysis datasets have also found massive importance in studying the atmosphere to understand better the role of aerosols and their impacts on the climate, such as European Centre for Medium-Range Weather Forecasts Re-analysis version (V)-5 or ERA-5 (Hersbach et al., 2020) and Modern-Era Retrospective analysis for Research and Application V2 or MERRA-2 (Buchard et al., 2017).

These projects could immensely improve the understanding of the distribution of different types of aerosols across the globe, as shown in **Figure 1.9**.

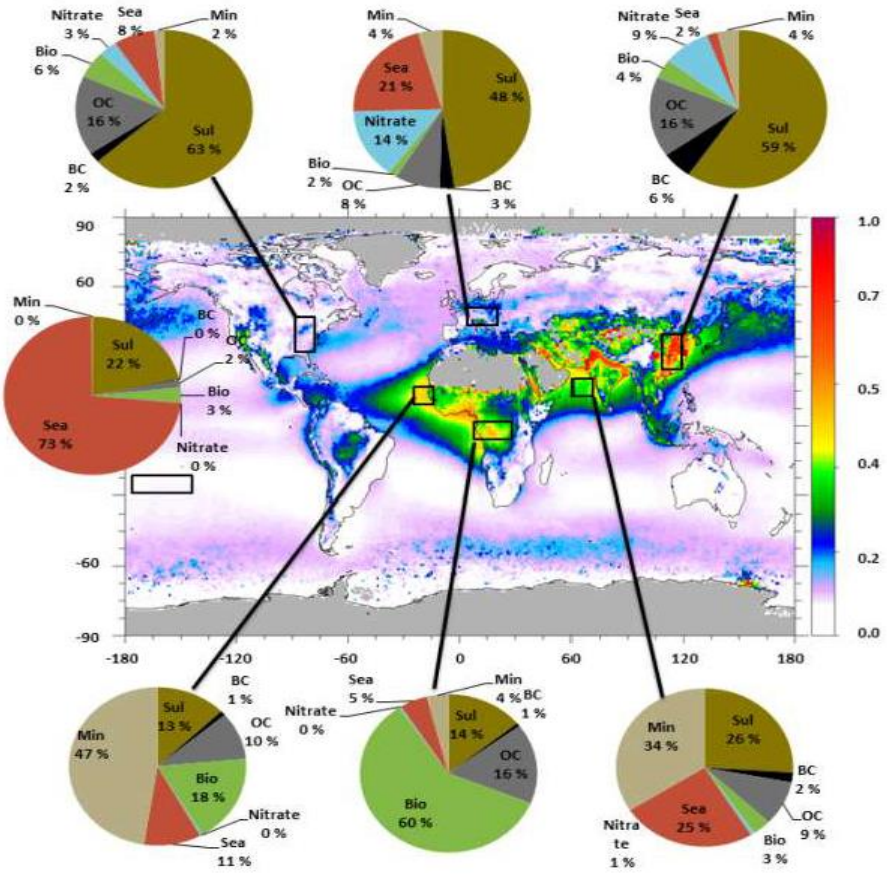

Figure 1.9 *The distribution of different types of aerosols (Bio: BB, Sea: SS, nitrate: NR, Sul: SF, OC, and BC) has been shown in the form of Pie charts across the globe (middle plot represents mean AOD retrieved from MODIS at 550 nm). The grey regions in the AOD plot imply insufficient data (based on Myhre et al. (2013)).*

From **Figure 1.9**, the heterogeneity in the distribution of aerosols is seen where the aerosol loading is highest in the Northern Hemisphere or NH (compared to the Southern Hemisphere or SH), especially over the South Asian and African continents. The maximum contributions are from the DU aerosols over the tropical and subtropical

regions, for instance, over the adjoining Atlantic Ocean (to the Sahara desert) and the Arabian Sea or AS (adjoining India) region, where the DU aerosols are contributing approximately 47% and 34%, respectively. The developed countries such as America and Europe, and the developing countries such as China contributes maximum SF aerosols to the atmosphere with 63%, 48%, and 59%, followed by the NR aerosols with 3%, 14%, and 9%, respectively. In this regard, there has been evidences of the decrease in the sulfur dioxide emissions over the America and EU regions since 1990 (Reis et al., 2012; Report et al., 2016; Vestreng et al., 2007). The global reductions in sulfur dioxide emissions were very prominent until the year 2000 due to the overall decrease over the America and EU regions, but later with the massive emissions from the China region, the global emissions also went up. Now, China is the country with the highest pollution emissions mainly due to sulfur dioxide and nitrogen dioxide, to the growth in industrialization, followed by Indian sectors (Krotkov et al., 2016). Nevertheless, there has been evidences implying decrease in the long-term trends over the China region due to sulfur emissions (Li et al., 2018; Saikawa et al., 2017b; Zhang et al., 2012). However, on the other side, the contributions from the Indian region are increasing due to the sulfur emissions (Aas et al., 2019; Report et al., 2016; Saikawa et al., 2017a). Also, the biomass burning (BB) aerosols dominate with 60% contributions alone from the South Africa (SAF) region, followed by the Atlantic Ocean with only 18% contributions. The Pacific Ocean has huge contributions of nearly ~73% from the SS aerosols, and at the same time, the AS, EU, and the Atlantic Ocean regions also have high contributions with 25%, 21%, and 11%, respectively. The OC aerosols dominates over almost all the regions except Pacific Ocean whereas the BC aerosols dominate mainly over the America, EU, China, and AS regions with overall 2%, 3%, 6%, and 2% contributions, respectively. Although the overall contributions of the BC aerosols to the total AOD are very less, but it induces enormous impacts on the atmosphere (see **Figure 1.3c**). At the same time, while climate change has been a major concern around the globe, no place has witnessed such drastic changes in emissions as it is seen over the South and East Asia region (Samset et al., 2019). Being the world's fast-developing region, the South and East Asia region is highly exposed to climate change due to its high population density, vehicular/ industrial emissions, and seasonal variations in precipitation efficiency. Many attempts have been made to understand this feature through its long-term trends and RF using satellites and reanalysis datasets over India and its adjoining seas in the previous studies. One such study was carried out by Samset

et al. (2019), where they found that a dipole pattern exists in the aerosol emissions while increasing aerosol trends in the free troposphere (or above ABL) region was reported recently by Ratnam et al. 2021.

With this broad overview of the heterogeneous distribution of aerosols across the globe, many scientists have attempted to estimate changes in the aerosols in close association with their dynamical aspects as well. For instance, the aerosols are associated with the decisive impacts involving the onset and strength of Northern Hemisphere summer monsoon systems (Samset et al., 2019). The increase in the DU aerosols and the pollution levels redistribute the latent heat in the atmosphere in such a way that, in return, it weakens the tropical cyclone intensities (Rosenfeld et al., 2012). The El-Niño southern oscillations (ENSO) have a huge impact on the aerosols variability, where high aerosols prevailed during the ENSO event leading to a decrease in the precipitation and hence an increase in the BB activities (Zhu et al., 2020). This increase in the BB activities leads to a higher concentration of carbonaceous aerosols while the La-Niña events follow the vice-versa pattern. Studies such as Wang et al. (2022) have stated that the El-Niño events can modulate the regional climate, thus influencing the air quality in the latitude regions as it has shown a positive correlation between the ENSO and AOD phases. Also, the variations in the SF aerosols present in the UTLS region are directly linked to the ozone variations via the extreme phases of the naturally occurring ENSO events (Shaheen et al., 2013). Very recently, Nandini et al. (2022), mentioned that these ENSO events can further modulate the aerosol loading, impacting the rainfall events, which can significantly enhance the DU induced rainfall patterns. Also, a positive response to the solar cycle (SC) due to the effects of aerosols has been observed by Ratnam et al. (2021). However, the changes in the total aerosols loading have also been observed due to the total solar radiation, diffuse radiation, and diffuse radiation fraction over the past 56 years, where the decrease of total solar radiation by 2.48% has been observed (Xie et al., 2021). The nonlinear relation between the Quasi-Biennial Oscillations (QBO) and stratospheric aerosols has been observed, provided when the stratosphere is unperturbed due to the volcanic events (Hommel et al., 2015). Numerous studies in the past have also found the slow-down of QBO due to the transport of aerosols or stronger tropical upwelling (Niemeier and Schmidt, 2017). At the same time, QBO also has a significant impact on the tropospheric winds and precipitation (Garfinkel and Hartmann, 2011; Seo et al., 2013), stratospheric air mass

transport to extra-tropics (Punge et al.,2009), and polar vortex (Holton, 1980) as well. Further, these dynamical issues pertaining to natural variability can have profound effects on both the columnar and vertical distribution of aerosols. Hence, it becomes imperative to consider these long-term variations while estimating the changes in the aerosols.

In this regard, several studies have been carried out to examine the long-term trends in the rapidly changing aerosol loading. However, only a few investigations have acknowledged its long-term implications through the combined optical, physical, morphological, and chemical properties of the aerosols (columnar and vertically), while isolating the above mentioned dynamical aspects. Hence, this has become main objective of the current thesis.

1.7 Problems addressed in the study

The GHG roles are more global as the gases are homogeneously mixed throughout the atmosphere and comparatively less uncertainties are experienced in this case. Unlike GHG, from the above discussions, we can say that the impacts due to the aerosols are more regional (depending on the source of origin) rather than global, and still high uncertainties exists in its examination. Also, it is quite clear that background meteorology plays a crucial role in the accurate quantifications of aerosols. The vertical extent of the aerosols is highly variable during the monsoon season over the Indian region, both in the troposphere and the UTLS region. Considering the importance of the evaluation of the vertical distribution of aerosols (regionally and globally) and background dynamics playing a pivotal role, the first objective of this thesis is outlined as follows:

In **Chapter 3,** the complete vertical and spatial distribution of EALs are obtained using the long-term ground-based and space-borne LIDAR observations.

This objective became the motivation to undertake the study examining clear picture of space-time columnar as well as vertical long-term changes in the various region-wise aerosol properties, excluding the effects due to prevailing background dynamics. Here, the continuous knowledge of the changing vertical patterns of the different components of aerosols can serve as an essential input to understanding the ARI induced climate changes. However, to accomplish the same on a global scale, we outlined that in order to have a profound understanding of 3D distribution of different

aerosol properties, we have to depend on the combination of various measurement techniques such as ground-based, space-borne, and reanalysis simulations with longer data base i.e., between 2001 and 2020. Before considering this, the reliability and accuracy of the datasets have to be appropriately evaluated with the ground-based stations (which are considered the standard ones) for the reference values. Generally, the long-term trends from various sensors are required because one sensor may vary from the other in terms of its retrieval algorithms, swath width, temporal variation, spatial resolution, and its calibration methods. Considering this, the latest version of all the data sets having improved retrieval algorithms and/or better horizontal resolutions needs to be undertaken. Not only this, but this study adopted a multivariate linear regression trend model approach for obtaining aerosol trends which isolates the long-term periodic natural oscillations occurring in the atmosphere, unlike linear regression trends reported in previous studies. Finally, the evaluation of trends due to various aerosol properties using multivariate as well as linear regression analysis is carried out and investigated how these changing trends are related to the mitigation policies implemented over different regions in a very compact manner. Also, the contribution of various aerosol properties, such as optical, physical, morphological, and chemical, to the total AOD values will be analysed extensively.

In this regard, in **Chapter 4,** the long-term trends in AOD across the globe obtained using multi-satellite measurements are presented. **Chapter 5** mainly discuss the global Trends in the Aerosols Optical, Physical, and Morphological properties obtained using Multi-sensor measurements. In **Chapter 6,** the global distributions of the trend variations in the Aerosols Chemical properties are presented. However, before going into the discussions on these topics, the details of the multiple long-term datasets that are used in the study are provided in **Chapter 2,** whereas the final conclusions drawn from the entire study and its future scope are briefly mentioned in **Chapter 7**.

Chapter 2

Dataset, Methodology, and Study region

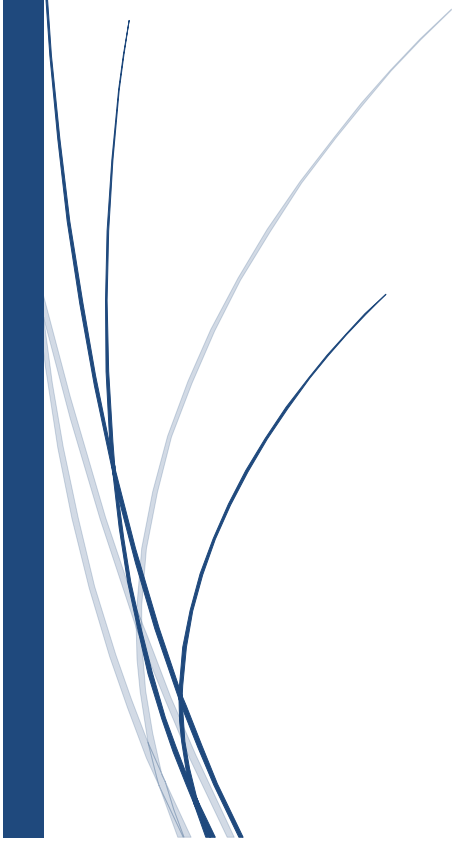

2.1 Introduction

There exist huge uncertainty in assessing various aerosol properties due to the highly variable 3D distribution of aerosol emission sources (IPCC, 2013), as introduced in **Chapter 1**. This problem gets even complicated while probing the vertical distribution of aerosols, as aerosols are partitioned within different altitudes. Thus, to obtain the long-term datasets, ground-based active remote sensing techniques play a significant role, which can probe the range-resolved profiles of aerosols from the surface with good vertical resolution. Although ground-based remote sensing techniques can provide datasets with low uncertainty and high temporal resolutions but being single point measurements, they are limited in their ability to represent the spatial distribution of the aerosols. Considering this, the space-borne active remote sensing technique is also utilized to have a global view of the vertical distribution of aerosols. These combined ground-based and space-borne datasets can fulfill the very first objective of the study.

At the same time, because of the short lifespan of aerosols (i.e., days to weeks), changes in the regional signatures of aerosols owing to their size, composition, shape, and ARI are crucial to identify over the varying polluted regions, across the globe. To achieve this, long-term datasets are essential to attain information on each mentioned aspect of aerosols. Therein, active and passive remote sensing measurements drawn from multiple space-borne sensors, reanalysis datasets, and ground-based sun-photometer networks, with improved retrieval algorithms, have been used, which are operational for the past two decades. Along with this, the background dynamical aspects are isolated from these long-term datasets using the multivariate regression trend model analysis. This covers the remaining objectives of the study. Therefore, in this chapter, all the remote sensing related instruments (active and passive) and the techniques to measure the long-term changes in various properties of aerosols are given in detail.

2.2 Remote sensing techniques

Remote sensing is a science of obtaining real-time information (spectral, spatial, and temporal) via Electromagnetic Radiations or EMR (in this case) about the target (i.e., aerosols being reflected or emitted by EMR) without physically coming in contact

with the target, as shown in **Figure 2.1**. The remote sensing technique can be further sub-divided into active and passive remote sensing, as discussed in the following sub-sections.

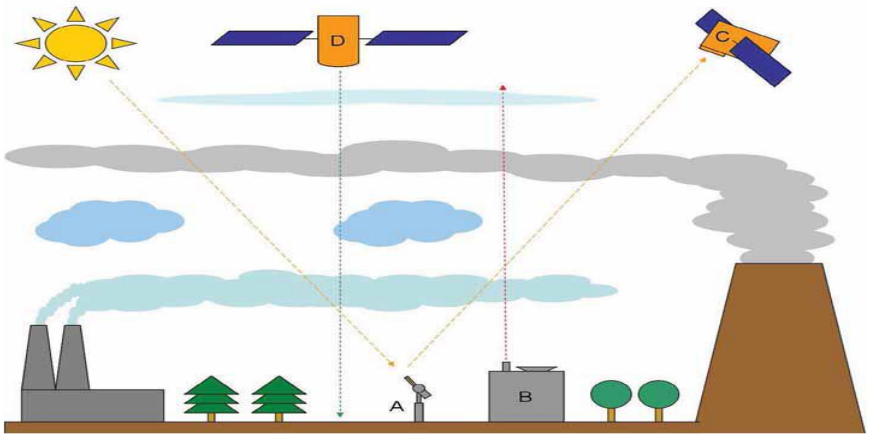

Figure 2.1 *Principles of (A and B) Ground-based and (C and D) Space-borne, remote sensing measurements. Here, A and C are passive instruments, using Sun as the energy source, whereas B and D are active instruments, using laser as the energy source (based on Mielonen, 2010)).*

2.2.1 Active remote sensing

In this case, energy (EMR) is generated and sent to detect the target from platforms B and D, as shown in **Figure 2.1**. Such techniques, which employ EMR as the source, can include SOund Detection And Ranging (SODAR), RAdio Detection And Ranging (RADAR), and LIDAR. Out of all, LIDAR is the best-suited optical range-resolved instrument to fulfill the first objective (see **Chapter 3**) of the study, i.e., to obtain vertical and spatial distribution of the aerosols. However, LIDAR is highly efficient in measuring the atmospheric aerosol constituents within the wavelength ranging from UV to IR spectrum. The history of LIDAR instrument dates back to the 1930s, and so far, a lot of advancement has been made in this technique since then. There exist five such techniques to measure this EMR interaction process with the atmospheric constituents:

(1). Elastic back-scatter LIDARs (middle-atmospheric temperature, clouds, and aerosols),

(2). Differential absorption LIDARs (ozone, water vapor),

(3). Raman LIDARs (lower atmospheric temperature, N_2 molecules),

(4). Resonance (fluorescence) LIDARs (metal such as Na, Fe, and Ca), and

(5). Doppler LIDARs (wind speed, wind velocity).

Out of all, the elastic back-scatter LIDAR is the most reliable technique to understand the presence and location of the aerosols. This LIDAR works on the principle of the time-of-flight technique, which provides the range distance (r) at which photons are backscattered by estimating the time delay between the transmission pulse (***P_0*,** using neodymium-doped yttrium aluminium garnet (Nd: YAG) laser) and the received photons (***P*,** using a telescope). Its working principle is explained with a simple schematic diagram in **Figure 2.2.**

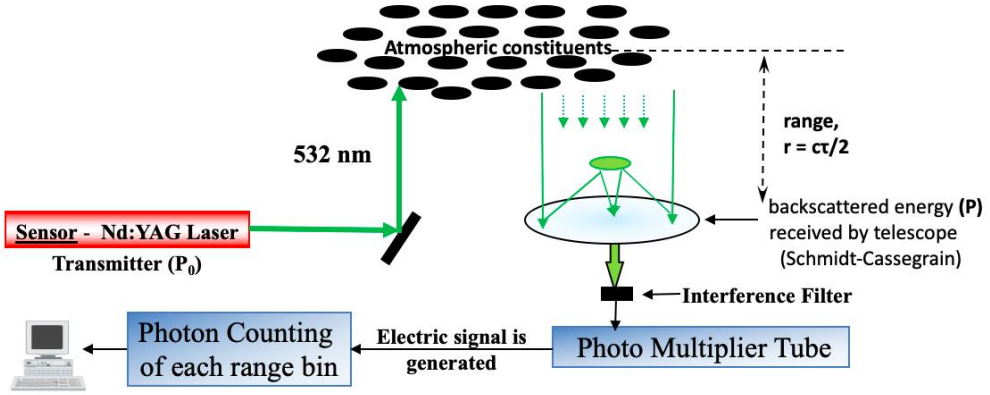

Figure 2.2 *Illustration of working principle of LIDAR.*

The received elastic backscattered photons counted for each range bin are analysed using the following LIDAR equation:

$$\boldsymbol{P}\,(\boldsymbol{r},\boldsymbol{\lambda}) = \boldsymbol{P_0}\frac{\boldsymbol{C}}{\boldsymbol{r^2}}\,\boldsymbol{\beta}\,(\boldsymbol{r},\boldsymbol{\lambda})\boldsymbol{T^2}(\boldsymbol{r}), \qquad (2.1)$$

where, $P\,(r,\lambda)$ is the detected back-scatter power,

P_0 is the laser pulse power for a single profile,

λ is the wavelength (m),

C is the system efficiency of transmitting and receiving optics,

r is the distance between the emission of laser and scattering processes taking place in the atmosphere and vice-versa (m),

$\beta\,(r,\lambda)$ is the wavelength dependent total (molecules and aerosols) volume back-scatter coefficient ($\frac{1}{m-sr}$), and

$T^2(r)$ is the probability of two-way (to and fro) single scattering transmission of light, defined as:

$$\boldsymbol{T^2(r) = \exp(-2\int_0^r \alpha\,(r,\lambda)dr}\,), \qquad (2.2)$$

where, $\alpha\,(r,\lambda)$ is the wavelength dependent total (molecules and aerosols) volume extinction coefficient ($\frac{1}{m}$) of the atmosphere.

To solve the LIDAR equation, various methods have been adopted by inverting the equation either for $\alpha\,(r,\lambda)\ or\ \beta\,(r,\lambda)$. For instance, the slope method is based on angular measurements (Kunz and de Leeuw, 1993) whereas extensive analytical calculations have to be made in the case of the Monte-Carlo method (Gutkowicz-krusin, 1993) for the homogeneous atmospheres. Another method includes the most widely used far-end boundary point solution method for inhomogeneous turbid atmospheres, famously known as the Klett method. This method is asserted to be stable w.r.t perturbations and estimated boundary layer values. However, before analysing the LIDAR equation using the Klett method, few corrections need to be made to the raw photon count signal, as discussed below:

First, background correction is made to ensure that the backscattered signal does not include the noise present in the atmosphere,

Second, the Signal to Noise Ratio (SNR) is made to ensure that we have received maximum signal in photon counts,

Third, a range correction is needed as due to multiple scattering in the atmosphere, there is an exponential decrease in the backscattered raw signal (i.e., P(r)). Klett, 1981 suggested that the logarithmic Range Corrected Signal (RCS) is a convenient variable to solve the LIDAR equation at constant $\boldsymbol{\lambda}$ (i.e., 532 nm), defined as follows:

$$S\,(r) = \ln(P(r)r^2) = \ln(RCS), \qquad (2.3)$$

This is normalized so that S-function is created,

$$S\,(r) = \ln\left(\frac{P(r)r^2}{P(r_0){r_0}^2}\right)$$

$$= \ln\left(\frac{\beta(r)}{\beta_0(r_0)}\right) - 2\int_{r_0}^{r}\alpha\,(r')dr' \qquad (2.4)$$

Here, r_0 is constant reference range. Differentiating **Equation 2.4** w.r.t range r, we get,

$$\frac{dS(r)}{dr} = \frac{1}{\beta(r)} \frac{d\beta(r)}{dr} - 2\alpha(r), \quad (2.5)$$

Here, **Equation 2.5** has the form of the non-linear differential equation (such as Bernoulli). To solve the presence of two unknowns (i.e., $\beta(r)$ and $\alpha(r)$) in a single equation, Klett suggested that the relation between α and β can be approximated using empirical power law:

$$\beta\,(r) = constant * \alpha\,(r)^k, \quad (2.6)$$

where the exponent k lies in the interval, 0.67 ≤ k ≤ 1.0 (Klett, 1981). Substituting **Equation 2.6** in **Equation 2.5**, we get,

$$\frac{dS(r)}{dr} = \frac{k}{\alpha(r)} \frac{d\alpha(r)}{dr} - 2\alpha(r) \quad (2.7)$$

Assuming k is a constant in **Equation 2.7**, the solution to this non-linear differential equation can be given as:

$$\alpha(r) = \frac{\exp\left[\frac{(S(r) - S(r_0))}{k}\right]}{\frac{1}{\alpha(r_0)} - \frac{2}{k}\int_{r_0}^{r} \exp\left[\frac{(S(r) - S(r_0))}{k}\right] dr'} \quad (2.8)$$

Based on this Klett solution for the LIDAR equation, Fernald, 1984 proposed taking into account the scattering properties due to both aerosols as well as molecular components as well for the two unknowns in the LIDAR equation (i.e., $\alpha(r)\ and\ \beta(r)$):

$$\boldsymbol{\alpha\,(r) = \alpha_{mol}\,(r) + \alpha_{aer}(r)}\ [\tfrac{1}{m}]$$

$$\boldsymbol{\beta\,(r) = \beta_{mol}\,(r) + \beta_{aer}(r)}\ [\tfrac{1}{m-sr}] \quad (2.9)$$

where the subscripts mol and aer denotes molecular and aerosol components. Another critical parameter that connects the two unknown (i.e., $\beta(r)$ and $\alpha(r)$) involved in solving the LIDAR equation includes the Lidar Ratio (S), which is defined as the ratio of particle extinction to back-scatter coefficient as follows:

$$\boldsymbol{S\,(r) = \frac{\alpha\,(r)}{\beta\,(r)}}\ [\text{sr}], \quad (2.10)$$

and it depends on particle composition, size, and shape properties. The main assumption involved in the Fernald method is the aerosol Lidar Ratio (S_a) which is held constant and can lead to high uncertainty in the retrieval. To transform **Equation 2.1** into the desired form, S_a is defined as:

$$\mathrm{S}_a = \frac{\alpha_{aer}(r)}{\beta_{aer}(r)}\,[\mathrm{sr}] \tag{2.11}$$

However, the S_m (molecular Lidar Ratio) is assumed to be constant over a wide range:

$$\mathrm{S}_m = \frac{\alpha_{mol}(r)}{\beta_{mol}(r)} = \frac{8\pi}{3}\,[\mathrm{sr}] \tag{2.12}$$

Now rearranging **Equations 2.8, 2.9, 2.11, and 2.12**, the equation for the total volume back-scatter coefficient is given as:

$$\beta\,(r) = \frac{RCS\,(r)*\exp\left(2\,(S-S_m)*\int_r^{r_{ref}}\beta_{mol}(r')dr'\right)}{\frac{RCS\,(r_{ref})}{\beta aer\left(r_{ref}\right)+\beta_{mol}(r_{ref})}+2\,LR\int_r^{r_{ref}}RCS\,(r')*\exp\left(2\,(S-S_m)*\int_{r'}^{r_{ref}}\beta_{mol}(r'')dr''\right)dr'}\left[\frac{1}{m-sr}\right] \tag{2.13}$$

Here, the term far-end means it involves an inverse integration starting from the reference height r_{ref}, where the aerosol back-scatter coefficient is usually considered negligible compared to the molecular back-scatter coefficient. To retrieve molecular volume backscattering coefficient (β_{mol}), molecular volume scattering coefficient (Collis and Russell, 1976) has to be determined first, which is defined as follows:

$$\sigma_{mol}(r,\lambda) = 3.732 * 10^{-6}\left(\frac{\lambda}{550}\right)^{-4.025-0.05627*\left(\frac{\lambda}{550}\right)^{-1.647}} * \frac{P(r)}{T(r)} \tag{2.14}$$

where $P(r)$ and $T(r)$ are the atmospheric pressure (hPa) and temperature (k) at range r, derived from the radiosonde observations. Also, the wavelength (λ) is held constant at 532 nm (in this case). Using **Equation 2.12**, the volume molecular backscattering coefficient β_{mol} can be determined as follows:

$$\beta_{mol}(r) = \frac{\sigma_{mol}(r)}{\left(\frac{8\pi}{3}\right)K_{bw}(\lambda)}\left[\frac{1}{m-sr}\right] \tag{2.15}$$

where, $K_{bw}(\lambda)$ is the king factor of the air. Finally, using **Equations 2.11, 2.13, and 2.15**, the aerosol volume extinction coefficient α_{aer} can be determined as follows:

$$\boldsymbol{\alpha_{aer}(r) = LR_{aer}\left(\beta\,(r) - \beta_{mol}\,(r)\right)\left[\frac{1}{m}\right].} \tag{2.16}$$

Fernald method also relies on far-end boundary extinction value α_0. Like the Klett method, the Fernald method is not sensitive to incorrect power-law approximation. Hence, the Fernald algorithm has been adopted to estimate α_{aer} in this study. Note that the single-scattering LIDAR can measure this value of α_{aer} with high accuracy. Using this approach, the complete vertical distribution of aerosols (i.e., through the estimation of α_{aer}) will be studied using the instruments detailed in the following sub-sections, and subsequent results will be shown in **Chapter 3**.

2.2.1.1 Ground-based LIDARs

2.2.1.1.1 Instruments and Datasets

A broad view of how to obtain α_{aer} from elastic back-scatter LIDAR is presented in detail in the above derivation. Utilizing this vast background knowledge about the operation and retrieval algorithm of aerosols properties from LIDARs, we can now obtain the vertical distribution of aerosols from ground-based measurements (i.e., B in **Figure 2.1**). This objective has been achieved with the help of ground-based MPL, giving measurements from surface to 8 km, and Mie LIDAR, giving ground measurements from 8 to 30 km.

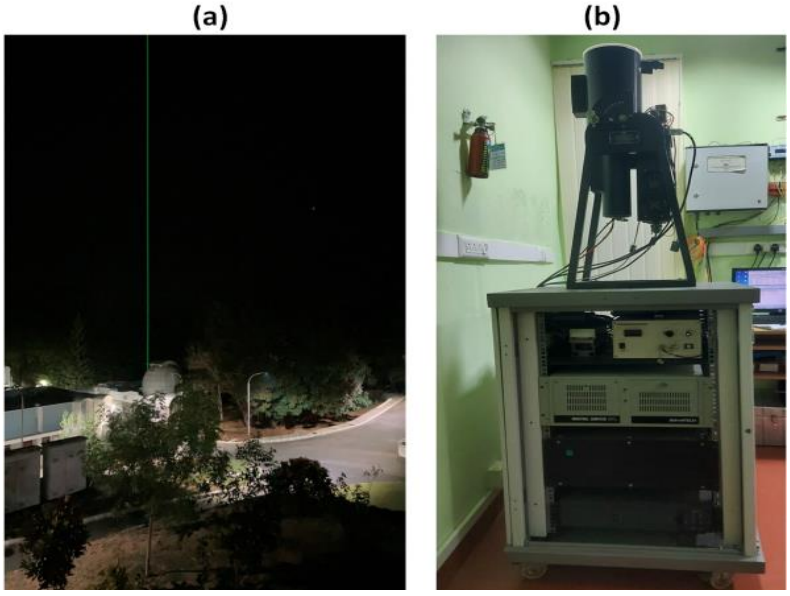

Figure 2.3 *(a) Mie and (b) Micro-Pulse LIDARs collocated at NARL, Gadanki, India.*

Both these LIDARs are collocated at National Atmospheric Research Laboratory (NARL), Gadanki, India, and are shown in **Figure 2.3**. Major specifications of the two LIDARs used in the study have been provided in **Table 2.1**. The Gadanki region (13.45^{o}N, 79.1^{o}E) is in a rural location that is situated about 120 km north-west

of Chennai and about 130 km from the Bay of Bengal (BoB) at an altitude of 375 m above mean sea level in southern peninsular India (**Figure 2.4a**). The laboratory is surrounded by small hills, villages, and the National Highway-18, a prominent source of forest fires, BB activities, and anthropogenic emissions. More details of the location have been reported in detail in Basha and Ratnam, 2009.

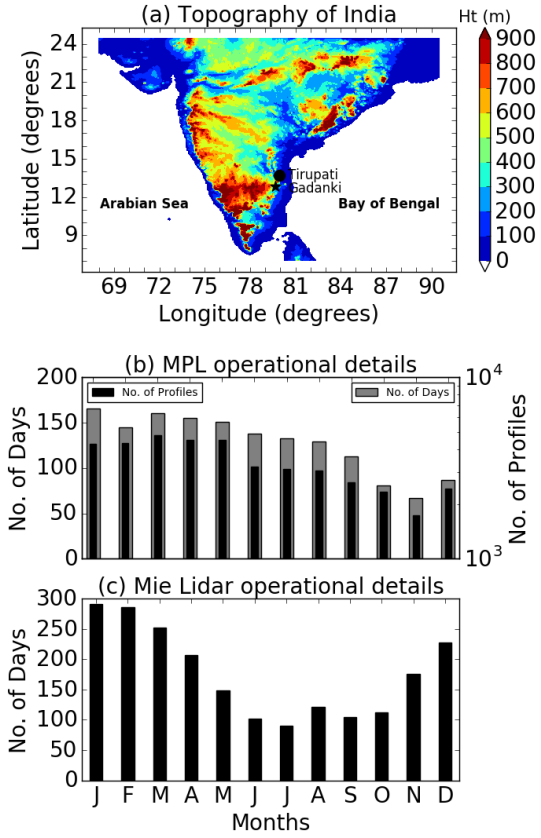

Figure 2.4 (a) *Topography map of the Indian sub-continent. The observational sites of Gadanki (star) and Tirupati (solid circle), where LIDAR measurements are made, are also over plotted.* ***(b)*** *Monthly distribution of the number of NT measurements available from both NARL and SVU MPL LIDARs (grey bars) from 2010 to 2018. The monthly number of profiles integrated every 15 minutes is also superimposed (black bars) with a top-right axis.* ***(c).*** *Monthly distribution of the total number of measurements available for NARL Mie LIDAR from 1998 to 2018.*

MPL was developed at NARL, Gadanki, to study aerosols optical properties and boundary layer characteristics (Kumar et al., 2010). This is operational from August 2010 to December 2018 with a dataset gap between December 2012 and April 2015. Another identical MPL system has been operational from January 2014 to December 2018 at the Sri Venkateswara University (SVU), Tirupati (13.6^{o}N, 79.2^{o}E) (**Figure 2.4a**). Note that SVU is located 30 km (aerial distance) away from NARL.

Recently, Prasad et al. (2019) reported a high level of consistency in the clear sky profiles of α_{aer} between these two LIDAR systems with the same time periods. So, the MPL measurements at SVU are considered to fill the data gap between the Gadanki observations. The number of days of observations in each month for the period between August 2010 and December 2018 for MPL (including the number of profiles from both LIDARs) is shown in **Figure 2.4b**. These two LIDARs are operated only on cloud-free days and for an average of 8 hours for about 100 days ($120x10^4$ profiles) in each month is available, as shown in **Figure 2.4b**.

	MPL	**Mie**	**CALIOP**
a). Laser	Nd: YAG (Pulsed Diode Pumped Solid State Laser(DPSS))	Nd: YAG (DPSS)	Nd: YAG (DPSS)
b). Wavelength	532 nm	532 nm	532 nm, 1064 nm
c). Pulse Width	< 10 ns	7 ns	20 ns
d). Pulse Energy	2 – 25 µJ	550 mJ (1998-2006) 650 mJ (since 2007)	110 mJ
e). Telescope Diameter Field of view (FOV)	Schmidt – Cassegrain 15 cm <400 µrad	Schmidt - Cassegrain 350 mm 1 mrad	Schmidt-Cassegrain 1.0 m 130µrad
f). Pulse Repetition rate	2500 HZ	20 Hz (1998-2006) 50Hz (since 2007)	20.16 Hz
g). Resolution	Vertical: 30 m Horizontal: Stationed	Vertical: 300 m Horizontal: Stationed	Vertical: 30 m for altitude range -0.5 to 8.2 km,60 m for altitude range 8.2 to 20.2 km and 180 m for altitude ranges 20.2 and 30.1 km. Horizontal: 0.333 km for altitude range -0.5 to 8.2 km and 1 km for altitude range 8.2 to 20.2km

Table 2.1 *Specifications of MPL, Mie, and CALIOP LIDARs.*

Mie LIDAR is a monostatic, pulsed, biaxial and dual-polarization system where the polarization beam splitter splits the beam into co- and cross-polarized components (subscripts denoted with P and S, respectively). Since March 1998, the Mie LIDAR was operational on cloud-free days over the Gadanki region. About 21 years of observations are available from Mie LIDAR, and its data statistics have been shown in **Figure 2.4c**. On average, about 200 days of data per month are available, with maximum days during winter months and minimum during monsoon months. Since the Gadanki region is influenced by both South-west or SW (Jun-Jul-Aug) and North-east or NE (Oct-Nov) monsoons, cloud-free days are generally fewer during these months. Nevertheless, data on such a massive scale for estimating the vertical profile of α_{aer} between 8 and 30 km has never been used so far to the best of our knowledge.

2.2.1.1.2 Cloud Screening

One of the most crucial steps in the retrieval of α_{aer} is the screening of clouds. Although the LIDAR measurements are carried out mainly on cloud-free/clear sky days, the occasional passing of clouds does exist. Hence, it is crucial to obliterate those profiles or consider the cloud-free backscattered signal below the cloud base. Many methods exist to detect clouds, such as the gradient method, variance method, scattering ratio method, and curve fitting method. Here, we have used the Wavelet Covariance Transform or WCT technique (Brooks, 2003) to identify the clouds, as it does not require any information beforehand, unlike other methods. Due to the characteristic shape of the signal, this technique is widely used to detect multi-layered and optically thin clouds (Pandit et al., 2015, 2014). The transform is defined as follows:

$$W_f(a,b) = \frac{1}{a}\int_{z_b}^{z_t} f(z)h\left(\frac{z-b}{a}\right)dz \qquad (2.17)$$

where,

$$h(\tfrac{z-b}{a}) = \begin{cases} +1, b-\frac{a}{2} \le z \le b, \\ -1, b \le z \le b+\frac{a}{2}, \\ 0, elsewhere. \end{cases} \qquad (2.18)$$

is a Haar function which is also known as a step function (Baars et al., 2008). In **Equations 2.17 and 2.18**, **a** is called dilation, chosen a priori, whereas **b** is called translation, representing the height above LIDAR. Threshold values varying linearly with altitude are chosen to avoid far-end false detection. Typical time-altitude contours

of the backscattered signals obtained from Mie LIDAR and MPL on a particular day, i.e., 26 May 2016, is shown in **Figure 2.5a and b**, respectively.

A strong backscattered signal can be observed up to 4 km from **Figure 2.5b** in MPL. Normalized RCS or NRCS observed at 01:30 IST, where the cloud was detected, is shown in **Figure 2.5d** along with the corresponding WCT profile. Normalization of RCS is required to ensure that the retrieval does not depend much on changing atmospheric conditions. Here, we have normalized the signal by taking the maximum of RCS (Amico et al., 2017). Cloud base is detected by a steep decrease of the LIDAR signal below threshold value followed by a substantial increase with the increasing cloud penetration or where the SNR is still high enough at the cloud top, as shown in **Figure 2.5d**. WCT is only the function of value **b,** whereas a value is kept constant (Pandit et al., 2014) after several inspections. NRCS signal after cloud screening is shown in **Figure 2.5f**.

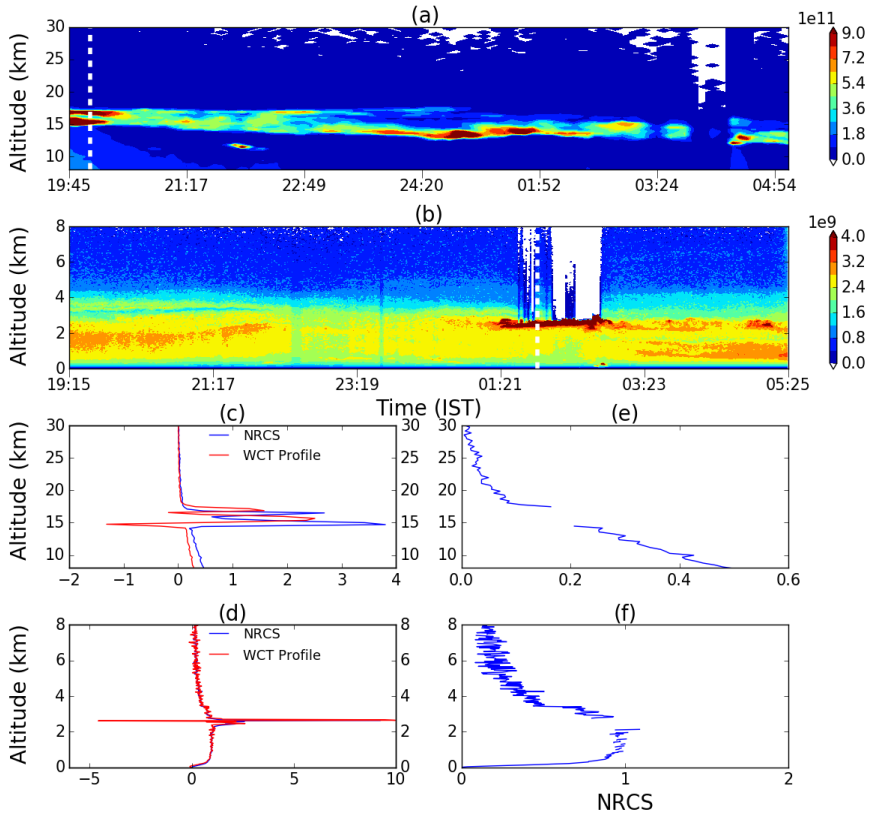

Figure 2.5 *Time-altitude contours of the LIDAR signal photon counts observed using (a) Mie (UTLS) and (b) MPL (troposphere) LIDARs, on 26 May 2016. The cloudy profiles (white dashed line) are also shown in the respective panels, (c and d) NRCS (blue color) and WCT profile (red color) for the corresponding cloud signal, (e and f) NRCS after cloud screening.*

Descending cirrus with the strong backscattered signal can be observed between 11 and 16 km in Mie LIDAR operated simultaneously on the same day (**Figure 2.5a**) as MPL. NRCS observed at 19:54 IST, where cirrus cloud was detected, is shown in **Figure 2.5c** along with the corresponding WCT profile. NRCS after cloud screening is shown in **Figure 2.5e**. NRCS intensity has not dropped sharply above the cloud due to high power laser energy and less attenuation due to the cirrus clouds. Following the WCT technique, we have identified such layers and have completely removed them before estimating the α_{aer} from the ground-based LIDARs. In addition to using the WCT, visual screening was also performed to identify cloud-free profiles from MPL and Mie LIDARs.

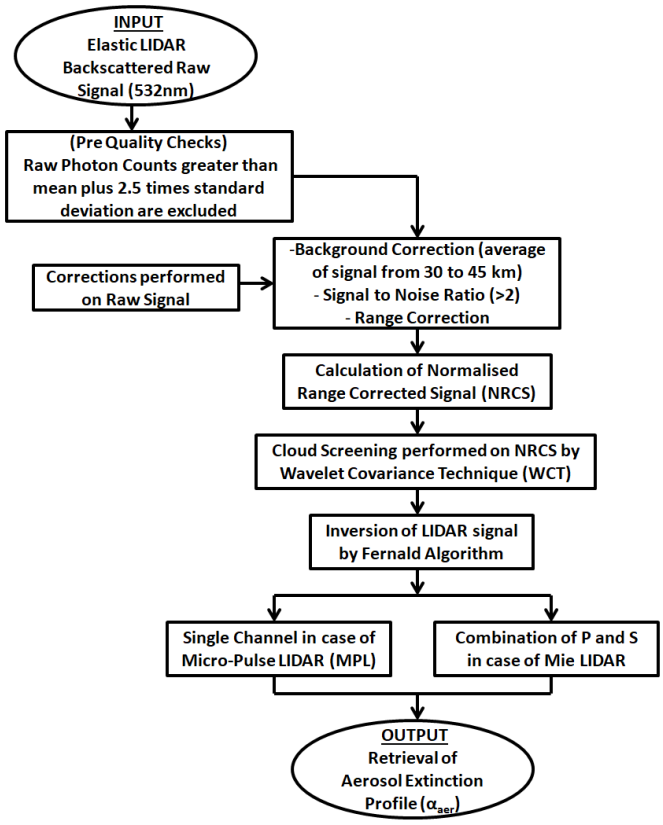

Figure 2.6 *Flow Chart showing the combined methodology used to retrieve* α_{aer} *profiles from the ground-based MPL and Mie LIDARs.*

The complete methodology discussed till now to retrieve α_{aer} profiles from the ground-based MPL and Mie LIDARs are presented as a flow chart in **Figure 2.6,** and the corresponding results drawn from these LIDARs will be shown in **Chapter 3**.

2.2.1.2 Space-borne LIDARs

Although ground-based techniques are more reliable and highly accurate, at the same time, the space-borne platforms can provide a better understanding of global

coverage (nearly) of highly variable aerosols in space and time (i.e., D in **Figure 2.1**). One such platform includes the CALIOP on-board CALIPSO satellite (Winker et al., 2009). CALIPSO was launched in low earth polar sun-synchronous orbit at an altitude of 705 km with 16 days repeat cycle, which provides an excellent opportunity to obtain aerosols over all types of heterogeneous surfaces across the globe. Due to CALIPSO's negligible swath beam width of ~ 70 m, it covers only 0.2% of the Earth's surface during its one cycle (Kahn et al., 2010). Initially, CALIPSO (launched on 28 April 2006) was a part of A(afternoon)-Train satellites (Winker et al., 2009), but in September 2018, it has lowered its orbit out of A-Train to C-Train (C for 'Cloudsat' and 'CALIPSO'), which is 16.5 km below the A-Train, as can be seen in **Figure 2.7**. However, the C-Train track intersects with the A-train about every 20 days to have simultaneity between both the Train instruments.

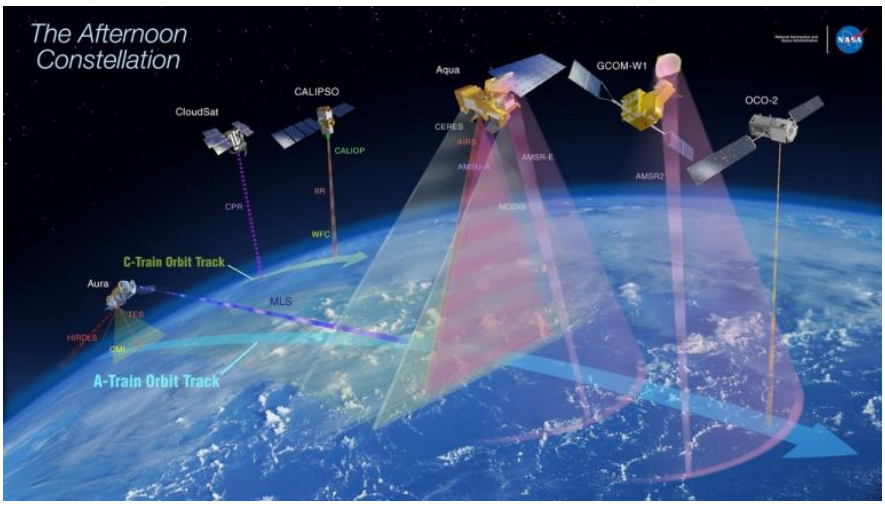

Figure 2.7 *Schematic representation of A-Train and C-Train constellation.*

Active remote sensing instrument, CALIOP is also equipped with Nd: YAG laser (similar to ground-based MPL and Mie LIDARs, see **section 2.2.1.1**) having dual-polarization and three elastic channels producing simultaneous pulses at two wavelengths, 1064 nm (first harmonic) and 532 nm (second harmonic). The pulse is transmitted at an energy of 110 mJ and received through a 1 m diameter telescope detected by PMTs for 532 nm and avalanche photodiodes for 1064 nm. The detailed specifications of CALIOP have already been provided in **Table 2.1**.

The retrieval of quantitative properties (i.e., α_{aer}) of aerosols from satellites is a much more complicated task (than ground-based), and hence CALIOP follows a multi-step procedure that involves three main algorithms (**Figure 2.8**) as follows:

(a). Selective Iterated Boundary Locator (**SIBYL**)

This is the first stage of the algorithm where all the atmospheric features (including aerosols/ clouds/ others) are detected over multi-level horizontal averaging schemes at 5, 20, and 80 km. This configuration repeats the 'scan, clear, average, scan again' sequence for all the horizontal averaging intervals mentioned above. From this, the SIBYL algorithm employs the full resolution search mode (FRSM) scan procedure to exclude clouds from aerosol averaged profiles using threshold arrays.

(b). Scene Classification Algorithm (**SCA**)

After the scanning of profiles in SIBYL, SCA determines whether the detected region is a feature (aerosol or cloud) or not. Once a feature (aerosol, in this case) is ascertained, Cloud Aerosol Discrimination (CAD) algorithm is applied to classify the feature types as either aerosol or cloud.

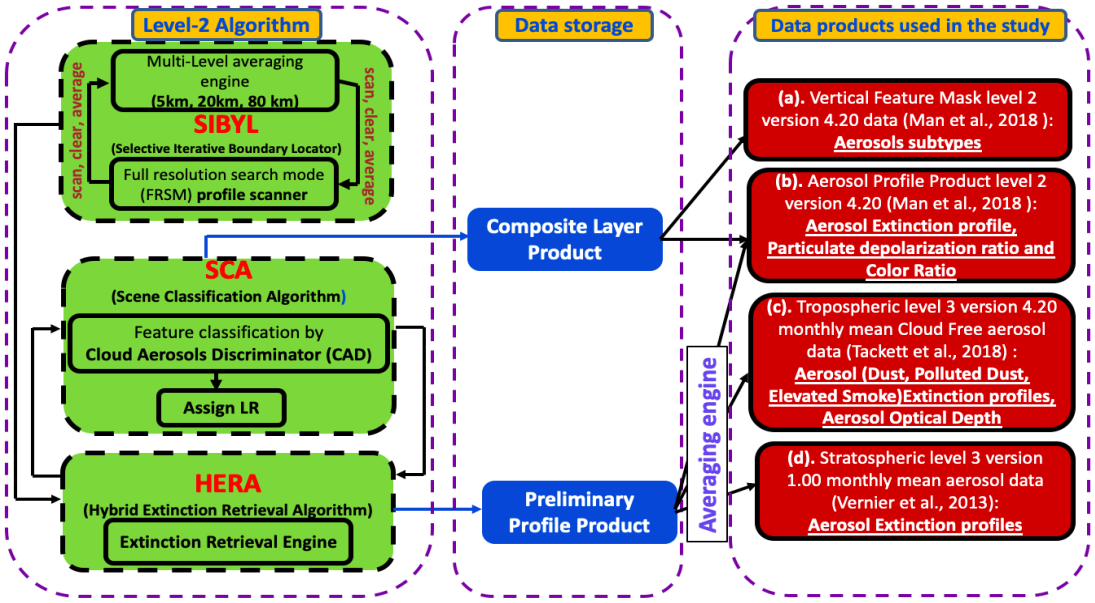

Figure 2.8 *Flow chart of level-2 algorithm and the CALIOP datasets (extending from 2006 to 2020, https://asdc.larc.nasa.gov/project/CALIPSO/) used in the study.*

CAD uses a probability density function which depends on mid-feature altitude ($z_{mid} = \frac{1}{2}(z_{top} + z_{base})$), mean attenuated back-scatter at 532 nm of feature, integrated total color ratio (χ) of the feature. This CAD score ranges from -100 to 100, indicating the negative values as aerosols. Once the feature type is classified as aerosols, S_a is assigned to each aerosol type within 30 % of the uncertainty. The S_a assigned to different aerosol types is given explicitly in **Table 2.2**.

(c). Hybrid Extinction Retrieval Algorithm (**HERA**)

Using the S_a values provided by SCA, α_{aer} profiles are retrieved. HERA will use the optical depth of each feature to adjust the S_a when SIBYL provides reliable

estimates. The accepted solutions (at both 532 and 1064 nm) are corrected later for the attenuation effects (i.e., two-way transmittance, $T^2(r)$). For the retrieval processing, CALIOP also uses the forward iterative solutions, such as two-component solutions given by Fernald, 1984; Klett, 1981, as used in ground-based observations (**Equation 2.16**). But here, the two-way particulate transmission (i.e., **Equation 2.2,** in case of single-scattering transmission) is modified (Young and Vaughan, 2009) as follows:

$$\boldsymbol{T_P^2(r) = \exp(-2\,\eta(r)\,\alpha_P(0,r))}, \qquad (\mathbf{2.19})$$

where $\boldsymbol{\eta(r)}$ is a parameter describing multiple scatterings by particles. The multiple-scattering is considered in the case of CALIOP due to the large distance between space-borne LIDAR and the Earth system, generating huge spot sizes at target altitudes (Vaughan et al., 2004). To solve this, iterative solutions developed by Platt, 1973; Elterman, 1967 are used in CALIOP's HERA algorithm for multi-scattering parameters, unlike the single-scattering solution mentioned in **section 2.2.1.**

Tropospheric Aerosols (V4)	**$S_{a(532)}$ (sr)**
Clean marine	23±5
Dust	44±9
Polluted continental/smoke	70±25
Clean continental	53±24
Polluted dust	55±22
Elevated smoke	70±16
Dusty marine	37±15
Stratospheric Aerosols (V4)	**$S_{a(532)}$ (sr)**
Polar stratospheric aerosols	50±20
Volcanic ash	44±9
Sulfate/other	50±18
Smoke	70±16

Table 2.2 *Aerosol Lidar ratios with uncertainties for tropospheric and stratospheric aerosol types at 532 nm assigned by the CALIOP V4 algorithms.*

The CALIOP sensor can provide the complete vertical profile information (using the above-mentioned algorithm) about the optical, morphological, and chemical properties of the aerosols due to the dual-polarization of the LIDAR. For the estimation of the vertical distribution of these properties of aerosols, a few quality control checks have to be applied beforehand, which include: (**1**) cloud-free, (**2**)

Atmospheric_Volume_Description (AVD = 3 (for aerosols)), (**3**) -100 ≤ CAD_Score ≤ -20 (**4**) Ext_QC = 0 or 1, and (**5**) the uncertainty flag. After applying all the quality flags to the dataset, various parameters (as mentioned in **Figure 2.7**) are obtained in this study to fulfill different scientific objectives as mentioned in **Chapter 1** and hence will be discussed in detail in **Chapters 3, 4, 5, and 6**.

2.2.2 Passive remote sensing

In this case, naturally available energies are considered the source (for example, the sun), A and C in **Figure 2.1**. One of such instruments that utilize the sun as the source of energy to study aerosols includes the most widely used radiometers or sun-photometers. These instruments can be carried in ground-based as well as space-borne platforms, which has been detailed in the following sub-sections.

2.2.2.1 Ground-based passive remote sensing

The method to retrieve aerosol properties using ground-based sun-photometers (A in **Figure 2.1**) was first introduced by Volz, 1959, where the spectral extinction of direct radiation beam was measured according to the straight forward Beer-Lambert-Bougher law, defined as follows:

$$\boldsymbol{V_\lambda = V_{0\lambda} d^2 \exp(\mathrm{OD}_\lambda m) * T_y} \qquad (\mathbf{2.20})$$

where V is digital voltage,

V_0 is extra-terrestrial voltage,

m is optical air mass,

d is the ratio of the average of actual earth-sun distance,

OD is total optical depth, and

T_y is the transmission of absorbing gases.

Thus, we can see from **Equation 2.20,** that the measured digital voltage at wavelength λ, i.e., V_λ, is a function of extra-terrestrial voltage ($V_{0\lambda}$), relative earth-sun distance (d), optical air mass (m), and exponent of the total optical depth (OD_λ). Here, OD_λ is the sum of Rayleigh and Aerosol Optical Depth (AOD) after corrections are implemented for the gaseous absorption like water vapor and other wavelength dependent trace gases (Holben et al., 1998).

As shown, the widely used Cimel Electronique 318A radiometers (i.e., AERONET) are solar-powered robotically pointed sun and sky spectral radiometers in **Figure 2.9a**. The AERONET (works on **Equation 2.20**)) is a ground-based network of sun/sky radiometers set up to provide quality-assured and calibrated datasets in the spectrum ranging from 0.34-1.02 µm wavelengths (O ' Neill et al., 2008), operational since 1993. It measures the ground-based columnar aerosols microphysical, optical, and radiative properties (Holben et al., 2001) across the globe. These robotic sun-photometers can make two basic measurements:

(a). Direct Sun measurements

These measurements are made in eight spectral bands between 340 nm and 1020 nm (440 nm, 670 nm, 870 nm, 940 nm, and 1020 nm) at approximately 10 sec, with an interval of 15 minutes. The direct sun measurement provides retrieval of spectral AOD and water vapor abundance information using the Beer-Lambert-Bouguer law (Holben et al., 1998), as shown in **Figure 2.9b**.

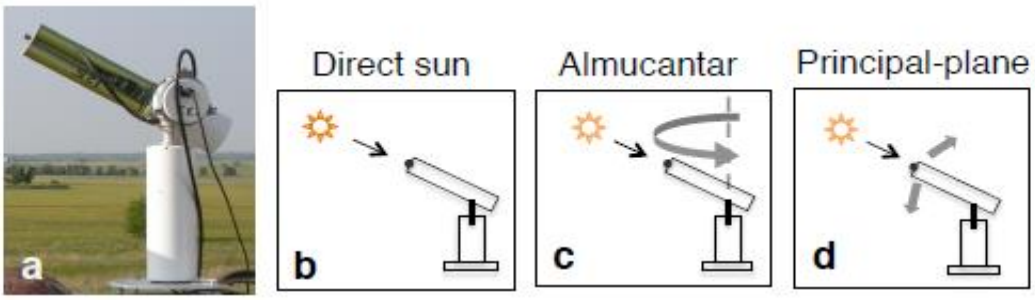

Figure 2.9. *(a) Cimel CE318 sun photometer and its radiance measurement modes (b) direct sun scan, (c) sky radiance almucantar scan, and (d) sky radiance principle-plane scan (based on Xu and Wang., 2015).*

(b). Sky radiance measurements

These radiance measurements are performed at 440 nm, 670 nm, 870 nm, and 1020 nm wavelengths, acquired from both almucantar (**Figure 2.9c**) and solar principal plane scan modes (**Figure 2.9d**). Here, the spectral measurements are made immediately after Langley's direct measurements, 20° from the sun. The sky spectral measurements provide various aerosol properties from the operational inversion algorithm of the sky radiances to derive:

(i). Complex refractive index,

(ii). Fractional volume of non-spherical particles, and

(iii). Volume particle size distribution $\frac{dV(r)}{dlnr}$ ($\mu m^3/ \mu m^2$) at 22 size bins.

From these microphysical parameters, aerosol single scattering albedo (SSA) and phase function can also be determined (Holben et al., 2001). Uncertainties can be included in the AERONET retrievals while estimating m, Rayleigh, ozone optical depth (OD_r, OD_o), and columnar precipitable water vapor. But due to low uncertainty range of AOD under cloud-free conditions of approximately ±0.01 for shorter wavelength (< 440 nm) and ± 0.02 for longer wavelength (Holben et al., 2001), AERONET datasets are widely accepted all across the globe.

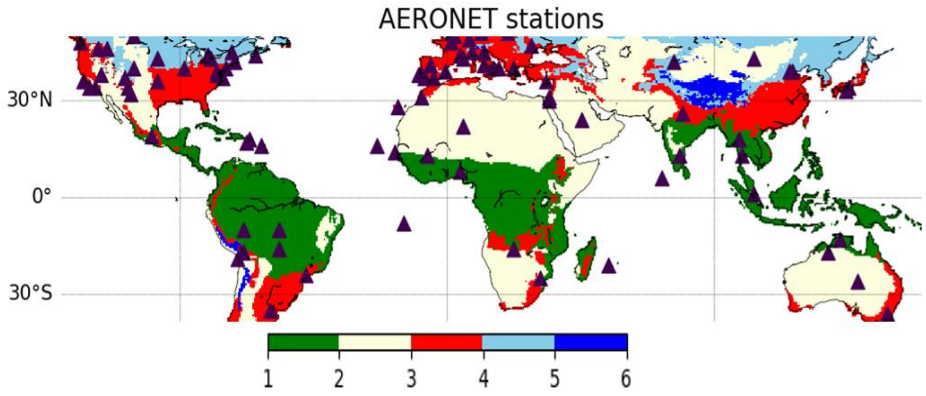

Figure 2.10 *Globally distributed ground-based AERONET stations (solid black triangles) having data above 10 years, i.e., from 2001 to 2020, marked on the climate classified regions. Where 1-2 is Equatorial, 2-3 is Arid, 3-4 is Warm temperature, 4-5 is Snow, and 5-6 is a Polar region. Data for climate classified regions can be downloaded from https://datacatalog.worldbank.org/dataset/world-maps-k%C3%B6ppen-geiger-climate-classification/.*

In this study, the datasets from both the scanning retrieval modes have been used. The dataset used in this study includes the parameters such as AOD, absorption aerosol optical depth (aAOD), scattering aerosol optical depth (sAOD), fine-mode aerosol optical depth (fAOD), and coarse-mode aerosol optical depth (cAOD). Here, the retrievals are obtained using a spectral de-convolution algorithm at a standard wavelength of 500 nm (O ' Neill et al., 2008). These ground-based observations are compared with the other techniques (such as space-borne and reanalysis, as will be seen in **sections 2.2.2.2 and 2.3**), for which we have interpolated AOD obtained at 500 nm to the standard wavelength of 550 nm, using the power law equation:

$$\mathrm{AOD}_{(550\ \mathrm{nm})} = \mathrm{AOD}_{(500\ \mathrm{nm})} \left(\frac{550}{500}\right)^{-\mathrm{AE}} \qquad (2.21)$$

where AE is the Angstrom exponent (440-870 nm). This study relies on eighty-two such AERONET sites distributed all across the globe and each having a maximum data span of about 10 years, as shown in **Figure 2.10**. The details of each AERONET site considered in this study are mentioned in **Table 4.1**.

This criterion could satisfy the maximum number of sites over Europe (approx. 20) and North America (approx. 25) regions. In addition to this, we have also used the sky-radiometer measurements from a tropical rural site Gadanki, which works on a similar principle as AERONET, and more details of which can be found in Madhavan et al. (2021). Note that the AERONET observations considered here provide direct measurements of an aerosol size where the particle radii of 0.6 μm is considered as a cut-off to separate between fine-mode and coarse-mode particles (O ' Neill et al., 2008) to estimate fAOD and cAOD. Specific details about the AERONET datasets used in this study are given in **Table 2.3,** and the corresponding results will be shown in **Chapters 4 and 5**.

Variable	Dataset Used	Spatial Resolution (lat× lon)	Time Period	Download Link
(i) Monthly AOD (ii) fAOD, (iii) cAOD, (iv) aAOD, and (v) sAOD.	**Level 2.0 version 3 cloud screened, quality assured AOD**	**Point observations**	**2001 to 2020**	**https://aeronet.gsfc.nasa.gov/**

Table 2.3 *Specifications of the AERONET datasets used in the study.*

2.2.2.2 Space-borne passive remote sensing

The history of space-borne measurements of aerosols remote sensing dates back to the 1970s when the first unmanned spacecraft measured aerosols with spectrophotometers and sun-photometers. After this, an era of satellite-based remote sensing measurements started, and a lot of advancements have been made in quantifying aerosols until then. However, retrieving aerosol properties using space-borne passive remote sensing (C in **Figure 2.1**) is a complex task as the observed signal is a combination of both surface and atmospheric (aerosols and molecules) constituents. The surface (such as land, snow, and deserts) signal is substantially larger than the atmospheric constituents due to high reflectivity. However, this study consolidates multiple satellite observations from the Earth Observing Systems (EOS), comprising the A-train satellites like Aqua (A) and Terra (T) satellites. Note that, these coordinated

polar sun-synchronous orbit satellites A-train and C-train (mentioned in section 2.2.1.2) cross each other within a few minutes, providing nearly coincident 3D (spatial, vertical, and temporal) observation of the aerosols distribution.

2.2.2.2.1 MODIS on-board Terra (T) and Aqua (A)

MODIS instrument (passive radiometer, shown in **Figure 2.7**) having 36 spectral bands ranging from 0.47-2.13 µm wavelength has a high capability of providing continuous daily (nearly 1-2 days) dataset due to its broadband imaging system of 2330 km swath width (Levy et al., 2013). On the one hand, where T is a 'morning' satellite with a local standard time (LST) of 10:30 AM, while A is a 'afternoon' satellite with an LST of 1:30 PM.

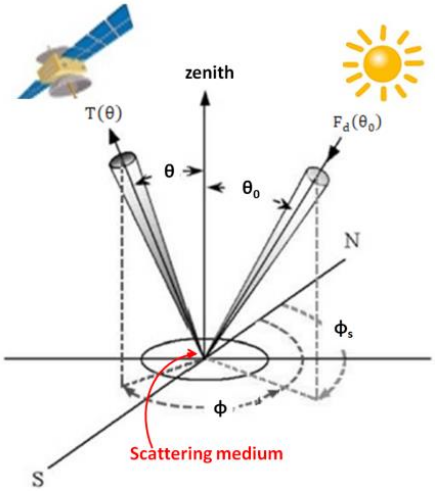

Figure 2.11 *Schematic representation of geometry for passive remote sensing satellite observations.*

However, the retrieval of aerosols with MODIS is based on the relation between the radiance measured at the TOA (ρ^*) and surface bidirectional reflectance properties ($\rho(\theta,\theta_0,\phi)$) (Kaufman et al., 1997), as given in **Equation 2.22.** The radiance measured by the sensor in the satellite depends on the geometry of the illumination and the observations and has been shown in the schematic diagram in **Figure 2.11**.

$$\rho^*(\theta,\theta_0,\phi) = \rho_a(\theta,\theta_0,\phi) + F_d(\theta_0)\,T(\theta)\,\rho(\theta,\theta_0,\phi)/(1-s\rho') \qquad (2.22)$$

where θ is view zenith angle,

θ_0 is solar zenith angle,

Φ is the azimuth angle of scattered radiation from the solar beam,

$\rho_a(\theta, \theta_0, \phi)$ is atmospheric path radiance,

$F_d(\theta_0)$ is a normalized downward flux for zero surface reflectance,

$T(\theta)$ is upward flux into satellite FOV,

s is atmospheric back-scatter ratio, and

ρ' is angular surface reflectance averaged on view and illumination angles. Here, ρ_a is related to AOD, aerosol scattering phase function $P_a(\theta, \theta_0, \phi)$ and SSA as follows:

$$\rho_a(\theta, \theta_0, \phi) = \rho_m(\theta, \theta_0, \phi) + SSA * AOD * P_a(\theta, \theta_0, \phi)/(4\mu\mu_0) \quad (\mathbf{2.23})$$

where, $\rho_m(\theta, \theta_0, \phi)$ is the path radiance due to molecular scattering,

μ and μ_0 are cosines of view and illumination angles, respectively,

Therefore, F_d, T and s are dependent on the aerosol type and loading (i.e., SSA, AOD and $P_a(\theta, \theta_0, \phi)$). However, **Equation 2.23** is only valid for single-scattering approximation of aerosols and can be applied only when AOD, Rayleigh scattering, and surface reflectance are low, but for situations with high values, multiple scatterings have to be considered.

The MODIS operational algorithm relies on the look-up table (LUT), which contains pre-computed simulations of the set of aerosol types and loadings that can describe a range of aerosol distribution globally. Here, the simultaneous inversion of two visible channels at 0.47 and 0.66 μm and one shortwave IR channel at 2.12 μm takes place (Levy et al., 2007). Inversion of these three channels leads to the estimation of AOD at 0.55 μm, which is used in this study. Recently, the accuracy assessment of MODIS C6.1 AOD retrievals against AERONET level 2 AOD across the globe was reported by Wei et al. (2019a) with a high Pearson correlation coefficient (R=0.907). Two algorithms have been developed for the study of aerosols:

(a). Dt algorithm, designed for the retrieval of AOD over dark surfaces which are non-reflective in the visible spectrum, which includes vegetated and open ocean regions,

(b). Db algorithm, designed for the retrieval of AOD over surfaces that are dark (bright) in near UV (visible) spectrums, which includes little vegetation, bright soil (or deserts), and urban regions.

However, in addition to this, a combined (DT + DB) product is also available, which is used in the study to retrieve $AOD_{(550\ nm)}$ across the globe. Presently, only the MODIS Dt algorithm has been used to create global long-term aerosol Fine Mode Fraction (FMF) products.

Variable	Dataset Used	Spatial Resolution (lat× lon)	Time Period	Download Link
i) Monthly AOD at 550 nm	**MODIS Terra MOD08_M3 (T)) and Aqua (MYD08_M3(A))**	**1° × 1°**	**T: 2001 to 2020** **A: 2002 to 2020**	**https://ladsweb.modaps.eosdis.nasa.gov/**
(ii) Optical_Depth_Ratio_Small_Land	**MODIS/Terra Aerosol Cloud Water Vapor Ozone Monthly L3 Global 1Deg (MOD08_M3 v5)**	**1° × 1°**	**2001 to 2020**	**https://zenodo.org/record/5105617#.YdfhF2hByUk**
(iii) Aerosol_Optical_Depth_Land_Mean (by MODIS DT-based Angstrom Exponent)	**MODIS/Terra Aerosol Cloud Water Vapor Ozone Monthly L3 Global 1Deg (MOD08_M3 v6.1)**	**1° × 1°**	**2001 to 2020**	**https://ladsweb.modaps.eosdis.nasa.gov/**

Table 2.4 *Specifications of the MODIS datasets used in the study.*

However, this dataset is considered highly unreliable and hence is not recommended for use. Considering this aspect, for this analysis, the FMF values obtained from Yan et al. (2021) have a high overall R of 0.68 and a Root Mean Square Error (RMSE) of 0.136 with the AERONET observations, and hence this dataset is used in the study. They have found that there existed two dense FMF centers around 0.9 and 0.65. These FMF values are multiplied with the total AOD values (derived from the MODIS monthly Terra collection 6.1 product) to finally retrieve the fAOD and cAOD values, as the Dt algorithm operates under the assumption of the bimodal log-normal distribution of aerosols. Here, the fAOD (cAOD) particles generally have radii between 0.1 and 0.25 (1 and 2.5) μm. More details about the datasets used in the study are given in **Table 2.4** and the results drawn from these observations will be shown in **Chapters 4 and 5**.

2.2.2.2.2 MISR on-board Terra (T)

Another space-borne passive instrument, MISR, is known for its unique shooting camera projections where it attains radiances at 9 varied angles (nadir, ±26.1°, ±45.6°, ±60.0°, and ±70.5°) in four spectral wavelengths of 446, 558, 672 and 866 nm

(Garay et al., 2020). These nine varied angles (symmetric in forward as well as aft directions) allow imaging of the same scene with different path lengths, thus reducing the uncertainty in the retrieval of aerosol properties, as shown schematically in **Figure 2.12**. Here, the time gap between the capturing of images by the first and last camera is nearly 7 minutes. However, due to its low swath width (relative to MODIS) constituting 360 km, its global coverage extends about once in 9 days across the equator.

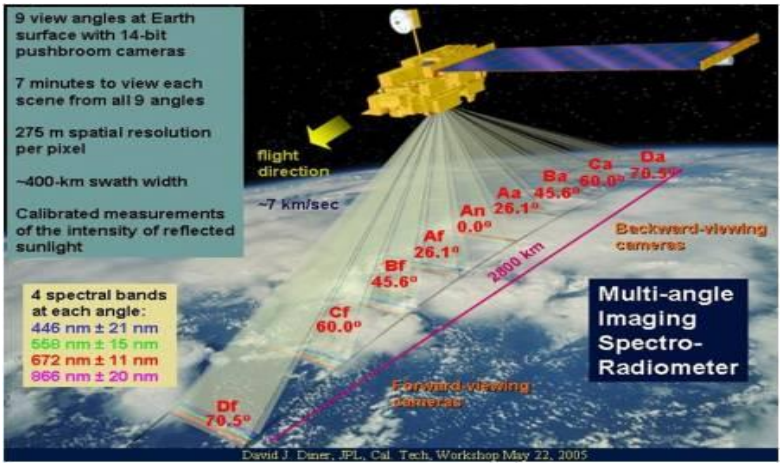

Figure 2.12 *Schematic representation of MISR satellite.*

MISR retrieval algorithm is based on the principle analysis of the multispectral, multi-angle TOA radiance measurements from which empirical orthogonal functions (EOFs) in satellite view angle are obtained. These EOFs describe the directional reflectance properties of the surface. These, along with the observations, are utilized to estimate aerosol optical properties, which are input to the LUT (discussed in previous **section 2.2.2.2.1**) of forward radiative transfer calculations. This retrieval algorithm selects a model based on the similarity of the angular shape of directional reflectance properties of the surface with each model. This subset is used as input to the original EOF algorithm. The minimization of the difference between EOF derived and LUT derived angular dependence is used for the selection of AOD (Martonchik et al., 1998).

According to the statistical comparison of MISR AOD (V23) against AERONET AOD, the value of R has increased to 0.81, RMSE has decreased to 0.154, and the percentage of retrievals that fall within EE ($\pm$ (0.05 + 0.2 $AOD_{AERONET}$)) has increased to 66.1% due to the improvement in the horizontal resolution and its cloud screening methods (Garay et al., 2020). Considering this into account, MISR (passive radiometer) is highly capable of providing direct information based on aerosol size (in terms of AOD), as mentioned in (Garay et al., 2020). The MISR instrument can provide

small, medium, large and non-spherical AOD values. Here, the particles of radii less than 0.35 µm, between 0.35 and 0.7 µm, and greater than 0.7 µm were considered as small-mode, medium-mode, and large-mode particles (Garay et al., 2020). More specific details of the dataset used in the study are mentioned in **Table 2.5,** and the results obtained will be discussed in **Chapters 4 and 5.**

Variable	Dataset Used	Spatial Resolution (lat× lon)	Time Period	Download Link
(i) Monthly AOD, **(ii) Small-mode AOD,** **(iii) Medium-mode AOD, and** **(iii) Large-mode AOD.** **(iv) aAOD**	**MISR V23 monthly AOD product (F15_0032)**	**0.5° × 0.5°**	**2001 to 2020**	**https://asdc.larc.nasa.gov/project/MISR/**

Table 2.5 *Specifications of the MISR datasets used in the study.*

2.3 Reanalysis Datasets

Apart from the remote sensing techniques mentioned in **section 2.2**, a reanalysis dataset is also utilized to analyse the long-term trends in the varying aerosol properties. This technique makes use of observations of the Earth system from the past collected datasets. However, due to the uneven distribution of the observational datasets, reanalysis fills the gaps with a modelling approach to have a complete picture of the variable across the globe.

MERRA-2 reanalysis is the immediate version of the updated Goddard Earth Observing System, V5 (GEOS-5) earth system model coupled with the Goddard Aerosol, Chemistry, Radiation, and Transport (GOCART) model to simulate aerosol emissions over the globe (Buchard et al., 2017). Assimilated data processes relies on a forecast model to combine measurements from the most recent observations, such as bias-corrected AOD retrieved from MODIS (T (2000-present) and A (2002-present)), AVHRR from 1979 to 2002, non-bias-corrected AOD from MISR (2000-2014) over bright surfaces, and direct AOD measurements from AERONET (Buchard et al., 2017) between 1999 and 2014, in a physically consistent manner. Che et al. (2019) conducted a study to validate MERRA-2 AOD values against AERONET and have found that the reanalysis dataset has performed exceptionally well with R=0.85 and RMSE of 0.12. The optical properties of aerosols, including aAOD and sAOD, obtained from the

MERRA-2 reanalysis dataset (Buchard et al., 2017), have been examined here. Specific details of the dataset used in the study are mentioned in **Table 2.6,** and derived parameters from this dataset will be shown in **Chapters 4, 5, and 6.**

Variable	Dataset Used	Spatial Resolution (lat× lon)	Time Period	Download Link
(i) Monthly AOD, **(ii) aAOD,** **(iii) sAOD,** **(iv) dust AOD,** **(v) sulfate AOD,** **(vi) organic carbon AOD,** **(vii) black carbon AOD, and** **(viii) sea-salt AOD**	**MERRA-2, Monthly mean, Single Level, Aerosol Diagnostics (M2TMNXAER) product named under 'tavgM_2d_aer_Nx: 2d'**	**0.5° × 0.625°**	**2001 to 2020**	**https://disc.gsfc.nasa.gov/datasets**
(ix) Planetary Boundary Layer height	**MERRA-2, Monthly mean, Single Level, Surface Flux diagnostics (M2TMNXFLX) product named under 'tavgM_2d_flx_Nx: 2d'**	**0.5° × 0.625°**	**2001 to 2020**	**https://disc.gsfc.nasa.gov/datasets**

Table 2.6 *Specifications of the MERRA-2 datasets used in the study.*

It is to be noted that the Level-3 monthly AOD datasets from all the satellite/reanalysis datasets (mentioned till now) have undergone several averaging between overestimation and underestimation of the error values of the instruments. As all the measurement techniques are at different spatial resolutions, as mentioned above (see **Tables 2.3, 2.4, 2.5, and 2.6 and Figure 2.8**), the nearest-neighbour interpolation method (Yousefi et al., 2020) has been applied to all of the AOD values (of each product) and re-gridded to 1° × 1° resolution to have a robust comparison among all the instruments used throughout the study.

2.4 Long-term trend analysis

This huge space-borne remote sensing (see **section 2.2**) and reanalysis (see **section 2.3**) long-term (between 2001 and 2020) datasets have gone into the analysis of changing patterns of various properties of aerosols via the long-term trends approach and will be discussed explicitly in **Chapters 4, 5, and 6**. Randel and Cobb, (1994) estimated a multivariate linear regression (MLR) trend model to analyse long-term trends in the time series of monthly averaged variables after isolating/removing specific

oscillations. This approach is considered explicitly in the study as it is well known that the conventional approach (i.e., linear trends) applied to any long-term data set will be highly biased based on its starting and ending points. Further, in **Chapter 1**, we highlighted the presence of the long-term period oscillations prevailing in the background, thus one needs to remove these oscillations to estimate the exact trend values effectively. In this study, monthly mean AOD datasets from all the discrete measurements (AERONET, MODIS (A), MODIS (T), MISR, CALIOP, and MERRA-2) are used, and the oscillations such as Semi-Annual Oscillation (SAO) with a period of 6 months, Annual Oscillations (AO) with a period of 12 months, QBO with a period of 23-30 months, ENSO with a period of 52-64 months, and SC with a period of 132 months are isolated while estimating the trend analysis. Before applying the trend analysis, quality checks were applied to each of the above-mentioned datasets to check the continuity of the data. A general expression for the model equation (Randel and Cobb, 1994) is as follows:

$$\mathbf{T(t)} = \boldsymbol{\alpha}\,\mathbf{(t)} + \boldsymbol{\beta}\,\mathbf{(t)\,t} + \boldsymbol{\gamma}\,\mathbf{(t)\,QBO\,(t)} + \boldsymbol{\delta}\,\mathbf{(t)\,Solar\,(t)} + \boldsymbol{\varepsilon}\,\mathbf{(t)\,ENSO\,(t)} + \mathbf{residual\_fit\,(t)} \quad (\mathbf{2.24})$$

where, T (t) is the total AOD time series, α(t) represents the seasonal coefficient, β(t) is the seasonal trend coefficient, γ (t), δ (t), and ε (t) are the corresponding QBO, Solar, and ENSO seasonal coefficients, respectively, and t is the time index (t=0,1,2,…N-1). These coefficients are determined at each grid using the harmonic expansion, as shown below for α (t):

$$\alpha(t) = A0 + \sum_{i=1}^{3}[A_i \cos\omega_i t + B_i \sin\omega_i t], \quad (\mathbf{2.25})$$

where, $\omega_i = 2\pi\, i/12$ and A_0, A_1, B_1,…..are the constants. A similar expansion can be carried out for β (t), γ (t), δ (t), and ε (t) coefficients as well. The QBO zonal wind (m/s) at 30 hPa at Singapore (1° N, 104° E) is used here as QBO (t) time series proxy, and the corresponding dataset can be downloaded from http://www.geo.fu-berlin.de/met/ag/strat/produkte/qbo/. The QBO is a quasi-periodic oscillation of the equatorial zonal winds, and this dataset can be viewed as a representative of the global belt near the equator. At the same time, Ottawa's monthly mean F10.7 cm solar flux indices are used as a time series proxy for SC, Solar (t), and the dataset for which can be available from ftp://ftp.geolab.nrcan.gc.ca/data/solarflux/monthly_averages/maver.txt. The solar radio flux emissions at 10.7 cm are an excellent indicator of solar activity, and Ottawa is considered to be one of the longest running records to monitor the same.

Further, Southern Oscillation Index (SOI), which is obtained by removing the monthly mean sea pressure level at Tahiti (18° S, 150° W) from Darwin (13° S, 131° E), is used as a time series proxy for ENSO (t). The difference between the pressure levels at these locations has observed a seesaw pattern that reflects the atmospheric components of ENSO. For instance, the pressure becomes below (above) average in Tahiti (Darwin), and SOI is negative during El-Niño while pressure behaves oppositely in the case of La-Niña, where SOI becomes positive. The dataset for the same can be downloaded from http://www.cpc.ncep.noaa.gov/data/indices/soi/. Furthermore, the error estimation for the statistical fits in the coefficients of oscillations is carried out using least square estimates according to Neter, 1983 as follows:

$$\sigma = \sqrt{\frac{S}{N_d - M}(X^T X)^{-1}} \quad (2.26)$$

where, N_d is the length of a dataset to be modelled, M is the total number of regression constants in the model, S is the sum of the square of residuals, and X is the input data matrix. The key element to apply the MLR trend analysis approach includes the availability of a sufficient span of the dataset, which is also one of the reasons behind choosing only those AERONET sites which have datasets above 10 years, as detailed in **Table 4.1**. However, for a few datasets having lesser data points (e.g., MODIS (fAOD and cAOD), aAOD, and Non-spherical AOD (nAOD)) used in the study, we have to anticipate the alternative approach, i.e., linear regression (LR) trend analysis. This approach is considered to be very simple and less sensitive to the breaks involved in the dataset. To implement this approach, an additional criterion is used to remove the noticeable influence of the annual cycle from the data, for which the datasets are firstly de-seasonalized by obtaining time series of the variable anomaly at each selected grid. Furthermore, the least-square fit (Neter, 1983) is applied to the monthly time series to obtain the coefficients of linear regression slopes (AOD/year) and minimize the sum of residual squares. The confidence level considered here is represented with the p-values ≤ 0.05, which is considered to be statistically significant.

Before applying the MLR trend analysis to the datasets, several key elements must be addressed, which includes **(1)** Sampling bias due to insufficient spatial and temporal coverage, **(2)** Biases in algorithm retrieval, **(3)** Sufficient span of the dataset, and **(4)** Potential effects due to QBO, ENSO, and SC on the measurements. With the aim to perceive the response of QBO, ENSO, and SC on the long-term AOD dataset, the multi-annual oscillations with the period between 2 to 11 years have been discussed

here. Our data consisted of the duration period between 2001 and 2020, which included seven El-Nino (2002-2003, 2004-2005, 2006-2007, 2009-2010, 2014-2015, 2015-2016, 2018-2019) and seven La-Nina (2005-2006, 2007-2008, 2008-2009, 2010-2011, 2011-2012, 2016-2017, 2017-2018) events. For reference purposes, we have utilized MODIS_A monthly dataset from 2002 to 2020 (as it is the best correlated dataset as discussed in **section 4.3.1**) and was subjected to show the AOD response due to QBO, ENSO, and SC fluctuations (**Figure 2.13**).

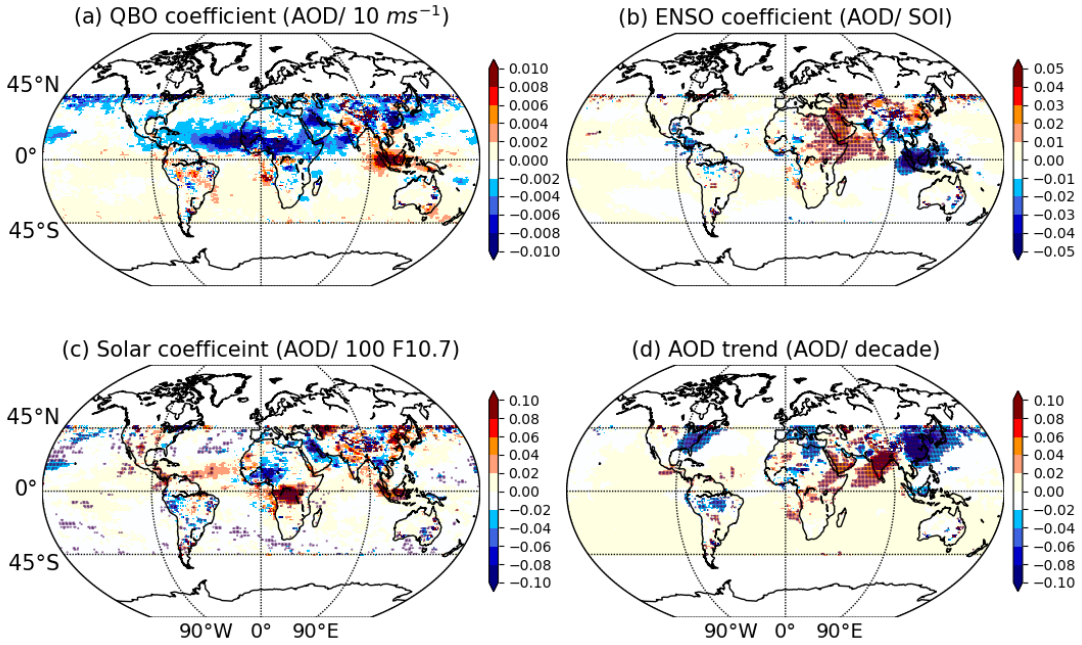

Figure 2.13 *The coefficients obtained after applying MLR trend analysis to MODIS_A dataset, extended from 2002 to 2020 for the (a) QBO coefficient, (b) ENSO coefficient, and (c) SC coefficient. (d) Trends were obtained after isolating long-term period oscillations from the dataset. The star marks in each subplot represent the significant values at a 95 % confidence level.*

A high negative (positive) QBO response on AOD was observed in North-Western Africa or NWA and its adjoining Atlantic waters, Middle-East or ME, AS, and Eastern and Central China or ECC (Indonesia, north and central India) region. The AOD response to ENSO fluctuations showed significantly high positive values over the ME and AS region, while negative values were encountered over Indonesia and North-West India. The SC response due to AOD was mostly positive (negative) over SAF, Indonesia, and a few parts of the Indian (NWA, ME) region. Note that to elucidate the effects due to SC fluctuations, we need a minimum of two SCs (~ 22 years of a

dataset) so as to over-ride this aspect, we have discussed the aerosol's annual and seasonal variations as well in **Chapter 4**.

2.5 Software Used

PYTHON programming language has been used in this study for scientific computing and to handle or analyse all the satellite/ reanalysis and ground-based datasets (discussed in **sections 2.1, 2.2, 2.3, 2.4**) to create the figures shown in this thesis. It is an open-source distribution platform used in the study to run on Windows 10 and LINUX platforms.

Chapter 3

Vertical and Spatial distribution of EALs obtained using ground-based and space-borne LIDAR observations

3.1 Introduction

The uneven vertical distribution of different types of aerosols has a varied impact on the incoming solar and outgoing terrestrial radiations (Charlson et al., 1992). It is considered as one of the greatest scientific challenges (Toth et al., 2016), which alone can contribute to an uncertainty of about 0.5 Wm^{-2} globally to the radiative forcing (Choi and Chung, 2014). The effects due to scattering and absorbing aerosols will be different if aerosols are present in the form of EALs, particularly the absorbing type. For example, if scattering aerosols are present aloft, cooling is expected at the surface, whereas warming is expected aloft in the case of absorbing type. In addition to this, the presence of absorbing aerosols (such as BC) in the EALs can also alter the vertical thermal structure of the atmosphere (Talukdar et al., 2019). Further, tropospheric (stratospheric) aerosols are completely different from the stratospheric aerosols due to their shorter (longer) residence times. Thus, knowledge of the spatial and vertical distribution of aerosols is essential to quantify the effect of dynamics and long-range transport in modulating the aerosols vertical structure.

Numerous measurement techniques exist to obtain the optical properties of aerosols, such as in-situ (balloon-borne and aircraft) and remote sensing (ground-based and space-borne) measurements. In particular, LIDAR (as discussed in **section 2.2.1**) is one of the most prominent ground-based active remote sensing tools which provide vertically resolved information. Over the Indian region, several studies have been carried out to understand the vertical distribution of aerosols in the lower troposphere using MPL (Jayaraman et al., 1995; Mishra et al., 2010; Niranjan et al., 2007; Prasad et al., 2019; Ratnam et al., 2018; Sarangi et al., 2016; Satheesh et al., 2006; Sinha et al., 2013). Some of these studies revealed the presence of EALs during monsoon and pre-monsoon seasons which is attributed to the long-range transport.

A few studies have been conducted on the vertical distribution of aerosols in the UTLS region as well using Mie LIDAR over Gadanki (e.g., Kulkarni et al., 2008; Thampi et al., 2009). Further, balloon-borne studies have also been carried out to obtain aerosol vertical distribution in the troposphere (Babu et al., 2008; Ratnam et al., 2020) and the UTLS region (Ramachandran and Jayaraman, 2011) over India. A very recently BATAL campaign was carried out jointly by the ISRO and NASA over

the Indian region to investigate the troposphere (Ratnam et al., 2020) and UTLS region aerosols (Vernier et al., 2018), as already discussed in **Chapter 1**.

Although the ground-based active remote sensing (such as LIDAR) and in-situ (such as balloon-borne) observations have good accuracy but it is limited to point measurement, as discussed in **Chapter 2**. Aircraft based measurements can resolve this aspect partially, but limitations exist due to their cost and altitude coverage. In this context, the CALIOP (Winker et al., 2009) satellite provides the vertical profile of α_{aer} from the surface to 30 km on a global scale (Sassen and Zhu, 2009; Yu et al., 2010). It plays an important role to fill the gap that exists from the above-mentioned techniques.

To the best of our knowledge, no study exists so far dealing with the complete vertical distribution of the aerosols. Thus, this chapter is aimed to investigate the vertical distribution of aerosols covering from near surface to the UTLS region using long-term observations of ground-based LIDARs (i.e., MPL (2010-2018) and Mie (1998-2018)) collocated at Gadanki (13.5^{o}N, 79.2^{o}E) region, as detailed in **section 2.2.1.1**. After evaluating the performance of CALIOP (2006-2018) measurements (see **section 2.2.1.2**) over Gadanki, we have used it to obtain the spatial distribution of aerosols. Plausible mechanisms for the formation and maintenance of these layers in the troposphere and UTLS region are explained using the supporting data. Further, dominant aerosol sub-types, including optical properties prevailing in EALs, are also reported in this study.

3.2 Prevailing background meteorological conditions

Monthly mean contours of temperature, RH, zonal, and meridional winds observed between the surface and 25 km using GPS radiosonde measurements over the Gadanki region averaged from 2010 to 2018 are shown in **Figure 3.1**. Background atmospheric meteorological conditions enduring over the observational site have been examined in this study for which the year is divided into four seasons, namely, winter (December-February), pre-monsoon (March-May), monsoon (June–September), and post-monsoon (October–November). Monsoon and post-monsoon seasons are also called as SW and NE monsoons, and the Gadanki region experiences both of these seasons more or less equally. The temperature remains constant above 5 km, though high temperatures during pre-monsoon are usually seen at lower altitudes (**Figure 3.1a**). Seasonal variation in temperature is again reflected above 18 km. The TTL (designated as the layer between convective outflow height (COH) and CPT

altitude) superimposed on the same panel extends from 14 to 18 km with mean tropical tropopause at 16 km. The high RH is seen in monsoon and post-monsoon seasons extending up to 12 km with a peak (~80%) between 2 and 4 km during SW monsoon (Jun-Sep) in **Figure 3.1b**. During the winter months, RH is restricted to ABL, which is also shown in **Figure 3.1b**. This ABL is detected using maximum gradient in the refractivity profile (Basha and Ratnam, 2009) on each day averaged during similar months of 2010-2018.

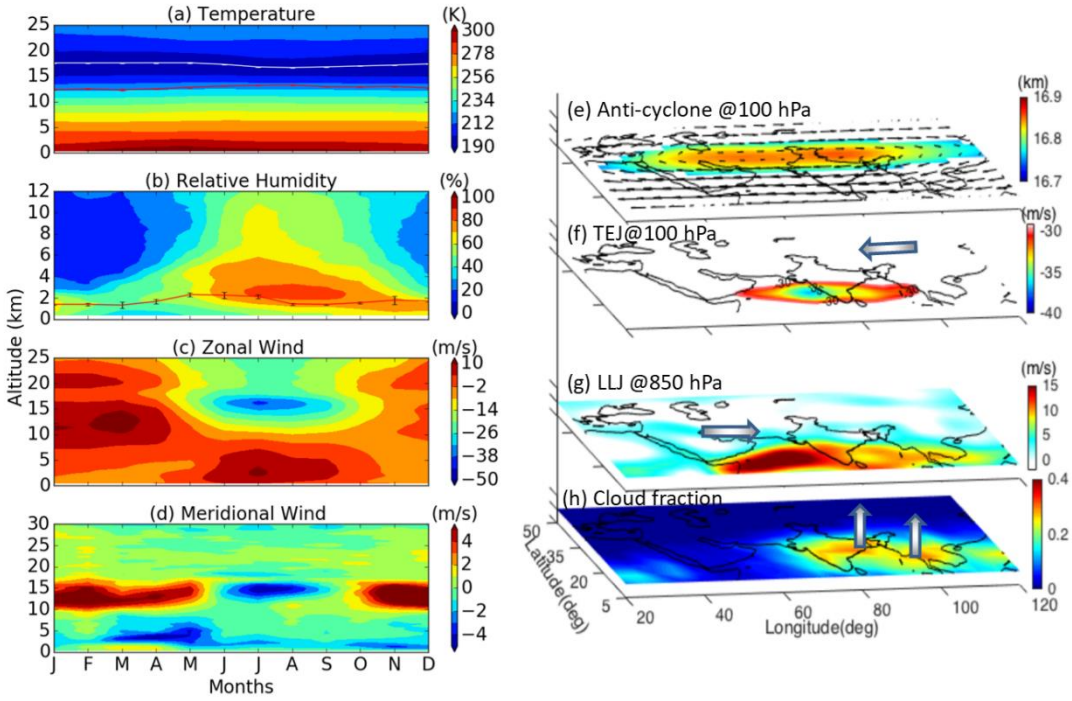

Figure 3.1 *Monthly mean contours of (a) temperature, (b) RH, (c) zonal wind, and (d) meridional wind, obtained using GPS radiosonde measurements over Gadanki, when averaged from 2006 to 2018. The CPT (white color) and COH (red color) detected using radiosonde averaged during the same time period are superimposed in (a). ABL detected using radiosonde is also superimposed in (b). (e) Geo-potential height at 100 hPa superimposed with wind vectors, (f) zonal wind at 100 hPa, and (g) zonal wind at 850 hPa obtained from ERA-Interim reanalysis data sets. (h) Cloud fraction obtained from CALIOP measurements.*

A strong westerly wind (> 10 ms^{-1}) and easterly wind (> 50 ms^{-1}) during monsoon season at altitudes of 2-4 km and 14-16 km can be noticed in the zonal winds (**Figure 3.1c**), which indicates the presence of LLJ and TEJ, respectively. During other months, zonal winds are mostly westerly throughout the altitudes. The moisture from the AS will be transported over the Gadanki region through LLJ,

which leads to high RH (**Figure 3.1b**) from 2-4 km during the monsoon and post-monsoon seasons. Meridional winds are very weak except between 10 and 15 km with southerlies (> 4 ms^{-1}) in all the seasons except during monsoon season, where it shows northerly with a similar magnitude (**Figure 3.1d**). Strong northerly is also observed between 2 and 5 km during the pre-monsoon season. These conditions remain the same throughout SI, as shown in **Figure 3.1f and g** for TEJ and LLJ, respectively, obtained from ERA-Interim reanalysis data averaged during 2010-2018. The presence of the ASMA is also clearly seen in the geo-potential height shown in **Figure 3.1e**. Cloud fraction obtained from CALIOP, which is shown in **Figure 3.1h,** reveals a high fraction extending from NE India to the head BoB. How these background meteorological and dynamical conditions affect the aerosol concentrations over the Gadanki region will be discussed in the later sections.

3.3 Results and Discussion

3.3.1 Comparison between ground-based and space-borne LIDARs

Before using CALIOP measurements (see **Figure 2.8b**) for obtaining vertical and spatial distribution, they are compared with the ground-based LIDAR observations (see **Figure 2.4**). A comparison between the profiles from NARL and SVU MPL with CALIOP has already been shown in the previous studies (Ratnam et al., 2018; Prasad et al., 2019). Here, we have used only the NT overpass dataset from CALIOP because of their high accuracy and ground-based LIDAR operations at these times. The comparison between satellite and ground-based measurements has been made with CALIOP 5 km aerosol layer products and the averaged seasonal α_{aer} profiles are calculated, as shown in **Figure 3.3**.

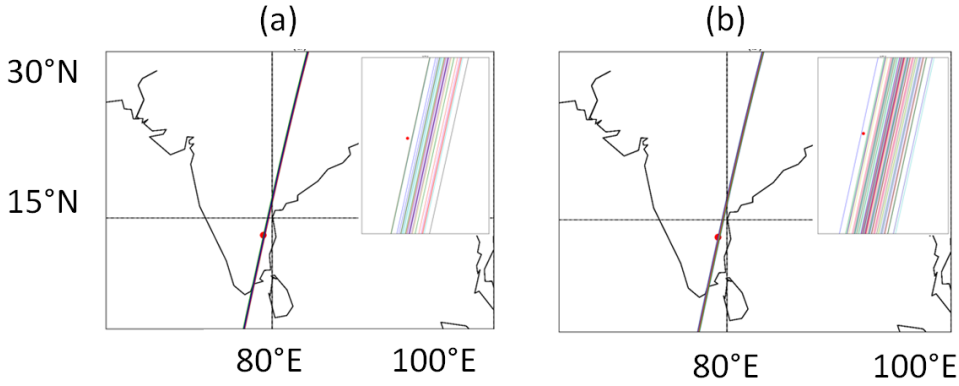

Figure 3.2 *CALIOP overpass tracks over Gadanki/ Tirupati on the days of (a) Mie and (b) MPL LIDAR operations.*

A total of 67 days (Winter: 16 days, Pre-monsoon: 23 days, Monsoon: 23 days, Post-monsoon: 5 days) of MPL observations are available on the CALIOP overpass days within 100 km from Gadanki/Tirupati from 2010 to 2018. The tracks of these overpasses are shown in **Figure 3.2**. The comparison between CALIOP NT profile data (Level-2, V4) and MPL data for these cases, including Standard Error (SE), obtained while segregating season-wise, is shown in **Figure 3.3a-d**. Since the chosen S_a in CALIOP retrievals is range dependent (varies with height depending upon the aerosol composition), α_{aer} profiles from ground-based LIDAR (i.e., MPL) are retrieved using different S_a i.e., at 20 sr, 40 sr, and 70 sr to investigate the influence of S_a on the magnitude of derived α_{aer} profiles. Note that S_a at 20-30 sr is categorized as a marine aerosol, 30-40 sr as a polluted marine aerosol, 40-60 sr as an urban aerosol, and 50-80 sr as wood BB aerosol (Müller, et al., 2007).

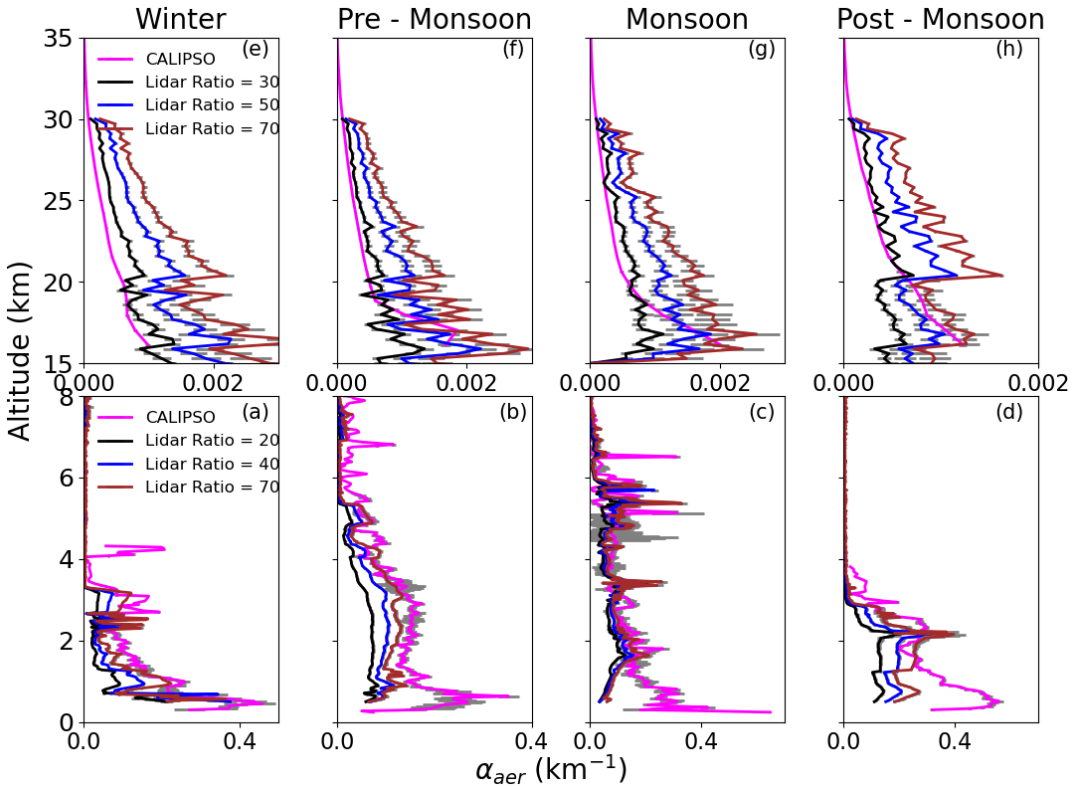

Figure 3.3 *Composite seasonal mean α_{aer} obtained from combined MPL (NARL and SVU) data up to 8 km using different S_a (20, 40 and 70 sr) during (a) winter, (b) pre-monsoon, (c) monsoon, and (d) post-monsoon seasons. CALIOP measured α_{aer} is also superimposed (pink color lines) in respective panels. The horizontal bars represent the SE values. (e) to (h) same as (a) to (d) but observed using Mie LIDAR with S_a at 30, 50, and 70 sr.*

In general, the higher the S_a, the greater the α_{aer} values are found as expected (as per **Equation 2.11**) in **Figure 3.3**. Superimposed CALIOP derived α_{aer} profiles show very good comparison with MPL derived α_{aer} with S_a at 70 sr during winter (**Figure 3.3a**) and to some extent during pre-monsoon with slight overestimation below 1 km (**Figure 3.3b**). However, none of the MPL α_{aer} values match with CALIOP α_{aer} values below 1 km but closely matches with α_{aer} values above 2 km during monsoon and post-monsoon seasons. This suggests that optical properties and aerosol types are quite different below and above 2 km during monsoon and post-monsoon seasons. S_a at 20 sr, 40 sr, and 70 sr corresponds to clean marine (CM), DU, and SM aerosols (Omar et al., 2009), respectively, where the SM aerosols dominates during winter and pre-monsoon seasons over the Gadanki region. Whereas CM and DU aerosols dominate above 2 km during the monsoon and post-monsoon seasons, respectively.

A similar exercise is performed between Mie LIDAR and CALIOP observations and the composite seasonal mean α_{aer} obtained at different S_a are shown in **Figure 3.3(e-h)**. There were a total of 48 cases where both CALIOP overpass and Mie LIDAR observations were available. This includes 18, 12, 13, and 5 days during winter, pre-monsoon, monsoon, and post-monsoon seasons, respectively. CALIOP observed α_{aer} for these days is also superimposed in the respective panels as well. Note that the data starts from 15 km in the case of CALIOP. In general, α_{aer} retrieved using S_a at 30 sr matches well with the corresponding CALIOP estimated α_{aer} above 20 km in all seasons. Below 18 km, it matches well with α_{aer} values retrieved using S_a between 50 and 70 sr. The VA or SF aerosols dominate in the UTLS region as it matches well with the S_a at 50 to 70 sr in all seasons except in winter. This suggests that optical properties and aerosol types are quite different in the UTLS region and the lower troposphere. Thus, it is clear that one can obtain aerosol types indirectly by combining the ground-based LIDARs and CALIOP observations. Since a good match (above 1 km) between ground-based LIDAR and CALIOP is being observed and hence latter can be used to obtain the spatial extent of α_{aer} up to 30 km.

3.3.2 Monthly mean α_{aer} from ground-based observations (surface to 30 km)

As mentioned earlier, to better understand the optical properties and the vertical distribution of aerosols, we have combined both the MPL and Mie LIDAR

observations to attain a complete aerosol profile (up to 30 km) in all seasons. MPL data is averaged between 2010 to 2018 (see **Figure 2.4**), and the monthly mean α_{aer} (with S_a at 40 sr) covering from surface to 8 km along with Standard Deviation (SD) obtained while averaging during the above-mentioned period is shown in **Figure 3.4b and d**, respectively. The ABL obtained from radiosonde measurements during the same period (2010-2018) is also superimposed in the respective panels. It is clear that maximum α_{aer} (~ 0.2 km^{-1}) values are restricted to below the ABL (< 2 km) during winter, whereas aerosols are distributed up to 4 km during pre and post-monsoon seasons. It is interesting to see α_{aer} (~ 0.15 km^{-1}) values extending up to 7 km with a very clean atmosphere (with α_{aer} < 0.1 km^{-1}) below 1.5 km during monsoon season. Large SD during monsoon and post-monsoon seasons suggest large day-to-day variations over the Gadanki region.

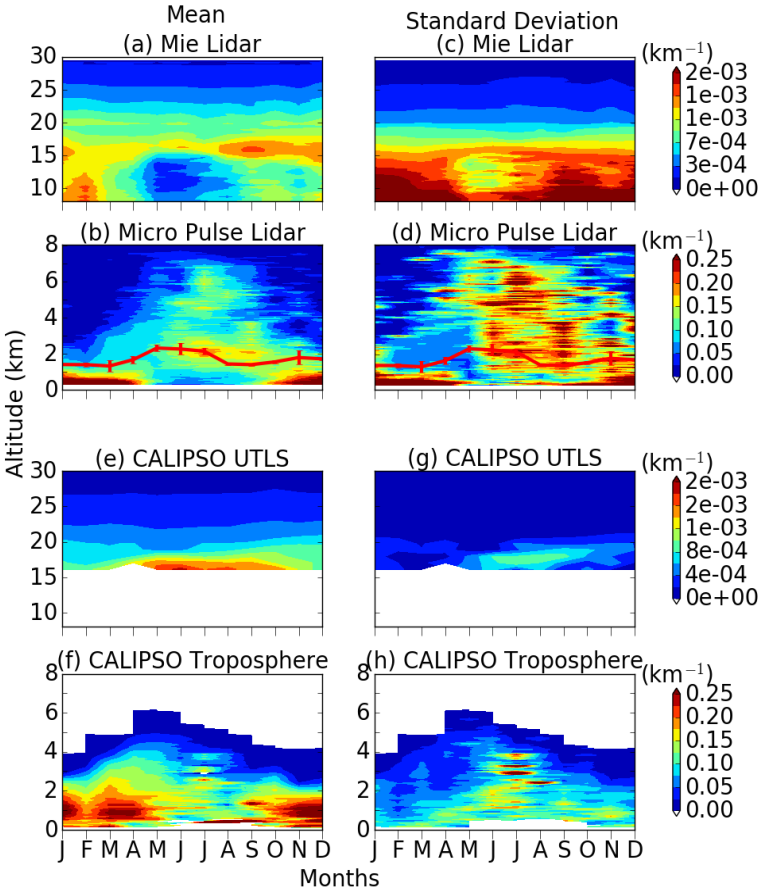

Figure 3.4 *Monthly mean variation of α_{aer} obtained using (a) Mie LIDAR (UTLS) averaged during 1998 to 2018 and (b) MPL (troposphere) averaged from 2010 to 2018. Their respective SD obtained while averaging are shown in (c) and (d). ABL (red line) detected using radiosonde is also superimposed in (b). (e) to (h) same as (a) to (d) but obtained from CALIOP measurements.*

Monthly mean α_{aer} (with S_a at 40 sr) from Mie LIDAR covering from 8 to 30 km along with SD obtained while averaging during 1998 to 2018 (see **Figure 2.4**) is shown in **Figure 3.4a and c**, respectively. The higher aerosol loading from 8 km extending up to 13 km was noticed during January and February months, and also an additional layer with high α_{aer} values (~0.001 km^{-1}) are observed at 15-18 km during the winter season. Since no deep convection is expected over this location during winter (Sunilkumar et al., 2012) to transport pollution from below, the higher aerosol loading during this period can be attributed to the horizontal advection. Moreover, aerosol loading is restricted to the ABL during this season (**Figure 3.4b**). However, the impact of strong westerly zonal wind from 8 to 18 km and southerly meridional wind from 10 to 15 km can be clearly seen in **Figure 3.1**. Brewer-Dobson circulation, which leads to the transport of tropospheric air into the stratosphere in the tropics, can also be one of the reasons behind the winter peak in α_{aer} values (Mohanakumar et al., 2008).

Interestingly, an enhanced thick aerosol layer is detected between 15 and 18 km persisting during late monsoon season to post-monsoon season over the site with strong enhancement in the α_{aer} (~ 0.002 km^{-1}) during August and September months. However, it is interesting to see a clean atmosphere (α_{aer} < 0.0003 km^{-1}) below 15 km altitude during the monsoon season. Strong TEJ with a magnitude of 50 m/s will be experienced over the site from 15 to 18 km (**Figure 3.1c**). Further, ASMA will be persisting during the monsoon season extending from ME to Asia (15^{o}N-45^{o}N; 30^{o}E-120^{o}E) region at 100 hPa level (Basha et al., 2020), as shown in **Figure 3.1e**. Any pollution entering this anticyclone will persist for a long time and looks like another EAL popularly known as ATAL (Vernier et al., 2011; 2018). Although the Gadanki region comes at the edge of this anticyclone (**Figure 3.1e**), but the impact of this layer can be seen from the ground-based LIDAR measurements as well.

In order to investigate the potential sources for the formation of both the EALs, one in the lower troposphere and another in the UTLS region, seasonal statistics of 7- day back trajectory analysis has been carried out using Hybrid Single-Particle Lagrangian Integrated Trajectory (HYSPLIT) model from Jan. 2010 to Dec. 2018 (Draxler and Rolph, 2003). **Figure 3.5** shows the mean trajectory frequency (%) during different seasons at 3 km (700 hPa) and 16 km (100 hPa) altitudes. Major sources reaching the site are coming from the ME, Africa, AS, and BoB. Aerosols are

mainly arriving from oceanic and continental air masses at 16 km altitudes during all seasons except monsoon season. The monsoon season marks the presence of LLJ in lower altitudes as it is most prominent at 3 km and TEJ at higher altitudes (i.e., at 16 km), leading to the formation of EALs. A clear reversal of air mass trajectories can be seen during the monsoon season in **Figure 3.5c**, where a significant amount of air mass is advected from the AS and TP through long-range transport in lower and higher altitudes, respectively.

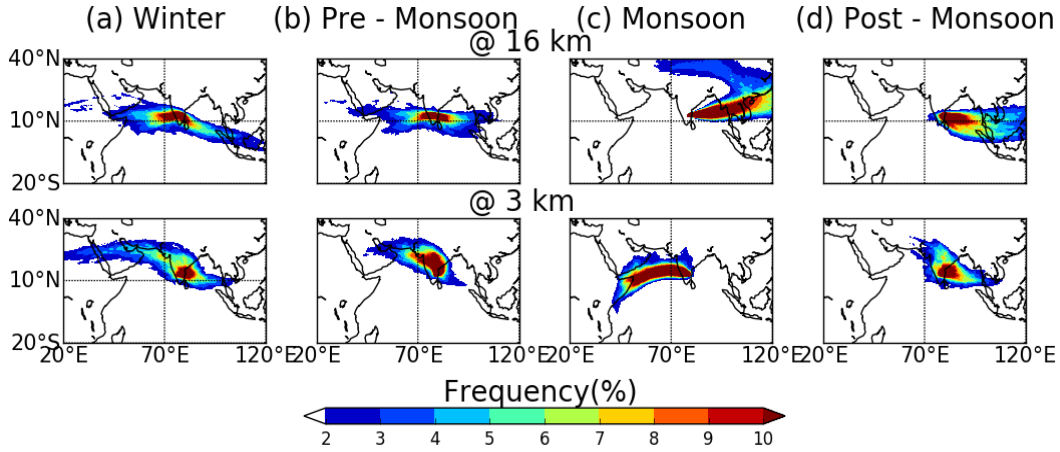

Figure 3.5 *7-day air mass back trajectory frequency (%) observed during (a) winter, (b) pre-monsoon, (c) monsoon, and (d) post-monsoon, at 3 km (or 700 hPa) in lower panels and at 16 km (or 100 hPa) in upper panels, over the Gadanki region from 2010-2018.*

3.3.3 Monthly mean α_{aer} from CALIOP measurements (surface to 30 km)

Using the latest version of CALIOP Level 3 V4 data averaged between 2010 and 2018 (see **Figure 2.8c and d**), the monthly mean α_{aer} covering from surface to 30 km along with SD obtained while averaging during the above-mentioned period is shown in **Figure 3.4(e-h)**. For the lower troposphere (**Figure 3.4f**), it is quite interesting to see the similar magnitude of α_{aer} (0.25 km^{-1}) for both the simultaneous observations. However, the higher aerosol loading below 1 km is persistent throughout, which is in contrast to the cleaner environment below 1 km during the monsoon period observed by ground-based LIDAR. This is mainly due to the overestimation of α_{aer} from the CALIOP satellite below 1 km irrespective of the season (Mamouri et al., 2009) and has also been reported by Prasad et al. (2019) over the Gadanki region. CALIOP observations also exhibit similar features of EAL, where maximum loading persists between 2 and 4 km during monsoon season. But an

additional enhancement is seen in the α_{aer} during pre-monsoon in CALIOP, which is not found in MPL observations, mainly due to fixed S_a used in the latter case. However, note that SD is very less during pre-monsoon when compared to monsoon season in the tropospheric altitudes in CALIOP measurements (**Figure 3.4h**). The existence of the aerosol layer extends up to 5 km, and a well-defined separation can be observed between the boundary layer and EAL in satellite measurements as well. Using four years of CALIOP measurements, similar results during monsoon season are also shown very recently by Niu et al. (2020) over the Indian region. Note that CALIOP observations for the UTLS region are averaged from 2006 to 2018, and the identical magnitude of α_{aer} (0.002 km^{-1}) is seen during monsoon season (**Figure 3.4e**). Thus, it is clear that two EALs are noticed, one in the troposphere (2-5 km) and the other in the UTLS region (16-18 km), in both independent observations. There exist few differences between the two, mainly because of the retrieval of the α_{aer} with fixed S_a in the case of ground-based LIDARs.

3.3.4 Vertical distribution of Aerosol sub-types obtained using CALIOP

After having obtained a good comparison between ground-based and space-borne instruments in **sections 3.3.1, 3.3.2, and 3.3.3**, in this sub-section, we have investigated the contribution of different aerosols sub-types, particulate color ratio (χ_{aer}) and the particulate depolarization ratio (β_{aer}) properties to these EALs over the Gadanki region, using CALIOP datasets (see **Figure 2.8a and b**). Based on the CALIOP's evaluation of S_a (see **Table 2.2**), aerosols sub-types vary with the corresponding regions (Man-Hae et al., 2018). **Figure 3.6** shows the occurrence frequency of different types of aerosols in the form of a pie chart observed in the troposphere (0-8 km) and UTLS region (8-20 km) during different seasons using CALIOP observations over the Gadanki region. Altitude variation of tropospheric aerosols justifies the existence of maximum aerosols up to 8 km where the major contribution is from polluted dust (PD) (44.6 %), polluted continental or PC/ SM (19.6 %), DU (20.7 %) and elevated smoke or ES (13.1 %) (**Figure 3.6b**). The dominance of PD aerosols in the troposphere can be attributed to the presence of anthropogenic aerosols over the site, which can be due to the presence of higher BB and DU aerosols from long-range transport processes. However, the DU aerosols have a unique property of both absorbing as well as scattering of solar and terrestrial

radiations and might even suppress precipitation by acting as CCN, thereby impacting Earth's radiation budget.

Stratospheric aerosols also play a vital role in altering the global climate by reflecting solar radiation and hence reducing the surface temperature (Kloss et al., 2020) or the greenhouse effect. **Figure 3.6a** reveals the dominance of VA (50.3 %) and SF/ other (49.7 %) aerosols in the UTLS over the Gadanki region. The observed dominance of SF aerosols is the apparent indication of the existence of the famous Stratospheric Sulfate Layer or sometimes known as the '*Junge Layer*', composed of 75% sulfuric acid and 25% water vapour over the Gadanki region (Wallace, John M, 2006). The SF aerosols have the property to reflect nearly all incoming solar radiation and hence cool the atmosphere. Nevertheless, traces of NR aerosols are also observed in the in-situ measurements from Hyderabad during the 2018 BATAL campaigns (Vernier et al., 2018), and nowadays, attention is being made for observing non-volcanic sources.

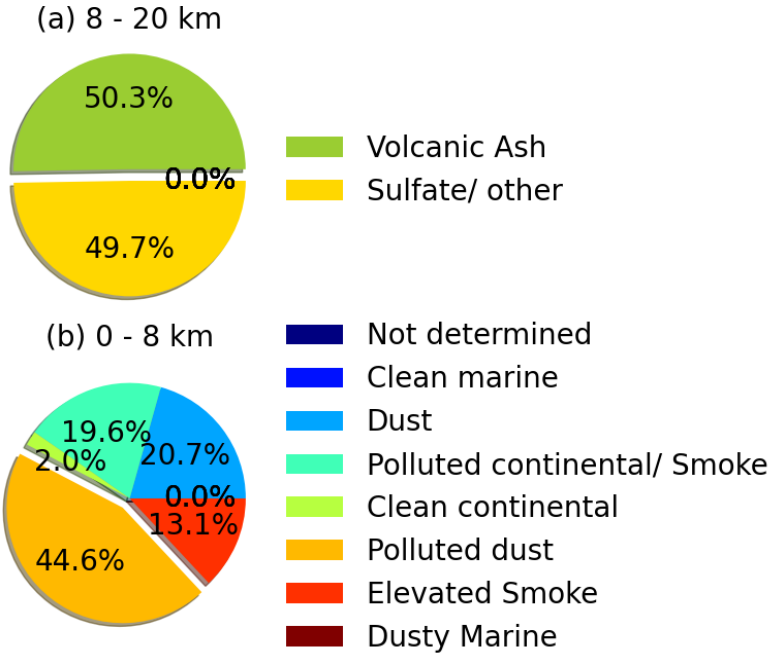

Figure 3.6 *Pie chart representing the percent occurrence frequency of the total aerosol subtypes observed using CALIOP measurements from (a) 8 to 20 km and (b) 0 to 8 km altitudes, over the Gadanki region.*

Further, the irregularity and size of the aerosol particles are analysed by looking into the β_{aer} and χ_{aer} profiles at 532 nm using CALIOP data are shown in **Figure 3.7**. The ratio of the backscatter coefficient at perpendicular to parallel 532 nm polarized channel is defined as β_{aer}. While the ratio of backscatter coefficients of

the particle at 1064 nm to 532 nm wavelength is defined as aerosol χ_{aer}. After applying all the quality flags to the CALIOP dataset (mentioned in **section 2.2.1.2**), the mode (characterized by the skewness of data distribution (Pan et al., 2016)) of the vertical distribution for the β_{aer} was obtained in this study. Working with the β_{aer} is a highly sensitive task as these values changes with the seasons and taking its average to represent the climatology can mislead. So, a seasonal representation (**Figure 3.7**) was carried out for this specific parameter below 20 km, where β_{aer} < 0.1 represented anthropogenic aerosols with spherical shape while β_{aer} > 0.2 represented the DU particles with non-spherical shapes (Pan et al., 2016).

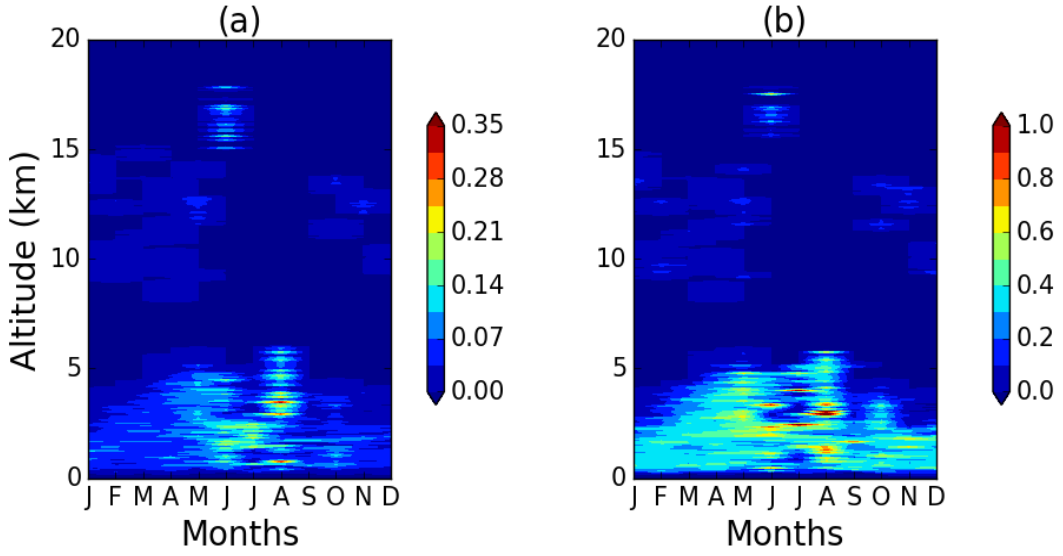

Figure 3.7 *Composite monthly mean profiles of particulate (a) β_{aer} at 532 nm and (b) χ_{aer} at 532 nm, obtained from CALIOP observations during 2010-2018, over the Gadanki region.*

Note that the frequency distribution of integrated χ_{aer} varies between 0.55 and 1.0 (Prasad et al., 2019), suggesting the presence of coarse-mode particles (0.6 < χ_{aer} < 1.2) in June and October months over the present site. Few studies have suggested the value of 0.6 for χ_{aer} as a threshold to separate fine-mode and coarse-mode particles (Sugimoto e al., 2002). The β_{aer} value less than 0.1 (above 0.2) represents anthropogenic aerosols with fine-mode and spherical shapes (DU particles with coarse-mode and non-spherical shapes) as mentioned in Kandler et al. (2011), Kobayashi et al. (2014). In the lower troposphere, the maximum β_{aer} values vary from 0.21 to 0.35 in the monsoon season from the surface to 6 km and 0.1 to 0.12 in the pre-monsoon season, whereas in other seasons, the values are usually below 0.12, as shown in **Figure 3.7a**. Similarly, the maximum χ_{aer} values ranges from 0.6 to 1.3

and extending up to 6 km during the monsoon season, while in other seasons, it is usually less than 0.6 values, as can be seen in **Figure 3.7b**. Hence, it indicates the presence of a large amount of non-spherical and coarse-mode particles during the monsoon season that exists due to the long-range transport over the site. Natural non-spherical particles such as DU and SS may prevail in the lower troposphere during monsoon season as β_{aer} values greater than 0.25 is noticed, particularly during August month. It is to be noted that the rainwater analysis over Gadanki has revealed the presence of 5 anions (F^-, Cl^-, NO_3^-, SO_4^{2-}, PO_4^{3-}) and 6 cations (Na^+, K^+, Ca^{2+}, Mg^{2+}, $Li^{+,}$ and NH_4^+) with the maximum concentrations from sodium and chloride particles during monsoon season (Jain et al., 2019). This feature is consistent with the CALIOP observations. In general, β_{aer} and χ_{aer} values varies between 0.1 - 0.2 and 0.2 - 0.8 under clean environment while they vary between 0.2 - 0.4 and 0.8 - 2 under polluted conditions (Liu et al., 2017). Similarly, in the UTLS region, the maximum β_{aer} and χ_{aer} values are observed during the monsoon season, especially in June month from 15 to 18 km, and minimum in other seasons over the Gadanki region. During monsoon season, the observed β_{aer} > 0.15 indicates the dominance of VA, while in other seasons β_{aer} < 0.15 is noticed, suggesting the presence of SF/ other aerosols (Man-Hae et al., 2018), as shown in **Figure 3.7a**. While the observed values for χ_{aer} are lower than 0.6 throughout and hence indicate the existence of fine-mode particles in the UTLS region, as can be seen in **Figure 3.7b**. However, we have seen the presence of fine-mode and spherical particles from 10 to 15 km in all the seasons except monsoon over the site. These results are also consistent with the aerosol subtypes presented above.

3.3.5 Spatial distribution of EALs using CALIOP

Since major features are matching between ground-based LIDAR and space-borne LIDAR measurements in **sections 3.3.1, 3.3.2, and 3.3.3**, the spatial extent of these EALs is obtained from CALIOP (see **Figure 2.8c and d**) and is presented in this sub-section. Characteristics of the EALs are analysed by averaging the α_{aer} between 2-3 (16-18) km in the lower troposphere (UTLS) region based on their maximum magnitude observed during different seasons and is shown in **Figure 3.8**.

From **Figure 3.8(e–h)**, it is clear that the lower tropospheric EAL is mostly confined within the tropical latitudes, with the maximum loading over Africa and the South Asian continent, where the maximum (minimum) loading is detected during

monsoon (post-monsoon) season. In the South Asian countries, a maximum loading (> 0.13 km^{-1}) is found in pre-monsoon and monsoon seasons, and lower α_{aer} (<0.09 km^{-1}) is observed during winter and post-monsoon except in east China region. From the global picture, it is clear that, other than in Asian countries, a clear atmosphere with α_{aer} values less than 0.05 km^{-1} is observed. However, in the subsequent **section 6.2.2**, the major aerosol types leading to the formation of these EALs will be discussed extensively. In the UTLS region (**Figure 3.8(a-d)**), the dominance of EAL exists in the tropical latitudes during monsoon and post-monsoon seasons only with high α_{aer} (> 0.0012 km^{-1}) values. Maximum aerosols are confined during monsoon with an enhanced peak (~0.0015 km^{-1}) covering India and China regions (**Figure 3.8c**).

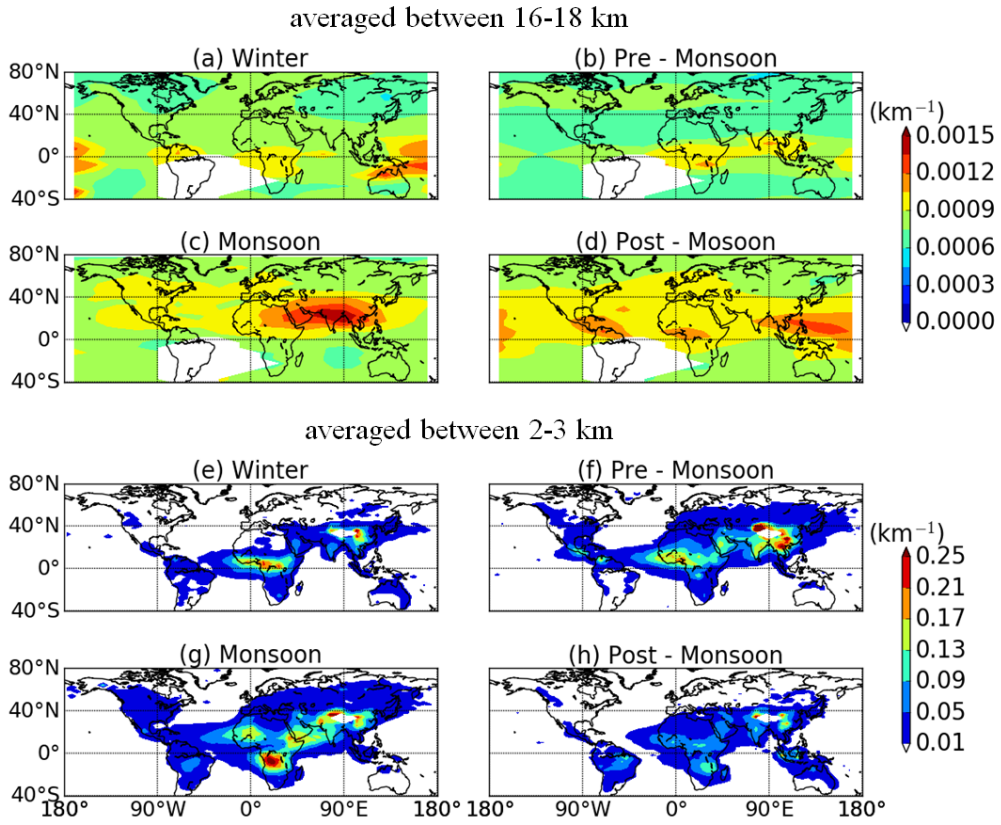

Figure 3.8 *Latitude – longitude variation of α_{aer} observed during (a) winter, (b) pre-monsoon, (c) monsoon, and (d) post-monsoon seasons observed using CALIOP observations, when averaged between 16 and 18 km altitudes. (e) to (h) same as (a) to (d) but averaged between 2 and 3 km altitudes.*

According to **Figure 3.1e,** ASMA will be persisting during the monsoon season extending from ME to Asia (15^{o}N-45^{o}N; 30^{o}E-120^{o}E) region at 100 hPa level (Basha et al., 2020). It is also well known that this EAL is well confined within the

ASMA region (Vernier et al., 2011; 2018), and the particles accumulated inside can alter the radiative balance of the atmosphere and can effectively transport tropospheric aerosols into the UTLS region (Randel et al., 2006; Park et al., 2007). In-situ observation from Gadanki, Hyderabad (17.47°N, 78.58°E), and Varanasi (25.27°N, 82.99°E) carried out as a part of BATAL campaigns also confirms the presence of these EALs (Vernier et al., 2018).

3.3.6 Latitude and longitudinal distribution of EALs using CALIOP

In the previous **section 3.3.5**, we have seen the spatial extent of the EALs, but the information on the vertical extent of layers at other latitudes and longitudes is missing. The longitude (latitude)-altitude of α_{aer} for troposphere averaged over the Indian region (8-32^{o}N latitude band) (67.5-97.5^{o}E longitude band) during different seasons is shown in **Figure 3.9**.

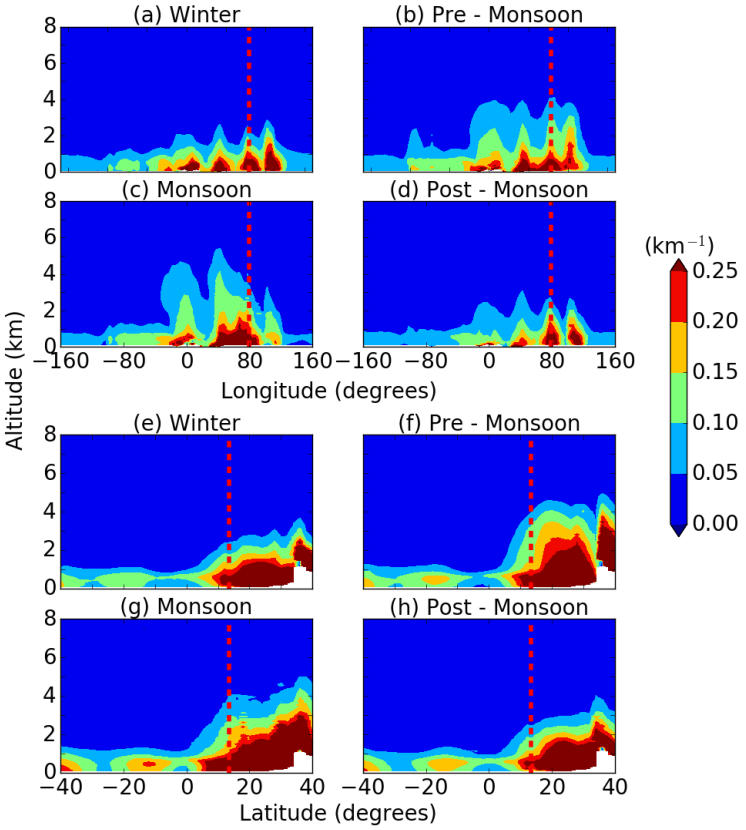

Figure 3.9. *Longitude-altitude distribution of α_{aer} observed in the troposphere region during (a) winter, (b) pre-monsoon, (c) monsoon, and (d) post-monsoon obtained from CALIOP measurements during 2006-2018, when averaged between 8-32^{o}N latitude bands. (e) to (h) same as (a) to (d) but for Latitude-altitude distribution of α_{aer} averaged between 67.5-97.5^{o}E longitude bands. Red dashed lines show the location of the Gadanki region.*

In general, higher α_{aer} values are seen over the land region when compared to the oceanic region as expected due to prevailing anthropogenic activity as well as long-range transport activities. It is also clearly evident that loading is confined up to 2 km with high α_{aer} values at the surface (> 0.25 km^{-1}) during winter and post-monsoon for both latitudinal as well as longitudinal variations. Aerosol loading is restricted within 80^{o}W to 120^{o}E in all seasons but with a slight variation during post-monsoon (**Figure 3.9a-d**). However, higher α_{aer} values (~0.15 km^{-1}) extend up to 4 km (6 km) during the pre-monsoon (monsoon) season between 30^{o}E and 40^{o}E, as shown in **Figure 3.9b** (**Figure 3.9c**). Similar changes are observed in the latitudinal variation where the aerosol loading is limited to up to 2 km during winter and post-monsoon with high α_{aer} values of about 0.25 km^{-1} (**Figure 3.9(e-h)**). Aerosols during pre-monsoon and monsoon are confined up to 4 km (**Figure 3.9f and g),** with the maximum α_{aer} values up to 0.15 (km^{-1}). The latitudinal extent of aerosols is from 10^{o}N to 40^{o}N, with a slight variation during monsoon season below 1 km in SH (**Figure 3.9g**).

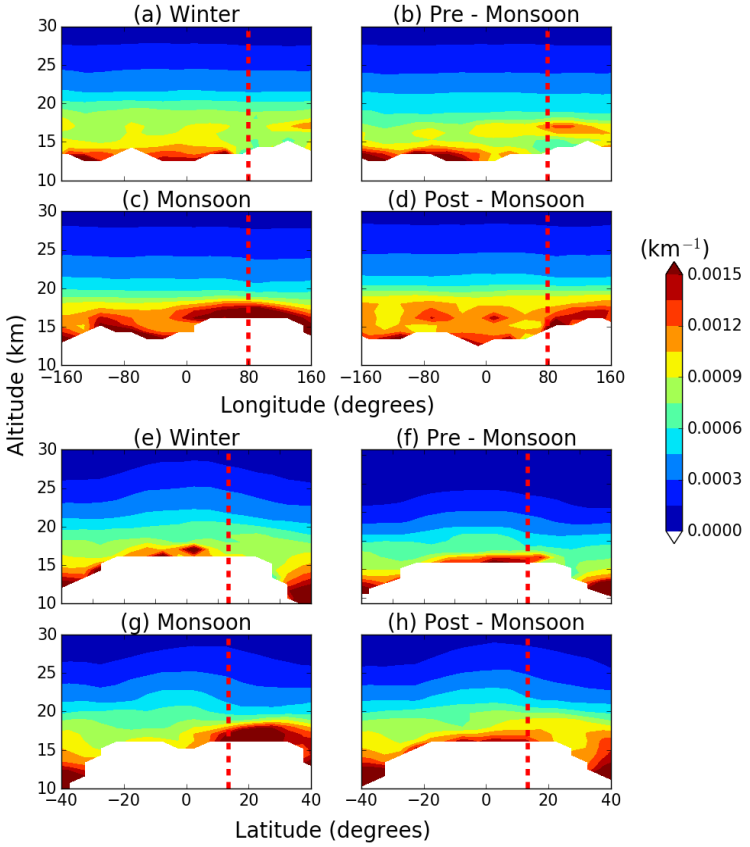

Figure 3.10. *Same as* ***Figure 3.9*** *but for UTLS region.*

Similarly, the longitude (latitude)-altitude of α_{aer} for the UTLS region averaged over the Indian region (8-32^{o}N latitude band) (67.5-97.5^{o}E longitude band) during different seasons, is shown in **Figure 3.10**. The longitudinal variation of the UTLS region α_{aer} depicted the appearance of maximum aerosols above 16 km from 10^{o}E to 130^{o}E during monsoon season (**Figure 3.10c**) with a magnitude of 0.0015 km$^{-1,}$ whereas during post-monsoon (**Figure 3.10d**) season, it varies between 80^{o}E and 160^{o}E with the magnitude greater than 0.0012 km^{-1}. Latitudinal patterns also follows the same trend where large aerosol loading is detected between 16 and 18 km during monsoon season with a magnitude of 0.0015 km^{-1} between 10^{o}N and 30^{o}N, unlike the other seasons. Spatial features are closely connected with the features detected by the regional analysis using ground-based remote sensing instruments.

3.4 Summary

Using long-term observations from ground-based (MPL and Mie) LIDARs collocated at the Gadanki region (13.5^{o}N, 79.2^{o}E), vertical distribution of the EALs covering both the troposphere and UTLS region are obtained. The spatial extent of these layers is obtained using simultaneous space-borne CALIOP LIDAR measurements. After comparing CALIOP observations with ground-based LIDARs, it is further utilized to obtain aerosol optical, physical, and chemical properties. Major findings drawn from this study are summarized below:

1. The vertical distribution of aerosol optical properties obtained from ground-based LIDAR measurements revealed the existence of two simultaneous EALs over the region. The lower troposphere (UTLS) aerosol layer extends between 2 to 5 (15 to 18) km with a magnitude of α_{aer} of ~ 0.15 (> 0.002) km^{-1}, during monsoon season. While in the winter season, aerosols are mostly confined to the surface in the troposphere, whereas horizontal advection is responsible for the high aerosol loading in the UTLS region.
2. A good comparison between ground-based and space-borne α_{aer} values are observed in both troposphere (above 1 km) and the UTLS region, which has been explained in this study by taking different S_a values i.e., 20, 40, and 70 (30, 50, and 70) sr in lower troposphere (UTLS) region. This exercise explains that aerosol types can be indirectly obtained by combining ground-based and space-borne observations as well.

3. α_{aer} profiles obtained with different S_a from ground-based LIDAR during different seasons does not match exactly with the space-borne LIDAR profile, suggesting the use of at least season dependent S_a while retrieving it from ground-based LIDARs.
4. Back trajectory analysis performed using the HYSPLIT model suggested that the origin of these EALs is mainly due to long-range transport by LLJ (TEJ) persisting during monsoon season for the lower (upper) layer, while in other seasons, the contribution is mainly from oceanic and continental air masses.
5. The aerosol chemical composition obtained for these EALs reveals the different occurrence frequency for different aerosol types as there is the dominance of PD (44.6%), PC (19.6%), DU (20.6%), and ES (13.1%) in the lower troposphere. At the same time, VA and SF aerosols contribute ~50.3% and 49.7%, respectively, for the UTLS layer.
6. The aerosols physical distribution revealed that the lower (UTLS) EAL is dominated by the non-spherical and coarse-mode (spherical and fine-mode) particles during the monsoon season.
7. Their spatial extent obtained from CALIOP revealed that the maximum aerosol loading extends from Africa to South Asian continents (ME and China Sea) for the lower troposphere (UTLS) layer. The maximum longitude (latitude)-altitude variation of α_{aer} extends up to 4 km (6 km) between 30°E and 40°E (10°N to 40°N) in the lower layer, while the loading extends between 16 to 18 km from 10°E to 130°E (10°N to 30°N) during monsoon season.

However, after having analysed the spatial and vertical distribution of the EALs across the globe (i.e., extending from Africa to South Asia in the lower troposphere region and from ME to China in the UTLS region), we will now further move to analyse the long-term changing patterns due to the various aerosol properties in the columnar as well as vertical distribution, using multi-source datasets across the globe in **Chapters 4, 5, and 6.**

❁❁❁

Chapter 4

Long-term Trends in AOD obtained across the globe using multi-satellite measurements

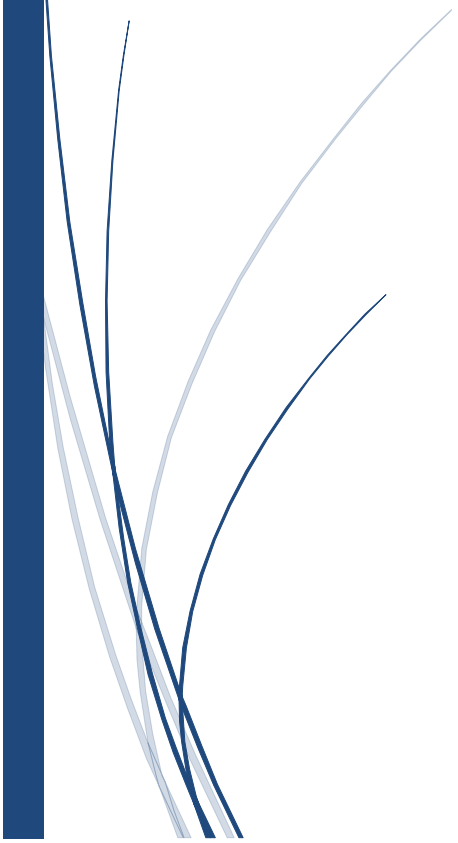

4.1 Introduction

Atmospheric aerosols are rapidly changing the regional and global climate owing to their dependency on high population densities, changes in land-use, urbanization as well as industrial growth (Kaur and Pandey, 2021; Liang and Gong, 2020; Masson-Delmotte et al., 2018). As a result, a broad spectrum of natural as well as anthropogenic emissions emerges from the DU activities, volcanic eruptions, SS, BB, fossil fuel burning, vehicular and industrial outflow, as discussed in detail in **Chapter 1**. In all these, AOD plays a crucial role in the assessment of columnar aerosol loading of the atmosphere. As uncertainty in the direct effect of aerosols can be characterised by the uncertainty in AOD measurements/ retrievals, which will further influence the estimates of aerosols RF. After having analysed the impact of background meteorology playing a major role in heterogeneous distribution of aerosols across the globe in **Chapter 3**, to fulfil the second objective, we analyse the long-term variations in the columnar AOD values while isolating the dynamical aspects, in this chapter.

With the objective to alleviate unfortunate health and climate effects and to assess the effectiveness of the rigorous emission control policies employed over various regions, it is critical to acknowledge its decadal discrepancies as well. Hence, it has been gaining huge interest among scientific (e.g., Mehta et al., 2016; Zhao et al., 2017; Mehta et al., 2018; Ratnam et al., 2021) as well as policy communities in recent years. Countries like the EU, United States, and China have already undertaken meticulous steps to lower the air pollution emissions in the past two decades, and these details have been discussed extensively in Zhao et al. (2017). However, to monitor this varying aerosol loading over different regions across the globe, many previous studies have assessed the long-term trends using different measurement techniques available (Che et al., 2019; Mehta et al., 2018; Ratnam et al., 2021; Samset et al., 2019; Wei et al., 2019b) but very few studies have examined this feature employing combined long-term ground-based, satellite-based as well as reanalysis datasets over this region. Although ground-based instruments have higher precision and are also highly capable of providing detailed aspects of the aerosols, but are typically point measurements. Therefore, the advent of satellite retrievals has become a key source in providing global aerosols scientific products. Several studies have reported the long-term LR trends using ground-based and/or satellite observations but are limited up to the year 2017 or

2018, dealing mostly with one or two observational data sources focusing either on specific marked regions or globally (Mehta et al., 2016; Hsu, 2012; Sogacheva et al., 2018; Wei et al., 2019b; Zhao et al., 2017). It is well known that the conventionally used LR trend methods applied to any long-term data sets will be highly biased based on the starting and ending years. Therefore, in addition to this, the MLR trend approach has been considered (see **section 2.4**), where the background dynamical aspects have been isolated while estimating the trend values. Further, it is important to analyse different satellite products from time to time as with the changing/ extending the time frame and the version of data products, the nature, and scenarios of trends can also change. More specifically, one of the critical components that evaluate the efficiency of the trend analysis is its mode of measurement as discrete techniques follow different retrieval algorithms, instrument swath width, and spatial and temporal resolutions. In a comparison of these trend results obtained from different data sources, insight on their consistency and association with other additional parameters (denoting their physical and chemical characteristics) can quantify the impact due to the changes in emission sources and the mitigation policies adopted in different regions from time to time. Taking advantage of the availability of improved long-term level-3 latest versions of all the datasets, twenty years of region-wise MLR trend analysis (see **section 2.4**) using the multi-platform datasets (see **sections 2.2 and 2.3**) including the ground-based (AERONET), satellite-borne (MODIS on-board A and T, MISR, and CALIOP), and reanalysis (MERRA-2) derived monthly AOD datasets have been examined in this chapter.

4.2 Statistical analysis

As the context of this study is to look into the global trends of the monthly AOD datasets, but before that, these satellite/reanalysis datasets are assessed with the ground-based AERONET stations. The parameters used in the literature to ascertain consistency in AOD retrievals include the linear R, RMSE (**Equation 4.1**), Mean Absolute Error (MAE, **Equation 4.2**), and Relative Mean Bias (RMB, **Equation 4.3**), where the values less (above) than unity specifies underestimation (overestimation). In order to examine these statistical parameters, we have considered AOD from AERONET (ground-based measurements) as true value (TV) and AOD due to discrete measurement techniques (MODIS, MISR, CALIOP, and MERRA-2) as predicted value (PV) in the respective cases, defined as follows:

$$RMSE = \sqrt{\frac{1}{n}\sum_{i=1}^{n}(AOD_{(PV)i} - AOD_{(TV)i})^2} \quad (4.1)$$

$$MAE = \frac{1}{n}\sum_{i=1}^{n}|AOD_{(PV)i} - AOD_{(TV)i}| \quad (4.2)$$

$$RMB = \frac{1}{n}\sum_{i=1}^{n}|AOD_{(PV)i} / AOD_{(TV)i}| \quad (4.3)$$

where, n is the total number of data points. Difference between RMSE and MAE is that RMSE is usually appropriate when large errors are undesirable whereas MAE is beneficial when interpretation standpoint is considered. One can mark that we are dealing with the long-term monthly averaged datasets of the AODs from all the respective techniques, therefore, AOD measurements from the observed values are compared with the pixels where the TVs are co-located (within one degree), as represented in **Figure 4.1**.

4.3 Results and discussion

4.3.1 Comparison against AERONET AOD observations

Joint AOD validation analysis of the monthly MISR (see **Table 2.5**), MODIS_A and T (see **Table 2.4**), CALIOP (see **Figure 2.8c**), and MERRA-2 (see **Table 2.6**) AODs against 82 world-wide sites of AERONET (see **Table 2.3**) AOD (and Gadanki sky-radiometer) monthly dataset, between 2001 and 2020 (2008 to 2020), is discussed in this section. Here, we aim to acquire a profound understanding of the efficiency in retrieved AOD among all techniques and its similarities and differences of the various statistical linear regression parameters, which include R, RMSE, MAE, and RMB. The number of samples quantified (N) over each site for co-located measurements is also mentioned in **Table 4.1**. AOD values from AERONET are chosen as the standard ones as their uncertainty does not exceed beyond ± 0.02 (Holben et al., 2001), as has been discussed in **section 2.2.2.1** as well.

As seen from **Figure 4.1a-d**, there exists a medium (ranging from 0.3 to 0.7) to high (above 0.7) R values (**Table 4.1**) over most of the places with the MISR observations against AERONET AOD obtained at 550 nm, suggesting that the two instruments had a strong concurrence with each other. Some of the lowest R (below 0.3) values, along with the low RMSE (0.04-0.18) and MAE (0.02-0.11) values, were spotted over shrub/ barren lands of the southern part of the South America (SAM) regions such as Trelew and for maritime sites such as Nauru with RMSE (=0.04) and MAE (=0.03) values over South Pacific Ocean. The shrub / barren land with sparse

vegetation cover tends to overestimate, as seen in **Figure 4.1d,** for low AOD values over the SAM region with RMB=1.49.

AERONET sites (Longitude(Degrees),Latitude(Degrees),Elevation(m))	MISR (R, N)	MODIS_A (R, N)	MODIS_T (R, N)	CALIOP (R, N)	MERRA-2 (R, N)
1. Alta_Floresta(-56.1,-9.8,277)	0.85, (119)	0.95, (142)	0.94, (151)	0.83, (102)	0.94, (185)
2. Arica(-70.3,-18.4,25)	0.28, (148)	0.43, (137)	0.44, (150)	0.29, (89)	0.78, (153)
3. Ascension_Island(-14.4,-7.9,30)	0.52, (141)	0.87, (138)	0.78, (148)	0.72, (72)	0.84, (148)
4. Belsk(20.7,51.8,190)	0.43, (105)	0.48, (100)	0.51, (115)	0.58, (106)	0.56, (129)
5. Birdsville(139.3,-25.8,46.5)	0.77, (115)	0.54, (118)	0.39, (118)	0.57, (107)	0.78, (118)
6. Bratts_Lake(-104.7,50.2,586.7)	0.69, (90)	0.8, (86)	0.75, (94)	0.62, (78)	0.83, (130)
7. BSRN_BAO_Boulder(-105.0,40.04,1604)	0.79, (141)	0.77, (145)	0.78, (158)	0.4, (105)	0.79, (164)
8. Burjassot(-0.42,39.5,104)	0.8, (124)	0.9, (130)	0.89, (130)	0.66, (129)	0.84, (130)
9. Canberra(149.1,-35.2,600)	0.8, (154)	0.51, (120)	0.57, (151)	0.37, (126)	0.94, (160)
10. Cape_San_Juan(-65.6,18.3,15)	0.69, (129)	0.86, (138)	0.86, (138)	0.76, (126)	0.86, (138)
11. Carpentras(5.05,44.08,107)	0.66, (156)	0.73, (160)	0.76, (162)	0.61, (148)	0.72, (162)
12. CART_SITE(-97.48,36.60,318)	0.72, (180)	0.82, (156)	0.83, (185)	0.62, (135)	0.85, (186)
13. CARTEL(-71.9,45.3,251)	0.46, (147)	0.68, (112)	0.62, (133)	0.26, (128)	0.75, (187)
14. CCNY(-73.9,40.8,100)	0.75, (158)	0.9, (153)	0.9, (161)	0.63, (120)	0.9, (164)
15. CEILAP-BA(-58.5,-34.5,26)	0.3, (199)	0.58, (134)	0.57, (188)	0.5, (116)	0.39, (206)
16. Chiang_Mai_Met_Sta(98.9,18.7,312)	0.81, (91)	0.87, (115)	0.82, (114)	0.88, (122)	0.95, (128)
17. CUIABA-MIRANDA(-56.07,-15.7,210)	0.81, (159)	0.85, (146)	0.85, (159)	0.93, (104)	0.93, (175)
18. Dakar(-16.9,14.3,21)	0.72, (110)	0.89, (114)	0.86, (111)	0.76, (113)	0.92, (115)
19. Dalanzadgad(104.4,43.5,1470)	0.72, (138)	0.64, (137)	0.68, (143)	0.43, (106)	0.81, (145)
20. Dunkerque(2.3,51.03,5)	0.44, (108)	0.74, (158)	0.76, (158)	0.24, (146)	0.79, (160)
21. Egbert(-79.78,44.2,264)	0.43, (143)	0.77, (178)	0.62, (189)	0.25, (135)	0.77, (196)
22. Evora(-7.9,38.5,293)	0.66, (113)	0.6, (118)	0.37, (117)	0.33, (118)	0.86, (118)
23. Granada(-3.6,37.16,680)	0.68, (143)	0.68, (149)	0.68, (149)	0.71, (133)	0.81, (149)
24. GSFC(-76.8,38.99,87)	0.73, (207)	0.865, (195)	0.895, (216)	0.685, (152)	0.865, (220)
25. Halifax(-63.5,44.6,65)	0.4, (125)	0.83, (139)	0.84, (139)	0.01, (128)	0.73, (139)
26. Ilorin(4.6,8.4,400)	0.78, (100)	0.73, (104)	0.72, (106)	0.86, (116)	0.96, (158)
27. IMAA_Potenza(15.7,40.6,770)	0.65, (130)	0.71, (135)	0.7, (135)	0.55, (128)	0.66, (135)
28. IMS-METU-ERDEMLI(34.2,36.5,3)	0.68, (142)	0.73, (146)	0.65, (146)	0.3, (121)	0.6, (146)
29. Ispra(8.6,45.8,235)	0.63, (94)	0.76, (78)	0.8, (90)	0.58, (41)	0.84, (104)
30. Izana(-16.4,28.3,2401)	0.68, (183)	0.86, (188)	0.85, (188)	0.77, (168)	0.83, (188)
31. Jabiru(132.8,-12.6,30)	0.86, (140)	0.44, (149)	0.39, (152)	0.53, (117)	0.9, (161)
32. Kanpur(80.2,26.5,123)	0.68, (184)	0.74, (87)	0.66, (103)	0.45, (139)	0.81, (206)
33. La_Laguna(-16.3,28.4,568)	0.68, (183)	0.86, (188)	0.85, (188)	0.77, (168)	0.83, (188)
34. La_Parguera(-67.04,17.9,12.4)	0.725, (144)	0.89, (151)	0.89, (151)	0.785, (135)	0.895, (151)
35. Lake_Argyle(128.7,-16.1,150)	0.83, (168)	0.63, (166)	0.53, (171)	0.86, (129)	0.92, (172)
36. Lecce_University(18.1,40.3,30)	0.71, (164)	0.61, (167)	0.59, (167)	0.44, (130)	0.66, (167)
37. Leipzig(12.4,51.3,125)	0.61, (149)	0.58, (121)	0.54, (138)	0.44, (137)	0.78, (190)
38. Lille(3.1,50.6,60)	0.56, (118)	0.59, (102)	0.57, (102)	0.04, (154)	0.82, (158)
39. Mainz(8.3,49.9,150)	0.37, (129)	0.5, (116)	0.54, (134)	0.34, (137)	0.62, (166)
40. Mauna_Loa(-155.5,19.5,3402)	0.48, (229)	0.56, (222)	0.59, (240)	0.38, (169)	0.61, (240)
41. MCO-Hanimaadhoo(73.1,6.7,13)	0.57, (113)	0.76, (128)	0.68, (128)	0.3, (112)	0.7, (128)
42. MD_Science_Center(-76.6,39.2,15)	0.71, (193)	0.87, (172)	0.9, (194)	0.68, (135)	0.9, (201)

Table 4.1 *(a) Correlation coefficient (R) and number of co-located observations (N) obtained between MISR (2001-2020), MODIS_A (2002-2020), MODIS_T (2001-2020), CALIOP (2006-2020), and MERRA-2 (2001-2020) against AERONET (2001-2020) observations. Location (Latitude, Longitude and Elevation (m)) for each AERONET site is also mentioned.*

For oceanic sites with low AOD values, MISR tends to overestimate (for a significant fraction of cases), such as in the regions over the South Atlantic, South Pacific, and the Indian Ocean, and it may be related to errors due to lack of surface information or sensor calibration (Kahn and Gaitley, 2015). For continental sites involving North Eastern America (NEA), EU, and ECC regions, MISR depicted medium to high R values with AERONET (maximum up to 0.81), having RMSE (0.03-0.41) and MAE (0.02-0.34) values. Although the sites such as the northern part of SAM, NWA, and the South and East Asia (SEA) region have seen good R values (above 0.5)

with the ground-based AERONET observations but these regions have seen comparatively higher (above 0.14) RMSE and MAE values. These analyses reflected that there exists a diversity of conditions and site to site variability of aerosol types where different mixtures of spherical and non-spherical aerosols dominate due to the large domains of vegetation cover (Wei et al., 2019a, 2019b). However, these statistical results are in good agreement with the recent study by Wei et al. (2019b) as well.

AERONET sites (Longitude(Degrees),Latitude(Degrees),Elevation(m))	MISR (R, N)	MODIS_A (R, N)	MODIS_T (R, N)	CALIOP (R, N)	MERRA-2 (R, N)
43. Mexico_City(-99.1,19.3,2268)	0.63, (155)	0.68, (151)	0.73, (166)	0.25, (113)	0.64, (166)
44. Missoula(-114.08,46.9,976)	0.44, (110)	0.8, (106)	0.76, (129)	0.62, (143)	0.81, (183)
45. Moldova(28.8,47.0,205)	0.8, (153)	0.66, (121)	0.73, (151)	0.61, (126)	0.83, (180)
46. Mongu(23.1,-15.2,1040)	0.83, (97)	0.83, (74)	0.89, (98)	0.87, (44)	0.96, (104)
47. Monterey(-121.8,36.5,50)	0.35, (125)	0.41, (138)	0.5, (138)	0.48, (122)	0.57, (138)
48. Moscow_MSU_MO(37.5,55.7,192)	0.78, (120)	0.59, (106)	0.68, (121)	0.39, (139)	0.86, (190)
49. Nauru(166.9,-0.52,7)	0.28, (112)	0.46, (112)	0.47, (119)	0.44, (76)	0.49, (120)
50. Nes_Ziona(34.7,31.9,40)	0.48, (128)	0.7, (115)	0.74, (130)	0.42, (75)	0.72, (131)
51. OHP_OBSERVATOIRE(5.7,43.9,680)	0.79, (106)	0.78, (113)	0.84, (113)	0.61, (108)	0.74, (113)
52. Osaka(135.5,34.6,50)	0.65, (125)	0.86, (139)	0.84, (140)	0.52, (137)	0.82, (140)
53. Palaiseau(2.2,48.7,156)	0.35, (144)	0.36, (114)	0.44, (140)	0.03, (159)	0.56, (169)
54. Palencia(-4.5,41.9,750)	0.63, (121)	0.43, (125)	0.33, (128)	0.4, (130)	0.78, (131)
55. Paris(2.3,48.8,50)	0.35, (144)	0.36, (114)	0.44, (140)	0.03, (159)	0.56, (169)
56. Railroad_Valley(-115.6,38.4,1437)	0.78, (186)	0.72, (179)	0.59, (190)	0.71, (152)	0.87, (192)
57. Red_Mountain_Pass(-107.7,37.9,3376)	0.63, (132)	0.63, (139)	0.7, (138)	0.45, (131)	0.73, (144)
58. REUNION_ST_DENIS(55.4,-20.9,93)	0.58, (128)	0.64, (136)	0.7, (136)	0.38, (133)	0.64, (136)
59. Rimrock(-116.9,46.4,824)	0.55, (182)	0.84, (178)	0.8, (199)	0.32, (146)	0.9, (209)
60. Rio_Branco(-67.8,-9.9,212)	0.86, (105)	0.94, (134)	0.96, (139)	0.88, (97)	0.94, (161)
61. Santa_Cruz_Tenerife(-16.2,28.4,52)	0.68, (183)	0.86, (188)	0.85, (188)	0.77, (168)	0.83, (188)
62. f_Paulo(-46.7,-23.5,786)	0.53, (132)	0.65, (129)	0.69, (146)	0.46, (63)	0.82, (151)
63. Saturn_Island(-123.1,48.7,193)	0.62, (161)	0.89, (172)	0.85, (189)	0.65, (138)	0.81, (189)
64. SEDE_BOKER(34.7,30.8,480)	0.48, (128)	0.7, (115)	0.74, (130)	0.42, (75)	0.72, (131)
65. SERC(-76.5,38.8,36.5)	0.73, (207)	0.865, (195)	0.895, (216)	0.685, (152)	0.865, (220)
66. Sevilleta(-106.8,34.3,1477)	0.65, (166)	0.6, (152)	0.37, (170)	0.55, (115)	0.79, (170)
67. Shirahama(135.3,33.6,10)	0.65, (125)	0.86, (139)	0.84, (140)	0.52, (137)	0.82, (140)
68. Silpakorn_Univ(100.04,13.8,72)	0.76, (95)	0.78, (107)	0.8, (106)	0.75, (125)	0.93, (132)
69. Sioux_Falls (-96.626, 43.74, 505)	0.67, (111)	0.76, (111)	0.65, (116)	0.81, (105)	0.85, (125)
70. Singapore(103.7,1.2,30)	0.45, (75)	0.64, (126)	0.72, (125)	0.68, (145)	0.88, (151)
71. Skukuza(31.5,-24.9,265)	0.54, (139)	0.53, (135)	0.62, (142)	0.5, (93)	0.8, (158)
72. Solar_Village(46.3,24.9,764)	0.85, (137)	0.91, (116)	0.91, (136)	0.82, (77)	0.92, (140)
73. TABLE_MOUNTAIN_CA(-117.6,34.3,2200)	0.59, (142)	0.78, (149)	0.81, (149)	0.3, (146)	0.87, (149)
74. Tamanrasset_INM(5.5,22.7,1377)	0.89, (113)	0.93, (113)	0.93, (116)	0.86, (115)	0.91, (116)
75. Thessaloniki(22.9,40.6,60)	0.58, (117)	0.73, (120)	0.74, (119)	0.55, (112)	0.62, (121)
76. Toravere(26.4,58.2,85)	0.6, (130)	0.78, (115)	0.75, (129)	0.29, (153)	0.75, (195)
77. Toronto(-79.4,43.7,186)	0.48, (136)	0.74, (152)	0.8, (152)	0.38, (143)	0.65, (153)
78. Trelew(-65.3,-43.2,15)	0.09, (133)	0.55, (129)	0.54, (130)	0.44, (117)	0.44, (139)
79. UCSB(-119.8,34.4,33)	0.52, (129)	0.72, (133)	0.75, (133)	0.54, (104)	0.84, (133)
80. Wallops(-75.4,37.9,37)	0.76, (156)	0.9, (149)	0.88, (162)	0.82, (129)	0.9, (162)
81. White_Sands_HELSTF(-106.3,32.6,1207.24)	0.81, (150)	0.62, (155)	0.58, (155)	0.63, (154)	0.86, (155)
82. XiangHe(116.9,39.7,36)	0.54, (134)	0.73, (16)	0.82, (16)	0.56, (124)	0.83, (146)
83. Gadanki(79.16,13.45,365)	0.703, (96)	0.704, (104)	0.73, (121)	0.72, (78)	0.726, (123)

Table 4.1 (b) *Extension of Table 4.1 (a).*

Results of regression analysis of monthly AOD values of MODIS_T and A against co-located AERONET sites at 550 nm wavelength are shown in **Figure 4.1e-l,** which suggests a strong correlation (**Table 4.1**) globally. However, in most of the regions such as North America, SAM, Africa, ECC, North Pacific Ocean, South Atlantic Ocean, Indian Ocean, and the South Pacific Ocean, both MODIS_T and A AODs exhibited more or less identical R values. Furthermore, MODIS_A has values of RMSE ranging from 0.02-0.24 and MAE values ranging from 0.02-0.18. Whereas, in MODIS_T, RMSE values range from 0.07-0.23, and MAE values range from 0.02-0.17. The most significant differences between both products prevailed over the EU,

Australia, and IGP regions, where MODIS_T was having a lesser correlation in comparison to MODIS_A with lower RMSE and MAE values. These results are also consistent with the recent study by Wei et al. (2019b), where they have found that MODIS_A has superior performance in terms of its statistical evaluation extending from the period 2000 to 2017. Differences between MODIS_T and A indicate possible dependencies on its issue with instrument characterization or geometry (Gupta et al., 2018), where there is an increase in positive biases only for MODIS_T in the near-nadir view and its accuracy began to fall off around 2007-2009. On the whole, since AOD measurements from MODIS_A are the most frequent (every 1-2 days) as compared to all the other techniques used and do not suffer from bias issues, unlike MODIS_T and hence it is the best correlated instrument found here with the ground-based values.

We have further encountered a frequent occurrence of medium to low R (for significant cases) values (**Table 4.1**) while dealing with CALIOP (**Figure 4.1m-p**) dataset at a wavelength of 532 nm. The comparatively lower R values were noticed over a few sites of North America, EU, and ECC regions which direct us to the fact that these regions have undergone drastic changes in aerosols since 2000 (Zhao et al., 2017). However, a good correlation was registered over NWA, SAF, ME, and the northern part of SAM (Amazon basin). The reason behind this can be the improved aerosols subtyping and the S_a algorithm selection scheme as mentioned in Kim et al. (2018). All the measurements made with CALIOP have low RMSE (0.02-0.32) and MAE (0.02-0.25) values, whereas higher values were observed over the northern part of the SAM, NWA, and SEA region. The higher differences in the values over these regions have been found in the study by Kim et al. (2018) as well, and the reason for this can be due to the corrected β_{aer} values in the V4 dataset which is intended to change the aerosols subtypes with higher S_a. Even it can arise due to the fact that CALIOP has only two observations (see **section 2.2.1.2**) in a month unlike other instruments having observations every 1-2 days. This limits the CALIOP detection and the retrieval errors which are influenced by low SNR during day time (DT) when all the coincidences with AERONET (Winker et al., 2013) are initiated. Recently, (Gupta et al., 2021) showed a high correlation of the α_{aer} profiles (from the surface to 30 km) between the ground-based LIDARs with the CALIOP observations over the Gadanki region.

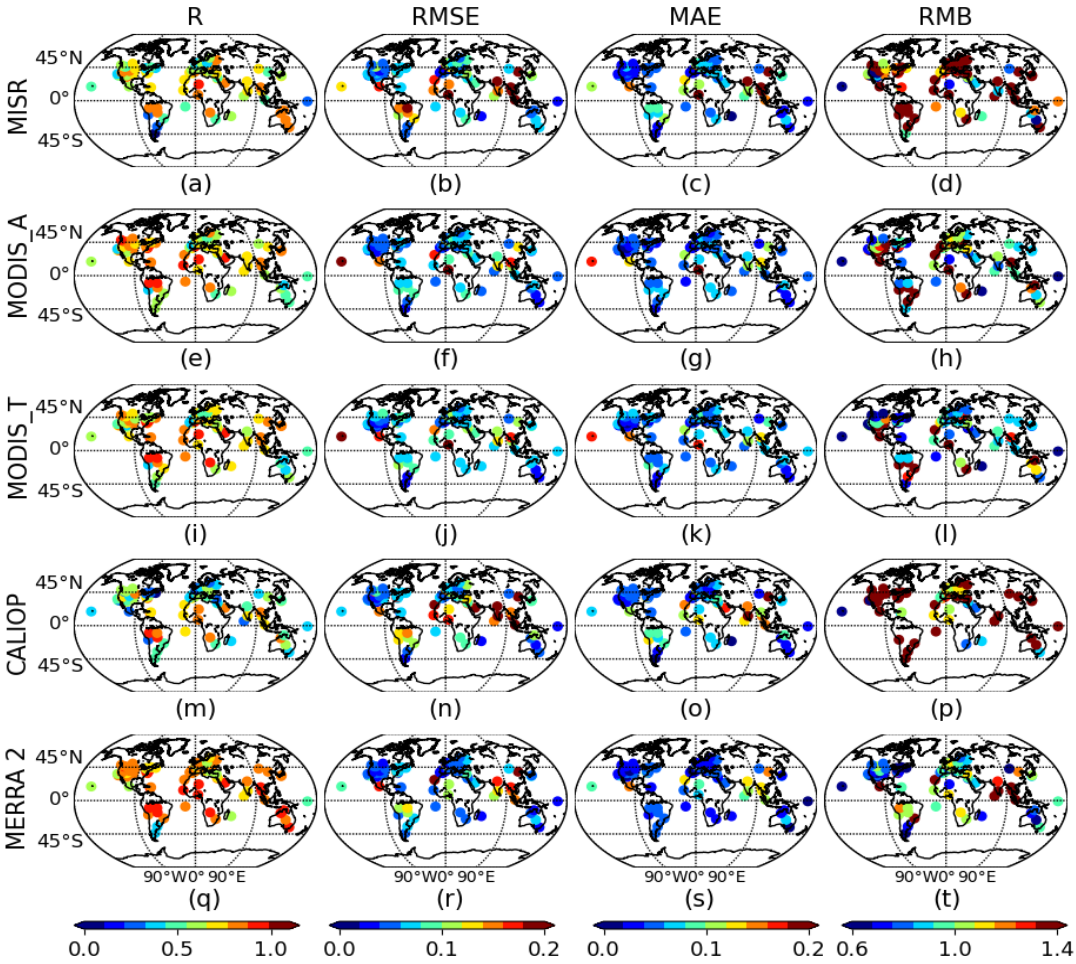

Figure 4.1 *R, RMSE, MAE, and RMB values obtained between (a-d) MISR (2001-2020), (e-h) MODIS_A (2002-2020), (i-l) MODIS_T (2001-2020), (m-p) CALIOP (2006-2020), and (q-t) MERRA-2 (2001-2020) AODs against the AERONET AOD, measured at 550 nm across the globe. Only the statistically significant values at a 95 % confidence level are shown here. For comparison purposes, each observational dataset has been interpolated to 1° × 1° grid resolution.*

The Reanalysis dataset also seemed to show a significant spatial agreement against AERONET observations at 550 nm (**Figure 4.1q-t**). MERRA-2 AOD dataset reported high R values (maximum sites exhibiting values above 0.6), along with low RMSE (maximum up to 0.19) and low MAE (maximum up to 0.15) values. It performs exceptionally well over SAF, South Atlantic Ocean, ME, Indian Ocean, Australia, and North and South Pacific Ocean, with the RMSE and MAE values less than 0.1. Apart from this, we have also noticed comparatively high RMSE and MAE values over the northern part of the SAM, NWA, and SEA region, and these results are in consistence with the previous studies (Che et al., 2019) as well. However, in most of the cases, the values of RMB are greater than 1, which is likely due to the certainty that AERONET

values were not comprehended in the MERRA-2 dataset reported until 1999 and due to the bias in MISR values (Buchard et al., 2017). Whereas underestimation in the AOD values was observed over the rest of the regions, which is attributed to the dearth of NR aerosols (Buchard et al., 2017) in the GOCART model of MERRA-2. Also, in all of the above comparisons, we have seen that the Gadanki sky-radiometer has performed exceptionally well, having high R values.

4.3.2 Spatial AOD Correlation

Till now, we observed statistically significant R values between ground-based and other techniques in **section 4.3.1**. But due to the limitations of ground-based observations to be only point measurement, henceforth inferences from other techniques such as satellite and reanalysis datasets (see **sections 2.2 and 2.3**) were carried forward. Furthermore, in order to have a profound understanding of the relationship between respective spatial AOD datasets, we have analysed their spatial correlations as well.

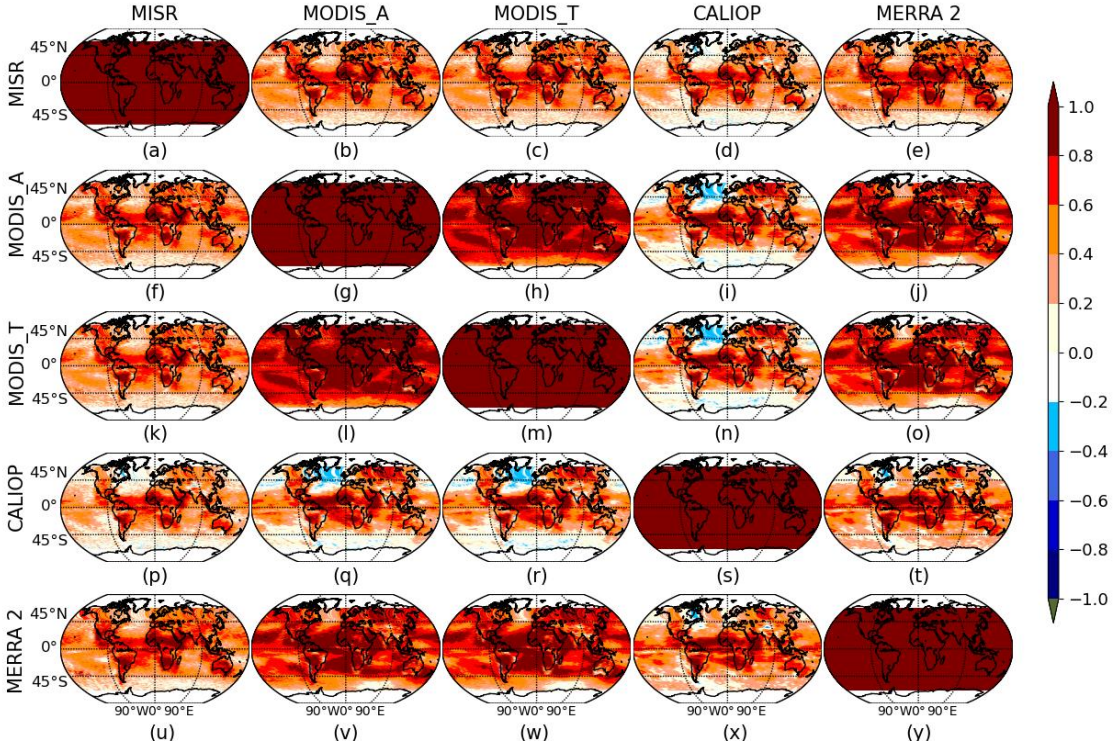

Figure 4.2 *The spatial correlation observed between (a-e) MISR, (f-j) MODIS_A, (k-o) MODIS_T, (p-t) CALIOP, and (u-y) Merra 2 AODs against MISR, MODIS_A, MODIS_T, CALIOP, and MERRA-2 AODs, respectively. Only the statistically significant values at a 95 % confidence level are shown here For comparison purposes, each observational dataset has been interpolated to 1° × 1° grid resolution.*

Every subplot in **Figure 4.2** was further divided such that the combinations were built for each measurement with the other techniques as well as itself, and as such, 25 corresponding subplots were displayed. As expected, diagonal subplots a, g, m, s, and y in **Figure 4.2** represents the one-to-one highest correlations between the MISR, MODIS_A, MODIS_T, CALIOP, and MERRA-2 datasets. It is clear that particularly high to medium R values dominated in the majority of the regions (**Figure 4.2**), indicating consistency in AOD retrievals even from different measurement platforms. Satellite sensors such as MODIS_A in **Figure 4.2f-j** and MODIS_T in **Figure 4.2k-o** had the highest R value (above 0.6) with each other (**Figure 4.2h and l**) across the globe. Essentially all subplots depicted high positive R values with the other sensors except for CALIOP over the North Atlantic Ocean, Southern Ocean, and a few parts of the Indian region. These results showed a moderate negative correlation (0.2 to 0.4) with all the techniques, the R values being highest with MODIS_T and A sensor. This may be true due to the differences in the temporal resolutions or when retrieval algorithms might not represent the accurate microphysical properties of aerosols as both the systems confide on different observing techniques. However, all the sensors have a high positive R values (above 0.8) over SAM, SAF, and NWA regions, yet the highest correlation being with reanalysis datasets. While other places have a moderate correlation, mostly having complex terrains, such as the East Coast of Africa and Brazil, where the transition from vegetation cover to bare land or vice-versa has happened. Apparently, the spatial correlation among retrieved AODs from distinct techniques (**Figure 4.2**) displayed a decent agreement and hence can be considered for the comparative study of spatio-temporal variability of aerosols.

4.3.3 Global analysis of aerosols loading

After having obtained a profound correlation between distinct measurement techniques in **section 4.3.2**, we further moved to examine their optical characteristics extensively in this section. We have analysed the columnar aerosol optical properties from ground-based (AERONET), space-borne (MISR, MODIS_T, and A, CALIOP), and the reanalysis (MERRA-2) datasets to provide mean (**Figure 4.3**) and seasonal (**Figure 4.4**) climatology of aerosols loadings across the globe. For the computation of monthly mean AOD values, only the quality assured values were used after applying all the flags. For the seasonal analysis, a year was further classified into four seasons, namely, NH Winter (December-January-February), Spring Equinox (March-April-May), and NH Summer (June-July-August), and Fall Equinox (September-October-

November). The mean, as well as seasonal AOD values, followed the same patterns in all the techniques used throughout the study, and these features have been reported in detail in Mehta et al. (2016). All the features of the mean AERONET AOD values were consistent with the MODIS_A, MODIS_T, and MERRA-2 sensors, as shown in **Figure 4.3**. Whereas the CALIOP (MISR) sensor has given the overestimated (underestimated) AOD values over the high aerosol loading regions (such as Africa, ME, and SEA regions) against AERONET (reference values) AOD values. These MISR and CALIOP features were in agreement with the previous studies of Kim et al. (2018); Wei et al. (2019b).

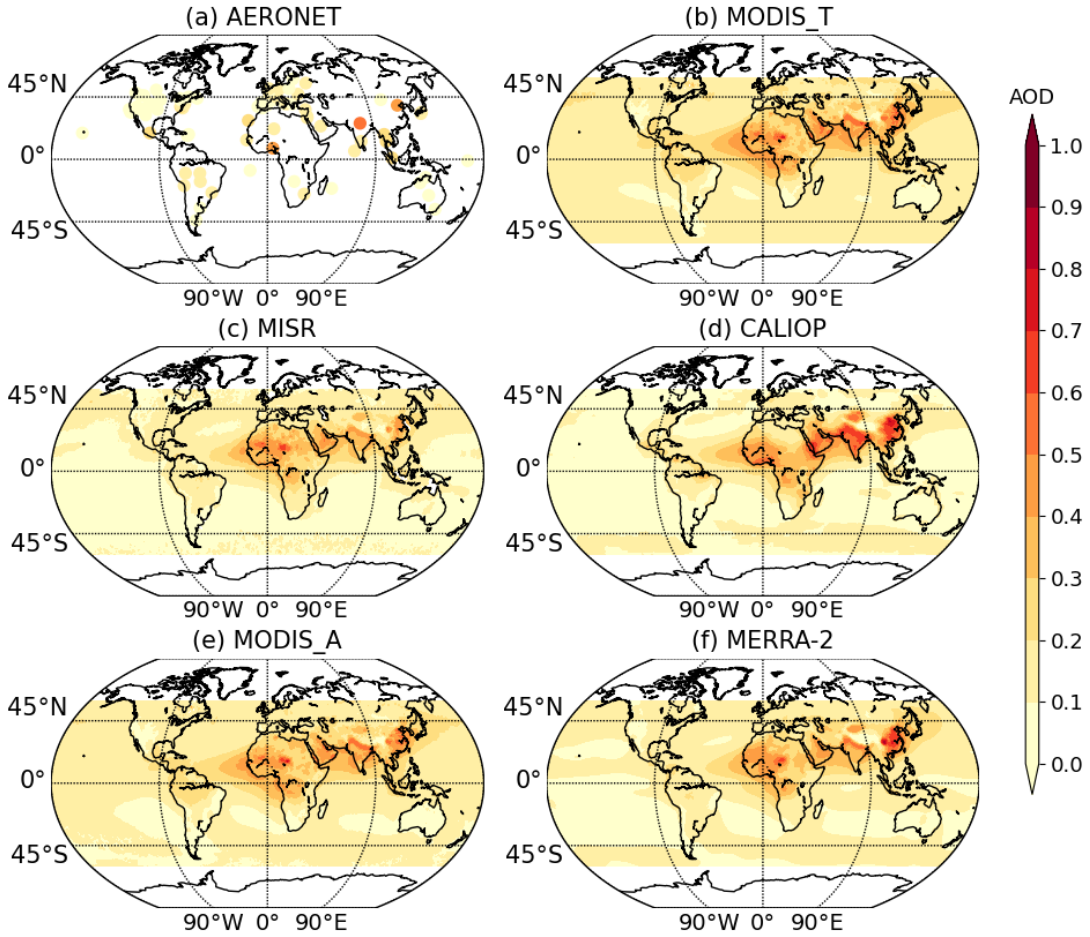

Figure 4.3 *Annual mean climatology of AOD observed by (a) AERONET, (b) MODIS_T, (c) MISR, (d) CALIOP, (e) MODIS_A, and (f) MERRA-2, between 2001 to 2020, across the globe. For comparison purposes, each observational dataset has been interpolated to 1° × 1° grid resolution.*

Seasonally also, the higher (lower) AOD values were seen in CALIOP (MISR) observations, but the overall pattern remained the same in the MISR measurements (when compared with the other techniques), while it was not the case with the CALIOP

observations (**Figure 4.4m-p**). In addition, the comparatively higher AOD values over the IGP belt region were well apprehended in all the sensors, and the lower AOD values over the rest of the Indian region were also well-separated. But it is not the case with the CALIOP sensor, as it has shown uniformity in the mean AOD values over the whole Indian region (**Figure 4.3d**). In the seasonal variation of the CALIOP observations, we have seen higher AOD values over the Indian region during the spring season as compared to the other techniques where the highest AOD values were observed during the NH summer season (**Figure 4.4**).

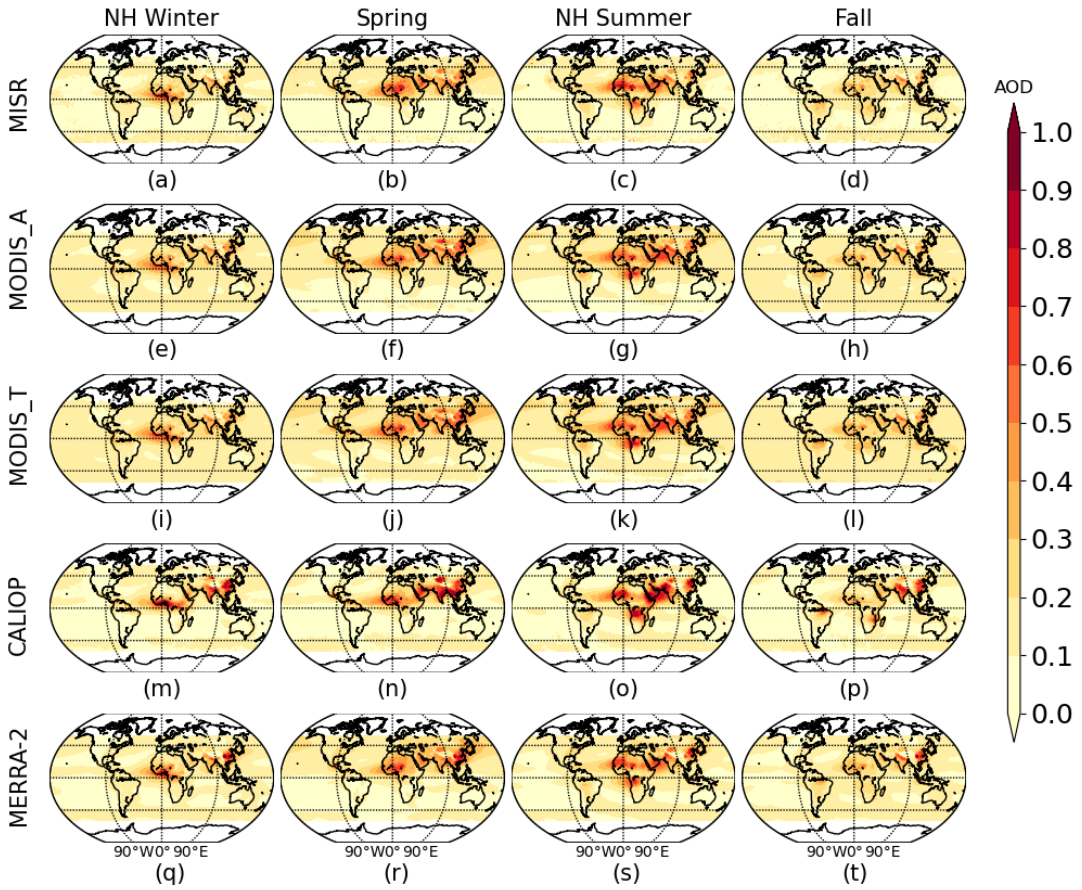

Figure 4.4 *Seasonal climatology of AODs observed during NH Winter (Dec-Jan-Feb), Spring (Mar-Apr-May), NH Summer (Jun-Jul-Aug-Sep), and Fall (Oct-Nov) seasons, using (a-d) MISR, (e-h) MODIS_A, (i-l) MODIS_T, (m-p) CALIOP, and (q-t) MERRA-2 datasets, on a global scale.*

In addition to this, the CALIOP has encountered higher AOD mean values (**Figure 4.3**), especially over the SEA region, and these examined characteristics were irrespective of any season (**Figure 4.4**) as well. This can be seen in accordance with the varying aerosol types over the region or the changing meteorology/ dynamics due to the much uncertain implications of the ASM (Li et al., 2016). This leads us to

conclude that there still exists huge uncertainty while measuring aerosols over the SEA region. On the other hand, it was noticed that CALIOP was showing comparatively lower AOD values (<0.1) over the regions where aerosol loading is already shallow, such as Oceanic regions, NEA, SAM, Australia, EU, and North Asia regions, respectively. While exceptionally high values were obtained over the regions with high aerosol loading. At the same time, the reanalysis dataset could accurately pick each varying feature of the mean (**Figure 4.3f**) as well as seasonal (**Figure 4.4q-t**) aerosol loadings.

4.3.4 Regional analysis of trends and inter-annual variability in the AOD

In order to understand the uncertain distribution and varying properties of the aerosols across the globe, continuous efforts are required to investigate its long-term trends, which can provide us reliable information about the atmosphere. For this, the MLR trend approach (see **section 2.4**) has been implemented on all the ground-based, space-borne and reanalysis datasets (see **sections 2.2 and 2.3**), and the contributions due to SAO, AO, QBO, ENSO, and SC have been isolated or removed from the datasets, as shown in **Figure 2.13**.

Regions	Lat_{min}, Lat_{max}	Lon_{min}, Lon_{max}	MISR	MODIS_A	MODIS_T	CALIOP	MERRA-2
1. NEA	30°N, 50°N	90°W, 60°W	**-0.002**	**-0.002**	**-0.002**	**-0.002**	**-0.002**
2. EU	35°N, 55°N	10°W, 40°E	**-0.002**	**-0.002**	**-0.002**	**-0.003**	**-0.001**
3. ME	13°N, 30°N	40°E, 60°E	0.002	**0.003**	0	**-0.006**	0.001
4. IGP	24°N, 30°N	68°,E 90°E	**0.002**	0.001	-0	0.004	**0.002**
5. ECC	20°N, 40°N	95°,E 120°E	**-0.004**	**-0.005**	**-0.005**	**-0.013**	-0
6. NWA	5°N, 25°N	30°W, 25°E	0.001	0.001	-0.001	0.001	-0.001
7. CI	22°N, 25°N	68°E, 90°E	**0.004**	**0.005**	**0.004**	**0.007**	**0.003**
8. SAF	12°S, 5°N	12°E, 35°E	0	0	-0	-0.003	0.001
9. AS	5°N, 20°N	60°E, 72°E	**0.002**	**0.003**	**0.004**	-0.001	**0.003**
10. SI	8°N, 22°N	72°E, 82°E	**0.005**	**0.007**	**0.006**	0.004	**0.004**
11. SAM	15°S, 1°S	80°W, 40°W	**-0.002**	**-0.001**	**-0.001**	**-0.009**	0
12. BoB	5°N, 20°N	85°,E 95°E	**0.001**	**0.002**	**0.002**	-0.001	**0.002**

Table 4.2 *Details of the selected region-wise geo-locations (lat and lon) and regional trend values in MISR, MODIS_A, MODIS_T, CALIOP, and MERRA-2 datasets. Here, p-values ≤ 0.05 (statistically significant at 95 % confidence level) are kept in boldface.*

The region-specific comprehensive details of inter-annual (**Table 4.2**) and seasonal (**Table 4.3**) mean AOD LR across the globe were also studied. This conventional LR trend analysis approach was also compared with the MLR trend analysis extensively in the following sub-section. For this, we have sub-divided the globe into 8 regions of interest (RoI) based on either being the most populous or the

regions having some significant trend values (whether increasing or decreasing). These RoI have been selected based on the results from **Figures 4.5 and 4.6**, namely NEA, EU, ME, NWA, SAF, SAM, ECC, and India with its adjoining sea regions. Vertical bars showed the SE in the inter-annual and seasonal LR trend values. Note that the boundaries were chosen rather arbitrarily with the objective of illustration purpose only, and the corresponding latitudes and longitudes information has been provided in **Table 4.2** as well.

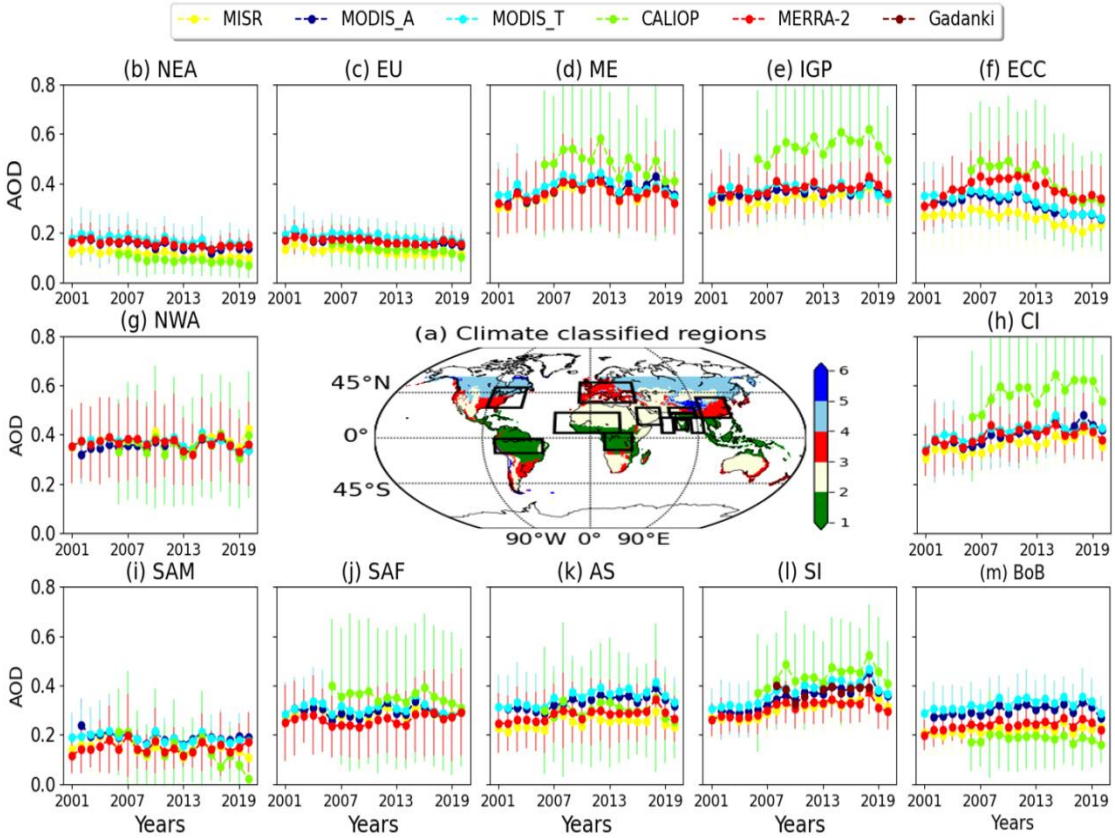

Figure 4.5 *(a) Global climate classified regions are same as in* ***Figure 2.10****. (b-m) Time series of the inter-annual variation in AOD obtained over different regions segregated based on either being the most populous or the regions having some significant trend values (whether increasing or decreasing). Vertical bars represent the SE values. Different regions selected are (b) NEA, (c) EU, (d) ME, (e) IGP, (f) ECC, (g) NWA, (h) CI, (i) SAM, (j) SAF, (k) AS, (l) SI, and, (m) BoB. (l) Inter-annual variation of AOD from Gadanki sky radiometer is also superimposed.*

4.3.4.1 North Eastern America (NEA)

NEA, the third largest populated country having a subtropical climate (**Figure 4.5a**), where the low mean AOD (≤ 0.25) values (**Figure 4.5b**) prevailed over the region. Here, the inter-annual AOD LR trends (**Figure 4.5b**) showed decreasing trend

values (**Table 4.2**) in all the measurements. Similarly, a statistically significant decreasing trend in the AOD (0.1 AOD/decade) values was also observed using the MLR trend analysis, as seen in **Figure 4.6** in all the techniques used in the study. Interestingly, these annual decreasing trend results were in accordance with the previous studies (Che et al., 2019; Wei et al., 2019b; Zhao et al., 2017) as well. However, the inter-seasonal LR trend values (**Table 4.3**) showed a maximum (minimum) decrease during NH summer and Spring (NH winter and Fall seasons) seasons. Over NEA region, a considerable decrease in the emission of pollutants is reported except for NH_3 and DU aerosols with the implementation of a series of Clean Air Act (CAA) Amendments in the 1990s (Hand et al., 2012; Zhao et al., 2017). Additionally, a very slight increasing trend was also observed over the Western region of North America (**Figure 4.6**) with MODIS_T and A, MISR, and MERRA-2 datasets, which are seen in connection with the decrease of precipitation over the region (Zhang et al., 2017) which needs to be examined further.

4.3.4.2 Europe (EU)

Low annual mean aerosol loading (≤ 0.35) values were noticed over the EU region as well. Inter-annual AOD variations (**Figure 4.5c**) showed the statistically significant decreasing LR trend values (**Table 4.2**), the highest (lowest) being with the CALIOP (MERRA-2) observations. On the other hand, negative (0.1 AOD/ decade) AOD trend (**Figure 4.6**) values were recorded in the MLR trend analysis as well. These decreasing annual trend values from both the approaches (LR and MLR) were in accordance with the previous studies (Che et al., 2019; Wei et al., 2019b; Zhao et al., 2017) over the EU region. However, in the fall (NH winter) season, the LR trend analysis showed insignificant AOD trend values with the MODIS_A and MODIS_T (MODIS_T, CALIOP, and MERRA-2) measurements, as seen in **Table 4.3**. This decrease in the total AOD trend values can be seen related to the decrease in sulfur dioxide and nitrous oxide emissions (Zhao et al., 2017) with the implementation of a similar CAA over the region.

4.3.4.3 Middle-East (ME)

Over the ME countries, high AOD values (between 0.2-0.8) were observed where the CALIOP observations had shown the highest SE (**Figure 4.5d**) over the region. The reason behind high SE in the CALIOP observations can be seen in **Figure 4.1n and o,** where high RMSE and MAE values were observed over the region. A statistically significant increasing LR trend in inter-annual variations (**Figure 4.5d**)

over the ME region was noticed (**Table 4.2**) only with the MODIS_A measurements. Similarly, a significantly increasing (0.1 AOD/decade) AOD trend values have been found over the Saudi Arabia region of ME from the AERONET, MISR, and MODIS_A measurements (**Figure 4.6**) using the MLR trend analysis, and this trend was in agreement with Wei et al. (2019b) as well. This increasing trend can be seen in association with the increasing temperature and decreasing humidity leading to the drying of soil or increases in DU emissions (Klingmüller et al., 2016) over the region. Although, CALIOP and MERRA-2 datasets have also reported high R values with the AERONET (**Figure 4.1**) observations, but a complete reversal in the trend values over the ME region was recognized with the MLR trend analysis approach. Here, a statistically significant decreasing trend value using both the trend (MLR as well as LR) analysis (**Figures 4.5d and 4.6d**) was noticed with the CALIOP datasets.

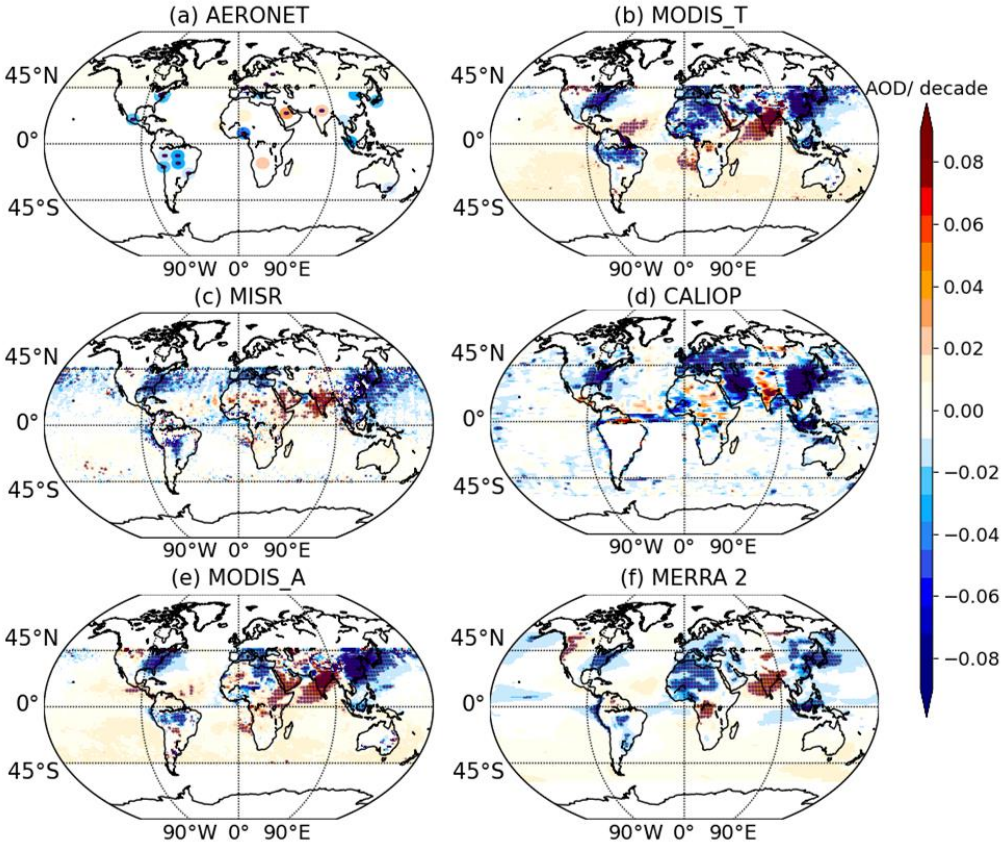

Figure 4.6 *Long-term trends observed in AOD, after removing the periodic oscillations (i.e., QBO, ENSO, and SC), obtained using (a) AERONET, (b) MODIS_T, (c) MISR, (d) CALIOP, (e) MODIS_A, and (f) MERRA-2 datasets, across the globe. The stippling regions in each of the subplots represent the trend values that are statistically significant at a 95 % confidence level. For comparison purposes, the observational dataset has been interpolated to 1° × 1° grid resolution.*

4.3.4.4 South America (SAM)

Low annual and seasonal mean AOD values (≤ 0.2) were observed over the SAM region. However, a statistically significant decreasing AOD LR trend pattern was well apprehended in the inter-annual analysis (**Figure 4.5i**) with the MODIS_T, MISR, and MODIS_A measurements (**Table 4.2**), with the highest values occurring during the NH summer and fall seasons. Similarly, there was an observed significant decrease in the AOD trend values (0.1 AOD/ decade) with the MLR trend analysis as well, as shown in **Figure 4.6**. This decrease in the AOD trend values can be attributed to the reduction in the deforestation fires since 2004 (Reddington et al., 2015). However, previously few studies have also reported negative but insignificant AOD trend values over the SAM region (Mehta et al., 2016; Hsu, 2012; Wei et al., 2019b), while our study has shown a statistically significant decreasing trend values with the long-term dataset using both the techniques (LR and MLR) over the region. Note that the CALIOP measurements over the SAM region were not considered here as the dataset suffers from a high level of noise due to South Atlantic Anomaly (SAA) and geomagnetic perturbations which enables high energetic particles to hit the LIDAR instrument, resulting in noises (Domingos et al., 2017).

4.3.4.5 North Western Africa (NWA)

The annual mean AOD values over the NWA region were found to be moderate (between 0.2 and 0.6). We could see here that all the measurement techniques (in the previous **sections 4.3.1 and 4.3.2**) have shown high R (above 0.7) values over this region but have also observed higher RMSE and MAE values as well (**Figures 4.1 and 4.2**). Statistically significant negative AOD trend (0.1 AOD/ decade) values were noticed over the NWA region (**Figure 4.6**) when measured with the AERONET, MODIS_T, CALIOP, and MERRA-2 datasets using the MLR trend analysis. These decreasing trend values observed over the NWA region were found to be consistent with the previously reported decreasing trend values in Che et al. (2019); Mehta et al. (2016) as well. The decreasing AOD trend over NWA could be linked with the stilling of surface winds (Ridley et al., 2014) over the DU aerosol regions, which is associated with the large scale modification in the circulation over the Sahel region. This decreasing trend pattern showed a decrease in the export of DU, mainly from the Sahara region into the Atlantic Oceans. On the contrary, we have noticed a statistically insignificant increasing trend (0.001 per year seen in **Table 4.2**) values when seen through the LR trend (**Figure 4.5g and Table 4.3**) analysis approach over this region.

		NEA	EU	ME	IGP	ECC	NWA	CI	SAF	AS	SI	SAM	BoB
MISR	a). Winter	**-0.001**	**-0.001**	**0.001**	**0.004**	**-0.002**	0.001	**0.004**	**0.001**	**0.003**	**0.006**	-0	**0.002**
	b). Spring	-0.002	**-0.002**	0.003	0.003	**-0.003**	-0	**0.003**	**-0.001**	**0.002**	**0.005**	**0**	**0.002**
	c). Summer	**-0.003**	**-0.002**	0.002	0.002	**-0.006**	**0.002**	**0.003**	**0.001**	0	-0	**-0.003**	-0
	d). Fall	**-0.001**	**-0.001**	0.002	**0.005**	**-0.004**	-0.001	**0.009**	**-0.001**	**0.004**	**0.008**	-0.003	0.001
	e). Annual	**-0.002**	**-0.002**	**0.002**	0.002	**-0.004**	0.001	**0.004**	**0**	**0.002**	**0.005**	**-0.002**	**0.001**
MODIS_A	a). Winter	**-0.001**	**-0.001**	**0.002**	0.002	-0	**0.003**	0.007	0.003	**0.004**	0.009	0	**0.003**
	b). Spring	**-0.003**	**-0.003**	0.003	0.003	**-0.003**	-0.001	0.002	**-0.001**	0.003	**0.007**	**0.001**	**0.003**
	c). Summer	**-0.004**	**-0.002**	0.003	0.003	**-0.007**	0	**0.005**	**0.001**	0.003	**0.004**	**-0.003**	-0.001
	d). Fall	**-0.001**	-0.001	**0.002**	-0.001	**-0.002**	-0.001	**0.006**	**-0.001**	**0.005**	**0.008**	-0.001	0.002
	e). Annual	**-0.002**	**-0.002**	**0.003**	**0.003**	**-0.005**	0.001	**0.005**	**0**	**0.003**	**0.007**	**-0.001**	**0.002**
MODIS_T	a). Winter	-0	-0	0.001	0.001	-0.001	0	0.007	**0.001**	**0.005**	0.008	**-0.001**	**0.002**
	b). Spring	**-0.003**	**-0.003**	0.001	0.001	**-0.004**	-0.002	-0	**-0.001**	**0.004**	**0.006**	0	**0.003**
	c). Summer	**-0.004**	**-0.003**	-0	-0	**-0.007**	-0.001	0.003	**0.001**	0.002	0.003	-0.002	-0
	d). Fall	-0	0	0.001	-0.002	-0.001	-0.001	**0.005**	**-0.002**	**0.005**	**0.007**	-0.002	0.002
	e). Annual	-0.002	**-0.002**	0	0	**-0.005**	-0.001	**0.004**	**-0**	**0.004**	**0.006**	**-0.001**	**0.002**
CALIOP	a). Winter	-0.001	**-0.001**	-0.003	**0.006**	**-0.012**	0.004	**0.007**	**0.001**	0.001	**0.007**	0.001	0
	b). Spring	**-0.002**	-0.004	**-0.011**	**-0.011**	**-0.014**	-0.006	-0	**-0.001**	0.002	0.002	0.002	-0.003
	c). Summer	**-0.004**	**-0.003**	**-0.011**	**-0.011**	**-0.016**	0.002	0.006	**-0.002**	0.002	0.004	**-0.012**	-0.004
	d). Fall	-0.001	**-0.002**	0.002	**0.009**	**-0.014**	-0	**0.012**	**-0.001**	0.002	**0.008**	**-0.015**	-0.001
	e). Annual	**-0.002**	**-0.003**	**-0.006**	**-0.006**	**-0.013**	0.001	**0.007**	**-0.002**	0.002	0.004	**-0.009**	-0.001
MERRA-2	a). Winter	**-0**	-0	-0	**0.004**	0.001	0.001	**0.007**	**0**	**0.003**	0.007	0.001	**0.002**
	b). Spring	**-0.002**	**-0.002**	0.001	0.001	0.002	-0.002	0.002	**-0.001**	**0.002**	**0.003**	**0.001**	**0.003**
	c). Summer	**-0.003**	**-0.002**	0.001	0.001	-0.002	-0.001	-0.001	0.005	0.001	-0	-0.001	0
	d). Fall	**-0**	**-0**	0.001	**0.005**	-0.001	-0.001	**0.007**	**-0.001**	**0.005**	**0.007**	0.001	0.002
	e). Annual	**-0.002**	**-0.001**	0.001	0.001	-0	-0.001	**0.003**	**0.001**	**0.003**	**0.004**	0	**0.002**

Table 4.3 *Same as* ***Table 4.2*** *but season-wise.*

4.3.4.6 South Africa (SAF)

The annual and seasonal mean AOD values noticed over the SAF region fall under the tropical climate region (**Figure 4.5a**), where low to moderate mean AOD (between 0.1-0.4) values were observed. There were a significant increasing AOD trend (0.1 AOD/ decade) values observed with the AERONET, MODIS, and MERRA-2

(**Figure 4.6**) datasets over the SAF and its adjoining South Atlantic Ocean regions when detected using the MLR trend analysis. This can be associated with the increase in crop residual burning in dry seasons (NH summer season), as reported by Kumar et al. (2014). Moreover, these values were in contradiction with the values previously reported by Mehta et al. (2016); Hsu, 2012; Wei et al. (2019b), where decreasing trend values were observed over the region. However, a recent study by Che et al. (2019) has also observed increasing AOD trend values over the SAF region with the reanalysis dataset in response to the changes in the regional fire activities. More specifically, we have noticed that LR trend analysis was not able to retrieve statistically significant AOD trend values over the whole Africa region.

4.3.4.7 India and its adjoining sea regions

The geography of the Indian region is very unique, covered from snow-capped mountains in the north to surrounded by sea coasts in the south, for which the Indian region was further sub-divided into the IGP, CI, SI, and its adjoining sea regions, including AS, and BoB. The landmass region of India comprising IGP, CI, and SI exhibited comparatively higher aerosol loading (> 0.3) values. The CALIOP sensor has shown a higher SE over the landmass region (SI, CI, and IGP), and this can be seen in association with the higher RMSE and MAE values, as discussed in **sections 4.3.1 and 4.3.2**. We have observed high positive, statistically significant AOD trend (0.1 AOD/ decade) values over the South Asia region, particularly SI and its adjoining AS and BoB regions, as seen in **Figure 4.6** using MLR trend analysis. The LR trend of the annual mean (**Figure 4.5e, h, k, l, and m)** and seasonal AOD values also depicted similar increasing trend values (**Tables 4.2 and 4.3**) with a 95% confidence level. Increasing trend values witnessed during NH winter and fall seasons were found to be the highest. Recently, Ratnam et al. (2021) also found that these increasing trend values in the SI region persisted due to the accumulation of pollutants above the ABL (or FT) altitudes through the long-range transport and an increase in the convection (vertical velocity) activities. A significant increase in AOD trend values over the SI and its adjoining AS and BoB regions were very prominent and were noticed in all the measurements (**Figures 4.5 and 4.6**). Additionally, we could also validate these results with the ground-based Gadanki sky-radiometer, which provided an increasing trend with a value of 0.003 per year. In contrast, a very prominent decreasing AOD trend was observed over the North-western region of India (**Figure 4.6**), which was seen to be associated with the increase in precipitation efficiencies, as mentioned explicitly in

Ratnam et al. (2021), using the MODIS_T sensor. The same feature was confirmed here with the other satellite sensors such as the MODIS_A, MODIS_T, MISR, and CALIOP observations as well.

4.3.4.8 Eastern and Central China (ECC)

China, one of the most populated countries, lies over the subtropical temperature climate region (**Figure 4.5a**) and has comparatively high aerosol loading (between 0.2-0.7) values over its Eastern part region. The LR trend analysis (**Figure 4.5f**) has reported statistically significant decreasing trend values over the region (**Tables 4.2 and 4.3**) in the MODIS_A, MODIS_T, CALIOP, and MISR observations, where the highest decreasing trend was noticed during the NH summer season. In particular, MLR trend analysis also exhibited statistically significant decreasing trend values (0.1 AOD/decade), mainly over the eastern part of the China region (**Figure 4.6**). Here, the reanalysis dataset has not shown any significant trend values over the region with the LR trend analysis. For the ECC region, Zhao et al. (2017) has explained that the decrease in trends was quite prominent and is mainly due to the implementation of China's 11^{th} (2006-2010) and 12^{th} (2011-2015) five-year plan control policies and the Air Pollution Prevention and Control Action Plan (2013-2017). In addition, the blue-sky defense (2018-2020) is also an important measure implemented in recent years, which is used to improve the air quality by reducing the emission of major pollutants related to particulate matter. More information can be obtained from Wei et al., 2021b, 2021a. This results in a decrease of all pollutants after 2011 except NH_3 and Non-Methane Volatile Organic Compounds.

As seen in **Figure 4.6**, all the measurement (ground-based, space-borne, and reanalysis) techniques have depicted almost similar patterns in the AOD trends (whether increasing or decreasing) but with a varied magnitude. The trend magnitude values were lower (higher) in reanalysis (CALIOP) datasets. We have also seen (in the same Figure) that the results from the MLR trend approach applied (**Figure 4.6b-f**) to the space-borne and the reanalysis datasets match exceptionally well with the ground-based measurements (**Figure 4.6a**) as well. However, on the other hand, the LR trend analysis (**Table 4.2**) could not perform well over the regions having huge aerosol variability, such as over NWA and SAF regions, where no significant trend values were obtained. Over SI, AS, and BoB regions, CALIOP noticed increasing insignificant trend values with the LR trend analysis. Similarly, over the ECC region, MERRA-2 could not give any significant trend values with the LR trend analysis. In addition to

this, note that these tropical regions (such as NWA, SAF, ME, ECC, India, and its adjoining waters) are the ones suffering from huge impacts due to these natural oscillations (**Figure 2.13**) and hence have been tried to be isolated rather effectively using the MLR trend analysis in this study.

4.4 Summary

In this study, we have examined the LR and MLR trend analysis in connection with the employed emission control policies to ascertain their spatial representativeness in regional as well as global scales, for the past two decades. We have used the AOD dataset obtained from satellite-based sensors comprising MODIS (onboard T and A), MISR, and CALIOP, and the reanalysis (MERRA-2) datasets between 2001 and 2020. Prior to that, a comparison of this entire long-term dataset is being carried out with AERONET observations to analyse the efficiency of these datasets. Major findings drawn from this study are summarized below.

i) A comparison of AOD values against the AERONET stations revealed the existence of high (above 0.7) to medium (ranging from 0.3 to 0.7) R values in MISR, MODIS_T, and MODIS_A sensors while medium (ranging from 0.3 to 0.7) to low (below 0.3) R values are observed in the CALIOP measurements. Low R values (for a fraction of cases) in CALIOP are subjected to differences due to the instrument view angle, spatial or low temporal (approximately two observations in a month) coverage, and the retrieval errors due to low SNR values. The reanalysis dataset has also performed exceptionally well, having high R values (above 0.7). Out of all, we have observed high RMSE and MAE values over the SAM, NWA, and SEA regions with all the datasets. Overall, we could observe a good correlation between all the spatial observations with AERONET, and we found that the MODIS_A is the best correlated instrument among all available sensors.

ii) A decent agreement is also noticed in the correlation analysis within the techniques covering huge spatial and temporal datasets. Here, MODIS_A and MODIS_T values are in exemplary accordance with the reanalysis (MERRA-2) dataset. In contrast, CALIOP observations have exhibited moderate negative values with MODIS_A and MODIS_T over the North Atlantic Ocean, which may be associated with the differences in the techniques engaged. Apparently, there is an underestimation (overestimation) of the MISR (CALIOP) derived AOD values when compared with those from the AERONET AOD values. At the same time, the CALIOP sensor has shown the highest aerosol loading (above 0.5) over the most polluted regions

(especially the SEA region), while the lowest values (below 0.1) are observed over the rest of the globe.

iii) In this study, we have used two types of trend analysis to ascertain their spatial representativeness. The first approach followed is the conventional LR trend analysis, and the second approach applied is the MLR trend analysis, in which the contributions due to QBO, ENSO, and SC are either removed or isolated. Using the same, decreasing AOD trend values (0.1 AOD/ decade) are noticed over the NEA, EU, and ECC regions with both the approaches (LR and MLR). These regions with decreasing trend values are majorly seen in accordance with the implementation of emission control policies. Prominent decreasing trends over the SAM (NWA) region are seen in connection with the decrease of fires (stilling of surface winds). The AOD trend analysis exhibited statistically significant increasing trend values (0.1 AOD/ decade), specifically over the ME and Indian regions. Whereas over the SAF region also, increasing aerosols trend values are observed, which is in contradiction to the decreasing insignificant trend values reported in the earlier studies.

iv) –When compared with the other measurements, CALIOP exhibited surprisingly statistically significant negative AOD trend values over the ME (0.006 per year) region, which is verified using both the trend approaches (LR and MLR). As compared to the MLR trend analysis, LR trend analysis could not perform well (giving insignificant trends) over the regions with high aerosol loadings, such as over the Africa region (in all techniques), SI, AS, and BoB regions (with CALIOP measurement) and over ECC region (with reanalysis dataset) respectively. Overall, the latest versions of the discrete measurement techniques (ground, satellite, and reanalysis) utilized throughout this study are able to establish profound spatial reliability in the AOD trend values when seen with the two different trend approaches, and hence it can be further utilised for future explorations.

From this study, the 8 RoI were identified based on changing long-term AOD trends (**section 4.3.4**), which will be further evaluated to estimate the contribution of optical, physical, and morphological (chemical) properties of aerosols in connection with the total AOD values in **Chapter 5** (**Chapter 6**).

Chapter 5

Global trends in Aerosols Optical, Physical, and Morphological properties obtained using Multi-sensor measurements

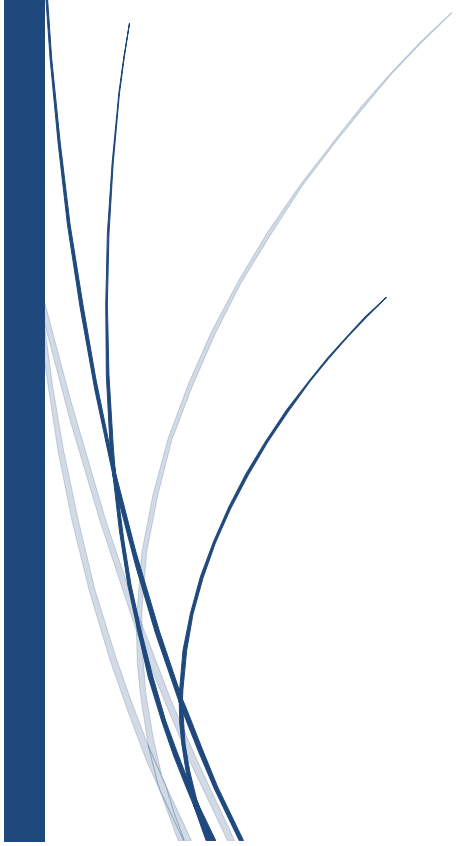

5.1 Introduction

One of the main drivers of the Earth's radiation budget and climate change is the drastic changes in the aerosols emissions (IPCC, 2013), owing to the contributions from the various natural/anthropogenic sources (primary) or the gaseous precursors (secondary) through complex feedback mechanisms (Seinfeld and Pandis, 2006). However, there still exists uncertainty with a factor of up to three due to the ARI alone, as discussed in **Chapter 1**. In the same context, large spatio-temporal variability in their chemical composition, size, and shape of aerosols also exists due to the presence of numerous sources involving different formation mechanisms from the highly polluted regions, which adds further complexity in the evaluation of ARI. Such crucial aspects are vital to examine for which there is a need to accurately describe the varying properties due to the heterogeneity of aerosols composition, which ultimately contributes to the total aerosol loading, and thus for the evaluation of the state-of-the-art global climate model simulations (Ramachandran et al., 2020).

Remarkable progress has been made in understanding the variability of total aerosol loading in terms of AOD at regional as well as global scales within the past two decades (Filonchyk et al., 2020; Mehta, 2015; Mehta et al., 2016; Ratnam et al., 2021; Samset et al., 2019; Gupta et al., 2022). Yet, despite the extensive research conducted in this area in the last two decades, there still exists a gap in associating the contribution of different types of aerosols with its plausible implications on the atmosphere (IPCC, 2013; Myhre et al., 2013), due to extreme heterogeneity in different aerosol properties. From the previous studies, it was found that so far, very limited studies exist to understand the trends in total AOD with other optical, physical, and morphological properties retrieved from various satellite measurements, and that too only at regional scales (Banerjee et al., 2021; Prijith et al., 2018; Ramachandran and Rupakheti, 2021; Zhao et al., 2017). To further examine in this direction, we considered ground-based measurements beforehand and compared the same with the space-borne and reanalysis datasets (see **section 4.3.1**). Thus, we conducted a complete study beforehand in Gupta et al. (2022), where the similarities, reliabilities, and differences between the mean total AOD loading and its long-term trends were discussed using all the datasets (ground-based/space-borne/reanalysis, see **sections 2.2 and 2.3**) that are to be considered here. This chapter will further provide insights on the association of trends in the properties

depicting its size (fine/coarse), shape (spherical/non-spherical), and optical (absorbing/scattering) characteristics with the observed trends in the total AOD values. Thus, the primary aim of this study is to investigate the region-wise long-term trends in the spatial and vertical distribution of the aerosols optical (absorbing/scattering), physical (size), and morphological (shape) properties so as to relate the trends of total AOD reported in **Chapter 4** with further implications to the regional climate change. In addition to this, we have also compared all the results derived from ground-based observations with the satellite-based/MERRA-2 global datasets for each aerosol characteristic. Furthermore, we have examined the association of trends in the total AOD with the trends obtained from different properties of the aerosols in connection with the implementation of pollution control policies over the 8 RoI (see **section 4.3.4**) in this study. Finally, we have summarized with the region-wise contribution of each property of aerosols with its future implications.

5.2 Results

It is often very stringent to gather accurate knowledge on the persisting aerosol types due to their vast variability in the atmosphere, and only a very few studies in the past have explored this aspect using different techniques (Banerjee et al., 2021; Penning De Vries et al., 2015; Ramachandran and Rupakheti, 2021). With the aim to have a thorough understanding of the behaviour of the changing aerosols optical (absorption/scattering), physical (size), and morphological (shape) properties, this study is further sub-divided into 8 RoI. In this study, only those regions which exhibited long-term variations in the total AOD trend values are chosen so that the trends associated with each of the aerosol properties (optical/physical/morphological) that ultimately lead to these variations can be investigated further. Note that here the MODIS_A dataset is only used, rather than the MODIS_T dataset, as it is highly correlated with the AERONET AOD values (as seen in **section 4.3.1**). Considering this broad view in the behaviour of the total AOD values, we have examined the mean climatology and long-term variations of the associated aerosol properties classified based on their optical, physical, as well as morphological characteristics in the following sub-sections. We will be discussing these aerosol properties where our primary focus will be on the 8 RoI, and the geographical boundaries selected for these regions are highlighted in **Table 4.2**. Also, a range (from lowest to highest) and the mode of the statistically significant trend values with all the instruments used to analyse the various aerosol properties, over the 8 RoIs, is provided in **Table 5.1**.

5.2.1 Trends in the Aerosols Optical Characteristics

Aerosols optical characteristics are vital in determining the direct climate effects on the atmosphere, owing to their ability to scatter and absorb the incoming radiation at different wavelengths. In this context, the spatial climatology and trends of the mean aAOD and sAOD are derived from the AERONET (see **Table 2.3**), MISR (see **Table 2.5**), and MERRA-2 (see **Table 2.6**) observations, as shown in **Figures 5.1 and 5.2,** respectively. Note that the aAOD mean values observed from MISR (**Figure 5.1b**) are four times lesser (in magnitude) than the values obtained from the AERONET (**Figure 5.1a**) and MERRA-2 (**Figure 5.1c**) observations. Also, the sAOD mean values (**Figure 5.2a, b, and c**) observed are higher than the mean aAOD values (**Figure 5.1a,b, and c**). Major findings drawn from these observations are as follows:

(i) The annual mean aAOD contribution to the total AOD from AERONET and MERRA-2 datasets was comparatively higher over the SAM, Africa, ME, IGP, and ECC regions (**Figure 5.1a and c**) than in the rest of the global regions. In the case of the MISR observations, we have noticed very low mean aAOD loading across the globe except Africa (and its adjoining oceans) and AS (**Figure 5.1b**) regions. This feature related to the variation in the magnitude of aAOD values using different datasets was reported in the previous studies as well, where the contribution of aAOD to the total AOD is 20% from AERONET observations (Ramachandran and Rupakheti, 2021), but it went up to 3.5% in the case of MISR (Zhao et al., 2017) measurements.

(ii) Associated long-term aAOD trends indicate insignificant decreasing values over the high aerosol loading regions, namely, SAM, NWA, EU, and IGP, with the AERONET observations (**Figure 5.1d**). However, similar statistically significant decreasing trends of aAOD, at the rate of 0.001/ decade, were noticed over the IGP, CI, and EU regions with the MISR (**Figure 5.1e**) dataset. Over the ECC and NWA (SAF) regions, decreasing (increasing) trends of aAOD at the rate of 0.001 and 0.002/ decade (0.001/ decade) were noticed with the MISR (MERRA-2) observations. Nevertheless, the decreasing trend over the ECC region is confirmed with the ground-based (**Figure 5.1e**) and reanalysis (**Figure 5.1f**) datasets in this study. Also, in a recent study by Ramachandran and Rupakheti (2021), showed a similar decreasing aAOD trend from AERONET observations over Kanpur and ECC region.

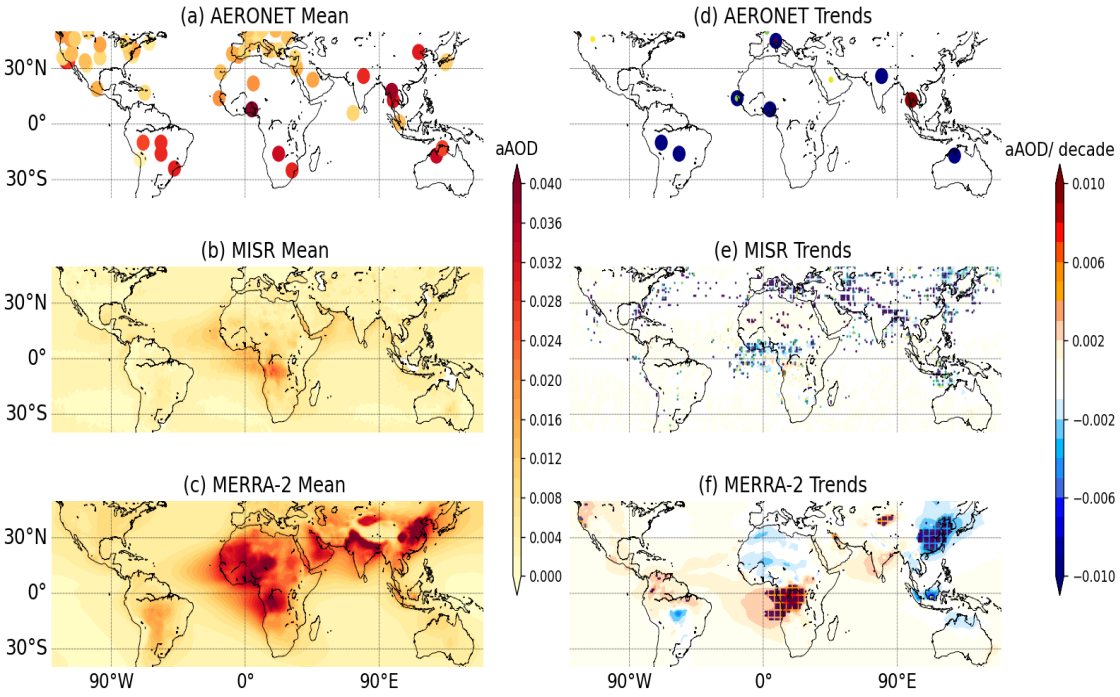

Figure 5.1 *Spatial distribution of the (a, b, and c) annual mean climatology and (d, e, and f) corresponding long-term LR trends, of aAOD obtained from the AERONET, MISR, and MERRA-2 observations, between the year 2001 and 2020, respectively. Stippling regions over the trend values represent the statistically significant values with a 95 % confidence level. For efficient comparison purposes, all the datasets shown in the figure have been interpolated to a common 1° × 1° grid resolution.*

(iii) The spatial distribution of annual mean sAOD and corresponding trends were found (**Figure 5.2**) to exhibit a similar pattern as that of aAOD (shown in **Figure 5.1**). However, higher annual mean sAOD contributions (~85.72 %) to that of the total AOD was found across the globe compared to the contribution of aAOD (~14.28 %) in the total AOD, when measured with the AERONET observations. We found higher mean sAOD values over the NWA, ME, IGP, and ECC regions using AERONET observations (**Figure 5.2a**). On a spatial scale, a higher annual mean sAOD contribution was observed over SAF, IGP, and its adjoining seas regions using the MISR and MERRA-2 observations (**Figure 5.2b and c**). At the same time, one can notice statistically significant increasing (decreasing) trends over India (NEA, SAM, EU, and ECC) with all the observations (**Figure 5.2d-f**) utilized here. These results are in good agreement with the observations from the AERONET datasets, as reported by Ramachandran and Rupakheti, 2021, over the South Asia regions extending from 2000

to 2020. However, the MERRA-2 observations have also reported increasing trends over the SAF region (Figure 5.2f) at the rate of 0.029/ decade.

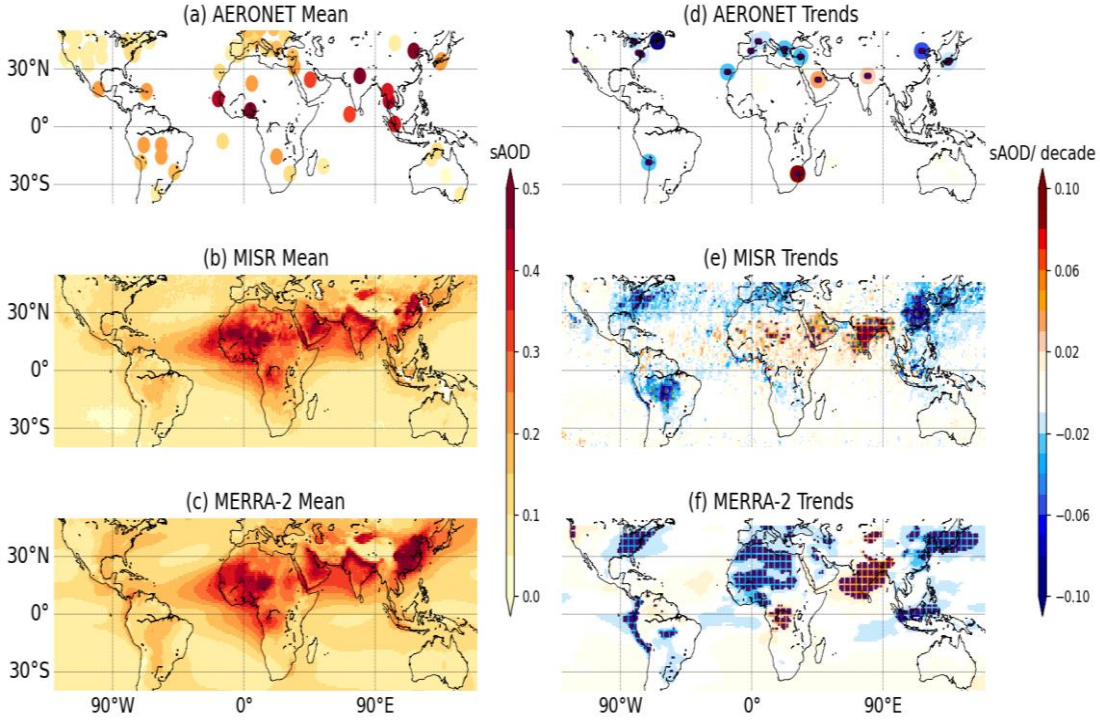

Figure 5.2 *Spatial analysis of the (a, b, and c) annual mean climatology and (d, e, and f) corresponding long-term trends, of sAOD obtained from the AERONET, MISR, and MERRA-2 observations between the year 2001 and 2020, respectively. All the further details are the same as in* ***Figure 5.1****.*

(iv) Over the ME region, comparatively low sAOD mean values were noticed in the AERONET (**Figure 5.2a**) to the MISR and MERRA-2 (**Figure 5.2b and c**) observations. Interestingly, in **Figure 4.6**, the ME region has encountered a contradiction in the increasing (decreasing) trends using the AERONET, MISR, and MODIS (CALIOP, and MERRA-2) datasets. Considering this, we found simultaneously increasing sAOD trends in the AERONET at 0.035/ decade and MISR at 0.031/ decade (**Figure 5.2d and e**) while a decreasing trend is observed in the MERRA-2 dataset (**Figure 5.2f**) over NWA (at 0.027/ decade) and ME at (0.021/ decade) regions. From this, we can state that there might be a possibility of the influence of the difference in retrieval techniques used to derive the sAOD values in AERONET and MERRA-2 datasets over these regions.

5.2.2 Trends in the Aerosols Size-dependent Properties

Aerosol size distribution, which is an indicator of the aerosol physical characteristics possessing different diameters (see **section 2.2**), can impact many aspects of the atmosphere, such as climate, visibility, rainfall, and human health as well. Hence, the fine-mode (coarse-mode) AOD is a suitable index for the measurement of columnar-integrated anthropogenic (natural) pollutants (Kaufman et al., 2001). Therefore, analysis of the annual mean and its corresponding trends in the fAOD (**Figure 5.3**) and cAOD (**Figure 5.4**) aerosols using AERONET (see **Table 2.3**), MODIS (see **Table 2.4**), and MISR (see **Table 2.5**) observations, where the dataset extends from 2001 to 2020, is discussed extensively in this sub-section. Although the size classifications for all the techniques considered here are different but according to Kahn and Gaitley, (2015), the small-mode (medium-mode and large-mode) aerosols obtained from the MISR observations can be considered as an equivalent to the fine-mode (coarse-mode) aerosols. Hence the latter case (i.e., fine/coarse-mode AOD or fAOD/ cAOD) will be considered as the standard criteria to denote the different size aerosols in the following sub-sections, so as to avoid any further confusion. Before the discussion, note that the fAOD and cAOD values retrieved from MODIS (**Figures 5.3b and 5.4b**) are twice in magnitude than the corresponding values obtained from AERONET (**Figures 5.3a and 5.4a**) and MISR (**Figures 5.3c and 5.4c**) observations. Major findings drawn from these observations are given as below:

(i) The spatial distribution of annual mean and trends of fAOD using ground-based (AERONET) and space-borne (MODIS and MISR) datasets show (**Figure 5.3**) a higher annual mean contribution of fAOD over SAM, NWA, EU, IGP, and ECC regions with AERONET measurements (**Figure 5.3a**), in comparison to the rest of the regions globally. These results are in accordance with the previously reported observations by Yan et al. (2021) using the AERONET database from 2008 to 2017, but with the exception of higher fAOD values over the NWA region as obtained in this study. This may be possible because of the differences in the time period of the datasets considered in both studies. Although the ground-based measurements are in good agreement with the space-borne observations, its global coverage has shown higher mean fAOD values over the SAF region from both the MODIS (**Figure 5.3b**) and MISR (**Figure 5.3c**) measurements as well. Also, higher values of fAOD were noticed over ME (NEA) using MISR (MODIS) observations.

(ii) The effects of long-term bearings of fAOD from the AERONET observations (**Figure 5.3d**) have shown significantly overall decreasing (increasing) trends over NEA at 0.036/ decade, SAM at 0.024/ decade, and EU at 0.014/ decade (IGP at 0.039/ decade) regions. Decreasing trends were noticed despite the higher mean fAOD values over the ECC region. However, the increasing trends in fAOD over the IGP region, when measured with the AERONET observations, are in good agreement with the previously reported trends (Kumar et al., 2022). Even the trends obtained from the FMF values using AERONET observations in Yan et al. (2021) are matching well with the trends found in this study.

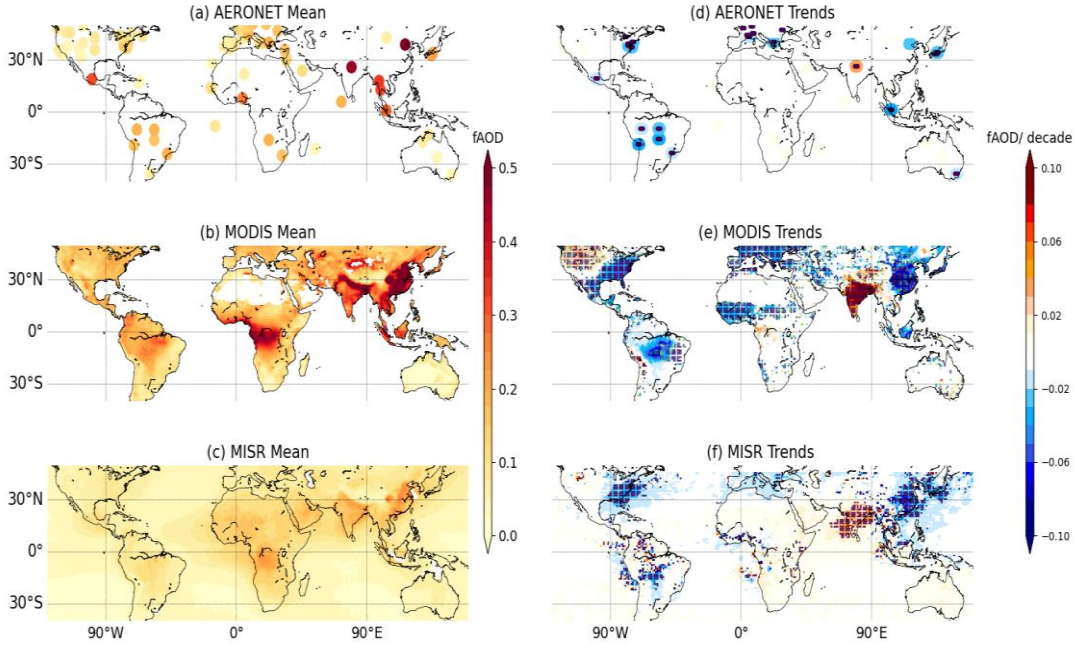

Figure 5.3 *Spatial distribution of the (a, b, and c) annual mean climatology and (d, e, and f) corresponding long-term trends, of fAOD obtained from the AERONET, MODIS, and MISR observations between the years 2001 and 2020, respectively. All the further details are the same as in* ***Figure 5.1****.*

(iii) Similar to the AERONET based trends of fAOD, MISR observations (**Figure 5.3f**) have shown statistically significant increasing (decreasing) trends over the whole India (NEA at 0.023/ decade, SAM at 0.042/ decade, EU at 0.021/ decade, and ECC at 0.029/ decade). These trends are consistent with those evaluated using the MISR dataset by Zhao et al. (2017) as well. Here, an exception was noticed over the NWA region where the significantly decreasing trends at 0.023/ decade was observed (which is in contradiction to that reported in Yan et al. (2021) with the MODIS observations). Interestingly, a slight significant decreasing trend of fAOD was noticed

over the North-Western region of India in the MODIS dataset (**Figure 5.3e**), which can be attributed to one of the reasons (besides increase in precipitation and vegetation) behind the decreasing total AOD trends over the region, as reported in Ratnam et al. (2021).

(iv) The global distribution of annual mean cAOD and trends estimated from the ground-based AERONET and space-borne (MISR and MODIS) datasets show (**Figure 5.4**) a similar pattern as that of fAOD (**Figure 5.3**). The annual mean contribution of the cAOD (to the total AOD) is equivalent (magnitude-wise) to the contribution of the fAOD (**Figure 5.4a-c**). Higher mean cAOD values were found over NWA, ME, and IGP regions from the ground-based AERONET observations (**Figure 5.4a**). In comparison to the AERONET based mean cAOD values (**Figure 5.4a**), corresponding MISR observations are higher and spatially consistent, which is prominent over the NWA (and its adjoining ocean), ME, India (specifically IGP), and AS regions (**Figure 5.4c**). The mean aerosol loading of cAOD observed from the MODIS observations (**Figure 5.4b**) also exhibits similar spatial features as that of the MISR observations (**Figure 5.5c**).

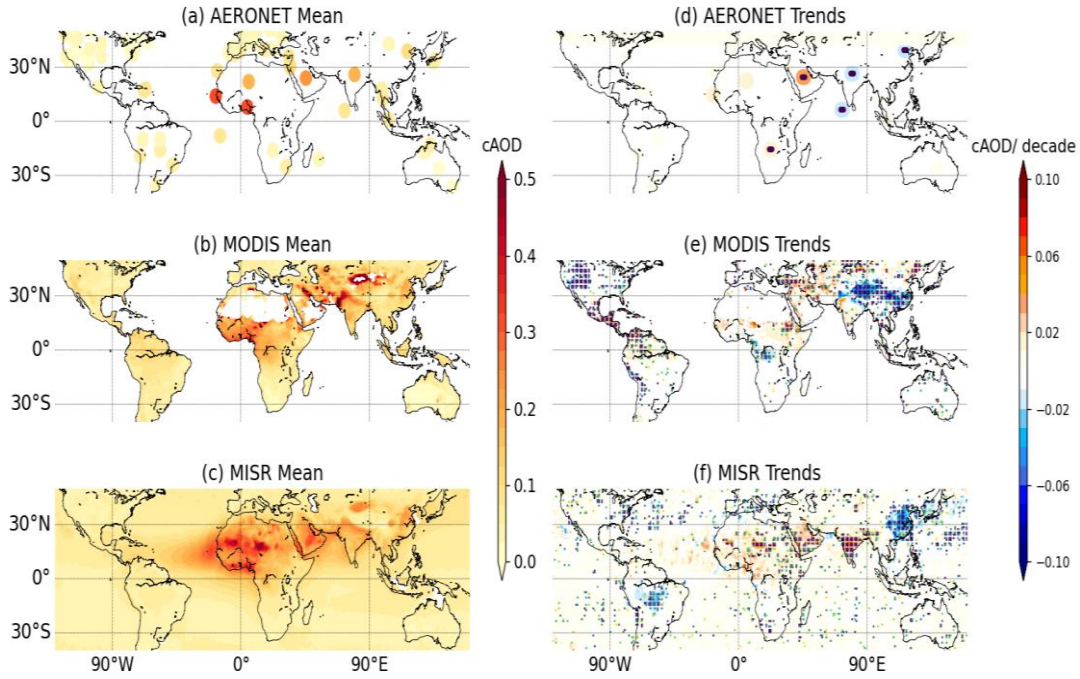

Figure 5.4 *Same as* ***Figure 5.3*** *but for cAOD.*

(v) However, the decreasing (increasing) cAOD trends were observed over IGP at 0.013/ decade, AS at 0.01/ decade, and ECC at 0.011/ decade (ME at 0.031/ decade), using the AERONET observations (**Figure 5.4d**). Here, a slightly decreasing trend in

cAOD, noticed over the IGP region, is in accordance with Kumar et al. (2022). A similar decreasing trend in cAOD was also noticed from the MODIS observations (**Figure 5.4e**) over the IGP (at 0.02/ decade) and NEA (at 0.01/ decade) regions. In contradiction to the decreasing trends observed over IGP and AS regions with AERONET and MODIS datasets, the MISR measurements have shown increasing trends due to cAOD over these regions. Apart from this, significant decreasing (increasing) trends in cAOD were observed over ECC at 0.02/ decade (NWA at 0.03/ decade) region using MODIS observations (**Figure 5.4e**), which is similar to that observed using MISR observations (**Figure 5.4f**). In MISR observations, one can spot that no other statistically significant trends were observed for cAOD (**Figure 5.4e**) but according to **Table 5.1**, decreasing (increasing) numerical cAOD values can be seen over NEA at 0.009/ decade, ECC at 0.023/ decade, AS at 0.013/ decade, and SAF at 0.018/ decade (NWA at 0.025/ decade, ME at 0.029/ decade BoB at 0.01/ decade, and SI at 0.031/ decade).

5.2.3 Trends in the Aerosols Shape-dependent Properties

The accurate determination of aerosols shape is a crucial issue as it has a significant impact on the realistic ARI measurements by both spherical as well as non-spherical aerosols. Hence, this sub-section discusses the analysis of the aerosols shape-dependent properties derived from the different approaches such as MISR (see **Table 2.5**) and CALIOP (see **Figure 2.8b**). The variations in the columnar nAOD retrieved from the MISR observations (**Figure 5.5**) and vertical distribution of β_{aer} retrieved from the CALIOP observations (**Figures 5.6 and 5.7**) are discussed, over all the 8 RoI. Major findings drawn from these observations are as follows:

(i) From the spatial distribution of annual mean nAOD (**Figure 5.5a**), we found that there exists higher annual mean loading over the NWA (and its adjoining ocean), ME, AS, and IGP regions than the rest of the globe. These annual mean observations for nAOD are in good agreement with Garay et al. (2020), where the MISR dataset with the latest version, V23, has been used spatially. Along with this, the statistically significant increasing (decreasing) nAOD trend values were observed over NWA at 0.02/ decade (SAM at 0.01/ decade and ECC at 0.01/ decade), as shown in **Figure 5.5b**. The decreasing nAOD trend values reported over the ECC region agree with the trends reported in Zhao et al. (2017), using the MISR dataset from 2001 to 2015.

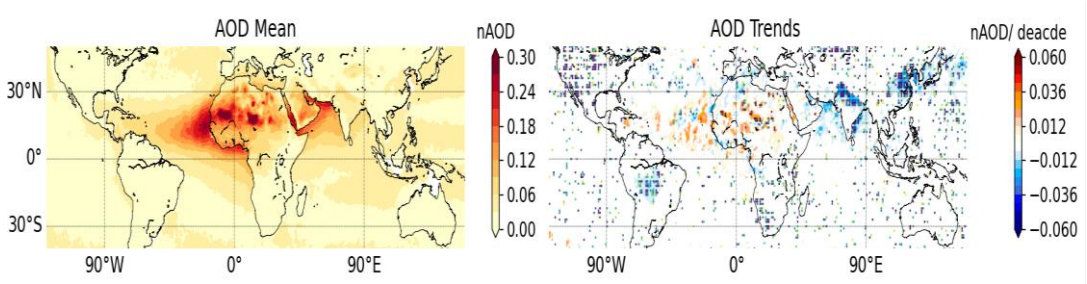

Figure 5.5 *Spatial distribution of the (a) climatology and (b) corresponding nAOD long-term LR trends, obtained from the space-borne MISR observations from 2001 to 2020. All the further details are the same as in* ***Figure 5.1****.*

Also, we could see similar decreasing trends of nAOD over the whole Indian region (IGP at 0.02/ decade, CI at 0.01/ decade, SI at 0.02/ decade, AS at 0.01/ decade, and BoB at 0.01/ decade) as well.

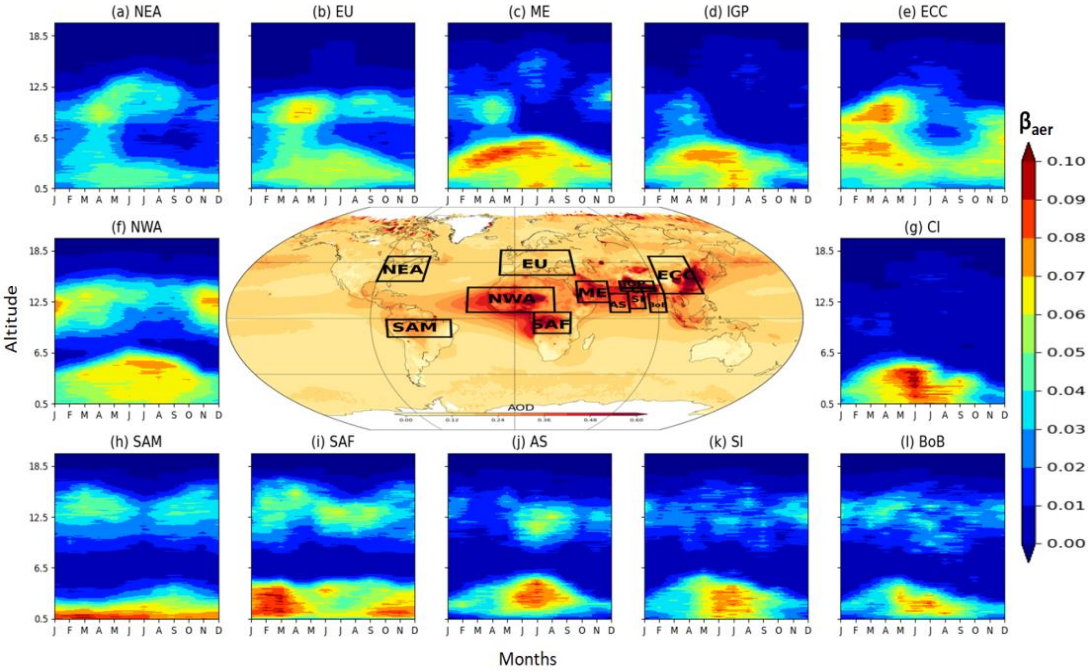

Figure 5.6 *Region-wise seasonal mean contour plots of the vertically resolved β_{aer} values from CALIOP sensor at 532 nm wavelength from the year 2007 to 2020. The black boxes (plotted on the MODIS AOD in the middle figure) represents the selected regions of interest including (a) NEA, (b) EU, (c) ME, (d) IGP, (e) ECC, (f) NWA, (g) CI, (h) SAM, (i) SAF, (j) AS, (k) SI, and (l) BoB region.*

(ii) The vertical distribution of β_{aer} from the CALIOP datasets exhibited maximum magnitudes below 8 km in all the regions, as seen in the climatology part of **Figure 5.6**. Interestingly, in the lower troposphere (below 8 km), specifically during the monsoon (only) season, i.e., June, July, August, and September, there exists high

β_{aer} (> 0.1) mean values over AS (**Figure 5.6j**), BoB (**Figure 5.6l**), CI (**Figure 5.6g**), IGP (**Figure 5.6d**), and SI (**Figure 5.6k**) regions, which cover the entire Indian region, indicating the presence of non-spherical particles. Few studies in the past have reported that background dynamics also plays a crucial role in the transport of particles through LLJ persisting during the monsoon season over the Indian region (Gupta et al., 2021; Prasad et al., 2019; Ratnam et al., 2018), at these altitudes.

(iii) Over the ME (**Figure 5.6c**), EU (**Figure 5.6b**), and NWA (**Figure 5.6f**) regions, the high β_{aer} mean values persisted irrespective of the season. Similar higher values of β_{aer} were also noticed over the ECC (**Figure 5.6e**) and SAF (**Figure 5.6i**) regions throughout the year except in the monsoon season. Lower mean β_{aer} values exist specifically over the NEA (**Figure 5.6a**) and SAM (**Figure 5.6h**) regions, indicating the presence of spherical particles over the region.

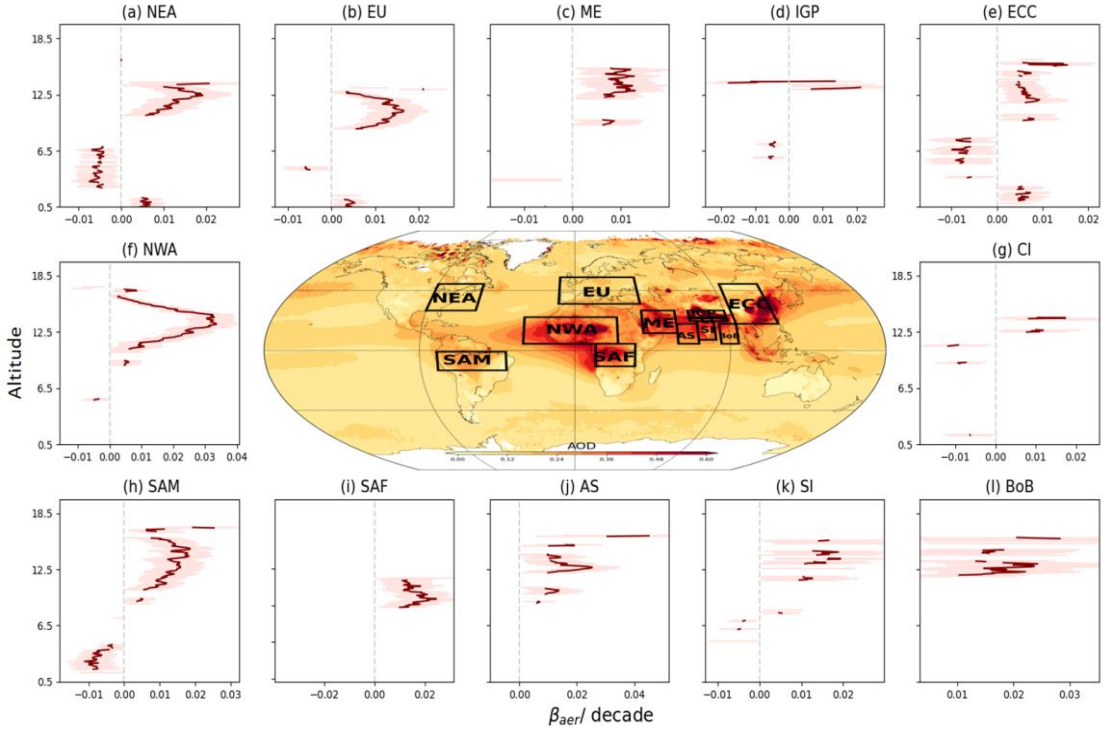

Figure 5.7 *Region-wise MLR trend analysis of the vertically resolved β_{aer} values from the CALIOP sensor at 532 nm wavelength from 2007 to 2020. Only statistically significant trend values are expressed here with the error bars. All the further details are the same as in* ***Figure 5.6****.*

(iv) The trends associated with the vertical distribution of β_{aer} revealed decreasing values between 2 to 7 km over the NEA (**Figure 5.7a**), EU (**Figure 5.7b**), and ECC (**Figure 5.7e**) regions, while increasing trends are found at all other altitudes. The same is the case with SAM (**Figure 5.7h**) region as well but decreasing β_{aer} trends

were observed below 5 km and increasing otherwise. However, over the NWA (**Figure 5.7f**), ME (**Figure 5.7c**), and SAF (**Figure 5.7i**) regions, we found increasing trends in β_{aer} values at higher altitudes.

(v) Over the Indian region, the vertical distribution of β_{aer} revealed the presence of non-spherical aerosols during the monsoon season (specifically) below 7 km (as mentioned above) and exhibited a significantly decreasing trend (**Figure 5.7d,g,k**) at these altitude range. Whereas, at altitudes above 7 km, significantly increasing trends in the vertical distribution of β_{aer} was found over the IGP, CI, SI, AS, and BoB regions (**Figure 5.7d,g,j,k,l**), with the exception of decreasing trend between 7 to 12 km over the CI region (**Figure 5.7g**).

Regions	AERONET trends (/ decade)min.,max.	MODIS trends (/decade) min.,max.	MISR trends (/decade) min.,max.	MERRA-2 trends (/ decade) min.,max.
(a). NEA				
Total AOD	-0.034, -0.018, -0.034	-0.07, -0.02, -0.05	-0.061, -0.02,-0.028	-0.042, -0.02,-0.022
aAOD	-	-	-	-
sAOD	-0.095, -0.014, -0.095	-	-0.058, -0.03,-0.032	-0.042, -0.02,-0.023
fAOD	-0.036, -0.011, -0.036	-0.07, -0.02, -0.05	-0.04, 0.043,-0.023	-
cAOD	-	-0.01, -0.01, -0.01	-0.038, 0.01,-0.009	-
nAOD	-	-	-	-
(b). SAM				
Total AOD	-0.03, -0.017, -0.03	-0.11, -0.01,-0.02	-0.096, 0.098,-0.067	-0.078, 0.023,-0.023
aAOD	-	-	-	-
sAOD	-	-	-0.11, 0.044,-0.068	-0.079, -0.02,-0.031
fAOD	-0.024, -0.014, -0.024	-0.09, 0.03,-0.02	-0.099, 0.096,-0.042	-
cAOD	-	-0.05, 0.05,0.01	-0.036, 0.02,-0.026	-
nAOD	-	-	- 0.01, 0.01,-0.01	-
(c). EU				
Total AOD	-0.06, -0.01, -0.06	-0.08, 0.02,-0.03	-0.058, -0.02,-0.025	-0.038, -0.02,-0.021
aAOD	-	-	-0.002, -0.001,-0.001	-
sAOD	-0.059, 0.085, -0.059	-	-0.052, -0.03,-0.031	-0.036, -0.02,-0.021
fAOD	-0.039, -0.011, -0.014	-0.08, -0.01,-0.03	-0.027, -0.02,-0.021	-
cAOD	-	-0.01, 0.04,0.01	-	-
nAOD	-	-	-	-
(d). ECC				
Total AOD	-	-0.3, 0.04,-0.11	-0.1, 0.092,-0.028	-0.046, 0.063,-0.021
aAOD	-	-	-0.002, 0.001,-0.001	-0.007, -0.003,-0.0
sAOD	-0.055, -0.055, -0.055	-	-0.14, 0.049,-0.068	-0.04, 0.062,-0.023
fAOD	-	-0.2, 0.04, -0.07	-0.098, 0.09,-0.029	-
cAOD	-0.011, -0.011, -0.011	-0.1, 0.05,-0.02	-0.074, 0.026,-0.023	-
nAOD	-	-	-0.02, 0.01,-0.01	-
(e). NWA				
Total AOD	-0.04, -0.04, -0.04	-0.14, 0.07,-0.04	-0.1, 0.09,0.037	-0.048, -0.02,-0.029
aAOD	-	-	-0.002, 0.002,-0.002	-
sAOD	-	-	-0.069, 0.079,0.031	-0.045, -0.02,-0.027
fAOD	-	-0.07, 0.01,-0.03	-0.096, 0.066,-0.023	-
cAOD	-	-0.05, 0.08,0.03	-0.032, 0.073,0.025	-
nAOD	-	-	-0.01, 0.02,0.02	-
(f). ME				
Total AOD	0.035, 0.035, 0.035	-0.017, 0.23,0.03	-0.03, 0.053,0.029	-0.026, 0.023,-0.022
aAOD	-	-	-	-
sAOD	0.035, 0.035, 0.035	-	0.03, 0.068,0.031	-0.024, -0.022,-0.021
fAOD	-	-0.07, 0.04,-0.03	-	-
cAOD	0.031, 0.031, 0.031	0.01, 0.08,0.02	0.008, 0.052,0.029	-
nAOD	-	-	-	-
(g). SAF				
Total AOD	-	-0.02, 0.03,-0.02	-0.09, 0.081,0.024	-0.026, 0.059,0.024
aAOD	-	-	-0.003, 0.003,-0.002	0.003, 0.011,0.001
sAOD	-	-	-	-0.023, 0.048,0.029

fAOD	-	-	-	-
cAOD	-	-0.04, 0.02,-0.02	-0.041, 0.045,-0.018	-
nAOD	-	-	-	-
(h). IGP				
Total AOD	0.018, 0.018, 0.018	-0.06, 0.16,0.06	-0.036, 0.094,0.036	0.02, 0.055,0.028
aAOD	-	-	-0.002, -0.001,-0.001	-
sAOD	0.028, 0.028, 0.028	-	0.03, 0.078,0.038	0.021, 0.054,0.024
fAOD	0.039, 0.039, 0.039	0.02, 0.19,0.04	-0.024, 0.066,0.029	-
cAOD	-0.013, -0.013, -0.013	-0.09, 0.06,-0.02	-0.008, 0.041,0.019	-
nAOD	-	-	-0.03, -0.01,-0.02	-
(i). CI				
Total AOD	-	-0.06, 0.15,0.09	0.022, 0.094,0.031	0.022, 0.057,0.028
aAOD	-	-	-0.002, -0.001,-0.001	-
sAOD	-	-	0.034, 0.074,0.046	0.021, 0.056,0.03
fAOD	-	-0.02, 0.19,0.08	0.021, 0.097,0.029	-
cAOD	-	-0.03, 0.06,-0.02	0.013, 0.032,0.026	-
nAOD	-	-	-0.02, -0.01,-0.01	-
(j). SI				
Total AOD	-	0.02, 0.15,0.06	-0.028, 0.099,0.042	0.021, 0.056,0.043
aAOD	-	-	-	-
sAOD	-	-	0.031, 0.1,0.049	0.02, 0.054,0.043
fAOD	-	0.02, 0.14,0.08	0.02, 0.072,0.032	-
cAOD	-	-0.02, 0.03,0.02	-0.015, 0.047,0.031	-
nAOD	-	-	-0.01, -0.01,-0.02	-
(k). AS				
Total AOD	-	-	-0.043, 0.065,0.027	0.02, 0.045,0.022
aAOD	-	-	-	-
sAOD	-	-	0.03, 0.057,0.038	0.02, 0.043,0.021
fAOD	-	-	0.02, 0.043,0.022	-
cAOD	- 0.01, -0.01, -0.01	-	0.012, 0.018,0.013	-
nAOD	-	-	-0.01, -0.01,-0.01	-
(l). BoB				
Total AOD	-	-0.05, 0.014,-0.05	-0.1, 0.089,0.036	0.02, 0.056,0.021
aAOD	-	-	-	-
sAOD	-	-	0.031, 0.076,0.034	0.02, 0.054,0.021
fAOD	-	0.02, 0.15,0.02	-0.089, -0.058,0.027	-
cAOD	-	0.02, 0.02,0.02	0.01, 0.018,0.01	-
nAOD	-	-	-0.01, -0.01,-0.01	-

Table 5.1 *Region-wise range (minimum to maximum) and mode of the statistically significant trend values (/ decade) for various aerosol properties (including aAOD, sAOD, fAOD, cAOD, and nAOD) obtained over 8 RoIs using AERONET, MODIS, MISR, and MERRA-2 observations, used in the study.*

5.3 Discussion and Inferences

In order to have an insight on the varying aerosol loading in the atmosphere, we tried to examine this feature in terms of region-wise long-term bearings (2001-2020) of the aerosols optical, physical, and morphological properties using multi-source datasets, as discussed briefly in the previous sections. We have analysed the aerosol properties only over those selected regions which are having significant trend values in the total AOD parameter. To be more specific, the regions showcasing significantly increasing trends in total AOD include SAF, ME, IGP, CI, SI, AS, and BoB, and those with significantly decreasing trends include NEA, SAM, EU, NWA, and ECC, as shown in **Figure 4.6**. However, these numerical values may differ from sensor to sensor to the overall trends as it can be biased towards the maximum or minimum values

prevailing over the region. With a view to associate the trends in the total AOD with changing optical, physical, and morphological characteristics of prevalent aerosols, we have examined the climatologically mean and trends of these aerosol properties in each of the selected RoIs (in the previous **section 5.2**). Here, we summarize the major findings for each region by linking the estimated trends in total AOD with those obtained for different aerosol optical, physical, and morphological properties.

(a) NEA: Beginning with the overall decreasing total AOD trend values over the NEA region, we find that here the major decrease is in synergy with the decrease in the secondary (i.e., fine-mode and scattering) aerosols. Further, an increase in the β_{aer} values at some altitudes and decrease in coarse-mode aerosols is also observed. The reason behind the decrease in its total AOD trend values can be attributed to the implementation of the CAA Amendments in the 1990s in the American region (Hand et al., 2012; Zhao et al., 2017). Altogether, approximately 85% of the contributions from anthropogenic aerosols consists of SF, particulate organic matter (POM), and BC aerosols to the total AOD values (Hand et al., 2014; Provençal et al., 2017). However, in Hand et al. (2012), they have clearly mentioned that the SF aerosols (which are fine-mode and scattering in nature) were decreasing at the rate of -2.7% per year. The results obtained over this region found a prominent decrease mainly due to the fine-mode and secondary aerosols.

(b) SAM: Decreasing trends in the total AOD was observed due to decrease in the fAOD, sAOD, β_{aer} and nAOD, over this region. The majority of the aerosols here comprises of SF and POM, which can arise due to the deforestation or BB activities taking place in the Amazon rainforests (Sena et al., 2013). At the same time, there are reports of decreasing AOD trends due to the reduction in deforestation fires since 2004, as mentioned in Reddington et al. (2015). Considering the decrease in total AOD, this study has found statistically significant decreasing trend values in the secondary and non-spherical aerosols over the SAM region.

(c) EU: EU also falls under one of the regions having decreasing trend in total AOD, which can be associated with the decrease in the fine-mode, absorbing, and scattering aerosols in the columnar loading. In contrast, an increasing trend in the β_{aer} values at some altitudes was found over this region. However, the EU region is a heavily industrialized continent where major contributions are from the SF (approximately 50%) aerosols and is also highly impacted by the advection of DU

(approximately 30%) aerosols from the Sahara Desert region as well (Pey et al., 2013; Tørseth et al., 2012). With the implementation of stringent regulation policies, a considerable reduction in anthropogenic pollutants was noticed over the region, notably POM and SF aerosol (Tørseth et al., 2012). In connection to this, the above discussion has shown major significant decreasing trends in the secondary aerosols and a slight reduction in the absorbing aerosols as well, over the region.

(d) ECC: Despite having high mean aerosol loading for the past two decades, we found a decreasing trend in the total AOD over this region, where the decrease in the trends of fine-mode, coarse-mode, absorbing, scattering, and non-spherical aerosols are noticed. In contrast, an increasing trend in the β_{aer} values was found over a few altitude ranges. Correspondingly, China is considered to be one of the most populated countries, having the most significant emissions from SF, OC, and BC aerosol (Klimont et al., 2013). The 11th (2006-2010) and 12th (2011-2015) five-year plan control policies and the Air Pollution Prevention and Control Action Plan (2013-2017) have been implemented over the China region after which a huge reduction has been noticed, from this study.

(e) NWA: Similar is the case with the NWA region as well, where we could perceive decreasing trends in the total AOD in the high aerosol loading region, mainly from the fine-mode and absorbing aerosols. The reason behind this decrease can be the stilling of surface winds or an increase in precipitation efficiencies along with anomalous cyclonic circulation over the NWA region (Ridley et al., 2014). However, in addition to this, we have found a significantly slight increase in the coarse-mode, scattering, and non-spherical AOD along with β_{aer} over this region. This could be due to the standout feature of the NWA region, which is the Sahara Desert, from where the DU aerosols are the major contributors to the columnar loading.

(f) ME: A significant variability in the total AOD mean values (from the different sensor measurements) were well reported in Gupta et al. (2022) over the ME region. Even the estimated trend values of different aerosol properties were found to be inconsistent with different sources of datasets in this region (**section 5.2.1iv**). This includes the observation of an increasing trend in the sAOD from the AERONET and MISR measurements, while a decreasing trend was found for the sAOD from the CALIOP and reanalysis (MERRA-2) dataset. As it is quite familiar that the cities here are majorly affected by the presence of DU aerosols, and the highest percentage of aerosols contributing to the total AOD over the region are the coarse-mode and

scattering aerosols only. At the same time, we could not notice any significant trend contribution from the other aerosol properties to the total AOD values over this region.

(g) SAF: An increase was noticed in the total AOD trends over the SAF region. Unlike the NWA region, the SAF is a tropical region characterized by rainforests where the majority of the aerosols originate from human-induced fires from agricultural activities. More than 50% of the global carbon emissions originate from the African region (Van Der Werf et al., 2010), and if this growth rate persists, some reports suggested that there can be a 30% increase in the emission rate by the year 2030 (Ayompe et al., 2020). The cause of which can be associated with the increase in the β_{aer}, absorbing, and scattering AOD over this region, as found in this study. However, a small decrease in the coarse-mode aerosols is also observed over the region. In particular, some previous studies also suggested that this increase can be due to the increase in transport of SS particles, increase in crop residual burnings in dry seasons (NH summer season), and warming-induced changes in its background meteorology (Kumar et al., 2014; Zhao et al., 2019).

(h) India: Over the whole Indian region (land and adjoining seas), the overall increase in the trends of the total AOD is associated with the major increase in the fine-mode and scattering aerosols, unlike over the NEA region. The recent increase in population densities, urbanization, and industrial growth over the Indian region has led to an increase in the consumption of fuel and emissions (which includes major contributions from aerosols such as SF, BC, and OC), since 1990 (Klimont et al., 2013). One can also note that the cities in the northern part of India are majorly affected by the advection of DU aerosols as well (Jin et al., 2021). Moreover, a recent study has reported that there is a decrease in the pre-monsoon dust loading by 10 to 20 % over the South Asia region (Pandey et al., 2017). Also, there have been pieces of evidences of decreasing trends in the BC aerosols (which are absorbing in nature) over the Indian region from the previous studies (Manoj et al., 2019; Ravi Kiran et al., 2019). In this regard, it is worth mentioning here that we have observed a slight decrease in the coarse-mode (IGP and AS), non-spherical (IGP, CI, SI, AS, and BoB), and absorbing (IGP and CI) aerosols over this region. Nevertheless, this subsequent decrease in anthropogenic aerosols can be associated with the implementation of rigorous standards like Deen Dayal Upadhyay Grameen Jyoti Yojana in 2014 (RGGVY, 2014), Bharat Stage II (BS-II), BS III, and BS-IV (IICT Policy Update, 2016), Pradhan Mantri Ujjwala Yojana launched in 2016 (MoPNG, 2016). Here the steps are taken to reduce fuel consumption and industrial

emissions by providing liquefied petroleum gas (LPG), and electricity to villages, so that solid-fuel cooking could be replaced with clean fuels over the Indian region. A recent study by (Chowdhury et al., 2019) has shown a reduction in $PM_{2.5}$ emissions of biomass, water and space heating, and kerosene lightning by 17.5, 11.9, and 1.3 % with the implementation of these policies over the Indian region. But as the decrease in the coarse-mode, absorbing, and non-spherical aerosols is much lower than the increase in the scattering and fine-mode aerosols, hence, this can be the reason behind the overall increase in the total AOD values over the region.

5.4 Summary

In this study, a comprehensive assessment of the long-term mean climatology and its corresponding trends in AOD parameter, due to the various optical (scattering/absorbing), physical (size), as well as morphological (shape) properties of the aerosols, has been made. This has been achieved using the multi-source datasets that includes the ground-based (AERONET), space-borne (MISR, MODIS, CALIOP), and the reanalysis (MERRA-2) measurements, where the dataset spans between 2001 and 2020. Here, the highest mean total aerosol loading was observed over Africa, ME, India, and ECC regions. Subsequently, this study has been designed in a region-wise manner, which includes only those regions having some significant total AOD trend values. We have observed a decrease (increase) in total AOD over the NEA, EU, SAM, NWA, and ECC (SAF and India) regions. The total AOD values can be associated as the combinations of either absorbing or scattering (optical properties), fine or coarse-mode (size-dependent/physical properties), and spherical or non-spherical (shape-dependent/morphological properties) aerosols. Therefore, we have examined the corresponding optical, physical and morphological properties in terms of the annual means and its corresponding long-term trends in this study. The main findings (after combining all the datasets) are summarized in the following based on the different aerosol properties considered in this study:

(i) Aerosols Optical Properties: ARI has indicated that there exists a high contribution of global scattering rather than the absorption aerosols (magnitude wise) in the total columnar extinction (or total AOD). In particular, region-wise, we have noticed the decreasing trends in both the aAOD and sAOD over EU and ECC regions, whereas the NEA and SAM regions have depicted decreasing trend in scattering aerosols alone. It should be noted that these are the same regions that have resulted in a significant decreasing trend in the total AOD as well. The ME and NWA regions have

exhibited contrasting trends in the scattering aerosols with different datasets, where AERONET and MISR (MERRA-2) derived sAOD values have shown increasing (decreasing) trends. We have spotted increasing trends in both the scattering and absorbing aerosols over the SAF region, which also reported an increase in its total AOD values. The scattering (absorbing) aerosols have indicated an increasing (decreasing) trend over the whole Indian region (NWA) region. Interestingly, over the IGP and CI regions, we have found decreasing trends in the absorbing aerosols, as deduced from the MISR observations.

(ii) Aerosols Size-dependent Properties: The global distribution of the mean aerosol loading of the fine-mode aerosols is much higher over the Africa, ME, India, and ECC regions than the coarse-mode aerosols. These are the same regions having high mean total columnar aerosol loading as well. However, region-wise, the low domination of the annual mean loading of the fine-mode aerosols over the NEA, SAM, and EU regions exhibits decreasing trends due to these aerosols. Also, the NWA region has observed high mean loading due to both the size aerosols but with decreasing (increasing) trends in the fine-mode (coarse-mode) aerosols over the region. At the same time, over the ECC region, despite the higher annual mean fAOD, and cAOD, this region exhibited decreasing trends owing to both size ranges. The ME (SAF) regions possess increasing (decreasing) trends in the coarse-mode aerosols alone. While on the other hand, the complete Indian (land and its adjoining seas) region has seen an increase in the fine-mode aerosol, which has contributed to its overall increase in the total AOD values. It is also worth mentioning here that IGP and AS regions have encountered a very small decrease in the coarse-mode aerosol as well. Here, the decrease in the total AOD value over the North-Western region of India can be seen in accordance with the decrease in the fine-mode aerosol.

(iii) Aerosols Shape-dependent Properties: Columnar distribution of the non-spherical (i.e., shape) aerosols has suggested the highest mean loading over the NWA and ME regions. However, decreasing (increasing) trends are observed over the SAM, India, and ECC (NWA) regions. Alongside this, we have also measured the vertical distribution of the β_{aer}. Using this parameter, we could notice one common criterion among the NEA, SAM, EU, NWA, and ECC regions (i.e., decreasing trends in total AOD), for which decreasing β_{aer} trends were observed between 2 and 7 km altitudes. However, the decreasing β_{aer} trend values existed below 5 km altitude, over

the SAM region. One can see that the SAF and ME regions have exhibited only increasing trends, and that too in the upper altitudes. Over the Indian region (which has observed an overall increasing trend in total AOD values), we have observed decreasing β_{aer} trends in the lower altitudes (below 7 km) while increasing trends at upper altitudes (above 7 km) for IGP, SI, AS, and BoB regions. However, we have seen a decreasing trend for the CI region until 12 km while increasing otherwise.

This reduction in the combined emissions of the pollutants by 78% since 1970 under the CAA over the United States and also the decrease of SO_2 (NO_X) by 63% (24%) under the Air Pollution Prevention Act over China (Uno et al., 2020) region till the year 2020 is quite encouraging. This has led to a drastic improvement in air quality and has lowered the risks of premature deaths and severe health effects as well. From this, we can anticipate that the developing regions like SEA (with high population density) and the African continents (which exhibited increasing trends in the aerosols) can also call for similar kinds of mitigation strategies. As from this study, we saw that the reason behind the decrease in the total AOD over the developed countries like the NEA region (i.e., due to reduction in its fine-mode and scattering aerosol) is precisely the cause of the overall increasing trend in the total AOD over the developing country like India. Also, aerosols behave differently when quantified in the vertical distribution of the atmosphere, as seen in **section 1.4.1**. For example, in the case of scattering aerosols, they are less efficient when placed above a bright surface, whereas absorbing aerosols are highly efficient when found above the cloud surface. Hence, the net effects of the aerosols are highly uncertain and are highly dependent on their vertical distribution. Thus, **Chapter 6** is intended to examine the chemical trends of aerosol types in the vertical profile of the atmosphere for a better understanding of the climatic response due to the implementation of these reduction strategies.

❁❁❁

Chapter 6

Global distributions of the trend variations in the Aerosols Chemical properties

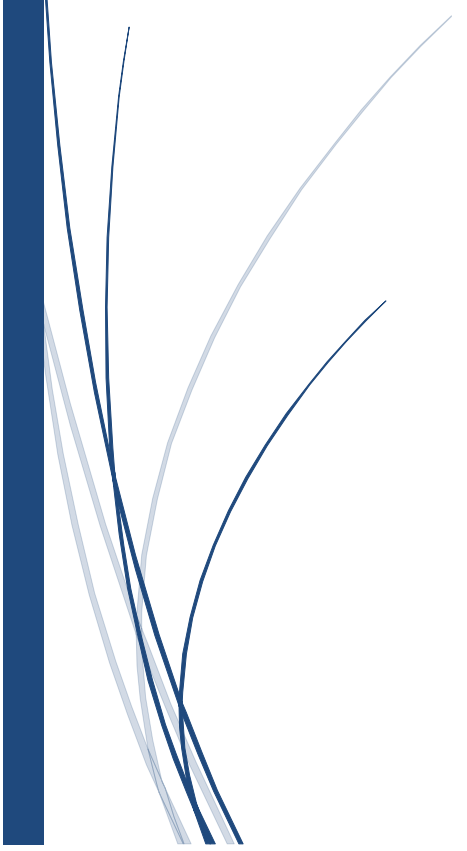

6.1 Introduction

The sources of the aerosols can be divided into either emitted directly into the atmosphere (known as natural or primary aerosols) or via the precursor gases (known as anthropogenic or secondary aerosols), as discussed in detail in **Chapter 1**. These different aerosols will have varying impacts on the atmosphere, ultimately depending on the underlying surface characteristics, population densities, industrial development, and meteorological conditions. For instance, the large values of AODs over the regions such as the northern parts of the African continent are mainly due to the dominance of the DU aerosols (Gavrouzou et al., 2021). Also, due to the increase in anthropogenic aerosols, there can be an increase in the El-Niño events in future, leading to an enhancement in the dust induced rainfall (Nandini et al., 2022). In this regard, a considerable amount of studies exist that have analysed the different chemical compositions in terms of AOD over different regions (Gunthe et al., 2021; Provençal et al., 2017), but their long-term impacts due to each component have not been quantified so far. Therefore, in this study, the region-wise columnar mean climatology and its corresponding AOD trends (using the MLR trend approach) due to the different components of aerosols using the MERRA-2 reanalysis dataset will be discussed in detail in the **section 6.2.1**.

Conventionally, it has been considered that the majority of the atmospheric aerosols are well confined within the ABL altitudes (Dentener et al., 2006, Stull., 2000, Charlson et al., 1992, Satheesh et al., 1999, Reus et al., 2001). At the same time, AOD is the complete vertical integration of the α_{aer} profiles, as detailed in **Chapter 1**. However, in the recent past years, the interest in the aerosols reaching the FT altitudes via convective activities or long-range transport has been widely increased (Jayaraman et al., 1995; Mishra et al., 2010; Niranjan et al., 2007; Prasad et al., 2019; Ratnam et al., 2018; Sarangi et al., 2016; Satheesh et al., 2006; Sinha et al., 2013). The presence of these EALs over a point location in the SI (i.e., Gadanki) region using the combined ground-based MPL and Mie LIDARs has already been observed comprehensively in **Chapter 3**. These kinds of layers are famously known as EALs which can have significant impacts on the climate system, as the residence times of the aerosols at these altitudes are higher (several weeks), and the diabatic heating induced due to absorption by the aerosols is more intense here (Wang et al.,

2013). Apparently, a recent study by Ratnam et al. (2021) has reported an increasing (decreasing) trend at the FT altitudes over the Indian (ECC) region. Also, it is mentioned in **section 3.3.5** and even shown in **Figure 3.8** that the higher aerosol loading in EALs persisting in the lower troposphere have extended from Africa to South Asian continents. So, it is exceedingly important to know the prevailing aerosol types that lead to the formation of these EALs. As the absorbing aerosols present in these EALs can drastically change the thermodynamic structure of the atmosphere (Talukdar et al., 2019; Wang et al., 2013) and can counteract the Twomey cloud brightening effects (Bender et al., 2016) as well. Nevertheless, to have a complete spatial/ or temporal detection with a good vertical resolution, we have to depend on the active remote sensing satellite sensors, such as CALIOP. Although CALIOP has been operational since the year 2006, but only a limited efforts have been made till now to examine the vertical distribution due to the different aerosol types considering the partitioning within different altitudes. Previously, few studies such as Gui et al. (2021); Mehta et al. (2018), have shown global vertical trends (with conventional LR approach) due to the different aerosols but assuming the averaged DT and NT analysis from the CALIOP datasets. Thus, a profound insight into the region-wise mean climatology and trends (using the MLR trend approach) due to the mixture of components of the different aerosols partitioned within different altitudes (i.e., ABL and FT) and timings (i.e., DT and NT) will be discussed in the **section 6.2.2**. Consequently, an immense effort has been made in this study to understand each aspect (columnar and vertical) of the changing aerosols chemical properties across the globe.

6.2 Results

Considering the broad view about the contributions of the different aerosol properties such as optical, physical, and morphological from **Chapter 5**, in this chapter, a detailed analysis has been carried out to further understand the contributions due to the heterogeneous distribution of the chemical properties of the aerosols. For which, this study has relied on the combined available measurement techniques such as satellite (i.e., CALIOP, see **Figure 2.8c**) as well as reanalysis (i.e., MERRA-2, see **Table 2.6**), where each of the retrieved datasets has a unique feature. For instance, MERRA-2 can provide the columnar distribution due to the different aerosol components, including SS, DU, SF, OC, and BC. Similarly, CALIOP can

provide the complete vertical distribution due to a mixture of various aerosol components such as PD, ES, and DU. One can see that the common link between the two datasets is the measurements of the DU aerosols, which remain essential to measure due to their massive abundance on the Earth (covering nearly one-third of the land surfaces) and the varying physical and chemical processes taking place due to the same. Therefore, this section will examine the mean climatology and trends (using the MLR trend approach, see **section 2.4**) due to the different aerosols chemical properties using both the independent measurement techniques over the 8 RoI (highlighted in **Table 4.2**).

6.2.1 Columnar distribution of Aerosols Chemical Properties

The mean columnar distribution of aerosols is highly inhomogeneous due to the significant spatial and temporal variations from local to regional to global scales (as already seen in the previous **Chapters 4 and 5**). Also, from **Figure 6.1a** here, high values due to total AOD are obtained over the Asia and tropical Africa regions than in the rest of the globe, when measured using the MERRA-2 dataset (which has observed a high correlation with the ground-based AERONET observations, as shown in **Figure 4.1q**). However, it is also quite evident from **Figure 6.2a** that statistically significant increasing (decreasing) trends prevailed over the Indian (NEA, EU, SAM, NWA, ECC, and ME) region using the same dataset. This global 2D representation of the total aerosol loadings (**Figure 6.1a**) is finally an outcome of the natural and anthropogenic aerosol emissions in the atmosphere. Therefore, the aerosol components contributing to the total AOD will be examined here in connection to the previous **section 5.3,** where the reason behind the increase/ decrease in the discrete aerosol properties has already been discussed in detail. In this regard, the long-term (2001-2020) average of the mean AOD (**Figure 6.1**) and their corresponding statistically significant trends (**Figure 6.2**) due to each aerosol component are very well captured using the MERRA-2 dataset. Their subsequently derived numerical values for the region-wise mean and trends (only significant) are provided in **Figure 6.3**. Further, in order to explore the contributions of each of the aerosol components and their evolutionary trends to the total AOD values, this section investigates in detail the region-wise aerosol properties as follows:

(i) Comparatively lower annual mean total AOD values are observed over the **NEA** region in **Figure 6.1a**, where the maximum contributions have been noticed due

to the SF aerosols of about 49 % from **Figure 6.3a**. The latest model used in the MERRA-2 has considered SF aerosols as the emissions from the DMS, sulfur dioxide (SO_2) from BB, and volcanic injection into the atmosphere (Buchard et al., 2017). The overall decrease in the total AOD trends (**Figure 6.2a**) is due to the decreasing SF aerosols (**Figure 6.2e**) with a significant contribution. These results are in conferment with (Aas et al., 2019; Hand et al., 2014; Provençal et al., 2017) and the discussions made in **section 5.3a** as well, where the significant decrease was seen due to the decrease in the fine-mode and scattering aerosols. Nevertheless, in addition to this, **section 4.3.4.1** has shown a significantly increasing trend over the Western region of North America, which here can be attributed to the increase due to OC aerosols over the region, as shown in **Figure 6.2b**.

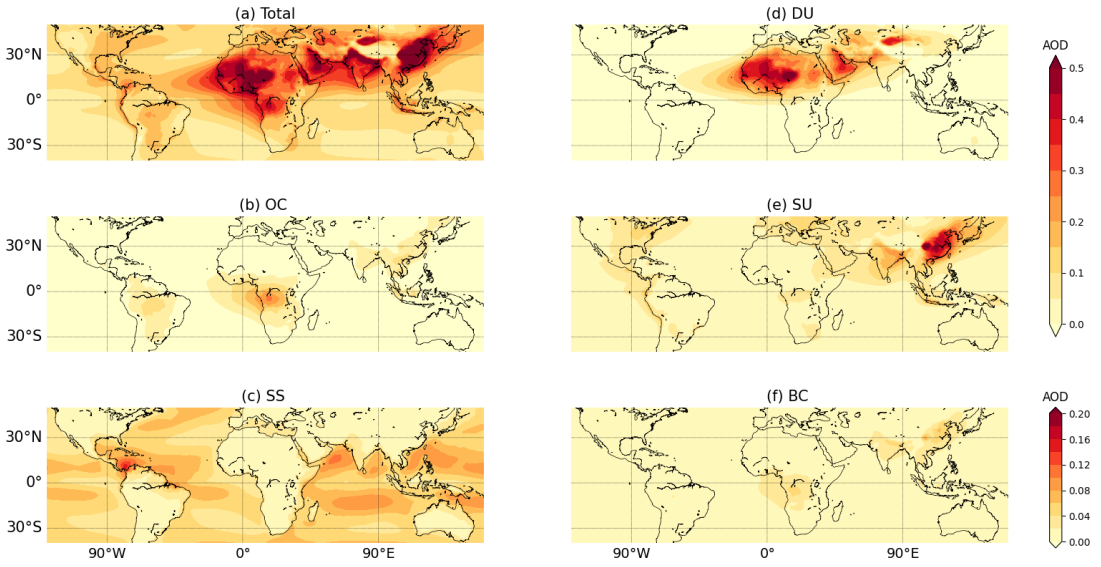

Figure 6.1 *Spatial distribution of the annual mean (a) Total, (b) OC, (c) SS, (d) DU, (e) SF, and (f) BC AOD climatology obtained from the MERRA-2 observations, between 2001 and 2020. The datasets shown in the figure have been interpolated to a typical 1° × 1° grid resolution.*

(ii) Over the **SAM** region, a low mean AOD loading persists with the maximum values up to 0.27 (**Figure 6.1a**) and having significant contributions of approximately 45% from the OC (**Figure 6.3a**) and 25% from the SF (**Figure 6.1e**) aerosols. Correspondingly, here the decrease in the total AOD trends (**Figure 6.2a**) has been seen following the decrease in the SS, SF, and BC aerosols (**Figure 6.2c,e, and f**). This decrease in the SF and SS aerosols is as per the decrease in the secondary and non-spherical aerosols, as found in **section 5.3b**. Also, the summary statistics in

Figure 6.2b has shown a range of decreasing (over central Brazil) to increasing (over north Brazil) OC AOD trend values over the SAM region.

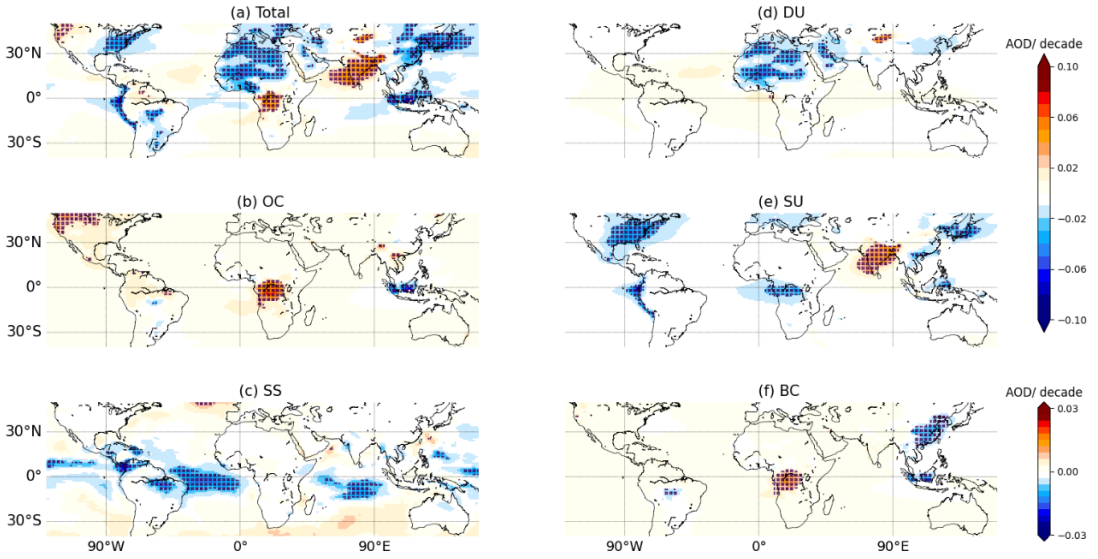

Figure 6.2. *Spatial distribution of (a) Total, (b) OC, (c) SS, (d) DU, (e) SF, and (f) BC AOD long-term MLR trends obtained after removing the long-term periodic oscillations (i.e., QBO, ENSO, and SC) from the MERRA-2 observations, between 2001 and 2020. Stippling regions over the trend values represent the statistically significant values with a 95 % confidence level. The datasets shown in the figure have been interpolated to a typical 1° × 1° grid resolution.*

(iii) EU also falls under the regions having low annual total AOD (**Figure 6.1a**) loading (maximum ranges up to 0.24 in **Figure 6.1a**) with the significant contributions of nearly 47% from the SF aerosols alone (**Figure 6.3a**). Simultaneously, a significant decrease in the total AOD values was also spotted here, as shown in **Figure 6.2a**, where this decrease is in conferment with the decrease due to the DU (**Figure 6.2d**) and SF (**Figure 6.2e**) aerosols. The previous studies (Aas et al., 2019; Pey et al., 2013; Tørseth et al., 2012) and **section 5.3c** have also marked the decrease due to secondary aerosols over the region. However, in addition to this, an increase due to SS aerosols is also observed (**Figure 6.3b**) and agrees with the increase in the β_{aer} values over the region from **section 5.3c**.

(**iv**) **ECC** comes under one of those regions having high total aerosol loading, with the maximum values ranging up to 0.83 (**Figure 6.1a**) and significant contributions from the SF aerosols of approximately 57% (**Figure 6.3a**). Yet a significantly decreasing total AOD trend has been noticed over the region (**Figure**

6.2a). The major aerosols contributing to this decrease are the SF aerosols (**Figure 6.2e**), which are according to Aas et al. (2019); Klimont et al. (2013). In addition to this, a decrease (increase) due to the BC (OC) aerosols has also been seen in **Figure 6.3b**. This increase due to the OC aerosols contradicts the observations in **section 5.3d**, where the decrease noticed over the ECC region was due to the decrease in nearly all the aerosol types.

(**v**) The **NWA** region also falls under the same category with the high values of total AOD (**Figure 6.1a**), ranging from maximum up to 0.64, having the highest contribution from the DU aerosols of approximately 76% (**Figure 6.3a**). This influence of DU aerosols on the NWA region is primarily associated with the presence of the Sahara Desert and Sahel regions (Gavrouzou et al., 2021). Here, the MERRA-2 dataset considers only the probability of sediments accumulated in the tropospheric depression regions as the DU aerosols (Buchard et al., 2017). **Figure 6.2a** has shown a decrease in the total AOD trends over the region where the maximum decrease is due to a decrease in the DU aerosols, whereas there is a slight decrease due to SS aerosols (due to the adjoining Atlantic oceans) as well. A similar decrease in the DU aerosols over the NWA region is also found in Ridley et al. (2014). Moreover, an increase in OC aerosols has also been noticed in this region. These observed trends due to the different aerosol types are in agreement to what has been observed in the **section 5.3e**, the reason for which has been attributed to the dearth of scattering aerosols in the GOCART model used for MERRA-2 analysis (Buchard et al., 2017).

(**vi**) Aerosol properties over the **ME** region have also shown similar behaviour to that of the NWA region due to their identical surface features, but here the maximum total AOD loading extends up to the value of 0.49 (**Figure 6.1a**) with 67% contributions from the DU aerosols (**Figure 6.3a**). Like the NWA region, we have also seen a decrease in the total aerosol loading (**Figure 6.2a**), where the significant decrease is attributed to the decrease in the DU aerosols (**Figure 6.2d**). This decrease in the DU aerosols agrees with the decrease in scattering aerosols found over the region with the MERRA-2 dataset in **section 5.3f**. In addition to this, a slight increase due to the SS and BC aerosols is also seen over the region.

(**vii**) Over the **SAF** region, an intermediate value of the total aerosol loadings (ranging up to 0.42) has been observed in **Figure 6.1a**, with the significant

contributions of approximately 54%, 16%, and 17% from the OC, DU, and SF aerosols, as seen in **Figure 6.3a**. We may note from **Figure 6.2a** that there is an overall increasing trend over the region where the major dominating aerosols are OC (**Figure 6.2b**) and BC (**Figure 6.2f**). The OC and BC aerosols considered in MERRA-2 are primarily an outcome of the fossil fuel, oxidation from the plant, and BB events (Colarco et al., 2010). A similar increase in the trend values is found in Van Der Werf et al. (2010) and **section 5.3g** as well, where the total AOD increasing trend is mainly due to an increase in its scattering and absorbing aerosols. Also, the statistically decreasing trends due to the SF aerosols have been spotted in **Figure 6.2e**. However, a slight decrease due to the coarse-mode aerosols was also seen in **section 5.3g**, but no such evidence was spotted here.

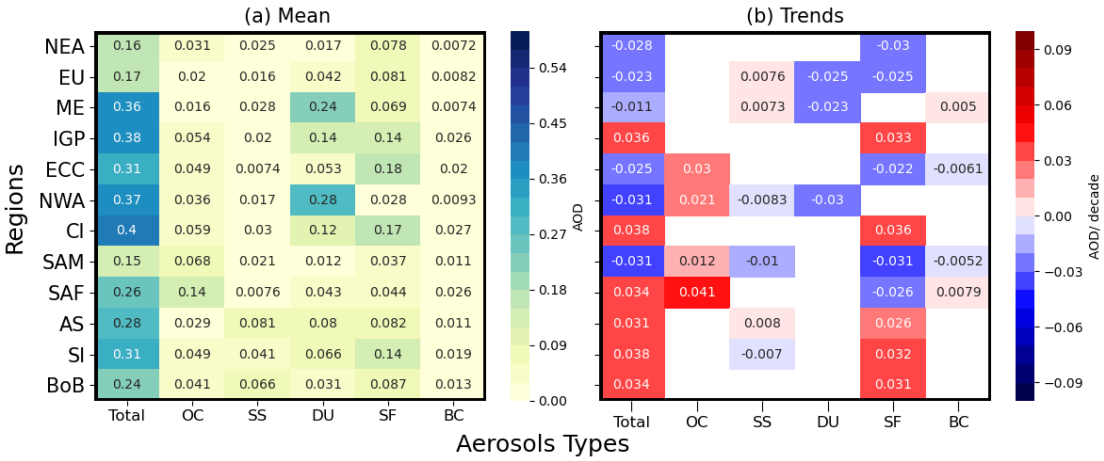

Figure 6.3 *The numerical values of the annual mean (a) climatology and its (b) statistically significant (only) trend values (/ decade) for Total, OC, SS, DU, SF, and BC AODs obtained over 8 RoIs, using MERRA-2 (2001-2020) observations.*

(**viii**) The **Indian** region has depicted high total aerosol loading after the ECC region with the maximum (minimum) AOD magnitude over the IGP (AS) region with the value of 0.55 (0.37), as can be seen in **Figure 6.1a**. Here, the significant contributions are observed from the SF (**Figure 6.3a**) aerosols with an approximation of 37%, 42%, 45%, 29%, and 36% over the IGP, CI, SI, AS, and BoB regions, respectively. The DU aerosols dominate with about 37%, 30%, 21%, 28%, and 13% over the IGP, CI, SI, AS, and BoB regions, respectively. Huge dominance from the SS aerosols is observed over the adjoining sea regions such as the AS (29%) and BoB (27%) regions. However, overall increasing AOD trends are very evident over the whole Indian region from **Figure 6.2a,** and this increasing trend is seen in connection

with the increase in the SF aerosols (**Figure 6.2e**) over the whole Indian region. These results are in accordance with the increase in fine and scattering aerosols over the region as discussed in **section 5.3h** and from a recent study by Aas et al. (2019) as well. In addition, we could also see an increase (decrease) due to SS aerosols over the AS (SI) region in **Figure 6.3b** as well.

6.2.2 Vertical distribution of Aerosols Chemical Properties

Apart from examining the mentioned above columnar chemical properties, a comprehensive investigation of the vertical distribution of different aerosol types also plays a crucial role. In this context, this sub-section deals with the contributions of vertical variations due to the mixtures of different components of aerosols (i.e., DU, PD, and ES) mean climatology (**Figure 6.4**) and its corresponding significant trends (**Figure 6.7**), using the CALIOP dataset. Note that the PD aerosols are considered the mixture of the DU and SM aerosols (Omar et al., 2009), whereas the ES aerosols are considered the elevated layers identified as SM when present above the ABL altitudes (Kim et al., 2018). Also, along with the examination of the total AOD and altitude-wise vertical variations (i.e., α_{aer}) of the aerosols, this study also discusses the mean and its trends in the ABL and FT AODs for each aerosol component as well. These region-wise divisions between the ABL and FT altitudes have been made based on the height of the planetary boundary layer, which is retrieved from the MERRA-2 dataset (**Table 2.6ix**). Also, the data below 0.5 km has not been accounted for here, as from **Figure 3.3** shows that the ground-based LIDAR does not agree with the CALIOP measurements below that altitude. However, for the reference purpose, we have compared the observations of the FT and ABL altitudes at 0.5 km with that of the surface levels at 0 km as well in this sub-section. This study has also been further partitioned based on the DT and NT observations as well, as there can be substantial differences arising due to the higher solar background signal in the DT (to that of the NT) measurements.

6.2.2.1 Mean climatology of type-dependent Aerosols

In continuation to **section 3.3.5**, where the EALs were found to have maximum loading from Africa to South Asia continents in the lower troposphere, but the significant aerosols contributing to their formation were not undertaken. So, here the region-wise findings (over 8 RoI, see **Chapter 4**) drawn from the different

altitude variations due to the DU, PD, and ES aerosols mean climatology (**Figure 6.4**), retrieved from the CALIOP's DT and NT measurements, are highlighted as follows:

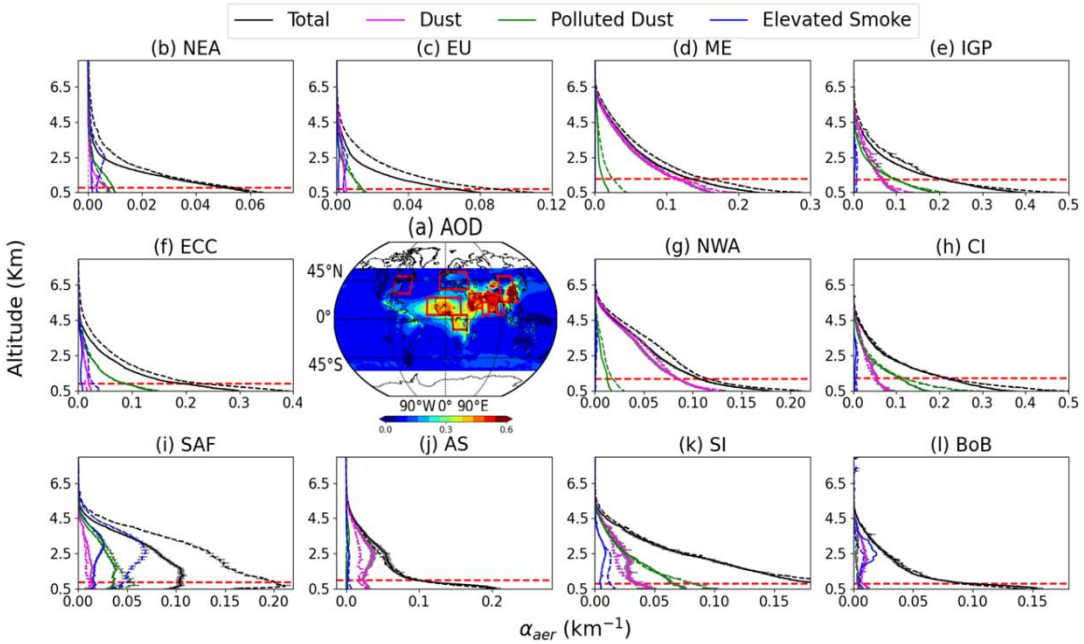

Figure 6.4 *Region-wise mean α_{aer} plots from the CALIOP sensor at 532 nm wavelength, from 2006 to 2020. (a) gives the global distribution of the total AOD climatology retrieved from the CALIOP dataset within the same period. The red boxes (plotted on (a)) represents the selected RoIs which includes (b) NEA, (c) EU, (d) ME, (e) IGP, (f) ECC, (g) NWA, (h) CI, (i) SAF, (j) AS, (k) SI, and (l)BoB regions. Note that the solid (dashed) lines represent the DT (NT) mean plots of the vertically resolved Total, DU, PD, and ES aerosols whereas the red dashed lines represent ABL altitudes, in the region-wise distribution of α_{aer} values.*

(**i**) **NEA** is one of those regions which have low total AOD (**Figure 6.4b**) values of about 0.06 (DT) and 0.078 (NT), where a drastic decrease in its α_{aer} values above 1 km altitude is seen in both DT as well as NT analysis. The contribution of approximately 13% (7%), 23% (15%), and 8% (21%) exist due to the DU, PD, and ES (to the total) aerosols in the DT (NT) analysis, as seen in **Figure 6.5 (Figure 6.6)**. Altogether, these results reveals comparatively maximum contributions from the PD (DU) aerosols over the region, where the FT AOD alone is adding approximately 78% (66%) to the atmosphere in the DT (NT) analysis. The transport of the DU aerosols from the Sahara Desert to the NEA region is consistent with Yu et al. (2015a). Here, the same exercise has been repeated while considering the surface (i.e.,

0 km) as the lower limit, and we could spot about 65% (69%) of the PD (DU) aerosols in the FT altitudes.

(**ii**) The **EU** region with the AOD values ranging from 0.075 (DT) to 0.12 (NT) has also shown a similar pattern in the aerosols vertical variations to that found over the NEA region, where a drastic decrease after the altitude of 1 km is seen in its total α_{aer} values (**Figure 6.4c**). Here, the DU, PD, and ES aerosols contributes approximately 20% (13%), 25% (19%), and 5% (12%) to the total aerosol loading in the DT (NT) observations, as seen from **Figure 6.5** (**Figure 6.6**). Overall, there are comparatively higher values due to the PD aerosols adding up to 84% (82%) to the FT AOD over the region in the DT (NT) observations. When repeated with the lower limit at 0 km, the same exercise has shown nearly 64% (69%) contribution of the PD aerosols due to the FT AOD in the DT (NT) observations.

(**iii**) This study has found comparatively higher total mean AOD values over the **ECC** region ranging from 0.22 (DT) to 0.29 (NT), with a gradual decrease in the mean α_{aer} values with the increasing altitudes (**Figure 6.4f**). Summary statistics have shown contributions of approximately 17% (15%), 43% (34%), and 8% (18%) due to the DU, PD, and ES aerosols in the DT (NT) observations over the region, from **Figure 6.5** (**Figure 6.6**). This region has spotted overall higher contributions from the PD aerosols, where the FT AOD has contributed to nearly 78% (81%) in the DT (NT) observations. When repeated considering the surface levels at 0 km, the same has shown a contribution of about 65% (66%) due to the PD aerosols in the FT altitudes in the DT (NT) observations.

(**iv**) **NWA** comes under those regions which are completely covered under deserts with the contributions of approximately 82% (75%), 11% (14%), and 1% (1%) due to the DU, PD, and ES aerosols (to the total AOD) in the DT (NT) observations (**Figure 6.4g**). The total AOD values vary from 0.29 during DT and 0.32 during the NT observations. This dominance of the DU aerosols is irrespective of the measurement timings where the higher AOD values are from the FT altitudes with contributions of about 71% (75%) when lower limits are set at 0.5 km and 65% (66%) at 0 km in the DT (NT) observations, as can be seen in **Figure 6.5b** (**Figure 6.6b**). Interestingly, an increase (with altitude) in the α_{aer} values due to the ES aerosols has also been spotted in the NT data at 3 and 4 km altitudes (**Figure 6.6d**). The behaviour which follows this pattern of increase in the concentration of aerosols with height

indicates the presence of the EALs. Nevertheless, there is a massive contribution due to the DU and PD aerosols as well, at this particular altitude.

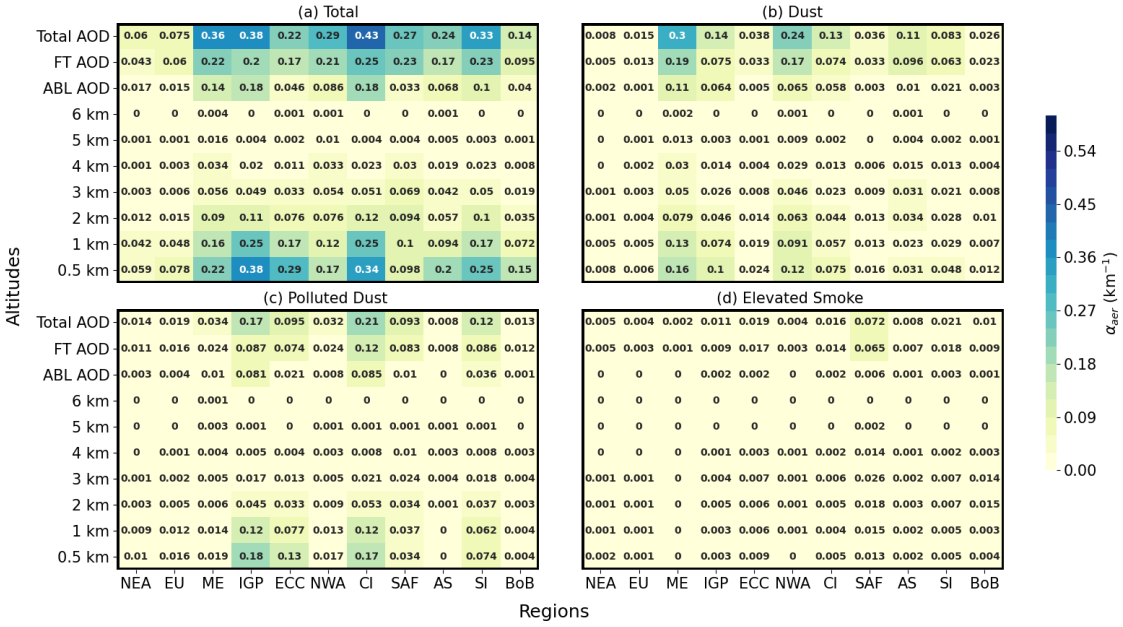

Figure 6.5 *Region-wise numerical mean values of the (a) Total, (b) DU, (c) PD, and (d) ES AODs (total, ABL, and FT) and α_{aer} (km^{-1}) at different altitude ranges, obtained during the DT observations over 8 RoIs using the CALIOP (2006-2020) observations.*

(**v**) Comparatively higher aerosols loading is observed over the **ME** region (**Figure 6.4d**) with contributions of approximately 83% (78%), 9% (15%), and 0.5% (0.2%) due to the DU, PD, and ES aerosols in the DT (NT) observations. Higher total AOD values vary from 0.36 in DT to 0.42 in NT measurements, as observed in **Figure 6.5a** (**Figure 6.6a**). The DU aerosols have the maximum contributions over this region, as per the Arabian Desert's presence. This pattern of the vast dominance of the DU aerosols over this region is similar to that over the NWA region, but the FT altitudes have the contribution of 63% (60%) in the DT (NT) measurements, as seen in **Figure 6.5b** (**Figure 6.6b**). When repeated while keeping the surface levels at 0 km altitude, the same exercise has shown the contributions of nearly 53% (51%) to the FT altitudes, due to the DU aerosols, in the DT (NT) observations.

(**vi**) The **SAF** region (**Figure 6.4i**) has shown moderate total annual AOD values ranging from 0.27 (DT) to 0.32 (NT). The contributions due to the DU, PD, and ES aerosols (to the total AOD) of approximately 13% (4%), 34% (20%), and 26% (50%) have been seen in the DT (NT) measurements over the region. Altogether,

we could observe higher contributions from the PD (ES) aerosols over the region, where the FT altitudes have contributed approximately 89% (94%) at surface levels of 0.5 km and 89% (90%) at 0 km altitude in the DT (NT) observations, as seen in **Figure 6.5c** (**Figure 6.6d**). Also, it is noteworthy that there is an increase in the total and PD (total, DU, and PD) mean α_{aer} values at 1 km altitude in the DT (NT) measurements over the region. However, there is an increase in the ES mean α_{aer} values at 1, 2, 3, and 4 km altitudes in both DT and NT observations (**Figures 6.5d and 6.6d**) as well.

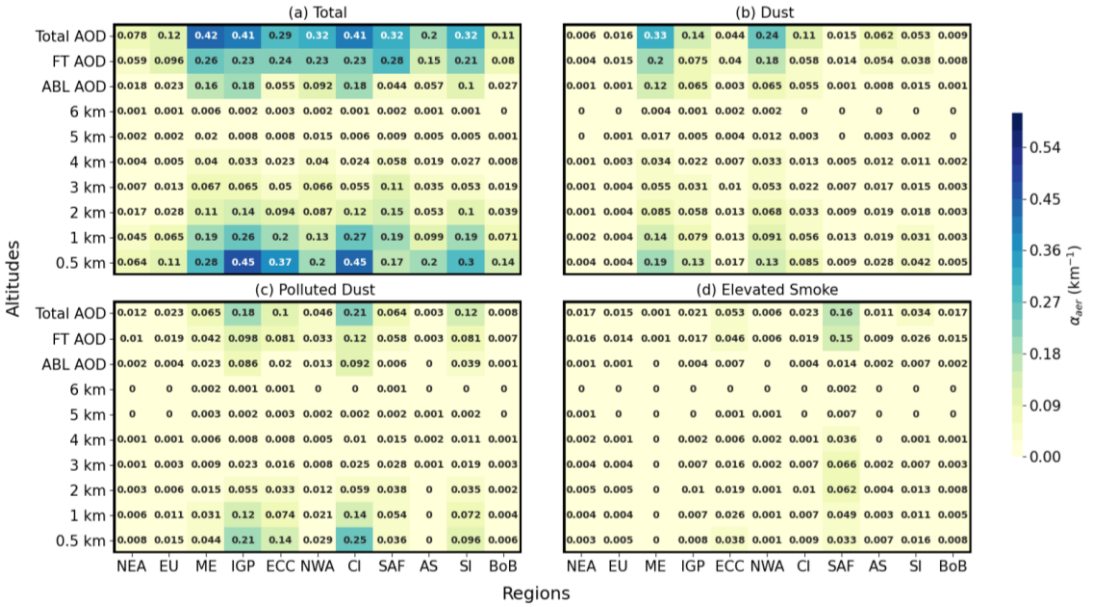

Figure 6.6 *Same as* ***Figure 6.5*** *but for NT.*

(**vii**) The **Indian** region, which is further sub-divided into the IGP (**Figure 6.4e**), CI (**Figure 6.4h**), AS (**Figure 6.4j**), SI (**Figure 6.4k**), and BoB (**Figure 6.4l**), comes under one of the regions having high total mean aerosol loading. Here, the approximate contributions (to the total AOD) found over IGP is about 36% (34%), 44% (43%), and 2% (5%), CI is 30% (26%), 48% (51%), 3% (5%), SI is 25% (16%), 36% (37%), 6% (2%), AS is 45% (31%), 3% (1%), 3% (5%), and BoB is 18% (30%), 9% (7%), 7% (15%) due to the DU, PD, and ES aerosols in the DT (NT) observations. Overall, over the IGP, CI, and SI regions, huge dominance due to the PD aerosols are found with contributions of approximately 51% (54%), 57% (57%), and 72% (67%) when surface levels are considered at 0.5 km and 38% (39%), 45% (42%), and 60% (57%) at 0 km, in the FT altitudes in the DT (NT) measurements, as shown in **Figure 6.5c** (**Figure 6.6c**). This influence of the PD aerosols over the SI

region is in accordance with the results discussed in **section 3.3.4** as well, where an analysis was carried out over the rural location in SI, i.e., the Gadanki region, and approximately 44% contribution was encountered from the columnar PD aerosols alone. Interestingly, we could also observe an increase in the mean ES α_{aer} values at 2 and 3 km (2 km) altitudes over the land region in the DT (NT) observations. Whereas over the adjoining sea regions (which includes AS and BoB), the major contributions are noticed from the DU aerosols of nearly 87% (87%) and 83% (89%) when surface levels are considered at 0.5 km and 80% (71%), and 78% (72%) at 0 km to the FT altitudes in the DT (NT) analysis, as seen in **Figure 6.5b** (**Figure 6.6b**).

Overall, it can be seen from the above discussions that the high values of AOD are found in the FT altitudes. However, in Bourgeois et al. (2018) they have mentioned that these higher contributions in the FT altitudes result from the local emissions (long-range transport) over the land (ocean) regions across the globe. Also, the NT observations have spotted relatively higher AODs in the FT altitudes, which is also in accordance with Bourgeois et al. (2018), where the global contribution from ABL (FT) is 38% (62%). The reason behind the higher values in the FT altitudes during NT observations is the low altitudes of the ABL, due to which most of the AODs are confined in the FT altitudes, as the chemicals are less diluted by turbulent mixing during night (Wallace, John M, 2006). Furthermore, it is found that the PD aerosols are mainly distributed only over regions with extensive anthropogenic activities and the downstream of the DU aerosols, such as the NEA, EU, ECC, and Indian (land) regions. On the other hand, the DU aerosols are mostly covered over the Desert regions and their adjoining waters, such as the NWA, ME, AS, and BoB regions. Lastly, the ES aerosols are mainly distributed over the regions exhibiting biomass burning activities, such as the India (land) and SAF regions. The enhancement of the different types of aerosols such as ES and PD in the FT altitudes indicates the lifting of the fine-mode aerosols through the vertical motion of the winds. Whereas, in the case of DU aerosols, pyro-convection, orographic lifting, and interaction of sea breeze with continental outflow can be the key reasons for its higher contributions in the FT altitudes (Bourgeois et al., 2015; Khan et al., 2015).

Moreover, in all the above mentioned region-wise contribution analysis of the aerosol components to the total AOD values, we could spot an overall missing value in the total percentages calculated due to the different aerosol types. The remaining or

missing percentages can be attributed to the other aerosols, including SF, NR, SS, and ammonium, persisting over the region, which are not evaluated in the CALIOP level-3 datasets. Here, the total AOD values retrieved from the CALIOP measurements have varied from the MERRA-2 total AOD values (see **section 6.2.1**), and the vertical mean α_{aer} values in Gui et al. (2021), as the α_{aer} values retrieved from the CALIOP sensor are further sub-divided based on measurement timings (i.e., DT and NT). Note that the SAM region is not considered from the CALIOP measurements due to the much prevalent SAA over the region (see **section 4.3.4.4**).

6.2.2.2 Changing patterns of Aerosols with Altitude

Major region-wise changing patterns drawn from the different altitude variations of the DU, PD, and ES aerosols (**Figure 6.7**), retrieved from the CALIOP's DT and NT measurements, are discussed in the following sub-section. This section will elaborate on the corresponding point-to-point statistically significant (only) trend analysis for the mean climatology (due to all the aerosol types) presented in the previous **section 6.2.2.1**. Also, note that since higher percentage of aerosols persists above ABL (or at FT altitudes) irrespective of the surface levels (i.e., 0 km and 0.5 km) considered in the previous section, so in this section, their corresponding trends will be discussed considering the 0.5 km altitude values only.

(**i**) In connection to the low aerosol loadings prevailing over the **NEA** region (see **section 6.2.2.1i**), we could notice a statistically significant decrease in the total AOD values with the magnitude of 0.018 (0.017) in the DT (NT) observations over the region in **Figure 6.7b**. Also, the maximum decrease is seen in the total aerosol loading at 0.5 km (1 km) and the FT altitudes in the DT (NT) observations, as seen in **Figures 6.8a and 6.9a**. However, corresponding to the previous **section 6.2.2.1i**, where a massive contribution from the mean PD aerosols in the DT data was observed, a corresponding decrease is observed here as well until 2 km altitude. In addition to this, we could also spot a decrease due to the ES aerosols in the DT observations at 3 km altitude. While in the NT data, a decrease is observed due to the PD (at 1 km) and ES (till 3 km) aerosols. In contrast to the decrease due to all the aerosols, a statistically significant increase in the DU aerosols has also been observed at 2 km altitude in the NT observations (**Figure 6.9**). This is in contradiction to the results found in **section 5.3a**, where a decrease in the coarse-mode aerosol was observed over the region. However, there has been evidence of the transport of DU

aerosols from the North Atlantic Ocean toward the NEA region (Yu et al., 2015a), which could be the reason associated with this increase. Overall, we could observe that the maximum decrease is extended to 3 km altitude irrespective of the measurement timings (**Figures 6.8 and 6.9**).

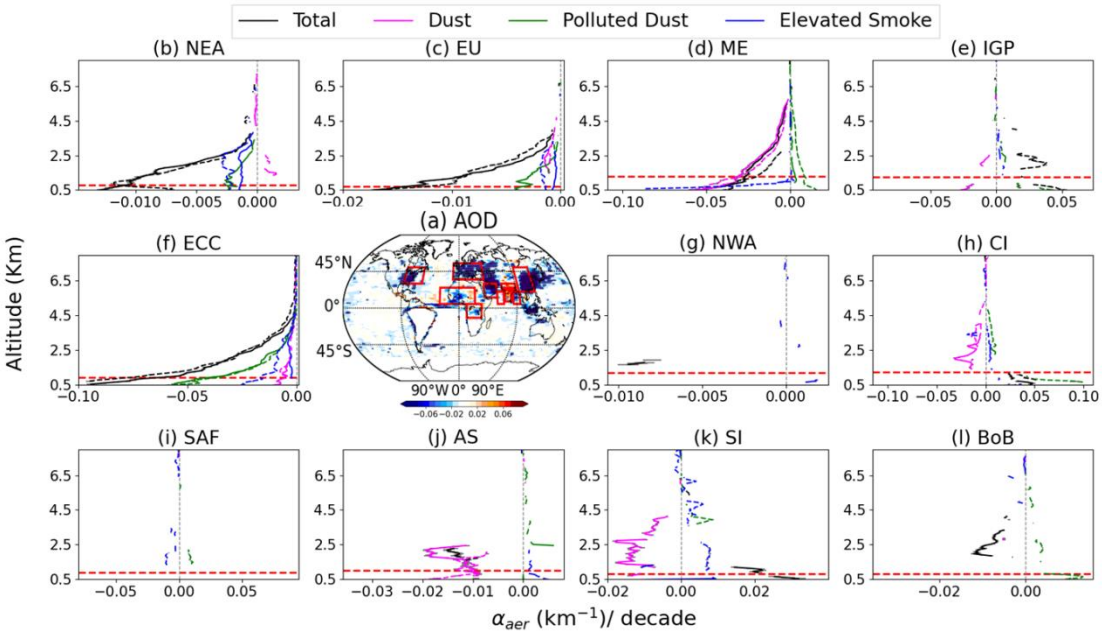

Figure 6.7 *Region-wise MLR trend analysis of the vertically resolved Total, DU, PD, and ES α_{aer} values from CALIOP sensor at 532 nm wavelength from 2006 to 2020. (a) gives the global distribution of the total AOD trend values retrieved from the CALIOP dataset within the same time period. Only the statistically significant trend values are expressed region-wise with the error bars. Further details are same as in* ***Figure 6.4****.*

(**ii**) **EU** also comes under the regions having low mean AOD values and has seen a decrease in the total aerosol loading with the magnitude of 0.018 (0.02) in the DT (NT) observations from the **Figure 6.7c**. This decrease has been higher, extending up to 1 km altitude in both DT and NT observations of the CALIOP sensor. As seen in **section 6.2.2.1ii**, there have been enormous contributions due to the PD aerosols over this region, and correspondingly maximum decrease is seen due to the same in the DT data at the FT altitudes (**Figure 6.8c**). In the DT observations, a decrease in the DU aerosols are seen at 2 and 3 km altitudes, whereas the ES aerosols decrease to 1 km altitude only. The NT observations have seen a decrease in the DU (from 2 till 4 km), PD (at 1km), and ES (till 2 km) aerosols, as shown in **Figure 6.9**. However, a considerable decrease is seen in the FT AOD compared to the ABL AOD values in all

the aerosol components in both the DT and NT observations (**Figures 6.8 and 6.9**), over the region. These decreasing trends in the region can be associated with the implementation of mitigation strategies over the region (Pey et al., 2013; Tørseth et al., 2012).

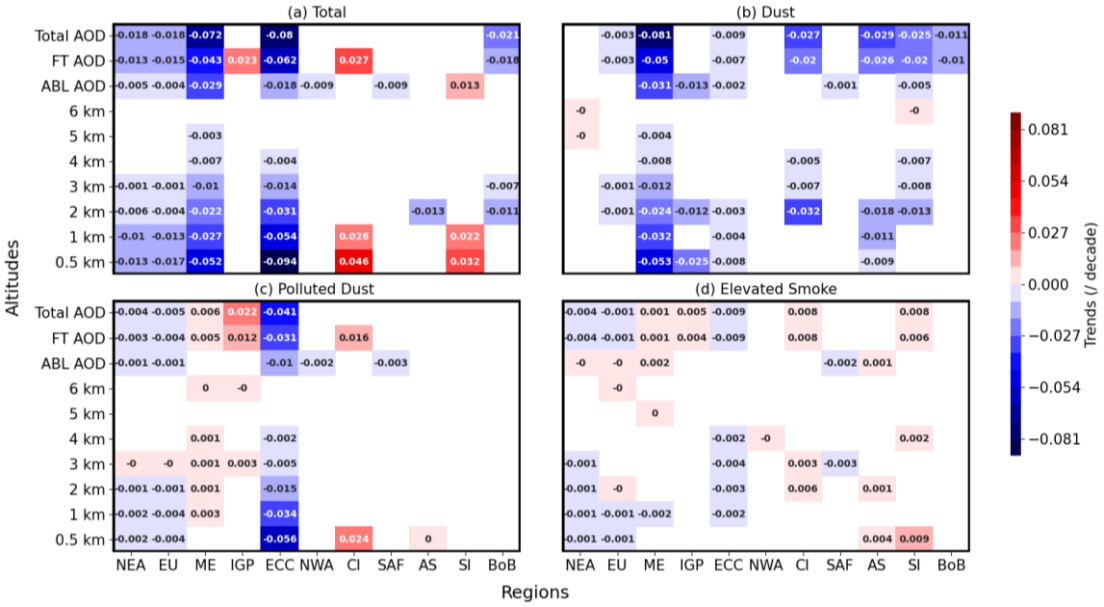

Figure 6.8 *Same as* ***Figure 6.5****, but the corresponding statistically significant numerical trend values (only) are shown here.*

(**iii**) **ECC** falls under the regions which have recently implemented the CAA policies due to the persisting massive aerosol loading, as discussed in **section 6.2.2.1iii**. The outcome of which has been seen with a gradual decrease (w.r.t altitude) in the total aerosol loading with the magnitude of 0.08 (0.092) in the DT (NT) observations from **Figure 6.7f**. Correspondingly, a statistically significant decrease in the DU and PD aerosols has also been noticed with altitude in both the DT as well as NT observations from **Figures 6.8 and 6.9,** respectively. There has been a considerable decrease due to the PD aerosols with the magnitude of 0.041 (0.038) in the DT (NT) observations, which seemed to be have huge contributions to the total aerosol loading over the region, as discussed in **section 6.2.2.1iii**. The gradual decrease is observed due to the ES aerosols as well, which extends up to the altitude of 5 km in the NT observations from **Figure 6.9.** Moreover, the decrease extended from 1 to 4 km in the DT with the maximum values at 2 and 3 km altitudes, as shown in **Figure 6.8.** From the same figure, we could also spot that the maximum decrease is prevalent in the FT altitudes due to all the aerosol components and is irrespective of

the measurement timings, which agree with Ratnam et al. (2021). Dong et al. (2017), also noticed decrease in the vertical distribution of aerosols above 0.3 km altitudes.

(**iv**) The previous **section 6.2.2.1iv** has already emphasised that the key feature of the **NWA** region is the Sahara Desert and Sahel regions, due to which there is a massive presence of the DU aerosols over the region. Minor contributions from the PD and ES aerosols were also seen in the mean climatology over the region. However, a slightly significant decreasing trend in the total aerosol loading was spotted extending from 1.6 to 1.9 km altitude in the DT observations, as shown in **Figure 6.7g**. Increasing trends due to the ES aerosols are also noticed below 3 km, whereas a decrease is observed above 3 km altitude over the region in the DT observations. In addition to this, a decrease (increase) in the PD aerosols is spotted in the ABL (FT) altitudes in the DT (NT) observations. But unfortunately, we could not observe any other correspondingly statistically significant trend values (due to the other aerosol types) over the region (**Figure 6.7g**).

(**v**) Aerosol loading over the **ME** region also behaves similarly to that of the NWA region, where there is a massive contribution from the DU aerosols, as seen in **section 6.2.2.1v**. Altogether this region has shown significantly decreasing trends in the total aerosol loading with a magnitude of 0.072 (0.04) in the DT (NT) observations, as shown in **Figure 6.7** (**Figure 6.8**). This decrease is in conferment with Mehta et al. (2018). Moreover, this decrease in the total aerosol loading is higher in the FT altitudes than the ABL altitudes. The major contribution behind this decrease is the gradual decrease (with altitude) in the DU aerosols over the region (**Figure 6.7d**), which overlaps with the decrease in the trends due to total aerosols as well. In contrast to this overall decrease in the aerosols over the region, an increase (higher in the FT altitudes) in the PD aerosols has also been observed in both the observational timings (**Figures 6.8c and 6.9c**). This increase in PD aerosols is lower than the decrease in the trends seen due to the DU aerosols over the region. A disparity is spotted due to the ES aerosols over the region where a decrease (increase) is seen at 1 km in the DT (NT) observations, as seen in **Figures 6.8d and 6.9d**, but an increase is spotted at the FT as well as ABL altitudes in the DT observations.

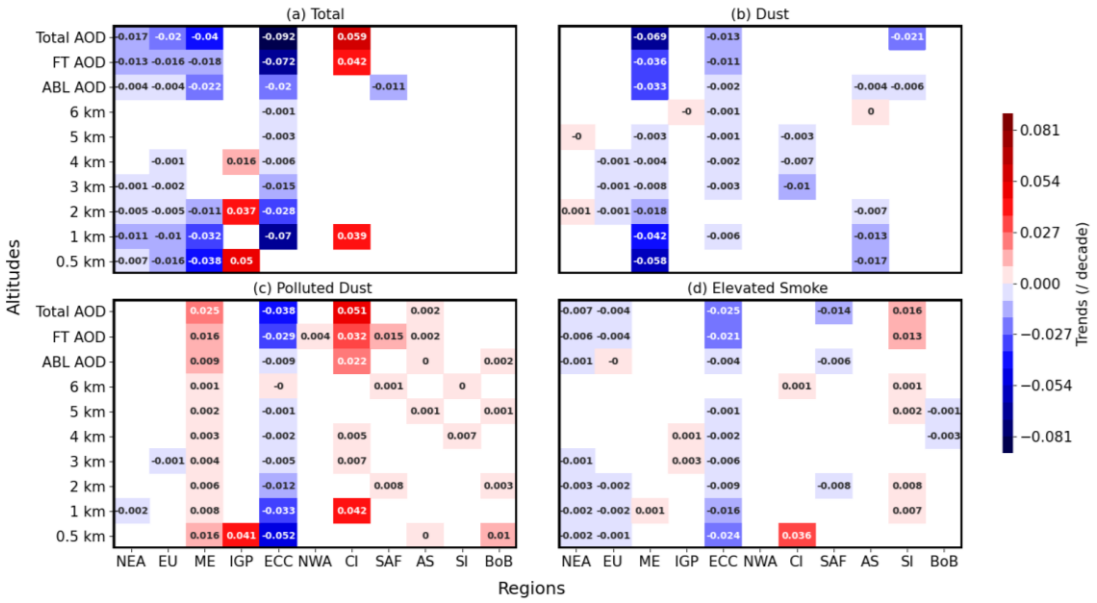

Figure 6.9 *Same as* ***Figure 6.6****, but the corresponding statistically significant numerical trends values (only) are shown here.*

(**vi**) The **SAF** is a tropical region bounded by the coastline stretch of the Indian and the South Atlantic Oceans with a moderate total annual mean aerosol loading, as discussed in **section 6.2.2.1vi**. Summary statistics over this region could not spot any significant trend values due to the total aerosol loading (**Figure 6.7i**), but an overall decrease has been perceived at the ABL altitudes in both the DT as well as the NT observations. This is following the results found in **section 4.3.4.6** as well, where the CALIOP sensor could not reproduce the trend values due to total aerosol loading over the region. However, a statistically significant decrease due to the ES (DU) aerosols has been spotted below 3.5 km (ABL altitudes) in the DT (**Figure 6.8d(b)**) and NT (**Figure 6.9d**) observations. These results agree with Kumar et al. (2014), where a decrease in the SM aerosols has been observed over the region. An increase due to the PD aerosols has also been seen in the NT examination between 1.4 to 2.3 km (or FT) altitude from the **Figure 6.7i**, whereas a decrease in the PD aerosols is spotted at ABL altitudes during DT analysis (**Figure 6.8c**).

(**vii**) The mean climatology due to the different types of aerosols prevailing over the **Indian** region, discussed in **section 6.2.2.1vii**, has shown higher contributions from the PD (DU) aerosols over the land (adjoining sea) regions. We have observed overall increasing trends due to the total aerosol loading over the IGP (**Figure 6.7e**), CI (**Figure 6.7h**), and SI (**Figure 6.7k**) regions in the FT altitudes,

which are in agreement with Ratnam et al. (2021). Nevertheless, the decreasing trends are noticed over the AS (**Figure 6.7j**) and BoB (**Figure 6.7l**) regions. Over the IGP region, we could notice increasing trends due to the majorly dominated PD aerosols and slightly dominated ES aerosols in the FT altitudes, whereas decreasing trends have been observed due to the DU aerosols in the ABL altitudes during both the DT (**Figure 6.8**) observations. This decrease in the DU aerosols over the Indian subcontinent is in conjunction with Kaskaoutis, 2011. Similarly, over the CI region, a decrease (increase) is observed in the pattern of the DU (PD and ES) aerosols in the FT altitudes in the DT observations (**Figure 6.8**), whereas the PD aerosols have increasing trends in both the FT as well as ABL altitudes in the NT observations (**Figure 6.9**). Finally, over the SI region, a decrease (increase) in the DU (ES) aerosols is exhibited at FT and ABL (FT) altitudes in the DT as well as NT observations. Over the AS and BoB regions, a decrease (increase) in the DU (PD) aerosols has been spotted in the DT (NT) observations. However, there are an increase (decrease) in the ES aerosols over the AS (BoB) region during DT (NT) in ABL (4 and 5 km) altitudes, as seen in **Figure 6.8d** (**Figure 6.9d**).

6.3 Summary

With the objective to have a long-term assessment of the aerosols changing chemical properties across the globe, we tried to analyse the different types of aerosols using the MERRA-2/ reanalysis and the CALIOP measurements. The multi-year datasets have been utilized in this study, where the MERRA-2 (CALIOP) data have been extended between 2001 and 2020 (2006 and 2020). More specifically, here, we tried to examine the complete global 3D picture of the mean climatology and its corresponding trends due to different aerosols compositions using both the observations. On the one hand, where MERRA-2 can provide the spatial 2D distribution (along latitude and longitude) of the different components of aerosols such as DU, SS, SF, BC, and OC, whereas CALIOP sensor came up with the mixtures of the different components of aerosols such as DU, PD, and ES with respect to the altitude variations, i.e., along the third axis. Note that the CALIOP measurements are further sub-divided based on their measurement timings (including the DT and NT) and the altitude variations (including ABL and FT) as well. Here, we have spotted overall high total AOD values in the NT (to that of DT) observations. The FT altitudes have shown higher AOD percentages when compared with the ABL

AODs due to nearly all the aerosol types persisting over all the regions. Eventually, the major region-wise combined information (from both MERRA-2 as well as CALIOP) on the aerosols chemical characteristics highlighted in this study are summarized as follows:

(**a**) **NEA**: The NEA region exhibits the low total annual mean aerosol loading in the atmosphere. Here, the maximum contributions are observed from the SF (49%) aerosols in MERRA-2 and the PD (23% during DT) and DU (21% during NT) aerosols in CALIOP measurements. Overall, decreasing trends are observed in the total aerosol loading over the region with a maximum decrease from the SF aerosols in MERRA-2 and PD and ES aerosols in CALIOP observations, where the decrease is higher in the FT altitudes.

(**b**) **SAM**: This region has also spotted a low total annual mean aerosol loading with the maximum contributions from the OC (45%) and SF (25%) aerosols. However, overall decreasing trends are observed in MERRA-2 observations, where the significant decrease is due to the decrease in SS, SF, and BC aerosols. CALIOP observations are not considered in this study due to the well-known SAA prevailing over this region.

(**c**) **EU**: The EU region also follows a similar pattern of low total annual aerosol loading, where the higher contributions are from the SF (47%) aerosols retrieved from the MERRA-2 and PD (25% during DT and 19% during NT) aerosols in the CALIOP dataset. Altogether, decreasing trends are found over this region due to the decrease in the DU, and SF aerosols in MERRA-2, and PD, DU, and ES aerosols, where the decrease is higher in the FT altitudes in the CALIOP measurements.

(**d**) **ECC**: A high total annual aerosol loadings have been found over the region where the significant contributions are from the SF (58%) aerosols in MERRA-2 and PD (43% during DT and 34% during NT) aerosols in CALIOP observations. Despite the high annual aerosol loading, overall decreasing trends are reported over the region due to a decrease in the SF and BC (PD, DU, and ES, where the decrease is higher in the FT altitudes) aerosols in the MERRA-2 (CALIOP) data sets. Moreover, a slight increase due to the OC aerosols is also observed in the MERRA-2 dataset.

(**e**) **NWA**: The higher total annual mean aerosol loading over this region is attributed to the dominance of DU aerosols in both the MERRA-2 (76%) as well as CALIOP (82% during DT and 75% during NT) observations. However, an overall decreasing trend due to the decrease in the DU (major) and SS (slight) aerosols is seen in the MERRA-2 measurements. Further, an increase in the α_{aer} values due to ES aerosols at 3 km altitude is observed in the DT observations in CALIOP measurements. In addition to this, an increase due to the OC aerosols has also been spotted over the region, whereas a high increase (decrease) in the PD aerosols has been perceived at the FT (ABL) altitude as well.

(**f**) **ME**: The aerosol loading over this region follows similar characteristics to the NWA region, where the high total annual aerosol loading persists due to the higher DU aerosols. This contribution is nearly 67% in MERRA-2 and 83% in the DT observations and 78% in the NT in the CALIOP measurements. On the whole, decreasing total aerosol trends are observed where the significant decrease is from the decrease in the DU (higher in the FT altitudes) aerosols. At the same time, there is a slight increase due to the PD (higher at FT altitude) and ES aerosols as well.

(**g**) **SAF**: This region has observed an overall moderate aerosol loading with the significant contributions from the OC (54%), DU (16%), and SF (17%) aerosols in the MERRA-2 and the PD (36% during DT), and ES (50% during NT) aerosols in the CALIOP datasets. Overall increasing trends have been noticed due to the increase in the BC and OC aerosols in the MERRA-2 datasets, but no significant total aerosol trends are analysed in the CALIOP observations over the region. Despite this, an increase (decrease) due to the PD aerosols has been spotted at the FT (ABL) altitude region. Also, decreasing columnar trends due to the SF aerosols are observed in addition to the decrease in the ES and DU aerosols at ABL altitude.

(**h**) **India**: The Indian region has spotted high total mean annual aerosol loadings with the significant contributions from the DU and SF aerosols in MERRA-2, and from the PD (over the IGP, CI, and SI), and DU (over the AS and BoB regions) aerosols in the CALIOP measurements. It was found that an overall increase in the total aerosol trends is prevailing over the whole region in MERRA-2, but in CALIOP observations, an increase (decrease) was found over the land (adjoining sea) region. Here, the maximum increase is from the increase in the SF, PD, and ES aerosols over the land regions. Moreover, the decrease due to the DU aerosols is also

found over the land (slight) regions such as CI and SI and its adjoining sea (major) regions as well, in the CALIOP observations. Also, the increase due to the PD (ES) aerosols is higher in the FT altitudes over the IGP, CI, and AS (IGP, CI, and SI) regions.

Along with the significant trends examined due to the various aerosols columnar chemical properties, the increase in the EALs over the tropical (including NWA, SAF, and the Indian) regions is also quite evident from the above analysis. Nevertheless, this interception can further lead to solar dimming or brightening events at the Earth's surface, which ultimately impacts the atmosphere (Stanhill and Cohen, 2001). Its potential implications on climate change, hydrological, and carbon cycle are well delineated in Wild, 2009. Also, in a recent study by Ghosh et al. (2022), it is mentioned that India has lost about 29% of solar power generation due to air pollution. However, this can slow down the monsoon circulations as well and thus reducing rainfalls over the Indian region by altering the surface temperature gradient (Ramanathan et al., 2001). Further, the absorption of the solar radiations by the atmospheric aerosols such as BC and DU during the pre-monsoon season can also advance the monsoon rainfall, consistent with the EHP hypothesis (Lau and Kim, 2006). It was also recently found by (Fadnavis et al., 2019) that the severity of the draughts has been amplified by 17% due to the EALs during El-Niño events over the South Asian regions. Hence, this analysis has demonstrated the increase in the contributions due to the different anthropogenic aerosols (spatially as well as vertically), which need to be addressed, while undertaking new mitigation strategies and to further accelerate the reduction in the air pollution. The RF estimates need to be made while considering these different aerosol types in future analysis.

Chapter 7

Conclusions and Future Scope

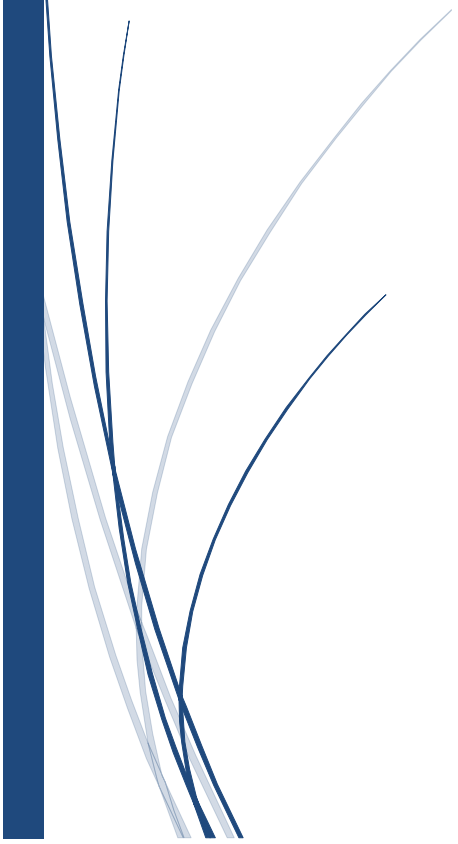

7.1 Conclusions

It is very well known that aerosols have decisive impacts on the local to regional to global climate change. In this regard, one of the essential issues remains to address is the vertical distribution of aerosols, which is a crucial input to the state-of-the-art climate models. However, massive modifications have been observed in the current apprehension of the altitude variations of the aerosols. Where their latest interpretation has elaborated the existence of the EALs in the atmosphere, unlike its conventional understanding. Apparently, the aerosols repercussions are immensely adverse when they are present aloft due to their higher residence time leading to the solar dimming/ brightening events. The effects seem to be different when the absorbing aerosols dominate at these altitudes, which ultimately affect the thermodynamic stability of the atmosphere and the cloud properties.

To address this crucial issue, the essential requirements involves the availability of long-term datasets (discussed in **Chapter 2**) probing the vertical distribution (from surface to 30 km) of the aerosols. Considering this, in **Chapter 3**, we have chosen a remote location in the SI (i.e., Gadanki) region, where the datasets from the combined MPL (2010-2018) as well as Mie (1998-2018) LIDARs are accessible. Using this dataset, analysis of the vertical distribution of aerosols optical properties has depicted the existence of co-located EALs, one in the lower troposphere identified using MPL and another in the UTLS region identified using the Mie LIDAR. These EALs are formed mainly during ISM period and have vertically expanded in the lower troposphere (UTLS) region from 2 to 5 km (15 to 18 km) altitude with the magnitude of α_{aer} values of ~ 0.15 (> 0.002) km^{-1}, as seen in **Figure 7.1a**. However, during the winter season, aerosols are mostly confined within the boundary layer altitude.

The background meteorology/ dynamics has shown the prevalence of LLJ (TEJ) persisting during the ISM in the lower troposphere (UTLS) region. Whereas the back-trajectory analysis (using the HYSPLIT model) has exhibited that the long-range transport brings the oceanic and continental air masses at these altitudes over the region. The contributions from the marine and continental aerosols were confirmed with the dominance of the PD (i.e., DM+SM) aerosols (~44%) in the lower

troposphere (**Figure 7.1b**). Simultaneously, the UTLS region is covered with the SF (~49.7%) and VA (~50.3%) aerosols.

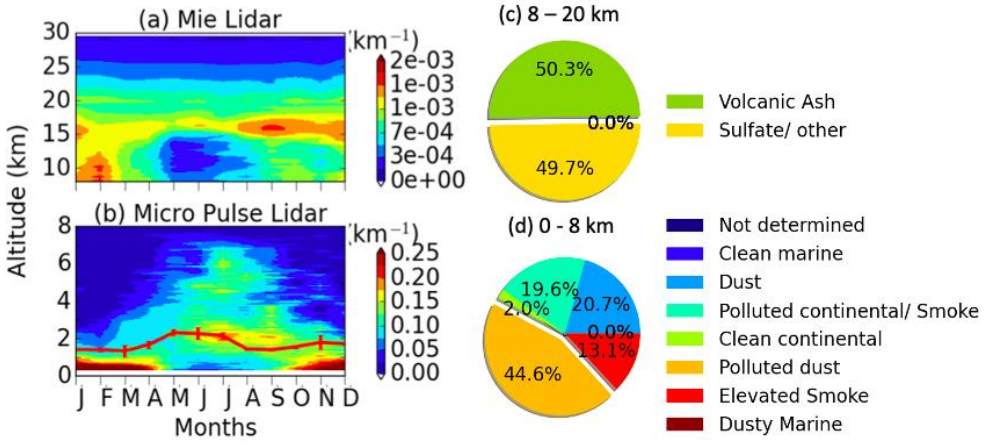

Figure 7.1 *Monthly mean variation of α_{aer} profiles obtained in (a) UTLS, and (b) troposphere, over the Gadanki region. The ABL altitude (red line) detected using radiosonde has been superimposed in (b). Pie Charts representing total aerosol types at (c) 8-20 km and (d) 0-8 km altitudes, obtained over the Gadanki region.*

To examine whether these EALs are only a local phenomenon or have spread across a wider distance, a view of its global distribution is required, for which we have to depend on the satellite observations. And the best accessible sensor available so far to accomplish this objective, is CALIOP. But before that, a comparison has been made between the ground-based and space-borne α_{aer} profiles, where a good correlation has been established between the two independent measurements. With this confidence, their spatial extent has been realized, which has shown that these EALs are distributed in the lower troposphere (UTLS) region, with higher aerosol loading extending from Africa to the South Asian continents (ME to the China Sea regions) when averaged between 2 to 3 km (16 to 18 km) altitudes.

These results have shown a considerable variation in dispersal of the aerosols across the globe, where the African and South Asian continents are exhibiting relatively higher aerosols loadings, than the rest of the world. Thus, to acknowledge the reason behind this disparity, we have comprehended the profound insights of their region-wise optical, physical, morphological, and chemical properties. Not solely their distribution but this study has also undertaken the long-term changes isolating the above seen meteorology aspects (using the MLR model), due to these different aerosol properties on the atmosphere as well.

Note that analysing all these aerosol properties globally at a time is a massive task, for which one has to depend on the multiple space-borne sensors (such as MODIS, CALIOP, and MISR, in this study). In addition to this, the reanalysis (like MERRA-2) dataset can also provide various aerosol properties and hence has been used in the study. But before employing all these datasets (detailed in **Chapter 2**), they have been compared primarily with the 82 ground-based AERONET (considered as ground truth) stations, spread across the globe. The AOD parameter, which is an integration of the α_{aer} from the surface to TOA, is used here to assess these measurements. And high (above 0.7) to medium (from 0.3 to 0.7) correlation values have been perceived among all the sensors, except CALIOP. However, an overall decent agreement has been established amidst all the independent sensors (ground-based, space-borne, and reanalysis).

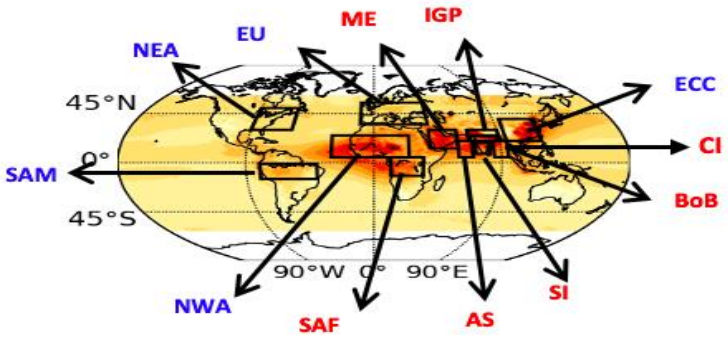

Figure 7.2 *Region-wise long-term total AOD trends obtained across the globe, where the increasing (decreasing) trend regions are marked with red (blue) color. Here, the selected regions (NEA, SAM, NWA, SAF, AS, SI, BoB, ECC, CI, IGP, ME, and EU) are plotted on the total annual mean AOD values.*

Utilizing all these datasets, the global distribution of the aerosols has shown (in **Chapter 4**) comparatively higher AOD loading over the NWA, SAF, IGP, ME, and ECC regions, than the rest of the globe. Correspondingly, their long-term trends have demonstrated a statistically significant increase (decrease) in the total AOD values over the Indian, ME, and SAF (NEA, EU, SAM, NWA, and ECC) regions, as shown in **Figure 7.2**. Henceforth, these regions (where significant AOD trends (increasing or decreasing) have been observed) are chosen as the 8 hotspot regions for the further analysis of the aerosol properties mentioned in the following.

Chapter 5 details the evaluation of the aerosols optical, physical, and morphological properties, over the selected hotspot regions. The optical properties considered in this study includes the discussions about the aerosols absorbing (i.e., aAOD) and scattering (i.e., sAOD) characteristics (**Figure 7.3**). Specifically, aAOD properties are decreasing (increasing) over the EU, ECC, and NWA (SAF) regions, which are in conferment with their total AOD trends. Notwithstanding, despite the overall increasing AOD trends over the Indian region, the IGP and CI have slightly decreased due to their aAOD properties. Further, the sAOD has seen an overall decrease (increase) over the NEA, SAM, EU, and ECC (SAF and whole Indian) regions. However, a disparity has been found over the ME and NWA regions, where the AERONET, MODIS, and MISR (CALIOP and MERRA-2) measurements have given an increase (decrease) in sAOD trends over the region.

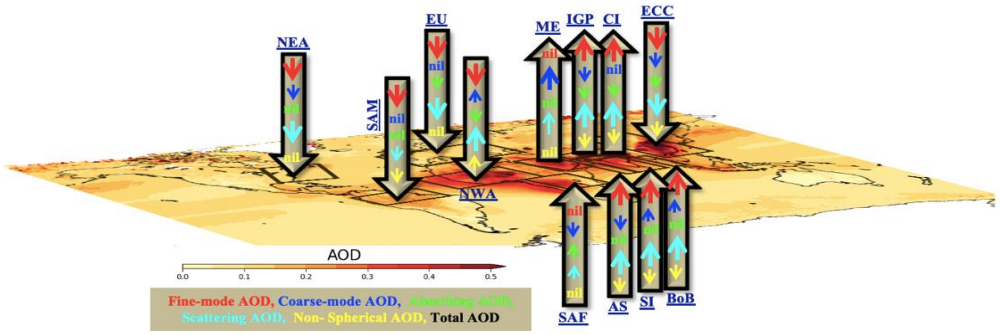

Figure 7.3 *Region-wise trends of the aerosols optical (absorbing AOD, scattering AOD), physical (fine-mode AOD and coarse-mode AOD), and morphological (non-spherical AOD) properties. Here, the selected regions (NEA, SAM, NWA, SAF, AS, CI, SI, BoB, ECC, IGP, ME, and EU) are plotted on the total annual mean AOD.*

The physical properties considered here include discussions about the aerosols size (i.e., fAOD/ cAOD) characteristics (**Figure 7.3**). Specifically, the fAOD properties of the aerosols are decreasing (increasing) over the NEA, SAM, EU, NWA, and ECC (whole Indian) regions. Whereas, the cAOD properties of the aerosols are decreasing (increasing) over the ECC (ME) region. These properties of aerosols agree with the total AOD trends analysed over these regions. But despite the increasing (decreasing) total AOD trends over the SAF, IGP, and AS (NWA), there is a decrease (increase) in the cAOD values.

The morphological properties considered here will include the discussions about the aerosols shape (i.e., nAOD) characteristics (**Figure 7.3**). To be specific,

there is an overall decrease in nAOD over the SAM and ECC regions. Whereas NWA (India) region has observed an increase (decrease) in the nAOD values, which contradicts their overall total AOD trends. However, a decrease between 2 and 7 km altitudes has been observed in the DPR values over the NEA, SAM, EU, NWA, and ECC regions. On the other hand, an increase in the DPR values in the upper altitudes has been noticed over ME, SAF, and the Indian (decrease in the values below 7 km is also spotted) region.

This increase or decrease in aerosols is also seen in connection with the mitigation policies implemented, which will be highly useful in the policymaker's perception in the current times of climate change situations.

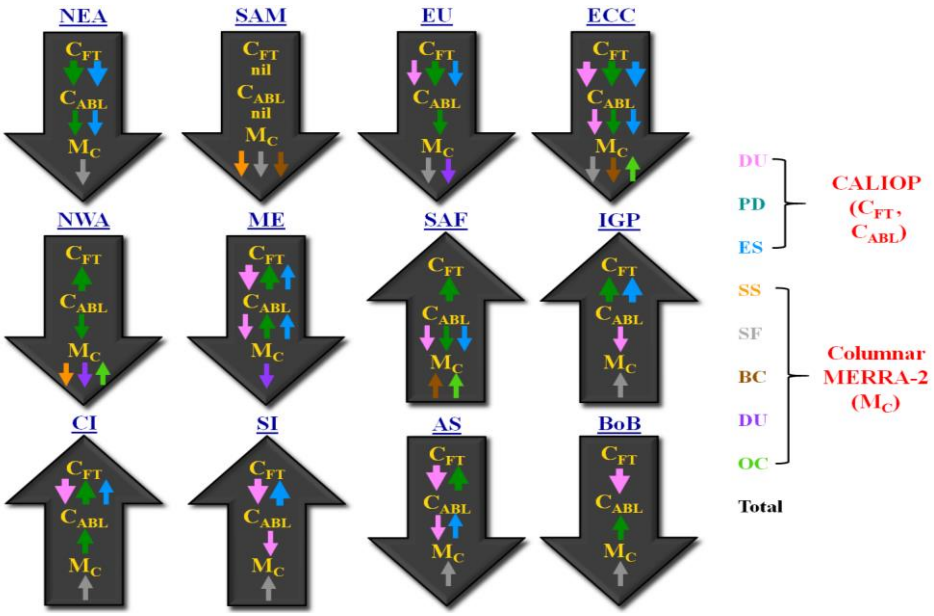

Figure 7.4 *Region-wise trends in the aerosols chemical properties retrieved from the MERRA-2 (columnar, M_c) and CALIOP (at the FT (C_{FT}) and ABL (C_{ABL}) altitudes) datasets. These trends (in the aerosols chemical properties) are over plotted on the total AOD trend values (in black arrows). Here, the selected regions include NEA, SAM, NWA, SAF, AS, CI, SI, BoB, ECC, IGP, ME, and EU.*

Lastly, we have also accounted for the chemical characteristics of the aerosols, both columnar as well as their vertical extent (**Figure 7.4**) in **Chapter 6**. Foremost, the columnar chemical AODs (from MERRA-2) could account for the decrease (increase) due to the SF aerosols over the NEA, SAM, EU, and ECC (whole Indian) regions. Whereas the SS (DU) aerosols are decreasing over the SAM and NWA (EU and NWA) regions. The BC aerosols are increasing (decreasing) over the SAF (SAM

and ECC) region, whereas the OC aerosols are increasing over the ECC, NWA, and SAF regions.

Again, returning to the evaluation of the altitude-wise long-term impacts due to the different aerosol types (DU, PD, and ES from CALIOP), this section is divided into the FT and ABL altitudes over the considered 8 hotspot regions (**Figure 7.4**). Here, the higher decrease in the FT altitudes has been delineated due to the PD aerosols over the NEA, EU, and ECC regions, the DU aerosols over EU, ECC, ME, CI, SI, AS, and BoB regions, and the ES aerosols over the NEA and ECC regions, than the ABL altitudes. However, an increase in the FT altitudes has been spotted due to the PD aerosols mainly over the tropical regions such as NWA, ME, SAF, IGP, CI, and AS regions, whereas the increase is due to the ES aerosols are over the Indian landmass regions.

7.2 Future Scope

To be specific, this study has dealt with the heterogeneity in the spatial and vertical distribution of the aerosols, from the local to regional to global scales. Beginning with the local scale, where over the Gadanki region, the role of the formation of simultaneous EALs has been well explained with the background meteorology/ dynamics. Moving from the local to global perceptive, a complete analysis has been conducted to examine the contributions of the aerosols over the 8 selected hotspot regions across the globe. For which an immense amount of information on the long-term changes due to the aerosols (isolating the background dynamical aspects) has been detailed in this study by analysing their optical, physical, morphological, and chemical properties. Even though, more knowledge still remains to be attained in this perspective, some of which are listed as follows:

(a) For achieving the goal of apprehension of the long-term changes in various aerosol properties, an MLR model has been implemented in this study, where the background contributions due to the naturally occurring oscillations such as ENSO, QBO, and SC, have been isolated. But in the future, it will be interesting to understand the contributions due to these oscillations (especially during the ISM period) to the vertical distribution of the aerosols. For instance, the recent study by Fadnavis et al. (2019) has shown that the draught events are increasing during the El-Niño period due to the presence of these EALs. However, the impacts of the

background contributions such as the changing temperature, RH, zonal wind, and vertical velocity on the vertical distributions due to different aerosols will be a very engaging topic for the henceforward research.

(b) One of the significant impacts of the EALs has involved the solar dimming or brightening events taking place. However, in the past, studies have shown that the surface solar radiations have undergone multi-decadal variations over time with anthropogenic influences (Wild, 2016). Also, Padma Kumari et al. (2007), have shown a decrease in the solar radiations reaching the surface over the Indian region, which increases the maximum and minimum air temperatures over the region. From the current study as well, it is quite prominent that the EALs are increasing mainly near the tropical regions, where these regions serve as the primary source of solar energy and are crucial for our ecosystem. Therefore, the proper analysis can be conducted in the forthcoming studies to evaluate the solar dimming or brightening events in connection with the persisting EALs in the atmosphere.

(c) In this study, vast knowledge about the vertical and spatial distribution of the different types of aerosols has been demonstrated profoundly, where one of the main reasons behind undertaking this study was to serve as the parameterization for the modeling perspective, as there still exists huge uncertainty while making accurate predictions. In this regard, the massive information gathered in this study can be further extended to estimate the RF due to the aerosols different types, provided the synergy of the long-term ground-based, space-borne, and reanalysis datasets. Not only this, but the long-term changes can also be estimated in the RF due to the different types of aerosols, using state-of-the-art artificial intelligence or machine learning approaches.

(d) Lastly, the presence of the absorbing aerosols in the EALs has been well pointed out in this study, which can further lead to the counter Twomey cloud effect as well. The presence of the absorbing aerosols above the cloud altitudes can modify the formation and evolution of clouds. Thus, in the future, the studies on the impacts of the EALs on the cloud formation processes can be marked as a good perspective to be accomplished.

Bibliography

Aas, W., Mortier, A., Bowersox, V., Cherian, R., Faluvegi, G., Fagerli, H., Hand, J., Klimont, Z., et al., 2019. Global and regional trends of atmospheric sulfur. Sci. Rep. 9, 1–11. https://doi.org/10.1038/s41598-018-37304-0

Albrecht, B.A., 1989. Aerosols, Cloud Microphysics, and Fractional Cloudiness. https://www.science.org/doi/10.1126/science.245.4923.1227

Amico, G.D., Amodeo, A., Baars, H., Binietoglou, I., Comeron, A., Pappalardo, G., Serikov, I., Wandinger, U., 2017. WP2-NA2 : Profiling of aerosols and clouds Assessment of all lidar calculus subsystems inside and outside.

Angell and Korshover, W.G.P., 1985. Ground-Based and Satellite Evidence for a pronounced Total Ozone Minimum in Early 1983 and Responsible Atmospheric Layers. https://ui.adsabs.harvard.edu/abs/1985MWRv..113..641A/abstract

Ansmann, A., Althausen, D., Wandinger, U., Franke, K., Muller, D., Wagner, F., Heintzenberg, J., 2000. Vertical profiling of the Indian aerosol plume with six-wavelength lidar during INDOEX: A first case study. Geophys. Res. Lett. 27, 963–966. https://doi.org/10.1029/1999GL010902

Ayompe, L.M., Davis, S.J., Egoh, B.N., 2020. Trends and drivers of African fossil fuel CO2 emissions 1990-2017. Environ. Res. Lett. 15. https://www.proquest.com/docview/2512978058

Baars, H., Ansmann, A., Engelmann, R., Althausen, D., 2008. Continuous monitoring of the boundary-layer top with lidar. https://acp.copernicus.org/articles/8/7281/2008/

Babu, S.S., Moorthy, K.K., Manchanda, R.K., Sinha, P.R., Satheesh, S.K., Vajja, D.P., Srinivasan, S., Kumar, V.H.A., 2011. Free tropospheric black carbon aerosol measurements using high altitude balloon: Do BC layers build their own homes up in the atmosphere? Geophys. Res. Lett. 38, 1–6. https://doi.org/10.1029/2011GL046654

Babu, S.S., Satheesh, S.K., Moorthy, K.K., Dutt, C.B.S., Nair, V.S., Alappattu, D.P., Kunhikrishnan, P.K., 2008. Aircraft measurements of aerosol black carbon from a coastal location in the north-east part of peninsular India during ICARB. J. earth Syst. Sci. 117, 263–271. https://link.springer.com/article/10.1007/s12040-008-0030-1

Banerjee, T., Shitole, A.S., Mhawish, A., Anand, A., Ranjan, R., Khan, M.F., Srithawirat, T., Latif, M.T., Mall, R.K., 2021. Aerosol Climatology Over South and Southeast Asia: Aerosol Types, Vertical Profile, and Source Fields. J. Geophys. Res. Atmos. 126, 1–19. https://doi.org/10.1029/2020JD033554

Basha, G., Ratnam, M.V., 2009. Identification of atmospheric boundary layer height over a tropical station using high-resolution radiosonde refractivity profiles: Comparison with GPS radio occultation measurements. J. Geophys. Res. Atmos. 114. https://agupubs.onlinelibrary.wiley.com/doi/full/10.1029/2008JD011692

Basha, G., Ratnam, M.V., Kishore, P., 2020. Asian summer monsoon anticyclone: trends and variability. Atmos. Chem. Phys. 20, 6789–6801. https://acp.copernicus.org/articles/20/6789/2020/

Bates, T.S., Quinn, P.K., Coffman, D.J., Johnson, J.E., Miller, T.L., Covert, D.S., Wiedensohler, A., Leinert, S., Nowak, A., Neusüss, C., 2001. Regional physical and chemical properties of the marine boundary layer aerosol across the Atlantic during Aerosols99: An overview. J. Geophys. Res. Atmos. 106, 20767–20782.

https://doi.org/10.1029/2000JD900578

Bauer, S.E., Koch, D., Unger, N., Metzger, S.M., Shindell, D.T., Streets, D.G., 2007a. Nitrate aerosols today and in 2030: A global simulation including aerosols and tropospheric ozone. Atmos. Chem. Phys. 7, 5043–5059. https://doi.org/10.5194/acp-7-5043-2007

Bauer, S.E., Mishchenko, M.I., Lacis, A.A., Zhang, S., Perlwitz, J., Metzger, S.M., 2007b. Do sulfate and nitrate coatings on mineral dust have important effects on radiative properties and climate modeling? J. Geophys. Res. Atmos. 112, 1–9. https://doi.org/10.1029/2005JD006977

Bender, F.A.M., Engström, A., Karlsson, J., 2016. Factors controlling cloud albedo in marine subtropical stratocumulus regions in climate models and satellite observations. J. Clim. 29, 3559–3587. https://doi.org/10.1175/JCLI-D-15-0095.1

Berkoff, T.A., Welton, E.J., Campbell, J.R., Scott, V.S., Spinhirne, J.D., 2003. Investigation of Overlap Correction Techniques for the Micro-Pulse Lidar NETwork (MPLNET). Int. Geosci. Remote Sens. Symp. 7, 4395–4397. https://doi.org/10.1109/igarss.2003.1295527

Bollasina, M., Nigam, S., Lau, K.M., 2008. Absorbing aerosols and summer monsoon evolution over South Asia: An observational portrayal. J. Clim. 21, 3221–3239. https://doi.org/10.1175/2007JCLI2094.1

Bourgeois, Q., Ekman, A.M.L., Krejci, R., 2015. Aerosol transport over the andes from the amazon basin to the remote Pacific Ocean: A multiyear CALIOP assessment. J. Geophys. Res. 120, 8411–8425. https://doi.org/10.1002/2015JD023254

Bourgeois, Q., Ekman, A.M.L., Renard, J.B., Krejci, R., Devasthale, A., Bender, F.A.M., Riipinen, I., Berthet, G., Tackett, J.L., 2018. How much of the global aerosol optical depth is found in the boundary layer and free troposphere? Atmos. Chem. Phys. 18, 7709–7720. https://doi.org/10.5194/acp-18-7709-2018

Brooks, I.M., 2003. Finding boundary layer top: Application of a wavelet covariance transform to lidar backscatter profiles. J. Atmos. Ocean. Technol. 20, 1092–1105. http://homepages.see.leeds.ac.uk/~lecimb/publications/JTECH2003.pdf

Brunamonti, S., Jorge, T., Oelsner, P., Hanumanthu, S., Singh, et al, 2018. Balloon-borne measurements of temperature, water vapor, ozone and aerosol backscatter on the southern slopes of the Himalayas during StratoClim 2016-2017. Atmos. Chem. Phys. 18, 15937–15957. https://doi.org/10.5194/acp-18-15937-2018

Buchard, V., Randles, C.A., da Silva, A.M., Darmenov, A., Colarco, P.R., Govindaraju, R., Ferrare, R., Hair, J., Beyersdorf, A.J., Ziemba, L.D., Yu, H., 2017. The MERRA-2 aerosol reanalysis, 1980 onward. Part II: Evaluation and case studies. J. Clim. 30, 6851–6872. https://doi.org/10.1175/JCLI-D-16-0613.1

Bullrich, K., 1964. Scattered Radiation in the Atmosphere and the Natural Aerosol. Adv. Geophys. 10, 99–260. https://doi.org/10.1016/S0065-2687(08)60007-2

Charlson, R.J., Schwartz, S.E., Hales, J.M., Cess, R.D., Coakley, J.J.A., Hansen, J.E., Hofmann, D.J., 1992. Climate forcing by anthropogenic aerosols. Science (80-.). 255, 423–430. https://pubmed.ncbi.nlm.nih.gov/17842894/

Che, H., Gui, K., Xia, X., Wang, Y., Holben, B.N., Goloub, P., Cuevas-Agulló, E., Wang, H., Zheng, Y., Zhao, H., Zhang, X., 2019. Large contribution of meteorological factors to inter-decadal changes in regional aerosol optical depth. Atmos. Chem. Phys. 19, 10497–10523. https://doi.org/10.5194/acp-19-10497-2019

Choi, J.-O., Chung, C.E., 2014. Sensitivity of aerosol direct radiative forcing to aerosol

vertical profile. Tellus B Chem. Phys. Meteorol. 66, 24376. https://www.tandfonline.com/doi/full/10.3402/tellusb.v66.24376

Chowdhury, S., Dey, S., Guttikunda, S., Pillarisetti, A., Smith, K.R., Girolamo, L. Di, 2019. Indian annual ambient air quality standard is achievable by completely mitigating emissions from household sources. Proc. Natl. Acad. Sci. U. S. A. 166, 10711–10716. https://doi.org/10.1073/pnas.1900888116

Coffey, M.T., Mankin, W.G., 1993. Observations of the loss of stratospheric NO2 following volcaniceruptions.Geophys.Res.Lett.20,2873–2876. https://doi.org/10.1029/93GL03151

Colarco, P., Da Silva, A., Chin, M., Diehl, T., 2010. Online simulations of global aerosol distributions in the NASA GEOS-4 model and comparisons to satellite and ground-based aerosol optical depth. J. Geophys. Res. Atmos. 115. https://doi.org/10.1029/2009JD012820

Collis, R.T.H., Russell, P.B., 1976. Lidar measurement of particles and gases by elastic backscattering and differential absorption. Springer Verlag, Berlin, Ger. 71–151. https://doi.org/10.1007/3-540-07743-x_18

De Reus, M., Krejci, R., Williams, J., Fischer, H., Scheele, R., Ström, J., 2001. Vertical and horizontal distributions of the aerosol number concentration and size distribution over the northern Indian Ocean. J. Geophys. Res. Atmos. 106, 28629–28641. https://doi.org/10.1029/2001JD900017

Dentener, F., Kinne, S., Bond, T., Boucher, O., Cofala, J., Generoso, S., Ginoux, P., Gong, S., Hoelzemann, et al., 2006. Emissions of primary aerosol and precursor gases in the years 2000 and 1750 prescribed data-sets for AeroCom. Atmos. Chem. Phys. 6, 4321–4344. https://doi.org/10.5194/acp-6-4321-2006

Deshler, Bryan J. Johnson, David J. Hofmann, and B.N., 1996. Correlations between ozone loss and volcanic aerosol at altitudes below 14 km over McMurdo Station, Antarctica 23, 2931–2934. https://agupubs.onlinelibrary.wiley.com/doi/abs/10.1029/96GL02819

Devara, P.C.S., 1998. Remote sensing of atmospheric aerosols from active and passive optical techniques. Int. J. Remote Sens. 19, 3271–3288. https://doi.org/10.1080/014311698213966

Devi, J., Tripathi, S.N., Gupta, T., Singh, B.N., Gopalakrishnan, V., Dey, S., 2011. Observation-based 3-D view of aerosol radiative properties over Indian Continental Tropical Convergence Zone: Implications to regional climate. Tellus, Ser. B Chem. Phys. Meteorol. 63, 971–989. https://doi.org/10.1111/j.1600-0889.2011.00580

Domingos, J., Jault, D., Pais, M.A., Mandea, M., 2017. The South Atlantic Anomaly throughout the solar cycle. Earth Planet. Sci. Lett. 473, 154–163. https://doi.org/10.1016/j.epsl.2017.06.004

Dong, Z., Li, Z., Yu, X., Cribb, M., Li, X., Dai, J., 2017. Opposite long-term trends in aerosols between low and high altitudes: A testimony to the aerosol-PBL feedback. Atmos. Chem. Phys. 17, 7997–8009. https://doi.org/10.5194/acp-17-7997-2017

Draxler, R.R., Rolph, G.D., 2003. HYSPLIT (HYbrid Single-Particle Lagrangian Integrated Trajectory) Model Access via NOAA ARL READY Website. NOAA Air Resources Laboratory, Silver Spring, MD. http://ready.arl.noaa.gov/HYSPLIT.php

Dunkerton, T.J., 1995. Stratosphere Adjacent To Monsoon Regions Stratosphere Up To a Maximum Height 100. https://agupubs.onlinelibrary.wiley.com/doi/abs/10.1029/95JD01263

Elterman, L., 1967. Aerosol measurements in the troposphere and stratosphere. J. Air Pollut. Control Assoc. 17, 596–596. https://doi.org/10.1080/00022470.1967.10469038

Fadnavis, S., Sabin, T.P., Roy, C., Rowlinson, M., Rap, A., Vernier, J.P., Sioris, C.E., 2019. Elevated aerosol layer over South Asia worsens the Indian droughts. Sci. Rep. 9, 1–12. https://doi.org/10.1038/s41598-019-46704-9

Farman, J.C., Gardiner, B.G., Shanklin, J.D., 1985. Large losses of total ozone in Antarctica. Nature 315, 207–210. https://www.nature.com/articles/315207a0

Fernald, F.G., 1984. Analysis of atmospheric lidar observations: some comments. Appl. Opt. 23, 652–653. https://doi.org/10.1364/AO.23.000652

Filonchyk, M., Hurynovich, V., Yan, H., 2020. Trends in aerosol optical properties over Eastern Europe based on MODIS-Aqua. Geosci. Front. 11, 2169–2181. https://doi.org/10.1016/j.gsf.2020.03.014

Fu, R., Hu, Y., Wright, J.S., Jiang, J.H., Dickinson, R.E., Chen, M., Filipiak, M., Read, W.G., Waters, J.W., Wu, D.L., 2006. Short circuit of water vapor and polluted air to the global stratosphere by convective transport over the Tibetan Plateau. Proc. Natl. Acad. Sci. U. S. A. 103, 5664–5669. https://doi.org/10.1073/pnas.0601584103

Garay, M.J., Witek, M.L., Kahn, R.A., Seidel, F.C., Limbacher, J.A., Bull, M.A., Diner, D.J., Hansen, E.G.E.G., Kalashnikova, O. V., Lee, H., Nastan, A.M., Yu, Y., 2020. Introducing the 4.4km spatial resolution Multi-Angle Imaging SpectroRadiometer (MISR) aerosol product. Atmos. Meas. Tech. 13, 593–628. https://doi.org/10.5194/amt-13-593-2020

Garfinkel, C.I., Hartmann, D.L., 2011. The influence of the quasi-biennial oscillation on the troposphere in winter in a hierarchy of models. Part I: Simplified dry gcms. J. Atmos. Sci. 68, 1273–1289. https://doi.org/10.1175/2011JAS3665.1

Garny, H., Randel, W.J., 2016. Transport pathways from the Asian monsoon anticyclone to the stratosphere. Atmos. Chem. Phys. 16, 2703–2718. https://doi.org/10.5194/acp-16-2703-2016

Gavrouzou, M., Hatzianastassiou, N., Gkikas, A., Korras-Carraca, M.B., Mihalopoulos, N., 2021. A global climatology of dust aerosols based on satellite data: Spatial, seasonal and inter-annual patterns over the period 2005–2019. Remote Sens. 13, 1–31. https://doi.org/10.3390/rs13030359

Gettelman, A., Kinnison, D.E., Dunkerton, T.J., Brasseur, G.P., 2004. Impact of monsoon circulations on the upper troposphere and lower stratosphere. J. Geophys. Res. D Atmos. 109, 1–14. https://doi.org/10.1029/2004JD004878

Ghosh, S., Dey, S., Ganguly, D., Baidya Roy, S., Bali, K., 2022. Cleaner air would enhance India's annual solar energy production by 6–28 TWh. Environ. Res. Lett. 17, 054007. https://doi.org/10.1088/1748-9326/ac5d9a

Gobbi, G.P., Barnaba, F., Van Dingenen, R., Putaud, J.P., Mircea, M., Facchini, M.C., 2003. Lidar and in situ observations of continental and Saharan aerosol: Closure analysis of particles optical and physical properties. Atmos. Chem. Phys. 3, 2161–2172. https://doi.org/10.5194/acp-3-2161-2003

Grant, Edward V. Browell, Jack Fishman, Vincem G. Brackett, Robert E. Veiga,Dominique Nganga,A. Minga,Bernard Cros, Carolyn F. Butler, Marta A. Fenn, Craig S. Long, and L.L.S., 1994. Aerosol-associated changes in tropical stratospheric ozone following the eruption of Mount Pinatubo. https://agupubs.onlinelibrary.wiley.com/doi/abs/10.1029/93JD03314

Gu, Y., Liao, H., Bian, J., 2016. Summertime nitrate aerosol in the upper troposphere and lower stratosphere over the Tibetan Plateau and the South Asian summer monsoon

region. Atmos. Chem. Phys. 16, 6641–6663. https://doi.org/10.5194/acp-16-6641-2016

Gui, K., Che, H., Zheng, Y., Zhao, H., Yao, W., Li, L., Zhang, L., Wang, H., Wang, Y., Zhang, X., 2021. Three-dimensional climatology, trends, and meteorological drivers of global and regional tropospheric type-dependent aerosols: Insights from 13 years (2007-2019) of CALIOP observations. Atmos. Chem. Phys. 21, 15309–15336. https://doi.org/10.5194/acp-21-15309-2021

Gunthe, S.S., Liu, P., Panda, U., Raj, S.S., Sharma, A., Darbyshire, E., Reyes-Villegas, E., et al., 2021. Enhanced aerosol particle growth sustained by high continental chlorine emission in India. Nat. Geosci. 14, 77–84. https://doi.org/10.1038/s41561-020-00677

Gupta, G., Ratnam, M.V., Madhavan, B.L., Prasad, P., Narayanamurthy, C.S., 2021. Vertical and spatial distribution of elevated aerosol layers obtained using long-term ground-based and space-borne lidar observations. Atmos. Environ. 246, 118172. https://doi.org/10.1016/j.atmosenv.2020.118172

Gupta, G., Venkat Ratnam, M., Madhavan, B.L., Narayanamurthy, C.S., 2022. Long-term trends in Aerosol Optical Depth across the globe obtained using multi-satellite measurements. Atmos. Environ. 273, 118953. https://doi.org/10.1016/j.atmosenv.2022.118953.

Gupta, P., Remer, L.A., Levy, R.C., Mattoo, S., 2018. Validation of MODIS 3km land aerosol optical depth from NASA's EOS Terra and Aqua missions. Atmos. Meas. Tech. 11, 3145–3159. https://doi.org/10.5194/amt-11-3145-2018

Gutkowicz-krusin, D., 1993. Multiangle lidar performance in the presence of horizontal inhomogeneities in atmospheric extinction and scattering. Appl. Opt. https://opg.optica.org/ao/fulltext.cfm?uri=ao-32-18-3266&id=40553

Haladay, T., Stephens, G., 2009. Characteristics of tropical thin cirrus clouds deduced from joint CloudSat and CALIPSO observations. J. Geophys. Res. Atmos. 114, 1–13. https://doi.org/10.1029/2008JD010675

Hand, J.L., Schichtel, B.A., Malm, W.C., Copeland, S., Molenar, J. V., Frank, N., Pitchford, M., 2014. Widespread reductions in haze across the United States from the early 1990s through 2011, Atmospheric Environment. Elsevier Ltd. https://doi.org/10.1016/j.atmosenv.2014.05.062

Hand, J.L., Schichtel, B.A., Malm, W.C., Pitchford, M.L., 2012. Particulate sulfate ion concentration and SO2 emission trends in the United States from the early 1990s through 2010. Atmos. Chem. Phys. 12, 10353–10365. https://doi.org/10.5194/acp-12-10353-2012

Hansen, J., Lacis, A., Ruedy, R., Makiko, S., 1992. POTENTIAL CLIMATE IMPACT OF MOUNT PINATUBO ERUPTION. Geophysi 19, 215–218. https://agupubs.onlinelibrary.wiley.com/doi/10.1029/

Hazra, A., Taraphdar, S., Halder, M., Pokhrel, S., Chaudhari, H.S., Salunke, K., Mukhopadhyay, P., Rao, S.A., 2013. Indian summer monsoon drought 2009: Role of aerosol and cloud microphysics. Atmos. Sci. Lett. 14, 181–186. https://doi.org/10.1002/asl2.437

Hegde, P.P. and Y.B.K., 2009. An integrated analysis of lidar observations in association with optical properties of aerosols from a high altitude location in central Himalayas. Atmos. Sci. Lett. 10, 249–254. https://doi.org/10.1002/asl

Herman, J.R., Celarier, E.A., 1997. Earth surface reflectivity climatology 102, 3–11. https://agupubs.onlinelibrary.wiley.com/doi/pdf/10.1029/97JD02074

Hernandez, G., Zawodny, J.M., Cisewski, M.S., Thornton, B., Panetta, A., Roell, M.M., Vernier, J.P., 2014. On the stratospheric aerosol and gas experiment III on the international space station. IEEE Aerosp. Conf. Proc. https://doi.org/10.1109/AERO.2014.6836380

Hersbach, H., Bell, B., Berrisford, P., Hirahara, S., Horányi, et al., 2020. The ERA5 global reanalysis. Q. J. R. Meteorol. Soc. 146, 1999–2049. https://doi.org/10.1002/qj.3803

Hofmann, D.J., Solomon, S., 1989. Ozone destruction through heterogeneous chemistry following the eruption of El Chichon. J. Geophys. Res. 94, 5029–5041. https://doi.org/10.1029/JD094iD04p05029

Holben, B.N., Tanré, D., Smirnov, A., Eck, T.F., Slutsker, et al., 2001. An emerging ground-based aerosol climatology: Aerosol optical depth from AERONET. J. Geophys. Res. Atmos. 106, 12067–12097. https://doi.org/10.1029/2001JD900014

Holben, Brent N, Eck, T.F., Slutsker, I. al, Tanre, D., Buis, J.P., Setzer, A., Vermote, E., Reagan, J.A., Kaufman, Y.J., Nakajima, T., others, 1998. AERONET—A federated instrument network and data archive for aerosol characterization. Remote Sens. Environ. 66, 1–16. https://www.sciencedirect.com/science/article/abs/pii/S0034425798000315

Holton, H.T., 1980. The influence of the Equatorial Quasi-Biennial Oscillation on the Global Circulation at 50 mb. J. Atmos. Sci. https://ui.adsabs.harvard.edu/abs/1980JAtS...37.2200H/abstract

Hommel, R., Timmreck, C., Giorgetta, M.A., Graf, H.F., 2015. Quasi-biennial oscillation of the tropical stratospheric aerosol layer. Atmos. Chem. Phys. 15, 5557–5584. https://doi.org/10.5194/acp-15-5557-2015. https://doi.org/10.1088/1748-9326/abc64f

Hsu, 2012. Global and regional trends of aerosol optical depth over land and ocean using SeaWiFS measurements from 1997 to 2010. Atmos. Chem. Phys. Discuss. 12, 8465–8501. https://doi.org/10.5194/acpd-12-8465-2012

Huebert,Timothy Bates,Philip B. Russell, Guangyu Shi, Young Joon Kim,Kimitaka Kawamura, Greg Carmichael, and T.N., 2003. An overview of ACE-Asia: Strategies for quantifying the relationships between Asian aerosols and their climatic impacts. https://agupubs.onlinelibrary.wiley.com/doi/full/10.1029/2003JD003550

Husar, R.B., Prospero, J.M., Stowe, L.L., 1997. Characterization of tropospheric aerosols over the oceans with the NOAA advanced very high resolution radiometer optical thickness operational product. J. Geophys. Res. Atmos. 102, 16889–16909. https://doi.org/10.1029/96jd04009

IICT Policy Update, 2016. India bharat stage VI emission standards. Int. Counc. Clean Transp. 10. https://theicct.org/sites/default/files/publications/India%20BS%20VI%20Policy%20Update%20vF.pdf

IPCC, 2013. IPCC CLIMATE CHANGE 2013 Climate Change 2013, Researchgate.Net. https://doi.org/10.1017/CBO9781107415324

IPCC, 2021. Climate Change 2021. Phys. Sci. Basis. Contrib. Work. Gr. 1 to Sixth Assess. Rep. Intergov. Panel Clim. Chang. https://www.ipcc.ch/assessment-report/ar6/

Jacobson, M.Z., 2016. Strong radiative heating due to mixing state of black carbon in atmospheric aerosol . mixing state of black carbon in atmospheric aerosols 409, 695–697. https://www.nature.com/articles/35055518

Jain, C.D., Madhavan, B.L., Ratnam, M.V., 2019. Source apportionment of rainwater

chemical composition to investigate the transport of lower atmospheric pollutants to the UTLS region. Environ. Pollut. 248, 166–174. https://doi.org/10.1016/j.envpol.2019.02.007

Jayaraman, A., Ramachandran, S., Acharya, Y.B., Subbaraya, B.H., 1995. Pinatubo volcanic aerosol layer decay observed at Ahmedabad (23 degrees N), India, using neodymium:yttrium/aluminium/garnet backscatter lidar. J. Geophys. Res. 100. https://agupubs.onlinelibrary.wiley.com/doi/abs/10.1029/95JD02195

Jensen, E.J., Diskin, G., Lawson, R.P., Lance, S., Bui, T.P., Hlavka, D., McGill, M., Pfister, L., Toon, O.B., Gaog, R., 2013. Ice nucleation and dehydration in the Tropical Tropopause Layer. Proc. Natl. Acad. Sci. U. S. A. 110, 2041–2046. https://doi.org/10.1073/pnas.1217104110

Jin, Q., Wei, J., Lau, W.K.M., Pu, B., Wang, C., 2021. Interactions of Asian mineral dust with Indian summer monsoon: Recent advances and challenges. Earth-Science Rev. 215, 103562. https://doi.org/10.1016/j.earscirev.2021.103562

Johnston, Mckenzie, R.L., Keys, J.G., Matthews, W.., 1992. OBSERVATIONS OF DEPLETED STRATOSPHERIC NO2 FOLLOWING THE PINATUBO VOLCANIC ERUPTION. Geophys. Res. Lett. 19, 211–213. https://agupubs.onlinelibrary.wiley.com/doi/abs/10.1029/92GL00043

Junge, C.W.C. and J.E.M., 1960. Stratospheric Aerosols. https://agupubs.onlinelibrary.wiley.com/doi/abs/10.1029/JZ066i007p02163

Kahn, R.A., Gaitley, B.J., 2015. Journal of Geophysical Research : Atmospheres An analysis of global aerosol type as retrieved by MISR. https://doi.org/10.1002/2015JD023322

Kahn, R.A., Gaitley, B.J., Garay, M.J., Diner, D.J., Eck, T.F., Smirnov, A., Holben, B.N., 2010. Multiangle Imaging SpectroRadiometer global aerosol product assessment by comparison with the Aerosol Robotic Network. J. Geophys. Res. Atmos. 115. https://doi.org/10.1029/2010JD014601

Kahnert, M., 2017. Optical properties of black carbon aerosols encapsulated in a shell of sulfate: comparison of the closed cell model with a coated aggregate model. Opt. Express 25, 24579. https://doi.org/10.1364/oe.25.024579

Kandler, K., Lieke, K., Benker, N., Emmel, C., others, 2011. Electron microscopy of particles collected at Praia, Cape Verde, during the Saharan Mineral Dust Experiment: particle chemistry, shape, mixing state and complex refractive index. Tellus B Chem. Phys. Meteorol. 63, 475–496. https://www.tandfonline.com/doi/abs/10.1111/j.1600-0889.2011.00550.x

Kaskaoutis, D.G., 2011. Contrasting aerosol trends over South Asia during the last decade based on MODIS observations. Atmos. Meas. Tech. Discuss. 4, 5275–5323. https://doi.org/10.5194/amtd-4-5275-2011

Kaufman, P. V. Hobbs, V. W. J. H. Kirchhoff, P. Artaxo, L. A. Remer, et al., 1998. Smoke, Clouds, and Radiation-Brazil (SCAR-B) experiment. https://agupubs.onlinelibrary.wiley.com/doi/abs/10.1029/98JD02281

Kaufman, Y.J., Smirnov, A., Holben, B.N., Dubovik, O., 2001. Baseline maritime aerosol: Methodology to derive the optical thickness and scattering properties. Geophys. Res. Lett. 28, 3251–3254. https://doi.org/10.1029/2001GL013312

Kaufman, Y.J., Wald, A.E., Remer, L.A., Gao, B.C., Li, R.R., Flynn, L., 1997. MODIS 2.1-μm channel - correlation with visible reflectance for use in remote sensing of aerosol. IEEE Trans. Geosci. Remote Sens. 35, 1286–1298. https://doi.org/10.1109/36.628795

Kaur, R., Pandey, P., 2021. Air Pollution, Climate Change, and Human Health in Indian Cities:ABrief Review. Front. Sustain. Cities 3. https://doi.org/10.3389/frsc.2021.705131

Kent, G.S., Farrukh, U.O., Wang, P.H., Deepak, A., 1988. SAGE I and SAM II Measurements of 1 μm Aerosol Extinction in the Free Troposphere. J. Appl. Meteorol. https://doi.org/10.1175/1520-0450(1988)027

Khalizov, A.F., Xue, H., Wang, L., Zheng, J., Zhang, R., 2009. Enhanced light absorption and scattering by carbon soot aerosol internally mixed with sulfuric acid. J. Phys. Chem. A 113, 1066–1074. https://doi.org/10.1021/jp807531n

Khan, B., Stenchikov, G., Weinzierl, B., Kalenderski, S., Osipov, S., 2015. Dust plume formation in the free troposphere and aerosol size distribution during the Saharan Mineral Dust Experiment in North Africa. Tellus, Ser. B Chem. Phys. Meteorol. 6. https://doi.org/10.3402/tellusb.v67.27170

Kim, M.H., Omar, A.H., Tackett, J.L., Vaughan, M.A., Winker, D.M., Trepte, C.R., Hu, Y., Liu, Z., Poole, L.R., Pitts, M.C., Kar, J., Magill, B.E., 2018. The CALIPSO version 4 automated aerosol classification and lidar ratio selection algorithm. Atmos. Meas. Tech. 11, 6107–6135. https://doi.org/10.5194/amt-11-6107-2018

Kim, Y.-S., Shibata, T., Iwasaka, Y., Shi, G., Zhou, X., Tamura, K., Ohashi, T., 2003. Enhancement of aerosols near the cold tropopause in summer over Tibetan Plateau: lidar and balloonborne measurements in 1999 at Lhasa, Tibet, China. Lidar Remote Sens. Ind. Environ. Monit. III 4893, 496. https://doi.org/10.1117/12.466090

Kirchstetter, T.W., Novakov, T., Hobbs, P. V., 2004. Evidence that the spectral dependence of light absorption by aerosols is affected by organic carbon. J. Geophys. Res. D Atmos. 109, 1–12. https://doi.org/10.1029/2004JD004999

Klett, J.D., 1981. Stable analytical inversion solution for processing lidar returns. Appl. Opt. 20, 211. https://doi.org/10.1364/ao.20.000211

Klimont, Z., Smith, S.J., Cofala, J., 2013. The last decade of global anthropogenic sulfur dioxide: 2000-2011 emissions. Environ. Res. Lett. 8. https://doi.org/10.1088/1748-9326/8/1/014003

Klingmüller, K., Pozzer, A., Metzger, S., Stenchikov, G.L., Lelieveld, J., 2016. Aerosol optical depth trend over the Middle East. Atmos. Chem. Phys. 16, 5063–5073. https://doi.org/10.5194/acp-16-5063-2016

Kloss, C., Sellitto, P., Legras, B., Vernier, J.-P., Jégou, F., et al., 2020. Impact of the 2018 Ambae eruption on the global stratospheric aerosol layer and climate. J. Geophys. Res. Atmos. e2020JD032410. https://agupubs.onlinelibrary.wiley.com/doi/full/10.1029/2020JD032410

Kobayashi, H., Hayashi, M., Shiraishi, K., Nakura, Y., Enomoto, T., Miura, K., Takahashi, H., Igarashi, Y., Naoe, H., Kaneyasu, N., others, 2014. Development of a polarization optical particle counter capable of aerosol type classification. Atmos. Environ. 97, 486–492. https://www.sciencedirect.com/science/article/abs/pii/S1352231014003537

Koike, Kondo, Y., Matthews, W.A., Johnston, P. V, Yamazaki, K., 1993. DECREASE OF STRATOSPHERIC NO2 AT 44oN CAUSED BY PINATUBO VOLCANIC AEROSOLS. https://agupubs.onlinelibrary.wiley.com/doi/10.1029/93GL01800

Kompalli, S.K., Babu, S.N.S., Moorthy, K.K., Satheesh, S.K., Gogoi, M.M., Nair, V.S., Jayachandran, V.N., Liu, D., Flynn, M.J., Coe, H., 2021. Mixing state of refractory black carbon aerosol in the South Asian outflow over the northern Indian Ocean during winter. Atmos. Chem. Phys. 21, 9173–9199. https://doi.org/10.5194/acp-21-9173-2021

Kosaka, Y., Xie, S.P., 2013. Recent global-warming hiatus tied to equatorial Pacific surface cooling. Nature 501, 403–407. https://doi.org/10.1038/nature12534

Krotkov, N.A., McLinden, C.A., Li, C., Lamsal, L.N., Celarier, E.A., Marchenko, et al., 2016. Aura OMI observations of regional SO2 and NO2 pollution changes from 2005 to 2015. Atmos. Chem. Phys. 16, 4605–4629. https://doi.org/10.5194/acp-16-4605-2016

Kulkarni, P., Ramachandran, S., Bhavani Kumar, Y., Narayana Rao, D., Krishnaiah, M., 2008. Features of upper troposphere and lower stratosphere aerosols observed by lidar over Gadanki, a tropical Indian station. J. Geophys. Res. Atmos. 113. https://agupubs.onlinelibrary.wiley.com/doi/full/10.1029/2007JD009411

Kumar, A., Pratap, V., Kumar, S., Singh, A.K., 2022. Atmospheric aerosols properties over Indo-Gangetic Plain: A trend analysis using ground – Truth AERONET data for the year 2009–2017. Adv. Sp. Res. https://doi.org/10.1016/j.asr.2021.12.052

Kumar, K.R., Sivakumar, V., Yin, Y., Reddy, R.R., Kang, N., Diao, Y., Adesina, A.J., Yu, X., 2014. Long-term (2003-2013) climatological trends and variations in aerosol optical parameters retrieved from MODIS over three stations in South Africa. Atmos. Environ. 95, 400–408. https://doi.org/10.1016/j.atmosenv.2014.07.001

Kumar, Y.B., Murthy, M.S., Krishnaiah, M., 2010. Development of LiDAR techniques for environmental remote sensing. Int. J. Eng. Sci. Technol 2, 5872–5881. https://citeseerx.ist.psu.edu/viewdoc/download?doi=10.1.1.625.4370&rep=rep1&type=pdf

Kunz, G.J., de Leeuw, G., 1993. Inversion of lidar signals with the slope method. Appl. Opt. 32, 3249. https://doi.org/10.1364/ao.32.003249

Lau, K. M., and K. M. Kim (2007), Does aerosol strengthen or weaken the Asian Monsoon?, in *Mountains: Witnesses of Global Change*, R. Baudo, G. Tartari, and E. Vuillermoz (Eds.), Elsevier B. V., Amsterdam, The Netherlands.

Lau, K. M., and K. M. Kim (2011), Effects of dust and black carbon on the variability of the South Asian monsoon, in *The Global Monsoon System: Research and Forecast*, edited by C. P. Chang, pp. 569–581, World Scientific Pub., Singapore. https://www.worldscientific.com/doi/10.1142/9789814343411_0033

Lau, K.M., Kim, K.M., 2006. Observational relationships between aerosol and Asian monsoon rainfall, and circulation. Geophys. Res. Lett. 33, 1–5. https://doi.org/10.1029/2006GL027546

Lawrence, M.G., Lelieveld, J., 2010. Atmospheric pollutant outflow from southern Asia: A review. Atmos. Chem. Phys. 10, 11017–11096. https://doi.org/10.5194/acp-10-11017-2010

Levy, R.C., Mattoo, S., Munchak, L.A., Remer, L.A., Sayer, A.M., Patadia, F., Hsu, N.C., 2013. The Collection 6 MODIS aerosol products over land and ocean. Atmos. Meas. Tech. 6, 2989–3034. https://doi.org/10.5194/amt-6-2989-2013

Levy, R.C., Remer, L.A., Dubovik, O., 2007. Global aerosol optical properties and application to Moderate Resolution Imaging Spectroradiometer aerosol retrieval over land. J. Geophys. Res. Atmos. 112, 1–15. https://doi.org/10.1029/2006JD007815

Li, J., Von Salzen, K., Peng, Y., Zhang, H., Liang, X.Z., 2013. Evaluation of black carbon semi-direct radiative effect in a climate model. J. Geophys. Res. Atmos. 118, 4715–4728. https://doi.org/10.1002/jgrd.50327

Li, M., Klimont, Z., Zhang, Q., Martin, R. V., Zheng, B., Heyes, C., Cofala, J., Zhang, Y., He, K., 2018. Comparison and evaluation of anthropogenic emissions of SO2 and NOx

over China. Atmos. Chem. Phys. 18, 3433–3456. https://doi.org/10.5194/acp-18-3433-2018

Li, X., Maring, H., Savoie, D., Voss, K., Prospero, J.M., 1996. Dominance of mineral dust in aerosol light-scattering in the North Atlantic trade winds. Nature 380, 416–419. https://doi.org/10.1038/380416a0

Li, Z., Lau, W.K.M., Ramanathan, V., Wu, G., Ding, Y., Manoj, M.G., Liu, et al., 2016. Aerosol and monsoon climate interactions over Asia. Rev. Geophys. 54, 866–929. https://doi.org/10.1002/2015RG000500

Liang, L., Gong, P., 2020. Urban and air pollution: a multi-city study of long-term effects of urban landscape patterns on air quality trends. Sci. Rep. 10, 1–13. https://doi.org/10.1038/s41598-020-74524-9

Lim, S., Lee, M., Kim, S.W., Laj, P., 2018. Sulfate alters aerosol absorption properties in East Asian outflow. Sci. Rep. 8, 1–7. https://doi.org/10.1038/s41598-018-23021-1

Liu, B., Ma, Y., Gong, W., Zhang, M., 2017. Observations of aerosol color ratio and depolarization ratio over Wuhan. Atmos. Pollut. Res. 8, 1113–1122. https://doi.org/10.1016/j.apr.2017.04.004

Ma, X., Jia, H., Tian, R., Yu, F., Li, J., 2020. Mixing state of black carbon and its impact on optical properties and radiative forcing over East Asia. Atmos. Chem. Phys. Discuss. 1, 1–21. https://acp.copernicus.org/preprints/acp-2020-54/

Madhavan, B.L., Krishnaveni, A.S., Ratnam, M.V., Ravikiran, V., 2021. Climatological aspects of size-resolved column aerosol optical properties over a rural site in the southernpeninsularIndia.Atmos.Res.249.https://doi.org/10.1016/j.atmosres.2020.105345

Mamouri, R.-E., Amiridis, V., Papayannis, A., et al., 2009. Validation of CALIPSO space-borne-derived attenuated backscatter coefficient profiles using a ground-based lidar in Athens, https://amt.copernicus.org/articles/2/513/2009/

Man-Hae, K., Omar, A.H., Tackett, J.L.,., others, 2018. The CALIPSO version 4 automated aerosol classification and lidar ratio selection algorithm. Atmos. Meas. Tech. 11, 6107. https://amt.copernicus.org/articles/11/6107/2018/

Manoj, M.R., Satheesh, S.K., Moorthy, K.K., Gogoi, M.M., Babu, S.S., 2019. Decreasing Trend in Black Carbon Aerosols Over the Indian Region. Geophys. Res. Lett. 46, 2903–2910. https://doi.org/10.1029/2018GL081666

Maring, D. L. Savioe, M. A. Izaguirre, and L.C., 2003. Vertical distributions of dust and sea-salt aerosols over Puerto Rico during PRIDE measured from a light aircraft. https://agupubs.onlinelibrary.wiley.com/doi/full/10.1029/2002JD002544

Mark, D. (1998), Atmospheric Aerosol Sampling, in Atmsopheric Particles, edited byR.M. Harrison and R. Van Grieken, pp. 29-94, John Wiley & Sons.

Martonchik, J. V., Diner, D.J., Kahn, R.A., Ackerman, T.P., Verstraete, M.M., Pinty, B., Gordon, H.R., 1998. Techniques for the retrieval of aerosol properties over land and ocean using multiangle imaging. IEEE Trans. Geosci. Remote Sens. 36, 1212–1227. https://doi.org/10.1109/36.701027

Masson-Delmotte, V., P.Z., Pörtner, H.-O., Roberts, D., Skea, J., Shukla, P.R., Pirani, A., Moufouma-Okia, W., Péan, C., Pidcock, R., Connors, S., Matthews, J.B.R., Chen, Y., Zhou, X., Gomis, M.I., Lonnoy, E., Maycock, T., Tignor, M., Waterfield, and T., 2018. Global Warming of 1.5°C. IPCC 291, 285. https://doi.org/10.1038/291285a0

McCormick, M.P., 1987. Sage II: An overview. Adv. Sp. Res. 7, 219–226.

https://doi.org/10.1016/0273-1177(87)90151-7

McFarquhar, G.M., Heymsfield, A.J., Spinhirne, J., Hart, B., 2000. Thin and subvisual tropopause tropical cirrus: Observations and radiative impacts. J. Atmos. Sci. 57, 1841–1853. https://doi.org/10.1175/1520-0469(2000)057

Mehta, M., 2015. A study of aerosol optical depth variations over the Indian region using thirteen years (2001-2013) of MODIS and MISR Level 3 data. Atmos. Environ. 109, 161–170. https://doi.org/10.1016/j.atmosenv.2015.03.021

Mehta, M., Singh, N., Anshumali, 2018. Global trends of columnar and vertically distributed properties of aerosols with emphasis on dust, polluted dust and smoke - inferences from 10-year long CALIOP observations. Remote Sens. Environ. 208, 120–132. https://doi.org/10.1016/j.rse.2018.02.017

Mehta, M., Singh, R., Singh, A., Singh, N., Anshumali, 2016. Recent global aerosol optical depth variations and trends - A comparative study using MODIS and MISR level 3 datasets.Remote Sens. Environ. 181, 137–150. https://doi.org/10.1016/j.rse.2016.04.004

Mehta, Masatomo Fujiwara, Susann Tegtmeier, M. Venkat Ratnam, S., Fadnavis, M.S., Schlager, and H., 2020. International Conference on the Asian Summer Monsoon Anticyclone : Gateway of surface pollutants to the stratosphere To : Earth Science Department Indian Institute of Technology Invitation to attend the International Conference on the Asian Summer Monsoon 603203. https://doi.org/10.13140/RG.2.2.16807.98728

Mie, 1908. Beiträge zur Optik trüber Medien, speziell kolloidaler Metallösungen. Annalen Der Physik,. https://onlinelibrary.wiley.com/doi/10.1002/andp.19083300302

Mielonen, 2010. EVALUATION AND APPLICATION OF PASSIVE AND ACTIVE OPTICAL REMOTE SENSING METHODS FOR THE MEASUREMENT OF ATMOSPHERIC AEROSOL PROPERTIES. https://helda.helsinki.fi/bitstream/handle/10138/23901/Contributions85.pdf?sequence=1

Mishra, M.K., Rajeev, K., Thampi, et al., 2010. Micro pulse lidar observations of mineral dust layer in the lower troposphere over the southwest coast of Peninsular India during the Asian summer monsoon season. J. Atmos. solar-terrestrial Phys. 72, 1251–1259. https://www.sciencedirect.com/science/article/abs/pii/S1364682610002452

Mitchell, J.F.B., Johns, T.C., 1997. On modification of global warming by sulfate aerosols. J. Clim.10,245–267.https://doi.org/10.1175/1520-0442(1997)010

Mohanakumar, K., 2008. Transport Processes in the Stratosphere and Troposphere. Stratos. Troposph. Interact. An Introd. 307–329.

MoPNG, 2016. Pradhan Mantri Ujjwala Yojana (PMUY) - modalities for implementation. https://mopng.gov.in/en/marketing/pmuy

Müller, D., Ansmann, A., Mattis, I., Tesche, M., Wandinger, U., Althausen, D., Pisani, G., 2007. Aerosol-type-dependent lidar ratios ob-695 served with Raman lidar. J. Geophys. Res. Atmos. 112. https://ui.adsabs.harvard.edu/abs/2007JGRD..11216202M/abstract

Myhre, G., Myhre, C.E.L., Bjorn H.Samset, Oslo, Trude Storelvmo, 2013. Aerosols and their Relation to Global Climate and Climate Sensitivity. Nat. Educ. Knowl. https://www.nature.com/scitable/knowledge/library/aerosols-and-their-relation-to-global-climate-102215345/

Nair, V.S., Babu, S.S., Moorthy, K.K., Sharma, A.K., Marinoni, A., Ajai, 2013. Black carbon aerosols over the Himalayas: Direct and surface albedo forcing. Tellus, Ser. B Chem. Phys. Meteorol. 65. https://doi.org/10.3402/tellusb.v65i0.19738

Nandini, G., Vinoj, V., Pandey, S.K., 2022. Arabian Sea Aerosol-Indian Summer Monsoon Rainfall relationship and its modulation by El-Nino Southern Oscillation. npj Clim. Atmos. Sci. 5. https://doi.org/10.1038/s41612-022-00244-8

Neter, J., 1983. John Neter_Applied Linear Regression Models.pdf.

Niemeier, U., Schmidt, H., 2017. Changing transport processes in the stratosphere by radiative heating of sulfate aerosols. Atmos. Chem. Phys. 17, 14871–14886. https://doi.org/10.5194/acp-17-14871-2017

Niranjan, Kandula, Madhavan, B.L., Sreekanth, V., 2007. Micro pulse lidar observation of high altitude aerosol layers at Visakhapatnam located on the east coast of India. Geophys. Res. Lett. 34, 5–9. https://doi.org/10.1029/2006GL028199

Niu, H., Kang, S., Wang, Y., Chandan, S., Rupakheti, D., Qian, Y., 2020. Measurements of light-absorbing impurities in snow over four glaciers on the Tibetan Plateau. Atmos. Res. 105002. https://www.sciencedirect.com/science/article/pii/S0169809520301319

NOAA, 2016: State of the Climate: Global Climate Report for Annual 2015.National Oceanic and Atmospheric Administration (NOAA) National Centers for Environmental Information (NCEI). Retrieved from:www.ncdc.noaa.gov/sotc/global/201513.

O ' Neill, N., Eck, T., Smirnov, A., Holben, B., 2008. Spectral Deconvolution Algorithm (SDA) Technical memo. Aeronet/Photons. https://aeronet.gsfc.nasa.gov/new_web/PDF/tauf_tauc_technical_memo.pdf

Omar, A.H., Winker, D.M., Kittaka, C., Vaughan, M.A., Liu, Z., Hu, Y., Trepte, C.R., Rogers, R.R., Ferrare, R.A., Lee, K.P., Kuehn, R.E., Hostetler, C.A., 2009. The CALIPSO automated aerosol classification and lidar ratio selection algorithm. J. Atmos. Ocean. Technol. 26, 1994–2014. https://doi.org/10.1175/2009JTECHA1231.1

Padma Kumari, B., Londhe, A.L., Daniel, S., Jadhav, D.B., 2007. Observational evidence of solar dimming: Offsetting surface warming over India. Geophys. Res. Lett. 34, 1–5. https://doi.org/10.1029/2007GL031133

Padmakumari, B., Maheskumar, R.S., Morwal, S.B., Harikishan, G., Konwar, M., Kulkarni, J.R., Goswami, B.N., 2013. Aircraft observations of elevated pollution layers near the foothills of the Himalayas during CAIPEEX-2009. Q. J. R. Meteorol. Soc. 139, 625–638. https://doi.org/10.1002/qj.1989

Pan, X.L., Uno, I., Hara, Y., Osada, K., Yamamoto, S., Wang, Z., Sugimoto, N., Kobayashi, H., Wang, Z.F., 2016. Polarization properties of aerosol particles over western Japan: classification, seasonal variation, and implications for air quality. Atmos. Chem. Phys. Discuss. 1–24. https://doi.org/10.5194/acp-2015-904

Pandey, S.K., Vinoj, V., Landu, K., Babu, S.S., 2017. Declining pre-monsoon dust loading over South Asia: Signature of a changing regional climate. Sci. Rep. 7, 1–10. https://doi.org/10.1038/s41598-017-16338-w

Pandit, A K, Gadhavi, H.S., Ratnam, M.V., Raghunath, K., Rao, S.V.B., Jayaraman, A., 2015. Long-term trend analysis and climatology of tropical cirrus clouds using 16 years of lidar data set over Southern India. Atmos. Chem. Phys. 15. https://acp.copernicus.org/articles/15/13833/2015/

Pandit, A.K., Gadhavi, H., Ratnam, M.V., Jayaraman, A., Raghunath, K., Rao, S.V.B., 2014. Characteristics of cirrus clouds and tropical tropopause layer: Seasonal variation and long-term trends. J. Atmos. Solar-Terrestrial Phys. 121, 248–256. https://doi.org/10.1016/j.jastp.2014.07.008

Pappalardo, G., Amodeo, A., Apituley, A., Comeron, A., Freudenthaler, V., Linné, H.,

Ansmann, A., Bösenberg, J., D'Amico, G., Mattis, I., Mona, L., Wandinger, U., Amiridis, V., Alados-Arboledas, L., Nicolae, D., Wiegner, M., 2014. EARLINET: Towards an advanced sustainable European aerosol lidar network. Atmos. Meas. Tech. 7, 2389–2409. https://doi.org/10.5194/amt-7-2389-2014

Parameswaran, K. O. Rose, a, nd B.V.K.M., 1984. AEROSOL CHARACTERISTICS FROM BISTATIC LIDAR OBSERVATIONS 89, 2541–2552. https://agupubs.onlinelibrary.wiley.com/doi/abs/10.1029/JD089iD02p02541

Park, M., Randel, W.J., Gettelman, A., Massie, S.T., Jiang, J.H., 2007. Transport above the Asian summer monsoon anticyclone inferred from Aura Microwave Limb Sounder tracers. J. Geophys. Res. Atmos. 112. https://agupubs.onlinelibrary.wiley.com/doi/full/10.1029/2006JD008294

Peng, J., Hu, M., Guo, S., Du, Z., Zheng, Jing, Shang, D., Zamora, M.L., Zeng, L., Shao, M., Wu, Y.S., Zheng, Jun, Wang, Y., Glen, C.R., Collins, D.R., Molina, M.J., Zhang, R., 2016. Markedly enhanced absorption and direct radiative forcing of black carbon under polluted urban environments. Proc. Natl. Acad. Sci. U. S. A. 113, 4266–4271. https://doi.org/10.1073/pnas.1602310113

Penning De Vries, M.J.M., Beirle, S., Hörmann, C., Kaiser, J.W., Stammes, P., Tilstra, L.G., Tuinder, O.N.E., Wagner, T., 2015. A global aerosol classification algorithm incorporating multiple satellite data sets of aerosol and trace gas abundances. Atmos. Chem. Phys. 15, 10597–10618. https://doi.org/10.5194/acp-15-10597-2015

Pey, J., Querol, X., Alastuey, A., Forastiere, F., Stafoggia, M., 2013. African dust outbreaks over the Mediterranean Basin during 2001-2011: PM10 concentrations, phenomenology and trends, and its relation with synoptic and mesoscale meteorology. Atmos. Chem. Phys. 13, 1395–1410. https://doi.org/10.5194/acp-13-1395-2013

Pitari, G., Cionni, I., Di Genova, G., Visioni, D., Gandolfi, I., Mancini, E., 2016. Impact of stratospheric volcanic aerosols on age-of-air and transport of long-lived species. Atmosphere (Basel). 7, 149. https://www.mdpi.com/2073-4433/7/11/149

Platt, 1973. Lidar and radiometric Observations of Cirrus Clouds. J. Atmos. Sci. https://journals.ametsoc.org/view/journals/atsc/30/6/15200469_1973_030_1191_larooc_20co2.xml

Prasad, P., Raman, M.R., Ratnam, M.V., Ravikiran, V., Madhavan, B.L., Rao, S.V.B., 2019. Nocturnal, seasonal and intra-annual variability of tropospheric aerosols observed using ground-based and space-borne lidars over a tropical location of India. Atmos. Environ. 213,185198.https://www.sciencedirect.com/science/article/abs/pii/S1352231019303899

Prijith, S.S., Rao, P.V.N., Mohan, M., Sai, M.V.R.S., Ramana, M.V., 2018. Trends of absorption, scattering and total aerosol optical depths over India and surrounding oceanic regions from satellite observations: role of local production, transport and atmospheric dynamics. Environ. Sci. Pollut. Res. 25, 18147–18160. https://doi.org/10.1007/s11356-018-2032-0

Prospero, J.M., 1999. Long-term measurements of the transport of African mineral dust to the southeastern United States: Implications for regional air quality. https://agupubs.onlinelibrary.wiley.com/doi/10.1029/1999JD900072

Provençal, S., Kishcha, P., da Silva, A.M., Elhacham, E., Alpert, P., 2017. AOD distributions and trends of major aerosol species over a selection of the world's most populated cities based on the 1st version of NASA's MERRA Aerosol Reanalysis. Urban Clim. 20, 168–191. https://doi.org/10.1016/j.uclim.2017.04.001

Punge, P. Konopka, M.A.G. and R.M., 2009. Effects of the quasi-biennial oscillation on low-

latitude transport in the stratosphere derived from trajectory calculations. https://agupubs.onlinelibrary.wiley.com/doi/full/10.1029/2008JD010518

Ramachandran, S., Jayaraman, A., 2011. Balloon-borne study of the upper tropospheric and stratospheric aerosols over a tropical station in India. Tellus B Chem. Phys. Meteorol. 55, 820–836. https://www.tandfonline.com/doi/abs/10.3402/tellusb.v55i3.16375

Ramachandran, S., Rupakheti, M., 2021. Trends in physical, optical and chemical columnar aerosol characteristics and radiative effects over South and East Asia: Satellite and ground-based observations. Gondwana Res. https://doi.org/10.1016/j.gr.2021.09.016

Ramachandran, S., Rupakheti, M., Lawrence, M.G., 2020. Aerosol-induced atmospheric heating rate decreases over South and East Asia as a result of changing content and composition. Sci. Rep. https://doi.org/10.1038/s41598-020-76936

Ramanathan, V., Carmichael, G., 2008. Global and regional climate changes due to black carbon. Nat. Geosci. 1, 221–227. https://doi.org/10.1038/ngeo156

Ramanathan, V., Chung, C., Kim, D., Bettge, T., Buja, L., Kiehl, J.T., Washington, W.M., Fu, Q., Sikka, D.R., Wild, M., 2005. Atmospheric brown clouds: Impacts on South Asian climate and hydrological cycle. Proc. Natl. Acad. Sci. U. S. A. 102, 5326–5333. https://doi.org/10.1073/pnas.0500656102

Ramanathan, V., Crutzen, P.J., Lelieveld, J., Mitra, A.P., Althausen, D., Anderson, J., Andreae, M.O., Cantrell, W., Cass, G.R., Chung, C.E., others, 2001. Indian Ocean Experiment: An integrated analysis of the climate forcing and effects of the great Indo-Asian haze. J. Geophys. Res. Atmos. 106, 28371–28398. https://agupubs.onlinelibrary.wiley.com/doi/10.1029/2001JD900133

Randel, W.J., Cobb, J.B., 1994. Coherent variations of monthly mean total ozone and lower stratospheric temperature. J. Geophys. Res. 99, 5433–5447. https://doi.org/10.1029/93JD03454

Randel, W.J., Park, M., 2006. Deep convective influence on the Asian summer monsoon anticyclone and associated tracer variability observed with Atmospheric Infrared Sounder (AIRS). J. Geophys. Res. Atmos. 111. https://agupubs.onlinelibrary.wiley.com/doi/full/10.1029/2005JD006490

Randel, W.J., Park, M., Emmons, L., Kinnison, D., Bernath, P., Walker, K.A., Boone, C., Pumphrey, H., 2010. Asian Monsoon Transport of Pollution to the Stratosphere 328, 611–613. https://pubmed.ncbi.nlm.nih.gov/20339030/

Ratnam, M.V., Prasad, P., Raj, S.T.A., Raman, M.R., Basha, G., 2021. Changing patterns in aerosol vertical distribution over South and East Asia. Sci. Rep. 11, 1–11. https://doi.org/10.1038/s41598-020-79361-4

Ratnam, M.V., Prasad, P., Roja Raman, M., Ravikiran, V., Bhaskara Rao, S.V., Krishna Murthy, B. V., Jayaraman, A., 2018. Role of dynamics on the formation and maintenance of the elevated aerosol layer during monsoon season over south-east peninsular India. Atmos. Environ. 188, 43–49. https://doi.org/10.1016/j.atmosenv.2018.06.023

Ratnam, M.V., Raj, S.T.A., Madhavan, B.L., Vernier, J.P., Kiran, V.R., Jain, C.D., Basha, G., Nagendra, N., Kumar, B.S., Pandit, A.K., others, 2020. Vertically resolved black carbon measurements and associated heating rates obtained using in situ balloon platform. Atmos. Environ. 117541. https://www.sciencedirect.com/science/article/abs/pii/S1352231020302764

Ravi Kiran, V., Venkat Ratnam, M., Krishna Murthy, B. V, Kant, Y., Prasad, P., Roja

Raman, M., Rao, S.V.B., Lakshmi Kumar, T. V, Maitra, A., 2019. An empirical method for source apportionment of black carbon aerosol: Results from Aethalometer observations at five different locations in India. Environ. Pollut. 254, 112932. https://doi.org/https://doi.org/10.1016/j.envpol.2019.07.100

Reddington, C.L., Butt, E.W., Ridley, D.A., Artaxo, P., Morgan, W.T., Coe, H., Spracklen, D. V., 2015. Air quality and human health improvements from reductions in deforestation-related fire in Brazil. Nat. Geosci. 8, 768–771. https://doi.org/10.1038/ngeo2535

Reid, J.S., Piketh, S.J., Walker, A.L., Burger, R.P., Ross, et al., 2008. An overview of UAE2 flight operations: Observations of summertime atmospheric thermodynamic and aerosol profiles of the southern Arabian Gulf. J. Geophys. Res. Atmos. 113, 1–14. https://doi.org/10.1029/2007JD009435

Reis, S., Grennfelt, P., Klimont, Z., Amann, M., ApSimon, H., Hettelingh, J.P., Holland, M., LeGall, A.C., Maas, R., Posch, M., Spranger, T., Sutton, M.A., Williams, M., 2012. From acid rain to climate change. Science (80-.).338, 1153–1154. https://doi.org/10.1126/science.1226514

Report, S.A., America, N., 2016. Towards Cleaner Air Scientific Assessment Report 2016: North America. https://unece.org/environment-policy/publications/towards-cleaner-air-scientific-assessment-report-2016

Reus, M. De, Krejci, R., Williams, J., Fischer, H., Scheele, R., Strm, J., 2001. particle loss rate is equivalent to 10-16 cm -3 per hour . This decrease takes place over the 106, 629–641. https://agupubs.onlinelibrary.wiley.com/doi/abs/10.1029/2001JD900017

RGGVY, 2014. Deendayal Upadhyaya Gram Jyoti Yojana Guidelines. https://www.ddugjy.gov.in/assets/uploads/1548234273fykio.pdf.

Ridley, D.A., Heald, C.L., Prospero, J.M., 2014. What controls the recent changes in African mineral dust aerosol across the Atlantic? Atmos. Chem. Phys. 14, 5735–5747. https://doi.org/10.5194/acp-14-5735-2014

Riemer, N., West, M., Zaveri, R.A., Easter, R.C., 2009. Simulating the evolution of soot mixing state with a particle-resolved aerosol model. J. Geophys. Res. Atmos. 114. https://doi.org/10.1029/2008JD011073

Righi, M., Hendricks, J., Sausen, R., 2016. The global impact of the transport sectors on atmospheric aerosol in 2030 - Part 2: Aviation. Atmos. Chem. Phys. 16, 4481–4495. https://doi.org/10.5194/acp-16-4481-2016

Rosenfeld, D., Rudich, Y., Lahav, R., 2001. Desert dust suppressing precipitation: A possible desertification feedback loop. Proc. Natl. Acad. Sci. U. S. A. 98, 5975–5980. https://doi.org/10.1073/pnas.101122798

Rosenfeld, D., Woodley, W.L., Khain, A., Cotton, W.R., Carrió, G., Ginis, I., Golden, J.H., 2012. Aerosol effects on microstructure and intensity of tropical cyclones. Bull. Am. Meteorol. Soc. 93, 987–1001. https://doi.org/10.1175/BAMS-D-11-00147.1

Russell, P.B., Hobbs, P. V., Stowe, L.L., 1999. Aerosol properties and radiative effects in the United States East Coast haze plume: An overview of the tropospheric aerosol radiative forcing observational experiment (TARFOX). J. Geophys. Res. Atmos. 104, 2213–2222. https://doi.org/10.1029/1998JD200028

Saikawa, E., Kim, H., Zhong, M., Avramov, A., Zhao, Y., Janssens-Maenhout, G., Kurokawa, J.I., Klimont, Z., Wagner, F., Naik, V., Horowitz, L.W., Zhang, Q., 2017a. Comparison of emissions inventories of anthropogenic air pollutants and greenhouse

gases in China. Atmos. Chem. Phys. 17, 6393–6421. https://doi.org/10.5194/acp-17-6393-2017

Saikawa, E., Trail, M., Zhong, M., Wu, Q., Young, C.L., Janssens-Maenhout, G., Klimont, Z., Wagner, F., Kurokawa, J.I., Nagpure, A.S., Gurjar, B.R., 2017b. Uncertainties in emissions estimates of greenhouse gases and air pollutants in India and their impacts on regional air quality. Environ. Res. Lett. 12. https://doi.org/10.1088/1748-9326/aa6cb4

Samset, B.H., Lund, M.T., Bollasina, M., Myhre, G., Wilcox, L., 2019. Emerging Asian aerosol patterns. Nat. Geosci. 12, 582–584. https://doi.org/10.1038/s41561-019-0424-5

Sarangi, C., Tripathi, S.N., Mishra, A.K., Goel, A., Welton, E.J., 2016. Elevated aerosol layers and their radiative impact over Kanpur during monsoon onset period. J. Geophys. Res. 121, 7936–7957. https://doi.org/10.1002/2015JD024711

Sassen, K., Zhu, J., 2009. A global survey of CALIPSO linear depolarization ratios in ice clouds: Initial findings. J. Geophys. Res. Atmos. 114. https://agupubs.onlinelibrary.wiley.com/doi/full/10.1029/2009JD012279

Satheesh, S.K., Krishna Moorthy, K., 2005. Radiative effects of natural aerosols: A review. Atmos. Environ. 39, 2089–2110. https://doi.org/10.1016/j.atmosenv.2004.12.029

Satheesh, S.K., Ramanathan, V., Li-Jones, X., Lobert, J.M., Podgorny, I.A., Prospero, J.M., Holben, B.N., Loeb, N.G., 1999. A model for the natural and anthropogenic aerosols over the tropical Indian Ocean derived from Indian Ocean Experiment data. J. Geophys. Res. Atmos. 104, 27421–27440. https://doi.org/10.1029/1999JD900478

Satheesh, S.K., Vinoj, V., Moorthy, K.K., 2006. Vertical distribution of aerosols over an urban continental site in India inferred using a micro pulse lidar. Geophys. Res. Lett. 33. https://agupubs.onlinelibrary.wiley.com/doi/full/10.1029/2006GL027729

Satheesh, S.K., Vinoj, V., Suresh Babu, S., Krishna Moorthy, K., Nair, V.S., 2009. Vertical distribution of aerosols over the east coast of India inferred from airborne LIDAR measurements. Ann. Geophys. 27, 4157–4169. https://doi.org/10.5194/angeo-27-4157-2009

Scarnato, B. V., Vahidinia, S., Richard, D.T., Kirchstetter, T.W., 2013. Effects of internal mixing and aggregate morphology on optical properties of black carbon using a discrete dipole approximation model. Atmos. Chem. Phys. 13, 5089–5101. https://doi.org/10.5194/acp-13-5089-2013

Seinfeld, J.H., Pandis, S.N., 2006. ATMOSPHERIC From Air Pollution to Climate Change SECOND EDITION.

Sena, E.T., Artaxo, P., Correia, A.L., 2013. Spatial variability of the direct radiative forcing of biomass burning aerosols and the effects of land use change in Amazonia. Atmos. Chem. Phys. 13, 1261–1275. https://doi.org/10.5194/acp-13-1261-2013

Seo, Wookap Choi, Daeok Youn, Doo-Sun R. Park, and J.Y.K., 2013. Relationship between the stratospheric quasi-biennial oscillation and the spring rainfall in the western North Pacifi. https://agupubs.onlinelibrary.wiley.com/doi/full/10.1002/2013GL058266

Shaheen, R., Abauanza, M., Jackson, T.L., McCabe, J., Savarino, J., Thiemens, M.H., 2013. Tales of volcanoes and El-Niño southern oscillations with the oxygen isotope anomaly of sulfate aerosol. Proc. Natl. Acad. Sci. U. S. A. 110, 17662–17667. https://doi.org/10.1073/pnas.1213149110

Shamjad, P.M., Tripathi, S.N., Pathak, R., Hallquist, M., Arola, A., Bergin, M.H., 2015. Contribution of Brown Carbon to Direct Radiative Forcing over the Indo-Gangetic Plain. Environ. Sci. Technol. 49, 10474–10481. https://doi.org/10.1021/acs.est.5b03368

Sinha, P.R., Manchanda, R.K., Kaskaoutis, D.G., Kumar, Y.B., Sreenivasan, S., 2013. Seasonal variation of surface and vertical profile of aerosol properties over a tropical urban station hyderabad, India. J. Geophys. Res. Atmos. 118, 749–768. https://doi.org/10.1029/2012JD018039

Sogacheva, L., Rodriguez, E., Kolmonen, P., Virtanen, T.H., Saponaro, G., De Leeuw, G., Georgoulias, A.K., Alexandri, G., Kourtidis, K., Van Der, R.J.A., 2018. Spatial and seasonal variations of aerosols over China from two decades of multi-satellite observations - Part 2: AOD time series for 1995-2017 combined from ATSR ADV and MODIS C6.1 and AOD tendency estimations. Atmos. Chem. Phys. 18, 16631–16652. https://doi.org/10.5194/acp-18-16631-2018

Solmon, F., Nair, V.S., Mallet, M., 2015. Increasing Arabian dust activity and the Indian summer monsoon. Atmos. Chem. Phys. 15, 8051–8064. https://doi.org/10.5194/acp-15-8051-2015

Stanhill, G., Cohen, S., 2001. Global dimming: A review of the evidence for a widespread and significant reduction in global radiation with discussion of its probable causes and possible agricultural consequences. Agric. For. Meteorol. 107, 255–278. https://doi.org/10.1016/S0168-1923(00)00241-0

Steven N. Rogak, R.C.F.& H.V.N., 1993. The mobility and structure of aerosol agglomerates. Aerosol Sci. Technol. 18, 25–47. https://doi.org/10.1080/02786829308959582

Stull, R.B., 1988. An introduction to boundary layer meteorology. An Introd. to Bound. layer Meteorol. https://link.springer.com/book/10.1007/978-94-009-3027-8

Sugimoto, N., Matsui, I., Shimizu, A., Uno, I., Asai, K., Endoh, T., Nakajima, T., 2002. Observation of dust and anthropogenic aerosol plumes in the Northwest Pacific with a two-wavelength polarization lidar on board the research vessel Mirai. Geophys. Res. Lett. 29, 1–4. https://doi.org/10.1029/2002GL015112

Sugimoto, N., Uno, I., 2009. Observation of Asian dust and air-pollution aerosols using a network of ground-based lidars (ADNet): Realtime data processing for validation/assimilation of chemical transport models. IOP Conf. Ser. Earth Environ. Sci. 7, 012003. https://doi.org/10.1088/1755-1307/7/1/012003

Sunilkumar, S. V, Parameswaran, K., Thampi, B. V, 2012. Distribution of Particulates in the Tropical UTLS over the Asian Summer Monsoon Region and Its Association with Atmospheric Dynamics. Atmos. Aerosols Reg. Charact. Phys. 113. https://www.intechopen.com/chapters/38768

Suresh Babu, S., Nair, V.S., Gogoi, M.M., Krishna Moorthy, K., 2016. Seasonal variation of vertical distribution of aerosol single scattering albedo over Indian sub-continent: RAWEX aircraft observations. Atmos. Environ. 125, 312–323. https://doi.org/10.1016/j.atmosenv.2015.09.041

Swap, R.J., Annegarn, H.J., Suttles, J.T., Haywood, J., Helmlinger, et al., 2002. The Southern African Regional Science Initiative (SAFARI 2000): Overview of the dry season field campaign. S. Afr. J. Sci. 98, 125–130. https://scholarworks.umt.edu/cgi/viewcontent.cgi?article=1024&context=chem_pubs

Talukdar, S., Venkat Ratnam, M., Ravikiran, V., Chakraborty, R., 2019. Influence of Black Carbon Aerosol on the Atmospheric Instability. J. Geophys. Res. Atmos. 124, 5539–5554. https://doi.org/10.1029/2018JD029611

Tanré, D., Haywood, J., Pelon, J., Léon, J.F., Chatenet, B., Formenti, P., Francis, P., Goloub, P., Highwood, E.J., Myhre, G., 2003. Measurement and modeling of the Saharan dust radiative impact: Overview of the Saharan Dust Experiment (SHADE). J. Geophys. Res.

Atmos. 108, 1–12. https://doi.org/10.1029/2002jd003273

Thampi, B. V, Sunilkumar, S. V, Parameswaran, K., 2009. Lidar studies of particulates in the UTLS region at a tropical station over the Indian subcontinent. J. Geophys. Res. Atmos. 114. https://agupubs.onlinelibrary.wiley.com/doi/full/10.1029/2008JD010556

Torres, O., Tanskanen, A., Veihelmann, B., Ahn, C., Braak, R., Bhartia, P.K., Veefkind, P., Levelt, P., 2007. Aerosols and surface UV products form Ozone Monitoring Instrument observations: An overview. J. Geophys. Res. Atmos. 112, 1–14. https://doi.org/10.1029/2007JD008809

Tørseth, K., Aas, W., Breivik, K., Fjeraa, A.M., Fiebig, M., Hjellbrekke, A.G., Lund Myhre, C., Solberg, S., Yttri, K.E., 2012. Introduction to the European Monitoring and Evaluation Programme (EMEP) and observed atmospheric composition change during 1972-2009. Atmos. Chem. Phys. 12, 5447–5481. https://doi.org/10.5194/acp-12-5447-2012

Toth, T.D., Zhang, J., Campbell, J.R., Reid, J.S., Vaughan, M.A., 2016. Temporal variability of aerosol optical thickness vertical distribution observed from CALIOP. J. Geophys. Res. Atmos. 121, 9117–9139. https://agupubs.onlinelibrary.wiley.com/doi/full/10.1002/2015JD024668

Turner, A.G., Annamalai, H., 2012. Climate change and the South Asian summer monsoon. Nat. Clim. Chang. 2, 587–595. https://doi.org/10.1038/nclimate1495

Twomey, 1977. The influence of Pollution on the Shortwave Albedo of Clouds. https://doi.org/10.1175/1520-0469(1977)034<1149:TIOPOT>2.0.CO;2

Uno, I., Wang, Z., Itahashi, S., Yumimoto, K., Yamamura, Y., Yoshino, A., Takami, A., Hayasaki, M., Kim, B.G., 2020. Paradigm shift in aerosol chemical composition over regions downwind of China. Sci. Rep. 10, 1–11. https://doi.org/10.1038/s41598-020-63592-6

Van Der Werf, G.R., Randerson, J.T., Giglio, L., Collatz, G.J., Mu, M., Kasibhatla, P.S., Morton, D.C., Defries, R.S., Jin, Y., Van Leeuwen, T.T., 2010. Global fire emissions and the contribution of deforestation, savanna, forest, agricultural, and peat fires (1997-2009). Atmos. Chem. Phys. 10, 11707–11735. https://doi.org/10.5194/acp-10-11707-2010

Varekamp, J.F.L. and K.L.P., 1984. THE 1982 ERUPTIONS OF EL CHICHON VOLCANO (CHIAPAS, MEXICO): CHARACTER OF THE ERUPTIONS, ASH-FALL DEPOSITS, AND GASPHASE JOHAN. J. Volcanol. Geotherm. Res. 23. https://www.sciencedirect.com/science/article/abs/pii/0377027384900568

Vaughan, M.A., Young, S.A., Winker, D.M., Powell, K.A., Omar, A.H., Liu, Z., Hu, Y., Hostetler, C.A., 2004. Fully automated analysis of space-based lidar data: an overview of the CALIPSO retrieval algorithms and data products. Laser Radar Tech. Atmos. Sens. 5575, 16. https://doi.org/10.1117/12.572024

Vernier, J.-P., Fairlie, T.D., Deshler, T., Venkat Ratnam, M., Gadhavi, H., Kumar, B.S., Natarajan, M., Pandit, A.K., Akhil Raj, S.T., Hemanth Kumar, A., others, 2018. BATAL: The balloon measurement campaigns of the Asian tropopause aerosol layer. Bull. Am. Meteorol. Soc. 99, 955–973. https://journals.ametsoc.org/view/journals/bams/99/5/bams-d-17-0014.1.xml

Vernier, J.-P., Thomason, L.W., Kar, J., 2011. CALIPSO detection of an Asian tropopause aerosol layer. Geophys. Res. Lett. 38. https://agupubs.onlinelibrary.wiley.com/doi/full/10.1029/2010GL046614

Vernier, T. D. Fairlie, M. Natarajan, F. G. Wienhold, J. Bian, B. G. Martinsson, S. Crumeyrolle, L. W. Thomason, and K.M.B., 2015. Increase in upper tropospheric and lower stratospheric aerosol levels and its potential connection with Asian pollution. J. Geophys. Res. Ocean. 2813–2825. https://doi.org/10.1002/2014JD022372

Vestreng, V., Myhre, G., Fagerli, H., Reis, S., Tarrasón, L., 2007. Twenty-five years of continuous sulphur dioxide emission reduction in Europe. Atmos. Chem. Phys. 7, 3663–3681. https://doi.org/10.5194/acp-7-3663-2007

Vinoj, V., Rasch, P.J., Wang, H., Yoon, J.H., Ma, P.L., Landu, K., Singh, B., 2014. Short-term modulation of Indian summer monsoon rainfall by West Asian dust. Nat. Geosci. 7, 308–313. https://doi.org/10.1038/ngeo2107

Volz, F., 1959. Photometer mit Selen-Photoelement zur spektralen Messung der Sonnenstrahlung und zur Bestimmung der Wellenlängenabhängigkeit der Dunsttrübung. Arch. für Meteorol. Geophys. und Bioklimatologie Ser. B 10, 100–131. https://doi.org/10.1007/BF02243122

Wallace, John M, P.V.H., 2006. Atmospheric Sceince: An introductory Survey.

Wang, S., Li, S., Xing, J., Yang, J., Dong, J., Qin, Y., Sahu, S.K., 2022. Evaluation of the influence of El Niño-Southern Oscillation on air quality in southern China from long-term historical observations. Front. Environ. Sci. Eng. 16. https://doi.org/10.1007/s11783-021-1460-0

Wang, Y., Khalizov, A., Levy, M., Zhang, R., 2013. New Directions: Light absorbing aerosols and their atmospheric impacts. Atmos. Environ. 81, 713–715. https://doi.org/10.1016/j.atmosenv.2013.09.034

Wei, J., Li, Z., Lyapustin, A., Sun, L., Peng, Y., Xue, W., Su, T., Cribb, M., 2021a. Reconstructing 1-km-resolution high-quality PM2.5 data records from 2000 to 2018 in China: spatiotemporal variations and policy implications. Remote Sens. Environ. 252, 112136. https://doi.org/https://doi.org/10.1016/j.rse.2020.112136

Wei, J., Li, Z., Peng, Y., Sun, L., 2019a. MODIS Collection 6.1 aerosol optical depth products over land and ocean: validation and comparison. Atmos. Environ. 201, 428–440. https://doi.org/10.1016/j.atmosenv.2018.12.004

Wei, J., Li, Z., Xue, W., Sun, L., Fan, T., Liu, L., Su, T., Cribb, M., 2021b. The ChinaHighPM10 dataset: generation, validation, and spatiotemporal variations from 2015 to 2019 across China. Environ. Int. 146, 106290. https://doi.org/https://doi.org/10.1016/j.envint.2020.106290

Wei, J., Peng, Y., Mahmood, R., Sun, L., Guo, J., 2019b. Intercomparison in spatial distributions and temporal trends derived from multi-source satellite aerosol products. Atmos. Chem. Phys. 19, 7183–7207. https://doi.org/10.5194/acp-19-7183-2019

Wilcox, L.J., Highwood, E.J., Dunstone, N.J., 2013. The influence of anthropogenic aerosol on multi-decadal variations of historical global climate. Environ. Res. Lett. 8. https://doi.org/10.1088/1748-9326/8/2/024033

Wild, M., 2009. Global dimming and brightening: A review. J. Geophys. Res. Atmos. 114, 1–31. https://doi.org/10.1029/2008JD011470

Wild, M., 2016. Decadal changes in radiative fluxes at land and ocean surfaces and their relevance for global warming. Wiley Interdiscip. Rev. Clim. Chang. 7, 91–107. https://doi.org/10.1002/wcc.372

Wilkins, 1953. Air pollution and the london fog of december 1952. J. R. Sanit. Inst. 74–1. https://journals.sagepub.com/doi/abs/10.1177/146642405407400101?journalCode=rsha

Winker, D.M., Tackett, J.L., Getzewich, B.J., Liu, Z., Vaughan, M.A., Rogers, R.R., 2013. The global 3-D distribution of tropospheric aerosols as characterized by CALIOP. Atmos. Chem. Phys. 13, 3345–3361. https://doi.org/10.5194/acp-13-3345-2013

Winker, David M., Vaughan, M.A., Omar, A., Hu, Y., Powell, K.A., Liu, Z., Hunt, W.H., Young, S.A., 2009. Overview of the CALIPSO mission and CALIOP data processing algorithms. J. Atmos. Ocean. Technol. 26, 2310–2323. https://doi.org/10.1175/2009JTECHA1281.1

Wu, Y.L., Davidson, C.I., Dolske, D.A., Sherwood, S.I., 1992. Dry deposition of atmospheric contaminants: The relative importance of aerodynamic, boundary layer and, surface resistances. Aerosol Sci. Technol. 16, 65–81. https://doi.org/10.1080/02786829208959538

Xie, H., Zhao, J., Wang, K., Peng, H., 2021. Long-term variations in solar radiation, diffuse radiation, and diffuse radiation fraction caused by aerosols in China during 1961-2016. PLoS One 16, 1–14. https://doi.org/10.1371/journal.pone.0250376

Xing, L., Fu, T.M., Cao, J.J., Lee, S.C., Wang, G.H., Ho, K.F., Cheng, M.C., You, C.F., Wang, T.J., 2013. Seasonal and spatial variability of the OM/OC mass ratios and high regional correlation between oxalic acid and zinc in Chinese urban organic aerosols. Atmos. Chem. Phys. 13, 4307–4318. https://doi.org/10.5194/acp-13-4307-2013

Xiong, X., Houweling, S., Wei, J., Maddy, E., Sun, F., Barnet, C., 2009. Methane plume over south Asia during the monsoon season: Satellite observation and model simulation. Atmos. Chem. Phys. 9, 783–794. https://doi.org/10.5194/acp-9-783-2009

Xu, X., & Wang, J. (2015). Retrieval of aerosol microphysical properties from AERONET photopolarimetric measurements: 1. Information content analysis. *Journal of Geophysical Research*, *120*(14), 7059–7078. https://doi.org/10.1002/2015JD023108

Xu, X., Zhao, W., Qian, X., Wang, S., Fang, B., Zhang, Q., Zhang, W., Venables, D.S., Chen, W., Huang, Y., Deng, X., Wu, B., Lin, X., Zhao, S., Tong, Y., 2018. The influence of photochemical aging on light absorption of atmospheric black carbon and aerosol single-scattering albedo. Atmos. Chem. Phys. 18, 16829–16844. https://doi.org/10.5194/acp-18-16829-2018

Yan, X., Zang, Z., Li, Z., Luo, N., Zuo, C., Jiang, Y., Li, D., Guo, Y., Zhao, W., Shi, W., Cribb, M., 2021. A global land aerosol fine-mode fraction dataset (2001–2020) retrieved from MODIS using hybrid physical and deep learning approaches. Earth Syst. Sci. Data Discuss. 5105617, 1–27. https://doi.org/10.5194/essd-2021-326

Young, S.A., Vaughan, M.A., 2009. The retrieval of profiles of particulate extinction from cloud-aerosol lidar infrared pathfinder satellite observations (CALIPSO) data: Algorithm description. J. Atmos. Ocean. Technol. 26, 1105–1119. https://doi.org/10.1175/2008JTECHA1221.1

Yousefi, R., Wang, F., Ge, Q., Shaheen, A., 2020. Long-term aerosol optical depth trend over Iran and identification of dominant aerosol types. Sci. Total Environ. 722. https://doi.org/10.1016/j.scitotenv.2020.137906

Yu, H., Chin, M., Bian, H., Yuan, T., Prospero, J.M., Omar, A.H., Remer, L.A., Winker, D.M., Yang, Y., Zhang, Y., Zhang, Z., 2015a. Quantification of trans-Atlantic dust transport from seven-year (2007-2013) record of CALIPSO lidar measurements. Remote Sens. Environ. 159, 232–249. https://doi.org/10.1016/j.rse.2014.12.010

Yu, H., Chin, M., Winker, D.M., Omar, A.H., Liu, Z., Kittaka, C., Diehl, T., 2010. Global view of aerosol vertical distributions from CALIPSO lidar measurements and GOCART simulations: Regional and seasonal variations. J. Geophys. Res. Atmos. 115.

https://agupubs.onlinelibrary.wiley.com/doi/10.1029/2009JD013364

Yu, H., Liu, S.C., Dickinson, R.E., 2002. Radiative effects of aerosols on the evolution of the atmospheric boundary layer. J. Geophys. Res. Atmos. 107. https://doi.org/10.1029/2001jd000754

Yu, P., Toon, O.B., Neely, R.R., Martinsson, B.G., Brenninkmeijer, C.A.M., 2015b. Composition and physical properties of the Asian Tropopause Aerosol Layer and the North American Tropospheric Aerosol Layer. Geophys. Res. Lett. 42, 2540–2546. https://doi.org/10.1002/2015GL063181

Zhang, L., Henze, D.K., Grell, G.A., Torres, O., Jethva, H., Lamsal, L.N., 2017. What factors control the trend of increasing AAOD over the United States in the last decade? J. Geophys. Res. 122, 1797–1810. https://doi.org/10.1002/2016JD025472

Zhang, Q., He, K., Hong, H., 2012. Cleaning China's air. Nature 484, 161–162. https://www.nature.com/articles/484161a

Zhao, A., Bollasina, M.A., Crippa, M., Stevenson, D.S., 2019. Significant climate impacts of aerosol changes driven by growth in energy use and advances in emission control technology. Atmos. Chem. Phys. 19, 14517–14533. https://doi.org/10.5194/acp-19-14517-2019

Zhao, B., Jiang, J.H., Gu, Y., Diner, D., Worden, J., Liou, K.N., Su, H., Xing, J., Garay, M., Huang, L., 2017. Decadal-scale trends in regional aerosol particle properties and their linkage to emission changes. Environ. Res. Lett. 12. https://doi.org/10.1088/1748-9326/aa6cb2

Zhu, A., Xu, H., Deng, J., Ma, J., Li, S., 2020. ENSO Effect on Interannual Variability of Spring Aerosols over East Asia. Atmos. Chem. Phys. Discuss. 1–32. https://acp.copernicus.org/articles/21/5919/2021/

List of Publications:

1. **Gupta, G**., Ratnam, M.V., Madhavan, B.L., Prasad, P., Narayanamurthy, C.S., 2021. Vertical and spatial distribution of elevated aerosol layers obtained using long-term ground-based and space-borne lidar observations. Atmos. Environ. 246, 118172. https://doi.org/10.1016/j.atmosenv.2020.118172.
2. **Gupta, G**., Venkat Ratnam, M., Madhavan, B.L., Narayanamurthy, C.S., 2022. Long-term trends in Aerosol Optical Depth across the globe obtained using multi-satellite measurements. Atmos. Environ. 273, 118953. https://doi.org/10.1016/j.atmosenv.2022.118953.
3. **Gupta, G**., et al., Global trends in the Aerosols Optical, Physical, and Morphological properties obtained using Multi-sensor measurements. (Manuscript communicated)
4. **Gupta, G**., et al., Global distribution of the trend variations in the Aerosols Chemical properties. (Manuscript ready for communication)

Conference Presentations:

- Presented '***Vertical and spatial distribution of elevated aerosol layers obtained using long-term ground based and space borne lidar observations***' in the International Symposium on Tropical Meteorology (INTROMET)-21 by Cochin University of Science and Technology, Kerala during November 23-26, 2021.
- Presented '***Long-term trends in Aerosol Optical Depth across the globe with special emphasis on South-East Asia obtained using multi-satellite measurements***' in the 21st National Space Science Symposium (NSSS) conducted by IISER, Kolkata during January 31-February 4, 2022.